



**José Antonio Pérez
de la Torre**

**Obtenção e caracterização de cristais e cerâmicos
de PZT**

**Obtaining and characterization of single crystals and
ceramics of PZT**



**José Antonio Pérez
de la Torre**

**Obtenção e caracterização de cristais e cerâmicos de
PZT**

**Obtaining and characterization of single crystals and
ceramics of PZT**

Dissertação apresentada à Universidade de Aveiro para cumprimento dos requisitos necessários à obtenção do grau de Doutor em Ciência e Engenharia de Materiais, realizada sob a orientação científica da Doutora Ana Maria de Oliveira e Rocha Senos, Professora Auxiliar do Departamento de Engenharia Cerâmica e do Vidro da Universidade de Aveiro, e do Doutor Pedro Manuel Lima de Quintanilha Mantas Professor Auxiliar do Departamento de Engenharia Cerâmica e do Vidro da Universidade de Aveiro

Dissertation presented to de University of Aveiro to obtain the Doctor degree in Materials Science and Engineering, under the scientific guidance of Dr. Ana Maria de Oliveira e Rocha Senos, Auxiliary Professor of the Department of Ceramics and Glass Engineering of the University of Aveiro, and Dr. Pedro Manuel Limas de Quintanilha Mantas, Auxiliary Professor of the Department of Ceramics and Glass Engineering of the University of Aveiro

I acknowledge the Portuguese Foundation for Science and Technology (FCT) for their financial support through a PhD grant (SFRH/BD/19992/2004)

Dedico esta tese a meus pais Silvio e Blaza pelo apoio incondicional de sempre. Obrigado pais.

o júri

presidente

Prof. Dr. Amadeu Mortagua Velho da Maria Soares
professor Catedrático do departamento de Biologia da Universidade de Aveiro

Prof. Dr. Jorge Riveiro Frade
professor atedrático do departamento de Engenharia Cerâmica e do Vidro da Universidade de Aveiro

Prof. Dr. Regina da Conceição Corredeira Monteiro
professora associada do departamento de Ciência dos Materiais da Faculdade de Ciência e Tecnologia da Universidade Nova de Lisboa

Prof. Dr. Mário António Caixeiro de Castro Pereira
professor Auxiliar do departamento de Física da Escola de Ciências da Universidade do Minho

Prof. Dr. Ana Maria Oliveira e Rocha Senos
professor Auxiliar do departamento de Engenharia Cerâmica e do Vidro da Universidade de Aveiro

Prof. Dr. Pedro Manuel Lima de Quintanilha Mantas
professor Auxiliar do departamento de Engenharia Cerâmica e do Vidro da Universidade de Aveiro

acknowledgments

It would not be fair to finish this thesis without mentioning all those people whose support has been very important during these years. Certainly, there are many to whom I must be grateful, and the doubt that somebody is forgotten in these few words is always present. That is why, in the first place, I want to send a message of general gratefulness to all those who surround me and in some way have contributed to this work, as well as to my scientific and human development.

First of all, I am deeply grateful to my supervisor Prof. Dr. Ana Maria de Oliveira e Rocha Senos for her continuous support and encouragement, for her frequent suggestions and discussions in many subjects, especially in materials science, for her careful revision and criticism of the manuscript, and more important, for her confidence in me to perform this thesis with the necessary freedom. I am also very grateful to my co-supervisor Prof. Dr. Pedro Mantas, for his scientific support and revision of the manuscript, cordial advice, and useful discussions in many subjects of this work.

I would like to express my sincere gratitude to all my colleagues from the Department of Ceramics and Glass Engineering for their valuable help, empathy and friendship during all these years, from the administrative and technical staff to all the PhD and Postdoc students of the 3rd floor, as well as all the members of the Ferroelectric Group, for the excellent atmosphere of work and scientific interchange in special to Professor Kholkin and to Surandra for revision of the manuscript, to Professor Agostinho, to Igor and Filipe for the collaborative work.

I want to express my grateful thanks to my best friends in Aveiro, Javier, Gerardo and Harvey for their sincere friendship. I am also fortunate for having many excellent friends during these years in Portugal, Rosario, Merche, Laura, Xana, David, Rogerio e Mariana, Duncan, Flori, Ricardo, Alexander ... my sincere gratitude to all this international group for their friendship and for sharing many parties and meals, for the stress relief after a working day.

I am exceedingly grateful to all my family, the main source of love and support during all my life, the primary inspiration since my first day in this scientific life, which will be with me wherever I am. Special gratitude goes to my parents Silvio and Blaza, who knew it from the beginning, to my brother and sister, who follows our steps, and to all my wonderful family to may new fathers Fidel, Elina, Laude and Jorge.

I am also very grateful to my family-in-law for accepting me as a son.

Last but not least, the most special gratitude is for my girlfriend Susana, who has become a special part of my life, who encourages me every day and trusts in me continually, who takes the main decisions at my side. Thank you Susana for your patience, your understanding in the most difficult moments, and your absolute support... in other words, thank you for love...

palavras-chave

cristais de PZT, fase morfotrópica, propriedades dielétricas, ferroelétricas, piezoelétricas, domínios ferroelétricos

resumo

É conhecido que as propriedades electromecânicas do zirconato titanato de chumbo, $\text{PbZr}_x\text{Ti}_{1-x}\text{O}_3$ (PZT), alcançam um máximo na região morfotrópica. Este trabalho foi desenvolvido na tentativa de explicar as causas deste máximo e a sua dependência com a microestrutura. Para conhecer essas causas, que provocam o aparecimento de um máximo nas propriedades electromecânicas foi necessário estudar cerâmicos com composições próximas da zona morfotrópica. Os cerâmicos foram caracterizados do ponto de vista dielétrico e estrutural e o máximo da constante dielétrica na região morfotrópica foi confirmado, assim como a sua dependência do tamanho do grão. A posição do máximo de permitividade está relacionada com o ponto onde ocorre a transição de fase da estrutura romboédrica para tetragonal.

Para conhecer as propriedades intrínsecas do PZT surgiu a necessidade de produzir monocristais destes compostos com dimensões e qualidade adequadas à medição das suas propriedades. No presente trabalho, fizeram-se crescer monocristais de PZT com boa qualidade e dimensões relativamente elevadas, usando um método de solução a alta temperatura, com um fluxo de $[\text{PbO-KF-PbCl}_2]\text{-B}_2\text{O}_3$, numa razão molar de 60/40 entre PZT e fluxo. Primeiro, optimizaram-se as condições de processamento, testando-se diferentes perfis de temperatura e percentagem de fluxo para promover o crescimento e melhorar a qualidade dos cristais de PZT. As condições identificadas como óptimas foram usadas para depois fazer crescer cristais de PZT. Os cristais obtidos evidenciaram uma morfologia cúbica com dimensões típicas de $\sim 3 \times 3 \times 3 \text{ mm}^3$.

A zona morfotrópica compreende as fases romboédrico e tetragonal e a fronteira entre ambos. A sua caracterização incidiu fundamentalmente na análise de cinco dos cristais obtidos, tendo sido seleccionados dois da fase romboédrico, dois da tetragonal e um com a composição química da fronteira entre aqueles dois fases. Os cristais foram caracterizados por medidas dieléctricas, ferroeléctricas e piezoeléctricas realizadas paralelamente ao eixo *c* (direcção [001]) ou perpendicularmente ao plano *ab* (110) (discrções de acordo com a análise da difracção de raios X). As medidas de difracção de raios X foram realizadas a 180 K para todos os cristais e a 300 K sempre que necessário. Neste estudo foram feitas duas modificações do diagrama de fases. A fase romboédrica de baixa temperatura (R3c) não é detectada para as composições com menos de 65% em Zr e, por outro lado, a região morfotrópica não existe em monocristais. Observaram-se ciclos de histerese saturados quando se aplicou um campo eléctrico alternado perpendicular ao plano *ab* do cristal. A polarização espontânea segundo o eixo ferroeléctrico foi estimada em cerca de $\approx 40 \mu\text{C}/\text{cm}^2$ para um cristal com 50% em Zr. O coeficiente piezoeléctrico d_{33} , medido segundo a direcção [001] (eixo polar), é de $\approx 20 \text{ pm}/\text{V}$ para um cristal com 50% em Zr. A estrutura de domínios foi estudada e foi observado que o número de domínios aumenta e o seu tamanho diminui perto da região morfotrópica. O padrão de domínios varia desde muito definido, para alta concentração de Ti, até desaparecer no centro da região morfotrópica. O máximo das propriedades electromecânicas deste material é explicado neste trabalho por uma diminuição da distorção da estrutura tetragonal o que a torna instável perto do centro da região morfotrópica fazendo com que pequenos campos eléctricos mudem a estrutura de uma fase para outra. Esta rápida mudança de fase provoca grandes variações na polarização, incrementando as propriedades dieléctricas e electromecânicas.

O presente trabalho estudou a possibilidade de usar os cristais de PZT como sementes para induzir o crescimento de grãos nos cerâmicos de PZT pela via de "seeded polycrystalline conversion (SPC)". Produziram-se cerâmicos de PZT com grãos grandes usando sementes com tamanho médio de $\sim 30 \times 30 \times 30 \mu\text{m}^3$. Dispersou-se uma pequena quantidade de sementes numa matriz de partículas finas de PZT contendo um excesso de fase líquida. Avaliaram-se os efeitos de vários parâmetros de processamento, tais como a composição e o excesso da fase líquida e as condições de sinterização, com o objectivo de obter cerâmicos densos com grãos grandes.

keywords

PZT, single crystals, morphotropic phase boundary, grain growth, dielectric properties, ferroelectric, piezoelectric, domains

abstract

The electromechanical properties of lead zirconate titanate $\text{PbZr}_x\text{Ti}_{1-x}\text{O}_3$ (PZT) materials achieve maxima values in the morphotropic phase boundary. The present research was stimulated by the interest on knowing the causes for these maxima and their dependence on the microstructure. To know the causes that provoke the appearance of a maximum in the electromechanical properties, it was necessary to study ceramics with compositions around the morphotropic phase boundary. The ceramics were characterized from the dielectric and structural viewpoints and the maxima in the morphotropic phase boundary were confirmed, as well as their dependence on the grain size. The position of the maximum of the permittivity is related to the point where the phase transition from the rhombohedral structure to tetragonal one occurs in single crystals.

For understanding the intrinsic properties of the PZT it was necessary to grow single crystals with suitable dimensions and adequate quality for measurements of the properties. In the present work, PZT single crystals were grown with sufficient size and quality, using a high temperature solution method, with a flux of $[\text{PbO-KF-PbCl}_2]\text{-B}_2\text{O}_3$ in a molar ratio of 60/40 between PZT and flux. Initially, the conditions of processing were optimized, followed by different profiles of temperature and flux amounts, to promote the crystal growth and quality of the PZT crystals. The conditions identified as best were used to grow PZT crystals. The crystals obtained showed a cubic morphology with typical size of $\sim 3 \times 3 \times 3 \text{ mm}^3$.

The morphotropic region comprises the rhombohedral and the tetragonal fields and the boundary between them. Its characterization was performed mainly on analysing five crystals, by selecting two of them of the rhombohedral field, other two of tetragonal field and the other one with the chemical composition of the boundary between those two fields. PZT crystals were characterized using dielectric, ferroelectric and piezoelectric measurements, which were carried out either parallel to c axis ([001] direction) or perpendicular to the plane ab (110) (in accordance with the x-rays diffraction analysis). The x-rays diffraction measurements were carried out at 180 K for all the crystals and also at 300 K whenever necessary. In this study, two modifications of the phase diagram were introduced. The low-temperature rhombohedral phase (R3c) does not appear for Zr composition less than 65% and, on the other hand, the morphotropic region does not exist in single crystals. Saturated hysteresis loops were observed when an alternative electric field was applied perpendicular to the ab plane of the crystal. The spontaneous polarization in the direction of the ferroelectric axis was estimated to be $\approx 40 \mu\text{C}/\text{cm}^2$ for a crystal with 50% of Zr. The piezoelectric coefficient d_{33} was measured in the [001] direction (polar axis) and is $\approx 20 \text{ pm}/\text{V}$ for a crystal with 50% in Zr. The domain distribution was studied and it was observed that the number of domains increases as the size decreases near the morphotropic boundary.

The domain pattern varies from a state of definite visibility for high Ti concentration, to a complete disappearance on approaching the centre of the morphotropic region. The maximum of the electromechanical properties of this material is explained in this work based on a decrease of the distortion of the tetragonal structure which becomes unstable near the centre of the morphotropic region and where a small electric field changes the structure from one phase to another. This fast change between phases provokes great variations in the polarization and hence increases the dielectric and electromechanical properties.

The present work also studied the possibility of using PZT crystals as seeds to induce the grain growth in PZT ceramic by the seeded polycrystalline conversion method (SPC). PZT ceramic with large grains were produced using seeds with average size of $\sim 30 \times 30 \times 30 \mu\text{m}^3$. A small amount of seeds was dispersed in a fine particle matrix of PZT, containing an excess of liquid phase. The effects of the different parameters such as composition, excess of liquid phase and sintering conditions were studied with the purpose of obtaining dense ceramic with large grains.

Table of contents

Introduction.....	1
1. CHAPTER 1: Background on ferroelectric materials and applications.....	4
1.1. Ferroelectricity and piezoelectricity: basic definitions	4
1.1.1. Applications of ferroelectrics	4
1.1.2. Ferroelectric phenomena and spontaneous polarization	6
1.1.3. Electric field and polarization	8
1.1.4. Pyroelectric effect and pyroelectric current	12
1.1.5. Piezoelectric coefficients and related properties.....	13
1.1.6. Ferroelectric and ferroelastic domains	19
1.1.7. Nonlinear dielectric properties, polarization switching and hysteresis loop.....	21
1.2. Perovskite types of ferroelectric materials	25
1.2.1. Lead titanate (PbTiO ₃ , PT).....	27
1.2.2. Lead zirconate (PbZrO ₃ , PZ).....	28
1.2.3. Lead zirconate titanate [Pb(Zr _x Ti _{1-x})O ₃ , PZT]	30
1.3. Effects of the microstructure on the piezoelectric properties.....	35
1.4. Theory for the morphotropic phase boundary (MPB).....	38
1.4.1. Principal ideas to explain the maxima of the electro-mechanical properties in the MPB	39
1.4.2. Causes for the occurrence of the phase coexistence in the MPB	44
1.5. Ferroelectric phase transition	47
1.6. Soft mode theory for the ferroelectricity	51
2. CHAPTER 2: Background on PZT single crystals growth by flux and seeded polycrystalline conversion.....	55
2.1. Single crystals growth	55
2.1.1. Methods for growing single crystals	55
2.1.2. Single crystal growth from the melt.....	56
2.1.3. Single crystal growth from solution (flux).....	57
2.2. PZT single crystals	61
2.2.1. Morphological and optical characterisation of PZT crystals	65
2.2.2. Optical properties of PZT crystal	66
2.2.3. Raman characterisation of the PZT crystals.....	67
2.2.4. Electrical and domain characterisation of PZT crystals.....	68

Table of contents

2.2.5.	Structural characterisation and phase diagram of PZT crystals	78
2.3.	The seeded polycrystalline conversion (SPC) and templated grain growth (TGG) processes	83
2.3.1.	Templated grain growth (TGG) in PZT	86
3.	CHAPTER 3: Materials processing and experimental techniques.....	88
3.1.	Ceramics preparation.....	88
3.1.1.	Synthesis of PZT powders	88
3.1.2.	Preparation of frits.....	88
3.1.3.	Pressing and sintering of PZT ceramics.....	89
3.2.	Preparation of PZT single crystal.....	90
3.2.1.	Crystals growth from flux	90
3.3.	Seeded polycrystalline conversion (SPC) method	94
3.4.	Electroding and surface preparation.....	95
3.5.	Phase identification and microstructure characterisation.....	97
3.5.1.	X-ray diffraction (XRD) of powders.....	97
3.5.2.	X-ray diffraction (XRD) of single crystals	97
3.5.3.	Scanning electron microscopy (SEM) and electron energy dispersive spectrometer (EDS)	98
3.5.4.	Electron probe microanalysis (EPMA).....	98
3.5.5.	Transmission electron microscopy (TEM).....	99
3.6.	Electric characterisation	99
3.6.1.	Measurement of dielectric properties.....	99
3.6.2.	Pyroelectric characterisation	100
3.6.3.	Piezoelectric characterisation.....	100
3.6.4.	Hysteresis loop	101
3.6.5.	Piezoresponse scanning force microscopy.....	102
3.7.	Raman scattering	104
4.	CHAPTER 4: Growth and characterisation of $\text{PbZr}_x\text{Ti}_{1-x}\text{O}_3$ single crystals.....	105
4.1.	Obtention of PZT single crystals.....	105
4.1.1.	Single crystal growth and optimization of the conditions.....	105
4.1.2.	Morphology of the grown crystals	109
4.2.	X-ray diffraction and chemical characterisation	110

Table of contents

4.2.1.	Rhombohedral single crystals	110
4.2.2.	Tetragonal single crystals.....	122
4.2.3.	Single crystals with chemical compositions near the MPB	127
4.3.	Raman study of the PZT52 single crystal	134
4.3.1.	Room temperature analysis	134
4.3.2.	Variation of the Raman spectra with temperature.....	137
4.4.	Dielectric, ferroelectric and piezoelectric properties	144
4.4.1.	Dielectric characterisation.....	144
4.4.2.	Hysteresis loop measurement in a pseudo cubic crystal	151
4.4.3.	Piezoelectric characterisation.....	152
4.4.4.	Piezoelectric force microscopy: distribution of domains.....	157
4.5.	Thermodynamics of the systems	168
5.	CHAPTER 5: Processing and characterisation of $\text{PbZr}_x\text{Ti}_{1-x}\text{O}_3$ ceramics	177
5.1.	PZT ceramics without a liquid phase	177
5.1.1.	Dielectric characterisation.....	178
5.1.2.	Piezoelectric response and distribution of domains	185
5.2.	Ceramic processing and X-ray characterisation.....	194
5.2.1.	Densification results.....	194
5.2.2.	X-ray diffraction analyses	198
5.2.3.	Microstructure evolution	200
5.2.4.	Dielectric characterisation.....	207
5.3.	PZT crystal growth using the seeded polycrystalline conversion method	213
6.	CHAPTER 6: General conclusions.....	217
	Future work	219
	Appendix I.....	221
	Appendix II.....	234
	References	238

GLOSSARY OF SYMBOLS

a, b, c	unit cell parameter
ac	alternate current
a_R	rhombohedral lattice parameter
a_T	tetragonal lattice parameter
A	electrode area
A_O	antiferroelectric orthorhombic phase
A_T	antiferroelectric intermediate phase (F2mm)
$\alpha_1, \alpha_{ij}, \alpha_{ijk}$	dielectric stiffness and higher order stiffness coefficients at constant stress
α, β, γ	unit cell angles
b_{ij}	piezoelectric polarization related coefficients
C	Curie-Weiss constant
c_{11}^E	compliance at constant electric field (E)
c_{ijkl}	elastic compliance coefficients
χ	dielectric susceptibility
χ_{ij}	dielectric susceptibility tensors
dc	direct current
d_R	diagonal of the rhombohedron lattice
d_{ijk}, d_{ij}	piezoelectric strain coefficients
D_i	electric displacement
δ	parameter associated to the degree of disorder in the system
ΔT	temperature change
E_i	electric field
E_{ex}	external electric field
E_a	activation energy
$E_{a.c}$	alternate electric field
E_C	coercive field
E_s	internal field
E_d	depolarizing field

Glossary of symbols

ϵ_{ij}	dielectric permittivity
$\epsilon_{r\ ij}$	relative dielectric permittivity
ϵ_0	dielectric permittivity of the vacuum (8.85×10^{-12} F/m)
ϵ''	imaginary part of the permittivity
ϵ'	real part of the permittivity
ϵ_{33}^T	permittivity in the direction of the polar axis (free)
ϵ_{11}^T	permittivity in the directions perpendicular to the polar axis (free)
ϵ_{33}^S	permittivity in the direction of polar axis (clamped)
ϵ_{11}^S	permittivity in the directions perpendicular to the polar axis (clamped)
ϵ_{max}	maximum of the permittivity
ϵ_{33}^X	dielectric constant at constant stress (X)
F_T	ferroelectric tetragonal phase
$F_{R(HT)}$	ferroelectric rhombohedral phase of high temperature
$F_{R(LT)}$	ferroelectric rhombohedral phase of low temperature
f	frequency
f_r	resonance frequency
f_a	antiresonance frequency
Φ_0	thermodynamic potential
G	Gibbs' free energy
g_{ij}	piezoelectric voltage coefficients
γ	parameter
γ	exponent
η_{ij}	inverse of the dielectric susceptibility (dielectric stiffness coefficient)
k_{ij}	electromechanical coupling coefficient
k_p	planar coupling factor
K	constant
LO	longitudinal optical modes
λ	the volumetric thermal expansion coefficient
M_{ijkl}	electrostriction constants written in voltage notation
n_1, n_2	constants

Glossary of symbols

n_o	refractive index for polarizations perpendicular to the incident direction (ordinary)
n_e	refractive indices for polarizations parallel to the incident direction (extraordinary)
ν	Poisson's ratio
P	polarization
P_S	spontaneous polarization
P_r	remanent polarization
$P_{S_i}(T_c)$	polarization at the Curie temperature (T_c)
p_i	pyroelectric coefficient
P_o	polarization at the transition temperature
P_c	paraelectric cubic phase
Q_{ijkl}	electrostriction constants written in polarization notation
Q_m	mechanical quality factor
S	entropy
S_{ijkl}	elastic stiffness coefficients
σ_i	surface charge density
$\sigma(\omega)$	conductivity in alternate current
T	temperature
T_c	Curie point
T_o	Curie-Weiss temperature
T_{max}	temperature of the maximum of the permittivity
TO	transversal optical modes
$\tan\delta$	tangent of the loss angle
U	internal energy
V	volume, voltage
W_e	elastic energy
ω_e	effective frequency
ω_r	resonance frequency
ω_p	hopping frequency
X, Y, Z	directions

Glossary of symbols

X_{ij}	stress
x_{ij}	strain
x_T	composition in the tetragonal field
x_R	composition in the rhombohedral field
\bar{x}	mean average composition
x_{ij}	spontaneous elastic strain
ζ, ξ	parameters
t	denotes the transposed matrix
$[]$	direction
$\langle \rangle$	equivalents directions
$()$	plane
$\{ \}$	equivalents planes
\leftrightarrow	phase transition

ABBREVIATIONS

AFM	Atomic force microscopy
B6T17	$\text{Ba}_6\text{Ti}_{17}\text{O}_{40}$
BT	BaTiO_3
CT	CaTiO_3
EDS	Electron energy dispersive spectrometer
EPMA	Electron probe microanalysis
HTS	High-temperature solution
IEEE	Institute of Electrical and Electronics Engineers
IPP	In-plane polarization
KN	KNbO_3
KNN	$\text{K}_x\text{Na}_{1-x}\text{NbO}_3$
KTN	$\text{KTa}_x\text{Nb}_{1-x}\text{O}_3$
LGD	Landau – Ginzburg – Devonshire
MPB	Morphotropic phase boundary
OPP	Out-of-plane polarization
PFM	Piezoelectric force microscopy
PLZT	Lead Lanthanum Zirconate Titanate
PMN	$\text{PbMg}_x\text{Nb}_{1-x}\text{O}_3$
PT	Lead titanate (PbTiO_3)
PZ	Lead zirconate (PbZrO_3)
PZT	Lead zirconate titanate ($\text{PbZr}_x\text{Ti}_{1-x}\text{O}_3$)
PZT52	$\text{PbZr}_{0.52}\text{Ti}_{0.48}\text{O}_3$
RTGG	Reactive templated grain growth
SEM	Scanning electron microscope
SPC	Seeded polycrystalline conversion method
SSPM	Scanning surface probe microscope
Td	Theoretical density
TGG	Templated grain growth
XRD	X-ray diffraction

Introduction

The human evolution is closely related to the knowledge and the use of different types of materials. In the first stages tools and commodities were obtained from wood and stone which were readily available in nature. In the successive periods, Man used other elements to produce goods that do not appear in natural state. Today, Man can manipulate and design materials down to the atomic level, in order to get desired properties. The production of materials with new properties implies new technological progress.

Materials are always present in our daily life. They are used in the construction of houses, streets, hospitals, etc., and more advanced materials are used for the construction of cars, aeroplanes or computers. In a computer, there are several sensors and actuators for the regular functioning of all the system. Sensors and actuators are produced with materials which undergo transformations throughout physical interactions (*e.g.*, changes in the shape, phase, etc.), sensing a change in its environment and adapting to correct such change through the use of a feedback system, whereas functional materials cover a broader range of materials whose physical and chemical properties are sensitive to changes in the environment, such as temperature, pressure, electric field, magnetic field, etc., having the ability to perform a certain “function” under a determined stimulus [1]. Ferroelectric and piezoelectric materials are examples of functional materials whose sensing and actuating capabilities account for a large number of applications that span over most industrial sectors [2, 3].

The capacity of a material to sense the environment is related with its crystalline structure. Crystalline structures are classified into 32 point groups and, of these, 20 present piezoelectric response, 10 of which are ferroelectric. The perovskite is one of the groups that can present ferroelectric properties. The family of ferroelectric perovskites displays a large diversity in its physical properties, which makes these materials attractive for fundamental research. On one hand, perovskite structure is relatively simple and, thus, attractive for studies, while, on the other hand, different representatives of the family exhibit a multitude of physical phenomena, such as pyroelectricity, ferroelectricity, piezoelectricity, among others [4].

Piezoelectricity is an effect related to the microscopic structure of the solid. Some ceramic materials become electrically polarized when they are stressed; this linear and reversible phenomenon is referred to as the direct piezoelectric effect. The direct

piezoelectric effect is always accompanied by the converse piezoelectric effect, where a solid becomes strained when placed in an electric field. The microscopic origin of the piezoelectric effect is the displacement of ionic charges within a crystal structure. In the absence of external stress, the charge distribution within the crystal is symmetric and the net electric dipole moment is zero. However, when an external stress is applied, the charges are displaced and the charge distribution is no longer symmetric. A net polarization develops and results in an internal electric field. A material can only be piezoelectric if the unit cell has no centre of inversion. Actually, a great number of piezoelectric ceramics has been discovered, among which appears the lead zirconate titanate (PZT) family, which are still the most widely used piezoelectric ceramics today.

A significant characteristic of PZT is its phase diagram, which is characterised by a boundary, known as the morphotropic phase boundary (MPB), between a tetragonal phase and a rhombohedral one at a zirconate content of about 52 molar percent $\text{Pb}(\text{Zr}_{0.52}\text{Ti}_{0.48})\text{O}_3$. One of the most important parameters describing the piezoelectric properties is the electromechanical coupling coefficient (k_{ij}). At compositions near the MPB, there is a maximum in the electromechanical coupling coefficient (k_{ij}) and in the relative permittivity ϵ_r . This feature, which is exploited in commercial compositions, facilitates applications in many different areas. The applications of PZT piezoceramics in sensors and actuators are two of the most recent and important application areas for these materials, particularly for the compositions near the MPB.

Several theories tried to explain the cause for the electro-mechanical properties maxima at the MPB. Mainly, they propose that the maxima are due to the increase of the number of possible directions for polarization in this region [5]. This number increases due to the coexistence of the rhombohedral and the tetragonal phases or to the presence of a monoclinic phase [6]. There is a controversy about the coexistence of the phases (or the presence of a monoclinic phase) [7]. Other explanations assign the maximum to the instability of the crystalline structure [8] or to the decrease of the unit cell distortion [9].

The width of the MPB was found to be dependent on the grain size, i.e., increasing when the grain size decreases [9]. However, the decrease of the width of the MPB with the increase of the grain size brings an increase of the electrical parameters. Therefore, to obtain PZT ceramics in the MPB with large grain size is an important issue, both from

technological and scientific point of views. This work pursues this goal, as a continuation of the investigation by R. Soares *et al.* [10], with the following objectives:

1. To obtain PZT ceramics with large grains for compositions around the MPB, using liquid phases.
2. To obtain PZT single crystals with compositions around the MPB and to use them as templates in the ceramics to enhance grain growth.
3. To characterize the electrical, structural, and piezoelectric behaviour of the ceramics and single crystals, in order to obtain the different thermodynamic parameters, which can help to understand the origin of the high electro-mechanical properties around the MPB.

The present thesis is organized in five chapters, which are divided as follows:

In chapter 1, “*Background on ferroelectric materials and applications*”, it is presented a brief review of the applications and the general characteristics of the ferroelectric and piezoelectric phenomena in ferroelectrics and related materials. In Chapter 2, “*Background on PZT single crystals growth and templated grain growth*”, it is provided a brief description of several methods used to grow ferroelectric crystals, in particular, the high-temperature self-flux solution method. In Chapter 3, “*Materials processing and experimental techniques*”, the details of the experimental work on the synthesis and processing of PZT powders, sample preparation procedures, single crystals growth method and characterisation techniques are described. In Chapter 4, “*Growth and characterisation of $PbZr_xTi_{1-x}O_3$ single crystals*”, the specific experimental conditions to obtain and to characterize $PbZr_xTi_{1-x}O_3$ (PZT) single crystals are analyzed and discussed. The main purpose of Chapter 5, “*Processing and characterisation of $PbZr_xTi_{1-x}O_3$ ceramics*”, is to present the processing and characterisation of PZT ceramics with improved performances of the dielectric properties, grain growth and the relation between them. Chapter 6 presents the general conclusions and the outline for some future work to complement the present one.

CHAPTER 1

Background on ferroelectric materials and applications

In this chapter, the general characteristics of the ferroelectric and the piezoelectric phenomena in ferroelectrics and related materials are reviewed with a special attention given to the PZT system. The fundamental issues associated with the ferroelectric phenomena, such as phase transitions, conductivity, appearance of domains and switching of polarization vector, will be outlined and followed by a brief description of the physical properties and structures of common ferroelectric materials with special attention to the perovskite family.

The structure and the electrical characteristics near the morphotropic phase boundary of the PZT ceramics are analysed. The historical development of the phase diagram of the PZ-PT system is also presented. Finally, a quick review of the Landau-Ginzburg-Devonshire (LGD) theory for the ferroelectricity and the phase transitions is presented.

1.1. Ferroelectricity and piezoelectricity: basic definitions

A material is ferroelectric when the spontaneous electric polarization can be reoriented between possible equilibrium directions (determined by the crystallography of the system) by the application of an appropriately oriented electric field. The required field intensity must be below the breakdown electric field. Ferroelectricity is distinguishable from the phenomena associated with electrets in two ways: 1) the polarization is spontaneous (i.e., the polarization is retained at zero electric field), and 2) the polarization direction is controlled by the symmetry of the crystal. Ferroelectricity is a property of a material which contains a ferroelectric phase in some accessible range of environmental conditions (from American National Standard IEEE “Standard Definitions of Terms Associated With Ferroelectric and Related Materials”).

1.1.1. Applications of ferroelectrics

The applications of ferroelectrics cover many areas of modern technologies, from high-dielectric constant capacitors to non-volatile memories and integrated optical devices.

Ferroelectric materials are deeply involved in the piezoelectric applications of ceramics due to the discovery of the electrical poling process that aligns the internal polarization of the crystallites within the ceramic and causes the ceramic to work very similarly to a single crystal. Ferroelectric ceramics, in general, are technologically simpler to manufacture than single crystal piezoelectrics and have greater variety in chemical formulations, forms (bulk, films) and fabrication methods. A comprehensive review of ferroelectric ceramics applications is given by Haertling [11] and Waser [12]. Application of ferroelectric ceramics can be classified by the form (bulk or films) or by the functional effect responsible for the device operation.

The first area of ferroelectric ceramics application was the engineering of capacitors. Here, the direct dielectric effect is exploited. Many ceramic capacitors are, in reality, high dielectric constant ferroelectric compositions which have their ferroelectric properties (hysteresis loop) suppressed by suitable chemical dopants while retaining a high dielectric constant over a broad temperature range. Historically, the first ferroelectric composition used for such capacitors was BaTiO_3 and its modifications. Nowadays, their number is enhanced by the lead containing relaxors and other compounds.

By far, the largest majority of applications for electro-active materials occurs in the area of piezoelectric ceramics. In this category, the ceramics are usually poled once and no polarization reorientation takes place after that during the life of the device. Depending on whether the direct or the converse piezoelectric effects or their combinations are employed, there are three categories of applications: (1) charge or voltage generators (direct piezoelectric effect). This class of devices includes various sensors, such as microphones, phonograph cartridges, gas ignitors, accelerometers, photoflash actuators, pressure sensors, impact fuses, etc. The operating characteristic varies from 10^{-3} to 10^3 V. (2) displacement actuators (converse piezoelectric effect). This class contains various actuators - loud speakers, camera shutters, buzzers, ink jet printer, micro-robots, relays, pumps and others. And (3) high frequency transformers and resonant devices. In this class, there are transducers, sonars, ultrasonic cleaners, ultrasonic welders, filters, transformers, delay lines and non-destructive testing. These devices operate at working frequencies from 10^3 to 10^6 Hz.

Transparent single crystals are traditionally used in electro-optic applications. Since late 1960s, when transparent Lead Lanthanum Zirconate Titanate (PLZT) ferroelectric

materials were first developed, ferroelectric ceramics have been thoroughly investigated and their characteristics studied up to the point that they have now taken their own place alongside the single crystals as legitimate candidates for certain electro-optic applications. The electro-optic properties of PLZT materials are intimately related to their ferroelectric properties: varying the ferroelectric polarization with an electric field, such as in the hysteresis loops, produces also a change in the optical properties of the ceramics [13].

Applications of ferroelectric materials in film form are growing due to the need towards miniaturization and integration of electronic components and due to the development of micro-technologies, fabrication and engineering of materials. Aside from the obvious advantages, such as smaller size, less weight and easier application in integrated circuit technology, ferroelectric films offer additional benefits, including lower operating voltage, higher speed and the possibility to fabricate unique micro-level structures. In addition, the sintering temperatures of the films are usually hundreds of degrees Celsius lower than those of the bulk and this often can be the deciding factor in a successful design for applications [14-17]. Among others, the most common ferroelectric film applications are non-volatile memories, integrated optics, electro-optic displays, micro-actuators, micro-transducers and capacitors.

Other applications of ferroelectrics explore the electrostrictive effect, the positive temperature coefficient of resistivity, the stress-induced depoling and the recent magneto-resistive effect, with great potential to be used, where the larger known response is obtained by using Metglas/PZT-fiber laminates [18].

1.1.2. *Ferroelectric phenomena and spontaneous polarization*

Ferroelectricity is a phenomenon discovered by Joseph Valasek in 1921 during his studies on single crystals of Rochelle salt ($\text{NaKC}_4\text{H}_4\text{O}_6 \cdot 4\text{H}_2\text{O}$) [19]. Since then, many ferroelectric materials have been discovered and several essential features of the phenomenon (accompanied with a number of phenomenological theories) were studied and described in several books [20-24].

Ferroelectric materials are characterized by a spontaneous polarization (P_s) that can be reoriented by the application of an electric field over some temperature range. This spontaneous polarization (dipole moment per unit volume) typically arises from small displacements of some of the ions off from their centre-symmetric position in the unit cell of the crystal structure. Some other ordering processes (order-disorder processes) can also result in a reversible dipole moment. Figure 1.1 illustrates the unit cell of the ABO_3 perovskite-type structure of $Pb(ZrTi)O_3$ showing the corresponding ionic

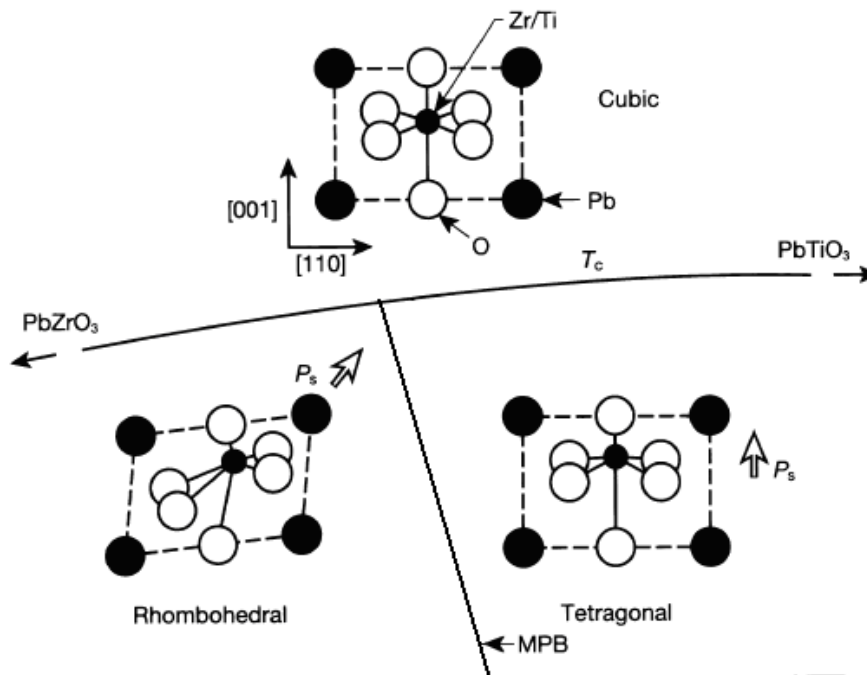


Figure 1.1 - A portion of the $PbTiO_3$ - $PbZrO_3$ phase diagram showing the structure changes at the Curie temperature (T_c). Above T_c the cells are cubic, while below T_c the structure is either tetragonal or rhombohedral. In the rhombohedral case the structure is elongated along the [111] direction and in the tetragonal one it is elongated along the [001] one. The rhombohedral and the tetragonal fields are separated by a boundary designated by morphotropic phase boundary (MPB).

displacements. Since electrical properties are strongly related to the crystal structure, the orientation of the spontaneous polarization usually coincides with the crystallographic axes. Most ferroelectric materials undergo a phase transition at a temperature (Curie point, T_c) below which they are polar (non-centre-symmetric) and above which they

present a centre-symmetric structure (loosing the spontaneous polarization). In this state the material is termed paraelectric (Figure 1.1).

1.1.3. *Electric field and polarization*

A crystal is said to be ferroelectric when it has at least two orientation states for the spontaneous polarization and it is easy to shift from one to another of these states by the application of an electric field. The two orientation states are enantiomorphic and therefore they only differ in the sign of the dielectric polarization vector at null electric field. This definition is simplified, because whether or not a real material is ferroelectric also depends on other aspects: crystal imperfections, electrical conductivity, temperature and pressure are factors that affect the reversibility of the polarization.

The linear relation between the electric field E_j applied to a dielectric and the induced polarization P_i

$$P_i = \chi_{ij} E_j \quad (1.1)$$

defines the dielectric susceptibility χ_{ij} of the material, a second rank tensor. Summation over the indices is implied in this expression. Relation (1.1) is only approximate, since the polarization P_i generally depends on higher order terms of the field E_j (similarly, in a general case, the dielectric susceptibility χ_{ij} is a function of the electric field).

The electric displacement (D_i) in a dielectric material is related to the applied electric field (E_j) by the following relation [25]:

$$D_i = \varepsilon_{ij} E_j \quad (1.2)$$

where ε_{ij} is the dielectric permittivity of the material and it is also a second rank tensor. The relative dielectric permittivity, ε_{rij} , is defined as,

$$\varepsilon_{ij} = \varepsilon_o \varepsilon_{rij} \quad (1.3)$$

where ε_o is the dielectric permittivity of the vacuum (8.85×10^{-12} F/m).

Expression (1.2) in presence of induced polarization can also be written as,

$$D_i = \varepsilon_o E_i + P_i \quad (1.4)$$

Inserting Equation 1.2 in 1.4, one gets

$$E_i = \eta_{ij} P_j \quad (1.5)$$

where η_{ij} is the inverse of the dielectric susceptibility (known as the dielectric stiffness coefficient), a second rank tensor related with the dielectric susceptibility by

$$\eta_{ij} = \chi_{ij}^{-1} \quad (1.6)$$

The dielectric susceptibility in a ferroelectric material depends on the electric field (E), temperature (T), frequency (f) and stress (X), among others. In general, the dielectric susceptibility is measured at low fields, where χ_{ij} has a linear response with the electric field (1-100 V/cm). The temperature dependence of the susceptibility shows a maximum, corresponding to the transition from ferroelectric to paraelectric state. The paraelectric state is described by an empirical law (Curie-Weiss law):

$$\varepsilon = \frac{C}{T - T_0} \quad (1.7)$$

where C is the Curie-Weiss constant and T_0 ($T_0 \leq T_C$) is the Curie-Weiss temperature, which is generally slightly lower than T_C in the case of a first-order phase transition, or equal to T_C ($T_0 = T_C$) for a second-order phase transition.

The behaviour of the susceptibility with the temperature and the frequency can be explained by a simple model. When the temperature is decreasing through the Curie point, a phase transition from the paraelectric cubic phase to the ferroelectric phase takes place due to the interaction of short and long range forces, freezing the soft mode (ferroelectric mode with frequency generally lower than 150 cm^{-1}). In the ferroelectric state, a group of ions is displaced with respect to others, forming a dipole. According to the soft mode theory, the probability of finding the polar ion in any of the sides of the double potential well is different (Figure 1.2), which gives origin to a polar state and the formation of a domain to minimize the electrostatic energy associated with the internal polarization. When the frequency is low, the ion can hop from one potential well to the other, in phase with the applied electric field, but when the frequency is high, the hop rate is out of phase with the electric field and the ion cannot hop to the other potential well. Therefore, the dielectric loss increases with frequency up to the resonance; for higher frequencies there is a difference of phase between the electrical field and the hopping rate and the dielectric loss decreases (Figure 1.3). The frequency where the dielectric loss has a maximum

corresponds to the resonance frequency (ω_r) and is characteristic for each material. The resonance frequency in a ferroelectric material is of the order of 10 MHz to a few GHz; for the PZT it is found near 200 MHz [26]. Figure 1.3 is characteristic for materials with dipolar relaxation. When the electrical field is applied to the material, the dipoles rotate in phase with the electrical field (this effect provokes a displacement of the charges in the material, increasing the dielectric losses). On the other hand, when the frequency is higher than a critical value (resonance frequency) it appears a difference in phase between the electrical field and the orientation of the dipoles. Therefore this difference of phase between the electric field and the dipolar response decreases the dielectric loss and dielectric constant (Figure 1.3).

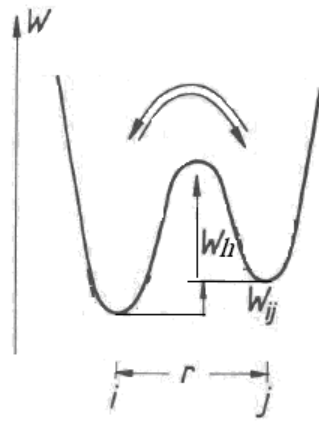


Figure 1.2 - Double potential well where Wh is the potential energy of the well, W_{ij} is the difference of potential energy of the particle in the position i and j with the distance (r) between the two equilibrium positions projected in the direction of the electric field.

When temperature increases, thermal vibrations increase and the potential barrier between the wells decreases facilitating the hopping of the ions. Therefore, the resonance frequency is shifted to higher values. At the Curie temperature (T_C) the barrier energy between the potential wells disappears and the material undergoes the phase transition from ferroelectric to paraelectric state. This is a simple model since in real materials other processes affect the dielectric permittivity and the losses.

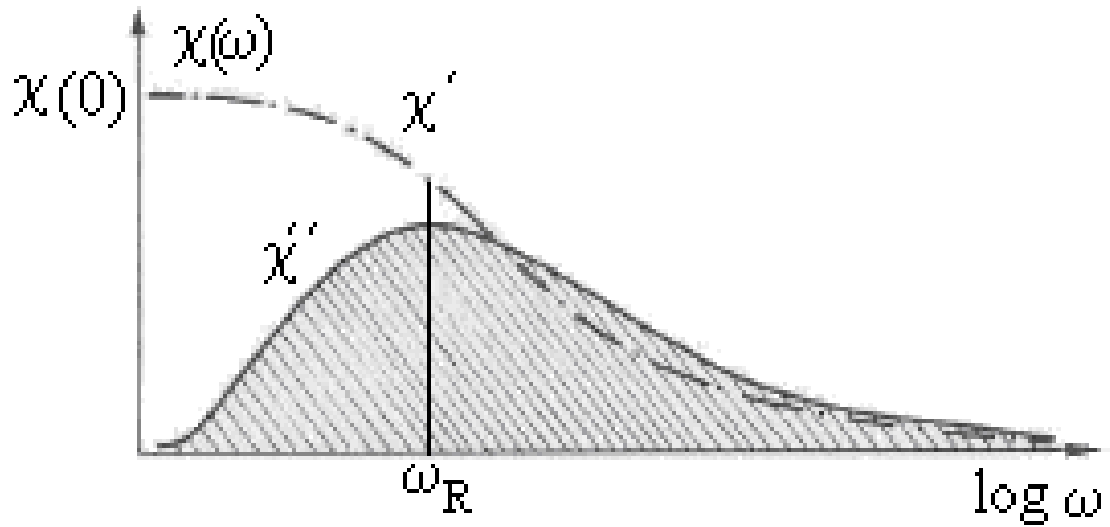


Figure 1.3 - Behaviour of the real χ' and the imaginary χ'' parts of the susceptibility with the frequency (ω). ω_R is the resonance frequency.

The dielectric loss is defined as the tangent of the loss angle, $\tan\delta$, and is the ratio between the imaginary, ε'' and the real, ε' parts of the permittivity [27]:

$$\tan \delta = \frac{\varepsilon''}{\varepsilon'} \quad (1.8)$$

The dielectric permittivity and the dielectric loss of a ferroelectric material are important electrical parameters that often have a peak at T_C , while the spontaneous polarization vanishes at this point.

In the high temperature region, where the crystal has cubic symmetry, the dielectric constant is independent on the crystallographic directions and is given by

$$\varepsilon^* = \chi + 1 \quad (1.9)$$

but in the temperature region where the crystal has lower symmetry, the dielectric constant is no longer independent on the direction and has to be described by a tensor. From the thermodynamic point of view it is more convenient to work in terms of the dielectric susceptibility (χ) and its reciprocal (η), the dielectric stiffness than the dielectric permittivity.

1.1.4. Pyroelectric effect and pyroelectric current

The pyroelectricity is the property of certain materials to generate an electrical potential when they are subjected to temperature changes. This is due to a change in the spontaneous polarization vector. The discovery of pyroelectricity can probably be attributed to the fact that high electric fields can develop across insulating pyroelectric materials when they are subjected to relatively small temperature changes. For instance, a crystal with a typical pyroelectric coefficient of $10^{-8} \text{ C/cm}^2 \text{ K}$ and a dielectric constant of 50 develops a field of 50 kV/cm , for a temperature change of only $25 \text{ }^\circ\text{C}$, sufficient to break-down the air.

The pyroelectric coefficient (p_i) is defined as the change of the spontaneous polarization, P_{s_i} , with temperature, T , by:

$$p_i = \frac{\partial P_{s_i}}{\partial T} \quad (1.10)$$

Equation (1.10) may also be written in the form of

$$\Delta P_{s_i} = p_i \Delta T = \sigma_i \quad (1.11)$$

where σ_i is the surface charge density induced in the material by the temperature change of ΔT . The charge due to the spontaneous polarization is usually masked by charges from the surrounding of the material and therefore it is experimentally easier to observe the variation in the spontaneous polarization rather than to measure the spontaneous polarization value itself.

When a sample is polarized, it has a remanent polarization (P_r) that can be determined experimentally: if this sample is heated up to the Curie temperature and the current that appears between the ends of the sample short circuit is measured, then P_r can be calculated. This current (i) is nominated pyroelectric current and it is determined by:

$$i = p_i A \frac{dT}{dt} \quad (1.12)$$

where A is the electrode area and dT/dt is the heating rate.

The spontaneous polarization can be obtained by

$$P_{s_i}(T_c) - P_{s_i}(T) = -\frac{1}{A} \frac{dt}{dT} \int_T^{T_c} i dT \quad (1.13)$$

where $P_{S_i}(T_c)$ is the polarization at the Curie temperature (T_c) and dt/dT is the inverse of the heating rate. The polarization at the Curie temperature is null in a second order phase transition, $P_{S_i}(T_c)=0$. In this case, the measurement of the pyroelectric current allows the direct determination of the value of the spontaneous polarization as a function of the temperature.

The spontaneous polarization can also be obtained from others methods, namely from hysteresis loops using a Sawyer-Tower bridge [28] or a pulsed-field method [29].

1.1.5. *Piezoelectric coefficients and related properties*

Piezoelectricity is the ability of a material to exhibit a polarization when subjected to a mechanical stress. The material will also show the converse effect by undergoing mechanical deformation (strain) under the application of an electric field. The piezoelectric effect was discovered by Jacques and Pierre Curie in 1880 during their study of the effects of pressure on the generation of electrical charge on crystals such as quartz, tourmaline and Rochelle salt [30-32]. They found that, if certain crystals are subjected to a mechanical force, they become electrically polarized and the degree of polarization is proportional (*i.e.*, linear) to the applied stress. For a crystal to exhibit the piezoelectric effect, its crystal structure should also be non-centrosymmetric, as in the case of ferroelectrics, with the exception of the 432 point group, which, although non-centrosymmetric, does not present piezoelectric effect. In fact, all ferroelectric materials are piezoelectric. Another group of materials more general than the ferroelectric one that presents piezoelectric effect are pyroelectric materials. Here, it is valid that all pyroelectric material are piezoelectric.

In order to present the relation for the piezoelectric effect, it is first necessary to introduce two mechanical parameters: stress and strain.

Stress and strain: stress and strain describe the elastic properties of a homogenous and continuous solid in thermodynamic equilibrium. Stress, X_{ij} , is defined as the force per unit area and is a second rank tensor. Components of the stress perpendicular to the surface are called normal stresses and those parallel to the surface upon which they act are called shear stresses. A tensile stress is conventionally defined as being positive and a compressive one as negative. The stress can be represented by a symmetrical tensor and it can be shown that this is true even if the stress is not homogeneous [33]. Due to the symmetrical properties of this tensor, it is possible to represent the stress by a reduced tensor notation. In the reduced

tensor, the directions X, Y and Z are represented by the subscripts 1, 2 and 3, respectively, and the shear stresses about these axes are represented by the subscripts 4, 5 and 6, depending on the orientation of the shear plane (Table 1.1).

Table 1.1 - Reduced tensor notation used to describe the stress tensor [34].

	Normal stress components			Shear stress components		
Index	11	22	33	23=32	13=31	12=21
Reduced index	1	2	3	4	5	6

A relative deformation of a body is called strain. The strain, x_{ij} , is therefore dimensionless and it is also a symmetrical, second order rank tensor.

For small strains (first approximation), a linear relation between stress and strain is obtained given by

$$x_{ij} = c_{ijkl} X_{kl} \quad (1.14)$$

This is the Hooke's law in which c_{ijkl} is the elastic compliance coefficients of the material, a fourth rank tensor.

The inverse relation

$$X_{ij} = s_{ijkl} x_{kl} \quad (1.15)$$

defines s_{ijkl} , the elastic stiffness coefficients, also a fourth rank tensor. Obviously,

$$c_{ijkl} = s_{ijkl}^{-1} \quad (1.16)$$

Due to the symmetry of the stress and the strain, there are only a maximum of 36 independent components for the c_{ijkl} and s_{ijkl} tensors and this number can be further reduced depending on the symmetry of the material.

We can now develop the piezoelectric effect. The direct and the inverse piezoelectric effects can both be expressed in tensor notation as:

$$P_i = d_{ijk} X_{jk} \quad (\text{for the direct piezoelectric effect}) \quad (1.17)$$

and

$$x_{ij} = g_{ijk} E_k \quad (\text{for the inverse piezoelectric effect}) \quad (1.18)$$

where g_{ijk} is the transposed matrix of d_{ijk} . The piezoelectric coefficients (d_{ijk}) for the direct and the inverse piezoelectric effects are thermodynamically identical. P_i is the polarization produced along the i -axis in response to the applied stress X_{jk} , and d_{ijk} ($\equiv g_{ijk}$) is the piezoelectric coefficient, a third rank tensor. For the inverse effect, x_{ij} is the strain generated along a specific orientation of the crystal in response to the applied electric field E_k along the k -axis. The units for the d coefficient are (C/N) or (m/V).

Since piezoelectric materials are anisotropic, their physical constants must depend on both the orientation of the applied stress and the electric field. Consequently, each constant generally has two subscript indices that refer to the directions of the two related quantities; for example, strain and electric field for piezoelectricity, or electric displacement and electric field for permittivity. The direction of positive polarization is assumed to coincide with the Z -axis of a rectangular system of X , Y and Z axes (see Figure 1.4).

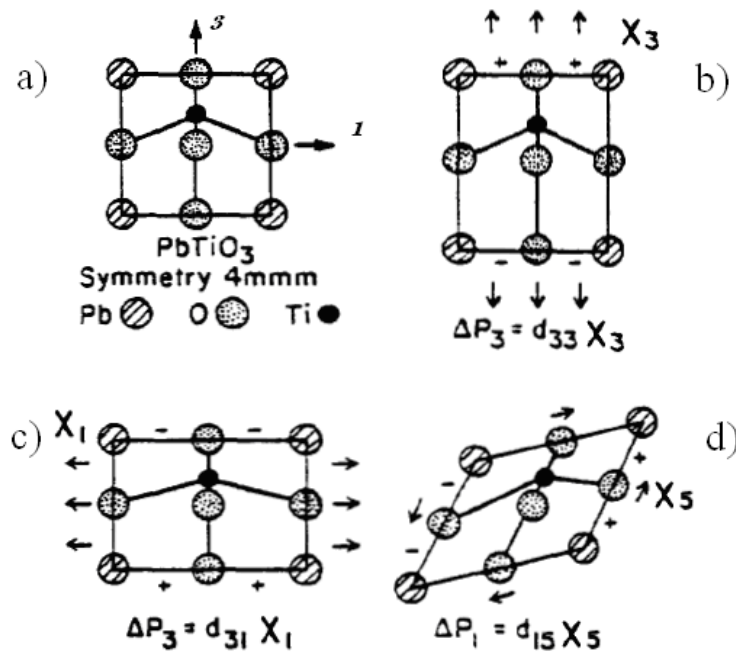


Figure 1.4 - Two dimensional description of the origin of the piezoelectric response in a single domain of a PbTiO_3 crystal. (a) Situation under no field. (b) Shift of the Ti cation away from the equilibrium position under stress X_3 . (c) Shift of the Ti cation back towards the cell centre under stress X_1 . (d) Tilting of the Ti position giving ΔP_1 , under a shear stress X_5 [34].

Another related property is the electrostrictive effect. This is a property observed in all dielectrics, regardless their symmetry. It produces a relatively small mechanical deformation under an applied electric field. A reversal of the electric field does not reverse the direction of the deformation: it is an example of a nonlinear coupling between elastic and electric fields. A mechanical deformation (x_{ij}) appears if an electric field (E_i) is applied on a dielectric (electrostrictive effect) and this is defined by

$$x_{ij} = M_{ijkl} E_k E_l \quad (1.19)$$

where M_{ijkl} are components of fourth-rank tensors called the electrostrictive coefficients (electrostriction constants written in voltage notation). The electrostrictive effect can also be expressed in terms of the vector of the induced polarization

$$x_{ij} = Q_{ijkl} P_k P_l \quad (1.20)$$

where Q_{ijkl} are components of fourth-rank tensors called the electrostrictive coefficients (electrostriction constants written in polarization notation). The electrostriction constants are related by [35]:

$$M_{ijmn} = \chi_{km} \chi_{ln} Q_{ijkl} \quad (1.21)$$

where χ_{km} and χ_{ln} are components of the dielectric susceptibility tensors. In ferroelectric materials the polarization at strong fields is a nonlinear function of the electric field, so that both Equations (1.19) and (1.20) cannot be valid together. In any case, experimental results show that Equation (1.20) is a more consistent way to describe the electrostrictive effect in dielectrically nonlinear materials [36].

Symmetry considerations: The fundamental postulate of crystal physics, known as Neumann's Principle, relates the symmetry of a crystal with the symmetry of its physical properties:

"The symmetry elements of any physical property of a crystal must include the symmetry elements of the point group of the crystal."

The point group of a crystal is the group of macroscopic symmetry elements of its structure. It is the basis for the division of crystals into 32 classes. Table 1.2 shows all crystal classifications and a scheme is presented in (Figure 1.5).

The Neumann's principle does not state the equality of the symmetry elements of a physical property to the symmetry elements of the point group. The physical properties often possess more symmetry elements than the point group.

Of the 32 crystal classes, 21 are non-centrosymmetric and, of these, 20 exhibit direct piezoelectricity (the remaining is the cubic class 432 that, due to the symmetry elements present in this group, does not present relative change of the positive and negative centres upon the application of a stress). Ten of these are polar and exhibit pyroelectricity. If this dipole can be reversed easily by the application of an electric field, then the material is also ferroelectric.

Since the spontaneous polarization occurs in materials with a unique polar axis, all pyroelectric materials are piezoelectric, but only some piezoelectric materials (those whose symmetry belongs to polar groups) can be pyroelectric (Figure 1.5).

The symmetry requirements may significantly reduce the number of nonzero and independent elements of a property tensor. For example, the number of independent elements in the piezoelectric tensor, Equations (1.17) and (1.18), are reduced from 27 to 18 because strain and stress are symmetrical properties and, since the piezoelectric tensor is symmetrical with respect to the same indices, $d_{ijk} \equiv g_{ijk}$, then, diagonalizing the tensor d_{ijk} , it is possible to reduce it to the form d_{ij} . The number of independent elements of d_{ij} may be further reduced by the symmetry of the material. For example, the point group $mm2$ allows 5 independent nonzero tensor elements, while the $3m$ symmetry allows only 4 of them [33].

Table 1.2 - Crystallographic classification of the materials into the 32 point groups [37].

Crystal Structure	Point Groups	Restrictions	Lattice type	Centrosymmetric	Non-centrosymmetric	
					Piezoelectric (20)	Pyroelectric (10)
(7)	(32)		(14)	(11)		
Triclinic	1, $\bar{1}$	$a \neq b \neq c, \alpha \neq \beta \neq \gamma$	P	$\bar{1}$	1	1
Monoclinic	2, m, 2/m	$a \neq b \neq c$ $\alpha = \gamma = 90^\circ \neq \beta > 90^\circ$	P, C	2/m	2, m	2, m
Orthorhombic	222, mm2, mmm	$a \neq b \neq c, \alpha = \beta = \gamma = 90^\circ$	P, C, I, F	mmm	222, mm2	mm2
Tetragonal	4, $\bar{4}$, 4/m, 422, 4mm, $\bar{4}2m, 4/mmm$	$a = b \neq c, \alpha = \beta = \gamma = 90^\circ$	P, I	4/m, 4/mmm	4, $\bar{4}$, 422, 4mm, $\bar{4}2m$	4, 4mm
Trigonal	3, $\bar{3}$, 32, $\bar{3}m, 3m$	$a = b \neq c$ $\alpha = \beta = 90^\circ \neq \gamma = 120^\circ$	P (R)	$\bar{3}, \bar{3}m$	3, 32, 3m	3, 3m
Trigonal	6, $\bar{6}$, 6/m, 622, 6mm, $\bar{6}m2, 6/mmm$	$a = b \neq c$ $\alpha = \beta = 90^\circ \neq \gamma = 120^\circ$	P	6/m, 6/mmm	6, $\bar{6}$, 622, 6mm, $\bar{6}m2$	6, 6mm
Cubic	23, m3, 432, $\bar{4}3m, m3m$	$a = b = c, \alpha = \beta = \gamma = 90^\circ$	P, I, F	m3, m3m	23, $\bar{4}3m$	

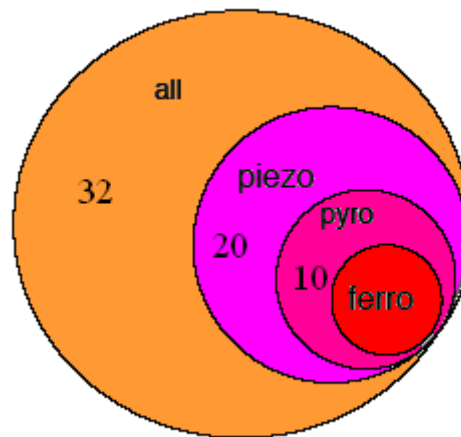


Figure 1.5 - The crystal classification scheme for the 32 point groups [23].

1.1.6. *Ferroelectric and ferroelastic domains*

Once the ferroelectric crystal is cooled down across the Curie point, an electrical polarization develops. If it develops uniformly throughout the crystal, a depolarizing field (E_d) will appear as shown in Figure 1.6(a) [27]. To minimize the electrostatic energy associated with the polarization interaction with the depolarizing field, the uniform alignment of electric dipoles only occurs in certain regions of the crystal, while in other regions polarization may be oriented oppositely, as shown in Figure 1.6(b). Such regions of uniform polarization are called ferroelectric domains and the interface between two adjacent domains (with thickness typically of the order of 10-100 Å) is called the domain wall [23]. Ferroelectric domains were first demonstrated in a study of spontaneous birefringence in barium titanate single crystals [38]. Walls that separate different orientations of the spontaneous polarization vector are ferroelectric domain walls, while those which separate different orientations of the spontaneous strain (associated with mechanical twinning) are ferroelastic domain walls. Inside a ferroelastic domain wall the dipole/strain orientation changes gradually from one domain orientation to another.

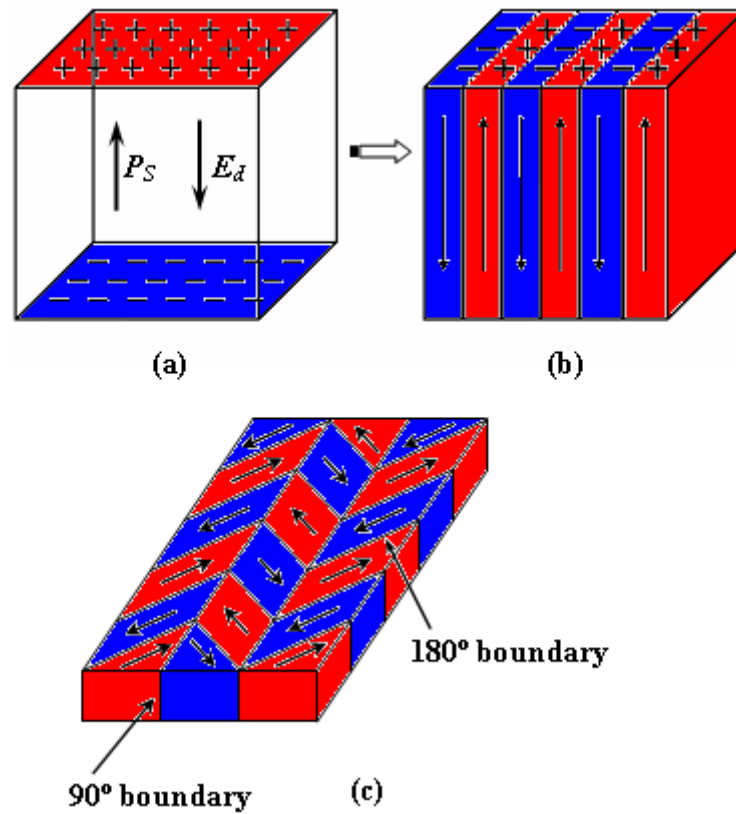


Figure 1.6 - (a) Surface charge and depolarizing field (E_d) associated with the spontaneous polarization (P_S). (b) Formation of 180° domains to minimize the electrostatic energy. (c) Schematic representation of 180° and 90° domain walls [25, 27].

The configuration of the ferroelectric domains depends on the crystal structure. The spontaneous polarization in an ideal ferroelectric crystal can be distributed with equal probability among several crystallographic directions of the centrosymmetric prototype structure (paraelectric phase). In a tetragonal phase, for example, the spontaneous polarization can be oriented only along three mutually perpendicular crystallographic directions, giving rise to two types of domain walls [see Figure 1.6(c)]: the walls that separate domains with oppositely oriented polarization (called 180° walls) and those which separate domains with mutually perpendicular polarization (called 90° walls). The 90° walls are both ferroelectric and ferroelastic domain walls, because they separate regions with different orientation of the polarization and strain. Since the formation of the domain walls requires some energy, there is a certain amount of energy (domain wall energy, W_{dw}) associated with them, in addition to the elastic energy (W_e) due to 90° domains [39]. The

switching of polarization by 180° does not involve elastic deformation, while the switching of 90° does involve elastic deformation and the energy of both is different. From energy considerations in real crystals, domain patterns depend on many factors, including the defect type and concentration, stress and electric history, temperature range relative to T_C , boundary conditions and even the history of the crystal growth [22].

From a phenomenological point of view, the multidomain state is not energetically favorable if the system is free from other constraints [40]. However, in reality, other forces (electrical and/or elastic) are always present during crystal growth and preparation. The external forces, in addition to the existence of multiple nucleation sites during phase transition, prevent the ferroelectric system to reach a single domain state. The presence of a large mechanical stress in a crystal results in the development of non- 180° domains wall configured to minimize the strain [41]. Thus, the natural state of a ferroelectric crystal is generally a multidomain configuration rather than a single domain one. Nevertheless, this multidomain state can usually be transformed into a single domain by applying an electric field parallel to one of the polar directions.

Ferroelectric properties of any ferroelectric material are largely determined by its static domain structure, together with nucleation of new domains and domain wall mobility. The way in which the material splits up into domains upon the transition from the paraelectric to the ferroelectric phase depends strongly on the mechanical and electrical boundary conditions imposed on the sample, as well as on the nature of the sample itself.

1.1.7. *Nonlinear dielectric properties, polarization switching and hysteresis loop*

The term “dielectric nonlinearity” is used to describe the relationship between dielectric displacement D and electric field strength E in nonlinear materials. It can be expressed by the dependence $\varepsilon(E)$, where ε is the dielectric permittivity of the material. The dielectric nonlinearity is usually accompanied by dielectric hysteresis. In general, dielectric hysteresis is the result of the delay in the polarization response of the dielectric to an electric field change which is expressed by a hysteretic field dependence of the dielectric polarization $P(E)$ and phase lag δ between the driving field and the response. The hysteresis and nonlinearity often have a common origin, although not necessarily always [37, 42].

The nonlinearity and the hysteresis (generally undesirable) have a deep influence on the application of ferroelectric materials. Except in memory applications, which are based on the polarization switching and hysteresis by external electric fields, the hysteresis is undesired in high precision sensor, actuator and capacitor applications. In most of the applications, nonlinearity is also undesired and the devices based on nonlinear materials usually need calibration. However, there are applications based on the dielectric nonlinearity, such as tuneable filters, variconds and other microwave devices.

The origins of the dielectric nonlinearity and hysteresis are complex and can be intrinsic and extrinsic. Intrinsic origins are those of the crystal lattice of the pure material. Correspondingly, extrinsic origins are related to non lattice contributions, such as movements of defects, grain boundary effects, displacement of interfaces (such as domain walls) and interphase boundaries. In most of ferroelectric materials, especially in ceramic and at weak fields, the extrinsic properties play a major role. Surfaces, boundaries and interface effects may give significant contributions to the polarization nonlinearity in thin films. However, the general dominant origin of extrinsic contributions to the dielectric, elastic and piezoelectric properties of ferroelectric materials, is the displacement of domain walls [43-48].

As described above, a ferroelectric crystal is in a polydomain state when it has just been grown and cooled down across its Curie point. Each individual domain can be reoriented upon the application of an external electric field of high enough strength. This dynamic process of domain reversal is called domain (or polarization) switching. The parameters of ferroelectric domains switching are anisotropic and depend on the temperature and the strength of the applied electric field [49, 50]. When the direction of the applied field is opposite to the polarization direction of a domain, a new domain may appear inside the old one by means of a nucleation and growth process. The motion of the domain wall depends not only on extrinsic physical mechanisms but also on the stress distribution, space charges and defects in the crystal [23].

When an alternate field of sufficiently high amplitude is applied to a ferroelectric material below T_C , the polarization shows a hysteretic behaviour with the applied electric field, as illustrated in Figure 1.7(a) [22, 23, 30]. The observation of the polarization-electric field (P-E) hysteresis loop is often used for the identification of the ferroelectricity. For a typical ferroelectric material, the first term in Equation 1.4 is negligible, $D_i \approx P_i$ and

the D - E and the P - E loops become equivalent. The application of a weak electric field generates a linear $P(E)$ relationship because the field is not large enough to disturb or switch any domain and the crystal will behave as a normal dielectric material (paraelectric), which can be described as:

$$P_i = \varepsilon_{rij} \varepsilon_o E_j \quad (1.22)$$

At low and at very high electric fields, a ferroelectric behaves like an ordinary dielectric with a high dielectric constant, but on approaching the coercive field (E_C) the domain walls can move from their equilibrium position and domains that are oriented favourably with respect to the direction of the electric field grow rapidly at the expenses of the domains with opposite polarization direction, producing a switching of net polarization and a large P - E non-linearity. Once most of the domains are switched, the material is said to reach its saturation polarization, where almost single domain state is attained. If the applied electric field is then removed, some of the domains will remain aligned and the crystal will have a remanent polarization (P_r). The extrapolation of the high field linear segment of the hysteresis loop back to the polarization axis can be used to measure the value of the spontaneous polarization (P_s), *e.g.*, the polarization of a single domain in the absence of an electric field. Following the P - E loop, the value of the negative electric field required to return the net polarization to zero is again the (negative) coercive field. Further increase of the field in negative direction will cause an alignment of the dipoles in this direction and the cycle can be completed by reversing the field direction once again. Thus, the relation between P and E is represented by the hysteresis loop shown in Figure 1.7(a) [22, 30].

In addition to the P - E hysteresis loop, polarization switching by an external electric field (E_{ex}) leads to a strain-electric field (x - E) hysteresis in ferroelectric materials, as shown in Figure 1.7(b) [20-22, 27, 30]. The shape resembles that of a butterfly and thus it is often referred to as the butterfly loop.

The initial loading cycle (Figure 1.7b) starts at zero strain and electric field (point *a*). There is no strain response until the electric field reaches the coercive field and the material switches to the polarized state. When the polarization does switch, the material goes from a cubic state to an elongated state. The electric-field is reduced to zero and then reversed in direction. At the coercive field, the polarization changes direction. During the switching process, the strain dips to negative values relative to the initial unpoled state.

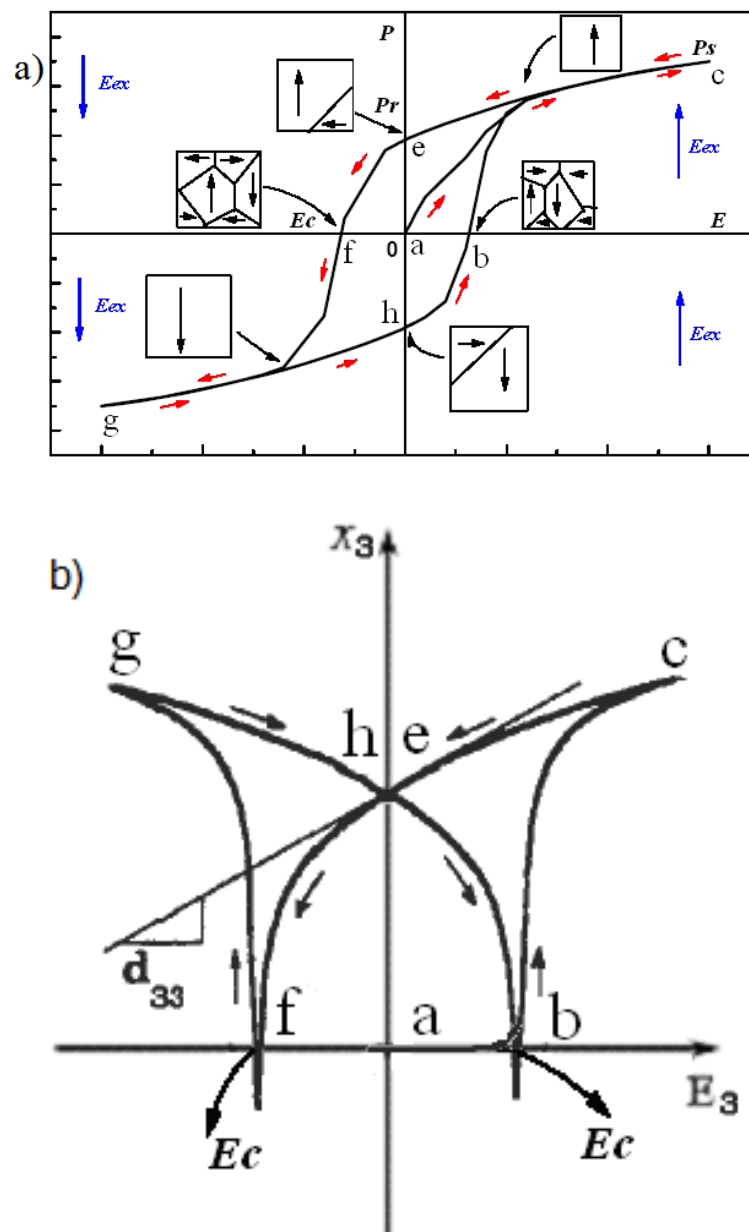


Figure 1.7 - (a) P - E hysteresis and (b) the x - E butterfly type loops [22, 23, 30]. The meaning of the letters in figure can be found in the main text.

After several cycles, a stable hysteresis loop develops, Figure 1.7b). The lettered sequences (Figure 1.7a and b) correspond to the same points in the loading cycle. At point (e) the material has positive remanent polarization and remanent strain. When a negative electric field is applied, the ions in the crystal structure experience a force that moves them toward a cubic state. This distorts the structure toward that of the unpoled ceramic. When the coercive field is reached at point (f), the direction of polarization begins to switch. After

the polarization has switched to the direction of the applied electric field, the electric field acts to stretch the unit cell, giving a positive strain at point (g). When the electric field is then reduced to zero, the remanent strain at point (h) coincides with that at point (e) but the remanent polarization is negative. Now, as a positive electric field is applied to the negatively polarized material, the ions in the crystal structure again experience a force that moves them toward a cubic state. The coercive field is reached at point (b), and the polarization has completely switched direction again at point (c). The electric field is reduced to zero and the material returns to point e with positive remanent polarization and remanent strain.

When the material is in the polarized state, the strain is linearly proportional to small changes in electric field at zero stress (due to the converse piezoelectric effect, Equation 1.18). The slope of the $x(E)$ curve near the zero electric field can be used to calculate the piezoelectric coefficient (d_{33} for the longitudinal strain) [20, 51, 52].

1.2. Perovskite types of ferroelectric materials

The ferroelectric materials can be classified in different types, depending on the structure, the application, the chemical composition, the nature (ceramic, crystals and polymers) and the type of phase transition, among others. According to their structure, the four main types of structures include the corner sharing oxygen octahedrons [30, 53-56], compounds containing hydrogen bonded radicals [57-59], organic polymers [60, 61] and ceramic polymer composites [62, 63]. The corner sharing oxygen octahedrons type compounds includes the perovskite [30, 53-56], the tungsten bronze [64, 65], the bismuth oxide layer [66-68] and the lithium niobate and tantalate [69-73]. Several properties of the bismuth oxide layer type of compound (SBT and SBN single crystals) was reported recently by H. Amorín *et al.* [3, 74]. Perovskite type ferroelectric materials are discussed in detail below.

Ferroelectric properties of ABO_3 perovskites were first discovered in barium titanate by Wul and Goldman in 1945 [75]. $BaTiO_3$ was, since then, considered not only a model system for ferroelectricity, but also the main material for practical applications. Shortly after that, a whole class of ferroelectric perovskites was discovered by several groups [76, 77]. Perovskite is a family name of a group of materials and the name of the mineral

calcium titanate (CaTiO_3 , CT) having a structure of the ABO_3 type. Many piezoelectric (including ferroelectric) ceramics, such as barium titanate (BaTiO_3 , BT), lead titanate (PbTiO_3 , PT), lead zirconate (PbZrO_3 , PZ), lead zirconate titanate ($\text{PbZr}_x\text{Ti}_{1-x}\text{O}_3$, PZT), lead lanthanum zirconate titanate ($\text{Pb}_{1-y}\text{La}_y\text{Zr}_x\text{Ti}_{1-x}\text{O}_3$, PLZT), lead magnesium niobate ($\text{PbMg}_x\text{Nb}_{1-x}\text{O}_3$, PMN), potassium niobate (KNbO_3 , KN), potassium sodium niobate ($\text{K}_x\text{Na}_{1-x}\text{NbO}_3$, KNN) and potassium tantalate niobate ($\text{KTa}_x\text{Nb}_{1-x}\text{O}_3$, KTN), have a perovskite type structure. Its simplest crystal structure is cubic (space group $Pm\bar{3}m$), which is the high temperature form for most ABO_3 oxides, but transforms to a pseudocubic (tetragonal, rhombohedral or orthorhombic) when the temperature decreases below the Curie point [23]. For simple perovskites such as PZT, the polarization is attributed mainly to the displacement of the B -site ion (titanium or zirconium in this case) from the centre of the BO_6 octahedron (Figure 1.8) [78].

The most commercially available ferroelectric materials belong to the perovskite family, which includes BaTiO_3 , lead titanate (PbTiO_3), potassium niobate (KNbO_3) and many compositions in the PZT system. In fact, PZT compositions are now the most widely exploited of all piezoelectric ceramics, both in research and industry; however, this system is very difficult to obtain in the form of high-quality single crystals [49, 79]. The ABO_3 structure is very tolerant to cation substitutions of both A and B lattice sites and hence may lead to complex compounds, such as $\text{Pb}(\text{Mg}_{1/3}\text{Nb}_{2/3})\text{O}_3$, $\text{Pb}(\text{Zn}_{1/3}\text{Nb}_{2/3})\text{O}_3$, $(\text{K}_{1/2}\text{Bi}_{1/2})\text{TiO}_3$, $\text{Pb}(\text{Fe}_{1/2}\text{Ta}_{1/2})\text{O}_3$, $\text{Pb}(\text{Co}_{1/4}\text{Mn}_{1/4}\text{W}_{1/2})\text{O}_3$, and, in many cases, to the solid solutions among them. The substitution of the alkaline-earth ions of the perovskite A site by Pb ions induces another soft mode, in which the A -site ions contribute to the spontaneous polarization, resulting in an enhancement of the ferroelectric polarization [41]. On the other hand, the molecular mass of the B -site ions has significant effect on the electromechanical coupling factors of lead-based perovskite piezoelectric materials [80, 81].

In this work PT, PZ and PZT are the most important perovskite materials which are discussed in detail below.

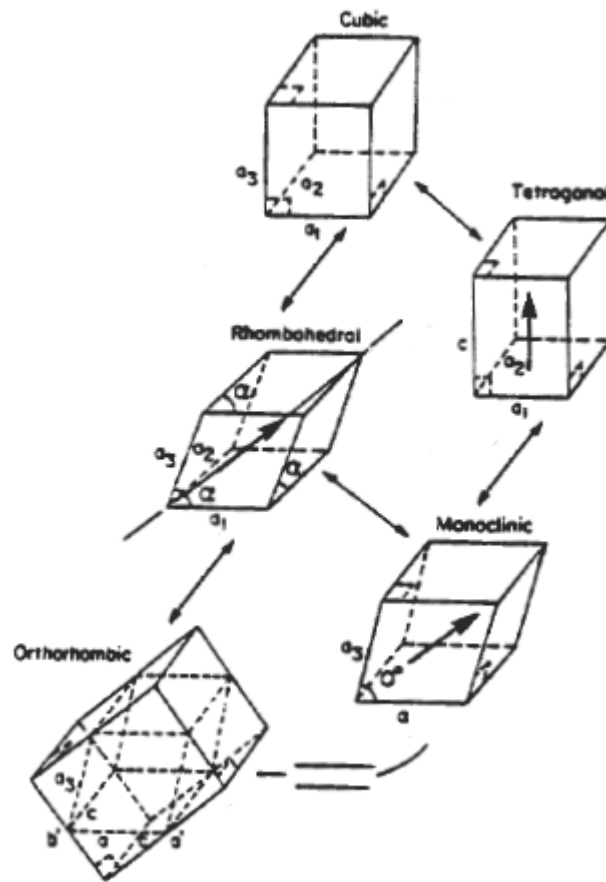


Figure 1.8 - Diagram to illustrate the phase transitions in perovskites of PZT [78].

1.2.1. Lead titanate ($PbTiO_3$, PT)

Lead titanate is a ferroelectric material having a structure similar to $BaTiO_3$ with a high Curie point ($490\text{ }^\circ\text{C}$) and a large P_s value: $52\ \mu\text{C}/\text{cm}^2$. On decreasing the temperature through the Curie point, the phase transition takes place from the paraelectric cubic phase to the ferroelectric tetragonal phase.

Lead titanate ceramics are difficult to fabricate, since PT undergoes a large volume change on cooling below the Curie point. The phase transition originates a very large strain, $> 6\%$, since the tetragonal ratio is $c/a = 1.064$ at T_c temperature. Hence, pure $PbTiO_3$ ceramics crack and fracture during fabrication. The spontaneous strain developed during cooling can be reduced by the addition of various cations, such as Ca, Sr, Ba, Sn or W, to obtain a crack free ceramic. One representative of the modified lead titanate compositions that has been extensively investigated is $(Pb_{0.67}Ca_{0.15}Sr_{0.06}Sm_{0.08})(Ti_{0.98}Mn_{0.02})O_3$. This composition has a lower c/a ratio of 1.024 and a Curie point of $255\text{ }^\circ\text{C}$) [30, 53, 54, 82-85].

The spontaneous polarization on cooling PbTiO_3 below the Curie point T_c is due to the change in the crystal structure. As shown in Figure 1.9 the paraelectric cubic phase is stable above 490°C , with the centre of positive charges (Pb^{2+} and Ti^{4+} ions) coinciding with the centre of negative ones (O^{2-}). Below the Curie point T_c , the centre of the positive charges is displaced relative to the negative one, leading to the formation of electric dipoles. The developed spontaneous polarization is the net dipole moment produced per unit volume of the dipoles pointing in a given direction [82].

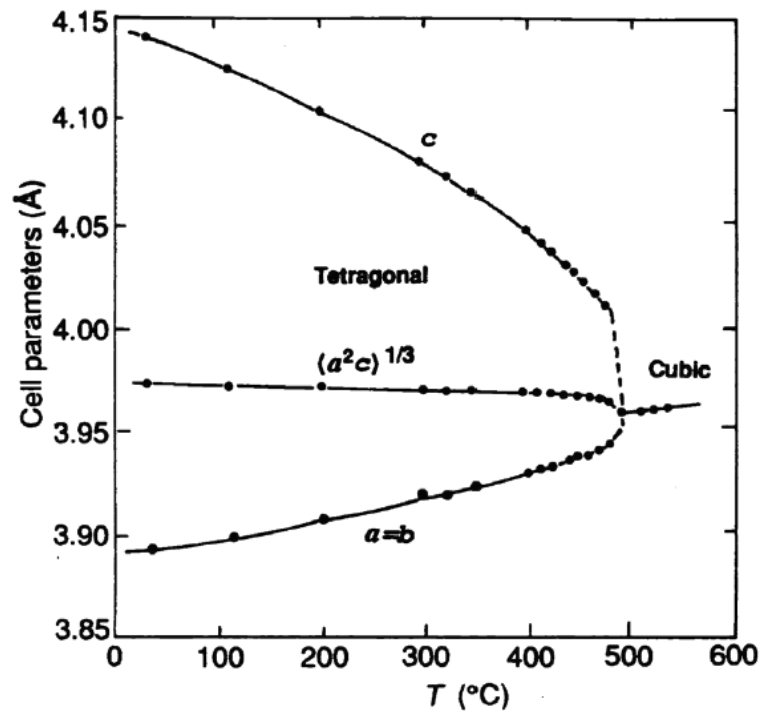


Figure 1.9 - Temperature dependence of the cell parameters of PbTiO_3 [23].

1.2.2. Lead zirconate (PbZrO_3 , PZ)

Lead zirconate is an antiferroelectric material at room temperature, with an orthorhombic perovskite structure and an antipolar arrangement along the $[100]$ direction. The orthorhombic phase remains stable up to $\sim 230^\circ\text{C}$ within the centrosymmetric space group Pbam [86-88] (in the literature it is also reported the space group Pba2 [89-91]) and then a transition occurs to a ferroelectric rhombohedral phase with a polarization along the $[111]$ direction, within the space group R3m [56, 92]. The rhombohedral phase is only stable in a narrow temperature range and transforms to a paraelectric cubic phase at \sim

232°C, within the space group $Pm3m$ [93]. Figure 1.10a illustrates the structure of $PbZrO_3$

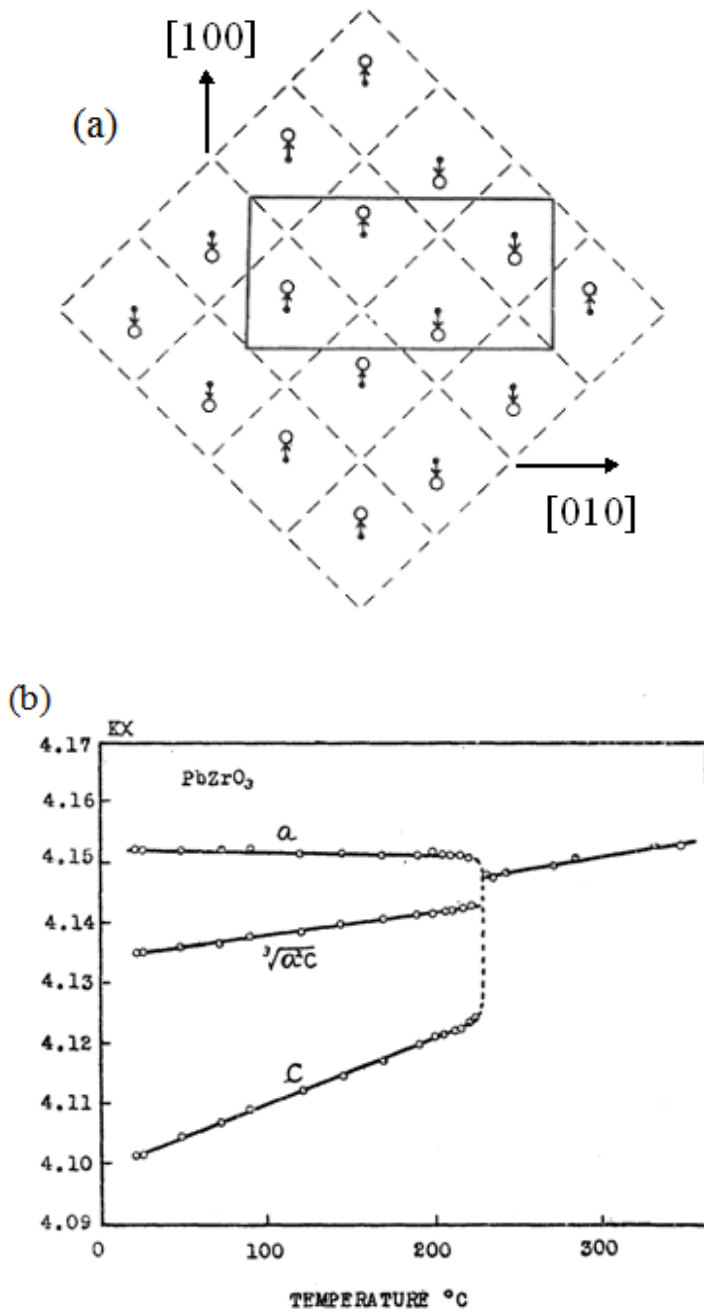


Figure 1.10 - a) the antiferroelectric structure of $PbZrO_3$; arrows represent the direction of shifting of the Pb ions and the solid line shows the orthorhombic unit cell [89]; b) temperature dependence of the cell parameters of $PbZrO_3$ [94].

viewed along (001) plane showing the anti-parallel displacement of Pb along [100]

direction which gives rise to its antiferroelectric character [89]. In Figure 1.10b it is shown the temperature dependence of the cell parameters and the calculated volume [94].

1.2.3. Lead zirconate titanate [$\text{Pb}(\text{Zr}_x\text{Ti}_{1-x})\text{O}_3$, PZT]

Lead zirconate titanate (PZT) is a solid solution of PbZrO_3 , antiferroelectric (orthorhombic structure), and PbTiO_3 , ferroelectric (tetragonal perovskite structure). PZT has a perovskite type structure with the Ti^{4+} and Zr^{4+} ions occupying randomly the B site (Figure 1.11). The PZ-PT phase diagram is shown in Figure 1.12. At high temperatures PZT has the cubic perovskite structure, which is paraelectric. On cooling below the Curie point line, the structure undergoes a phase transition to form a ferroelectric tetragonal or rhombohedral phase. The rhombohedral and tetragonal fields are separated by an almost vertical boundary (Figure 1.12a) denominated morphotropic phase boundary (MPB). In the tetragonal phase, the spontaneous polarization is along the $\langle 001 \rangle$ directions while in the rhombohedral phase the polarization is along the $\langle 111 \rangle$ directions. As shown in Figure 1.13 to Figure 1.15, most physical properties, such as dielectric, piezoelectric constants, electro-mechanical coupling factor (k_p) and remanent polarization (P_r), show an anomalous behaviour at this boundary.

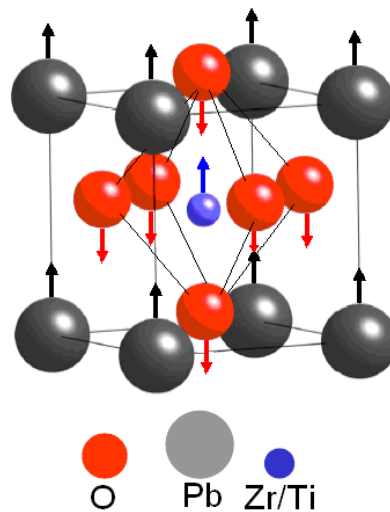


Figure 1.11 - Unit cell of the PZT showing the structure changes at the Curie temperature: $(\text{Zr}/\text{Ti})^{4+}$ ions displaced relatively to the O^{2-} ions.

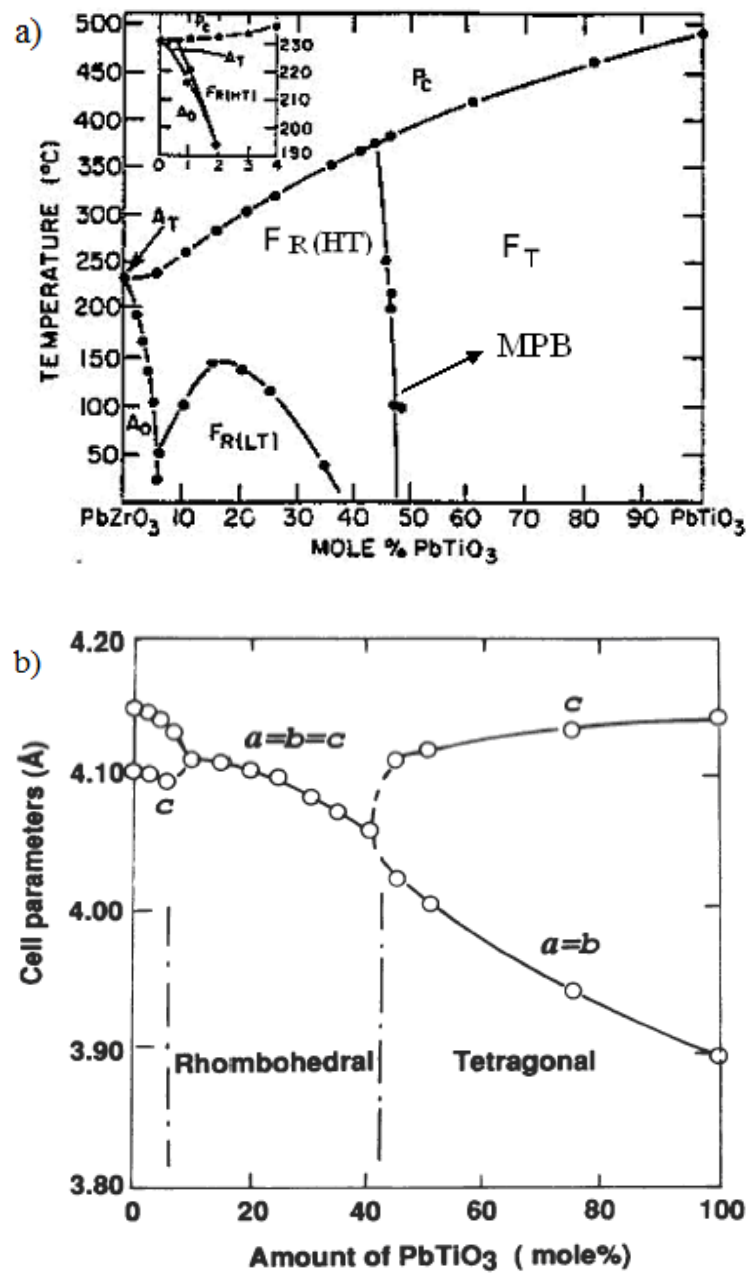


Figure 1.12 - a) Phase diagram of the $PbTiO_3$ - $PbZrO_3$ [34]; b) lattice parameter change at room temperature [77]. The symbol P_c represents the cubic phase, F_T the ferroelectric tetragonal phase, A_0 the antiferroelectric orthorhombic phase, A_T the antiferroelectric intermediate phase ($F2mm$), $F_R(HT)$ the ferroelectric rhombohedral phase of high temperature and $F_R(LT)$ the ferroelectric rhombohedral phase of low temperature.

The MPB at room temperature has a chemical composition of $\sim 52/48$ for the Zr/Ti ratio. PZT ceramics with the MPB composition show excellent piezoelectric properties. The

poling of the PZT ceramic (see Section 1.5) is also easier at this composition because the spontaneous polarization within each grain can be switched to one of the 14 possible orientations (eight $\langle 111 \rangle$ directions for the rhombohedral phase and six $\langle 001 \rangle$ directions for the tetragonal phase). Below the Zr/Ti ratio of 95/5, the solid solution is antiferroelectric with an orthorhombic phase. On the application of an electric field to this composition a double hysteresis loop is obtained [30].

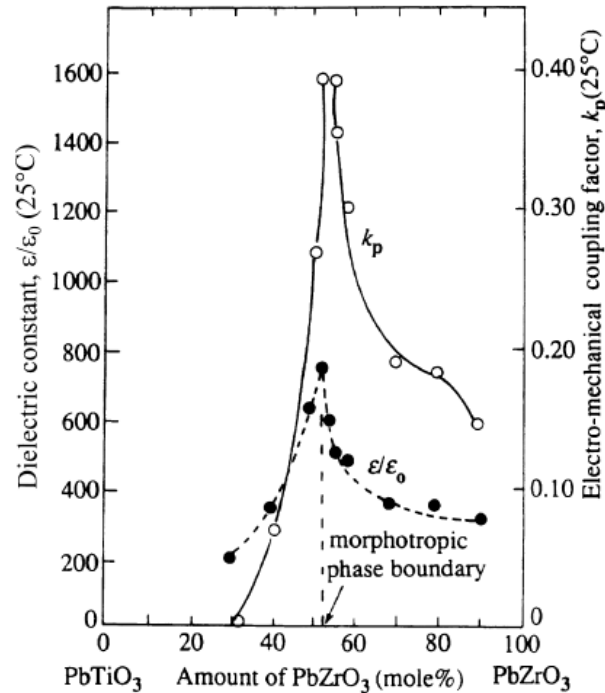


Figure 1.13 - The effect of the composition on the dielectric constant and electromechanical planar coupling factor k_p in PZT ceramics [30].

In order to suit specific requirements for some applications, piezoelectric ceramics can be modified by doping them with the same or with different valence as the ions of the lattice. PZT ceramics having the composition of the MPB are doped with different ions to form "hard" and "soft" PZT's. The first additives used in compositional modification of PZT were the isovalent ions with the Pb^{2+} , Ti^{4+} and Zr^{4+} . These ions are partially replaced by other cations with the same chemical valency and similar ionic radii. An example is $\text{Pb}_{0.95}\text{Sr}_{0.05}\text{Zr}_{0.52}\text{Ti}_{0.48}\text{O}_3$, where 5% of the A-sites have been replaced by Sr^{2+} . The major effect of such isovalent additives is to lower the Curie point, giving enhanced permittivity.

Hard PZT's are doped with acceptor ions such as K^+ or Na^+ , for the A site, or Fe^{3+} , Al^{3+} or Mn^{3+} , for the B site. The acceptor ions create oxygen vacancies in the lattice, which cannot be removed by sintering the ceramic in an oxygen atmosphere [95, 96]. Hard PZT's usually have lower permittivity, piezoelectric coefficients, dielectric losses and increased conductivity. The reason for this is that a significant part of the total measured loss is due

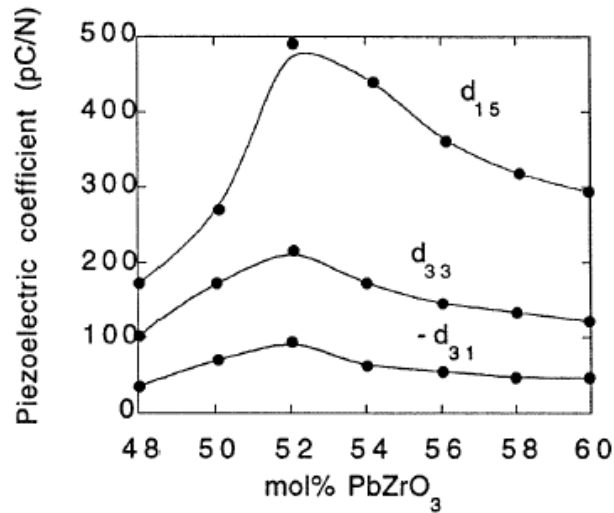


Figure 1.14 - Piezoelectric coefficients of $Pb(Zr,Ti)O_3$ ceramics as a function of composition in the vicinity of the morphotropic phase boundary [30].

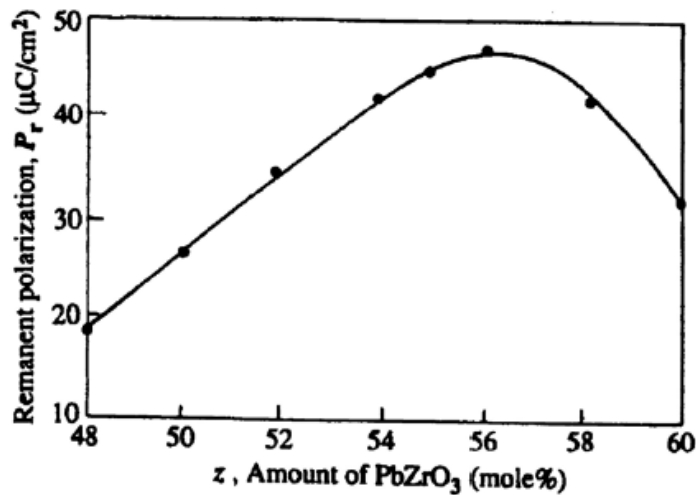


Figure 1.15 - Variation of the remanent polarization (P_r) with the composition in the $Pb(Zr,Ti)O_3$ near of the morphotropic phase boundary [30].

to domain-wall motion, which is reduced in hard ceramics. They are more difficult to pole and depole, thus making them ideal for applications in high electric fields. On the other hand, soft PZT's are doped with donor ions such as La^{3+} , for the A site or Nb^{5+} or Sb^{5+} , for

the B site, leading to the creation of A site vacancies in the lattice [97-100]. Soft PZT's have a higher permittivity, larger losses, higher piezoelectric coefficient and are easy to pole and depole. They can be used in applications requiring very high piezoelectric properties. In Figure 1.16 it is plotted the typical loss behaviour for hard and soft PZT material [101].

The changes in the dielectric properties are ascribed to the lead vacancies, which are assumed to be present due to lead volatilization during sintering, resulting in the increase of the domain wall mobility. In general, when donor ions with large ionic radii, such as La^{3+} , Nd^{3+} , etc., occupy the A-sites to replace Pb^{2+} ions, extra positive charges are introduced into the lattice due to the fact that the valence of the doping ions is higher than that of Pb^{2+} ions and a Pb vacancy is created in the lattice to maintain electro-neutrality. When donor ions with small ionic radii, such as Nb^{5+} , Ta^{5+} , etc., enter into the perovskite lattice, they occupy the B-sites to replace Zr^{4+} or Ti^{4+} ions. Since the doping ions have a higher valence than +4, extra positive charges enter the lattice and again Pb vacancies have to be created to ensure electro-neutrality. These Pb vacancies make the transfer of atoms easier than in a perfect lattice; thus domains move with smaller electrical fields (or smaller mechanical stresses).

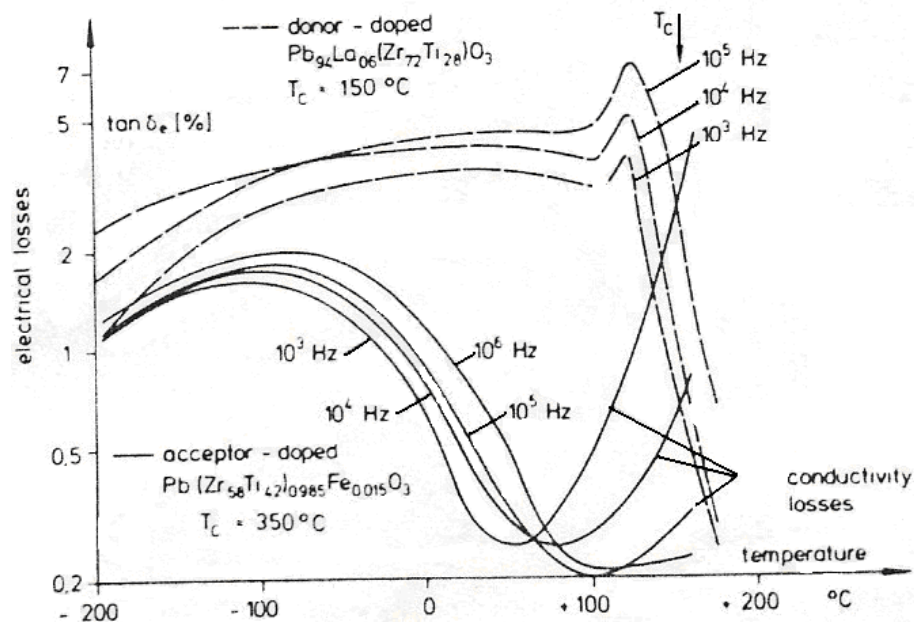


Figure 1.16 - Comparison of the temperature dependence of the electrical losses of typical donor and acceptor-doped PZT and PLZT ceramics, with the frequency as parameter [101].

It has been confirmed [102] that the undoped PZT ceramics possess p-type conductivity due to the lead oxide evaporation during the sintering process, which creates Pb vacancies in the sintered PZT ceramic. Therefore, in a PZT ceramic doped with acceptor ions, where a n-type space charge is created due to oxygen vacancies, the centres of the negative charges (n-type) and the positive one (p-type), which cause the appearance of an internal field E_s inside the grains of PZT and this field E_s inhibits domain motion. The inhibition of the domain motion reduces the dielectric losses and therefore the mechanical quality factor (Q_m) is enhanced. Q_m indicates the rate of energy stored with respect to the energy dissipated per cycle of the electric field.

Apart from the above-mentioned additives, there are some other doping ions, such as Ce, Cr or U, which can have different valences that induce the role of both a soft and a hard ferroelectric. For example, Cr-doped PZT ceramics have high Q_m values, while their dielectric loss increases and k_p decreases. Co-doping, *i.e.* with two or more doping elements, is also frequently used for better piezoelectric properties. For example, MnO_2 - Nb_2O_5 co-doped PZT ceramic is better than that of single doping of Nb^{5+} or Mn^{4+} in terms of its higher k_p and Q_m values, lower permittivity and excellent temperature stability [103].

1.3. Effects of the microstructure on the piezoelectric properties

The microstructure of ceramics includes factors such as grain size (and grain boundaries), density (and porosity) and homogeneity. The grain size of PZT ceramics depends on the composition and the sintering conditions. In general, the grain size of PZT ceramics increases, with increasing the sintering temperature and time, from submicron to about 10 μm . The metal oxide dopants affect the grain growth during sintering. Some metal oxides may hinder the grain growth. For example, the average grain size decreases from 5.5 μm , in undoped PZT ceramics, to 2.7 μm in PZT ceramics upon doping with 0.3 wt.% Fe_2O_3 , while the Q_m value increases from 300 to 900 [95]. It was also shown that, when the PZT is Fe_2O_3 doping over 0.8 wt.%, particles containing Fe^{3+} ions precipitate at grain boundaries and the properties of the ceramics deteriorate. Because the solid solubility limit of Fe in PZT is about 0.8 wt.% and the remaining Fe^{3+} ions precipitate at grain boundaries, Fe^{3+} ions can hinder the PZT grain growth. On the other hand, some dopants (e.g. CeO_2) in PZT ceramics are helpful to promote the grain growth [23].

The effect of the grain size on the piezoelectric properties was reported by Okazaki *et al.* [104], for PZT ceramics with the composition $\text{Pb}(\text{Zr}_{0.51}\text{Ti}_{0.49})\text{O}_3$ doped with 0.1 wt.% MnO_2 with a density of $7.70 \sim 7.85 \text{ g/cm}^3$, who showed that the piezoelectric properties of the PZT ceramics increase approximately linearly with the increase of the grain size (Figure 1.17). However, Demartin *et al.* [105] and Ichinose and Kimura [106] reported that the maximum electrical properties are obtained at a critical grain size of 2 to 3 μm for PZT ceramics doped with Nb and partially substituted with $\text{Pb}(\text{Sb,Nb})\text{O}_3$. The deterioration of the piezoelectric properties with decreasing the grain size is probably related to fewer domains and less mobile domain walls [107]. Mishra and Pandey [108] also pointed out that below a critical size, the formation of ferroelectric domains is not energetically favourable.

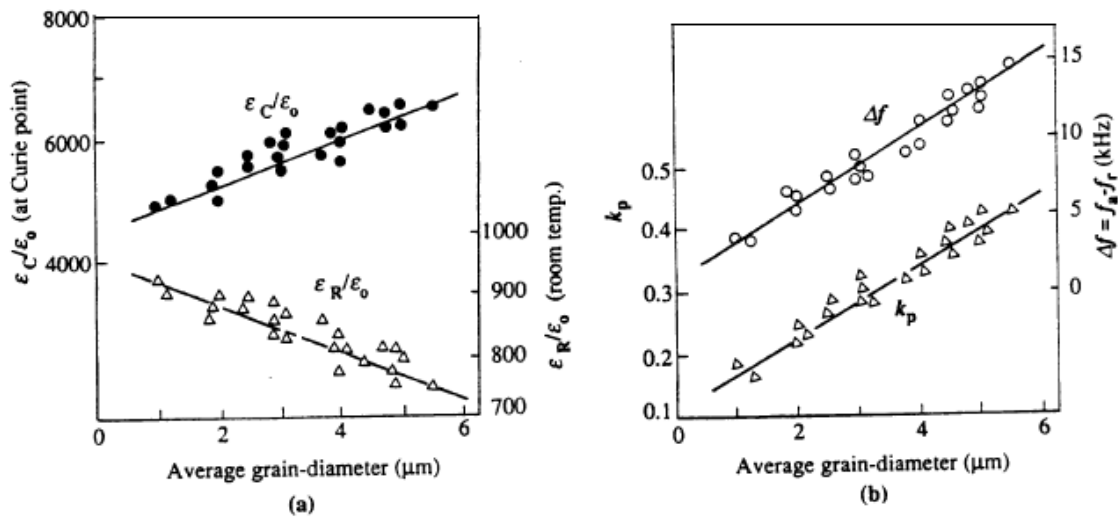


Figure 1.17 - Dependence of the dielectric and piezoelectric properties on the average grain size of the ceramic $\text{Pb}(\text{Zr}_{0.51}\text{Ti}_{0.49})\text{O}_3$ doped with 0.1 wt.% MnO_2 [109]. The symbols ϵ_C and ϵ_R are the dielectric permittivity at the Curie and room temperature, respectively, and Δf is the difference between the resonance f_r and antiresonance f_a frequencies.

The porosity also affects the piezoelectric properties and is dependent on the sintering conditions. Sintering in oxygen atmosphere is reported to facilitate the pore-elimination process [110]. PZT ceramics possess higher densities and the grain growth is slower with the increase of the oxygen partial pressure. Despite the difference in grain size and density, there are not significant differences in k_p values and it was observed that in both

atmospheres k_p does not increase linearly with the increase of the grain size from 0.5 to 1.6 μm (Figure 1.18).

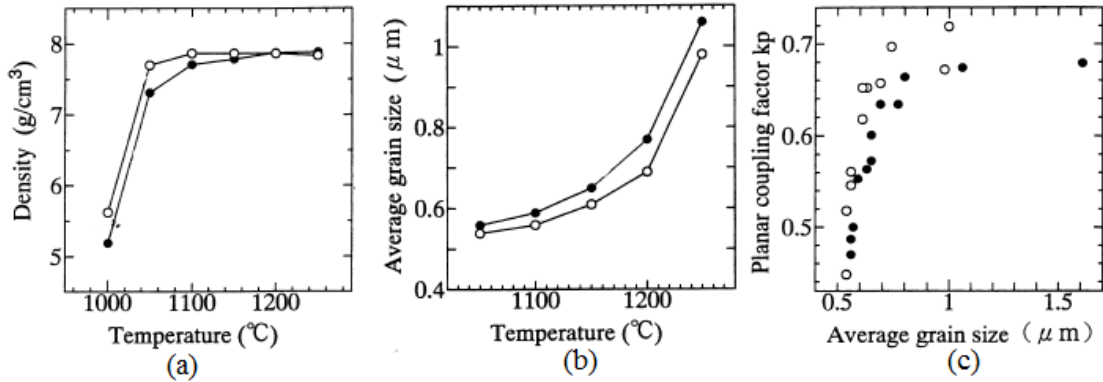


Figure 1.18 - Effect of the sintering atmosphere (\bullet air and \circ oxygen) on (a) the density, (b) the grain size and (c) the planar coupling coefficient k_p , in PZT ceramics partially substituted with $\text{Pb}(\text{Sb},\text{Nb})\text{O}_3$ [111].

The chemical homogeneity is found to have a more pronounced effect on the piezoelectric properties than on the density and the grain size. Kim *et al.* [112] reported that, for the same PZT composition processed via different routes, the electrical properties are very different. PZT ceramics processed via the conventional mixed-oxide route had significantly lower dielectric and piezoelectric properties than those processed via chemical preparation techniques (sol-gel, hydrosol, aerosol, microemulsion, etc.). This difference in the degree of chemical homogeneity in the PZT ceramics is reflected in those properties, ϵ_r and k_p , which are very dependent on the Zr/Ti ratio. The piezoelectric properties of the materials sintered at 1000°C are also inferior to those sintered at 1200°C, though they have similar density and grain size. The lower values are believed to be related to a lower crystallinity of the materials [112].

There have been many attempts to investigate the influence of the grain size on the piezoelectric properties in PZT ceramics. In general, grain size studies were limited in the range of 1.0 - 10 μm in bulk ceramics [113]. The variations in properties with grain size showed little consistency. Reasons for those inconsistencies are believed to be related to the processing and to the control of the grain boundary resistivity that lead to a space-charge accumulation, which masks the size-effect response in the ferroelectric grains [113].

One of the intrinsic microstructural characteristics in ferroelectric PZT ceramics is the development of internal stresses due to strains occurring during the paraelectric-ferroelectric transition [114]. In addition, the thermal expansion anisotropy of the tetragonal crystals may also contribute to the stress development. According to the internal stress model proposed by Buessem *et al.* [115] the large internal stress developed during cooling of PZT is released by the formation of a polydomain structure. A polydomain structure is possible if the grain is large enough to contain multiple domains. Consequently, the internal stress along the grain boundary would be substantially relieved in large PZT grains by the possible formation of multidomain structures. For small PZT grains, however, the formation of polydomain structure may not occur. Consequently, the internal stress increases during the cooling. Such a stress will not be relieved by the formation of 90° domains and leads to a decrease in T_C [115, 116]. In Kamel *et al.* work [115, 116] it was found that increasing the grain size maximizes the dielectric and piezoelectric properties as compared to properties of grain size often used in practice. The dielectric contribution of grain boundary, porosity, etc. (extrinsic dielectric contributions), increases with increasing grain size due to the increased number of domain walls.

It is worth noting that the most striking effects of the grain size, however, are on the mechanical rather than on the electrical properties. Both flexural strength and Vickers' hardness increase dramatically with the decrease of grain size [106].

1.4. Theory for the morphotropic phase boundary (MPB)

From the application point of view the most interesting compositions in the PZT system lie near the centre of the PZ - PT phase diagram, where tetragonal and rhombohedral phases are separated by a boundary which is nearly independent on temperature. The composition of this so-called morphotropic phase boundary (MPB) is approximately 52/48 (Zr/Ti) at room temperature. The piezoelectric coefficients, electromechanical coupling coefficients, dielectric permittivity and remanent polarization measured on ceramic samples reach a peak near the region of the morphotropic phase boundary (Figure 1.13 to Figure 1.15), not necessarily at the same composition [30], which explains why these compositions are technologically so interesting.

Actually there are two main questions, whose answers are not accepted by all the scientific community, related to the MPB. One is related with the cause of the maximum in the electro-mechanical properties in the MPB and the other one is related with the coexistence of the rhombohedral and tetragonal phases in this region. In this section we are trying to put the different positions in confrontation.

1.4.1. *Principal ideas to explain the maxima of the electro-mechanical properties in the MPB*

Up to now good-quality single crystals of PZT with compositions in the middle of the phase diagram were not available and therefore comparable measurements could not be made on single-domain single crystals, which could help to answer the two questions. Calculations using the thermodynamic phenomenological theory (Appendix I) have shown that a peak in the piezoelectric coefficients and dielectric permittivity is expected at the MPB in monodomain single crystals [117-119]. An exception for the appearance of such a peak is the behaviour of the polarization for which theoretical calculations do not predict a peak in single crystals at the MPB. The results of the thermodynamic calculations have been recently confirmed by a experimental study of the properties of single-crystal (epitaxial) PZT thin films [120] which clearly showed a peak in the permittivity but not in the polarization at the MPB. Properties of random-oriented polycrystalline PZT thin films [121] are in qualitative agreement with results obtained on bulk ceramics.

The maximum of the permittivity in the vicinity of the MPB in polycrystalline materials is explained by the large number of possible orientations of the polarization vector, which facilitates the domains reorientation. For the phase coexistence model, there are six equivalent polar axes in the tetragonal state giving a total of six possible domain states with 90° and 180° walls. The distortion in the rhombohedral phase is along the body diagonal of the cubic state giving rise to eight possible domain states with 180° , 109° and 71° domain walls. At the MPB, the free energies of the rhombohedral and tetragonal phases are equal and it is possible that the electrical poling field easily induces the switching between tetragonal and rhombohedral domain states. There are thus 14 available directions along which polarization may be reoriented by the poling field, leading to a large remanent polarization for compositions near the MPB [5]. The large remanent polarization at the MPB in randomly oriented PZT also helps to increase the peak in the

piezoelectric coefficients at the MPB. Other interpretations of the origin of the peak in the properties of PZT at the MPB have also been proposed [8, 122]. Carl *et al.* have shown [8] experimentally that the peak in k_p at the MPB is essentially due to the maximum value of ε_{33}^x as is expressed by the expression for the planar coupling coefficient (k_p):

$$k_p^2 = \frac{2}{1-\nu} (g_{31})^2 \frac{(\varepsilon_{33}^x)}{(c_{11}^E)} \quad (1.23)$$

where ν is the Poisson's ratio, g_{31} the piezoelectric voltage constant, ε_{33}^x the dielectric constant at constant stress (X) and c_{11}^E is the compliance at constant electric field (E). Theoretical arguments have also been advanced to show that the maximum of the electromechanical response at MPB is not linked with the phase coexistence. This maximum is due to the peak in the dielectric constant caused by the instability of the tetragonal phase in the transition region from the tetragonal to rhombohedral phase as a function of the composition at room temperature [122].

In the Mishra *et al.* work [122], the authors correlated the temperature variation of k_p with structural changes for compositions close to MPB to confirm that the phase coexistence at MPB is not responsible for the peak in the electromechanical response. Phase coexistence, in fact, is shown to lead to a lowering of the electromechanical response. On the other hand they showed that the maximum electromechanical response as a function of composition (x) occurs in the tetragonal phase field, just outside the two-phase MPB region in the (x, T) plane.

Rosario *et al.* [9, 123] also found a decrease of the distortion of the unit cell when the compositions approach the MPB (Figure 1.19). They established a direct relation between the decrease of the unit cell distortion and the increase of the dielectric properties, arriving to the conclusion that the decrease of the unit cell distortion in the tetragonal and in the rhombohedral phase is responsible for the increase of the electro-mechanical properties in the MPB (Figure 1.20). Using a phenomenological theory of phase transitions Zhang *et al.* [123] arrived to the same result as Soares *et al.* [9].

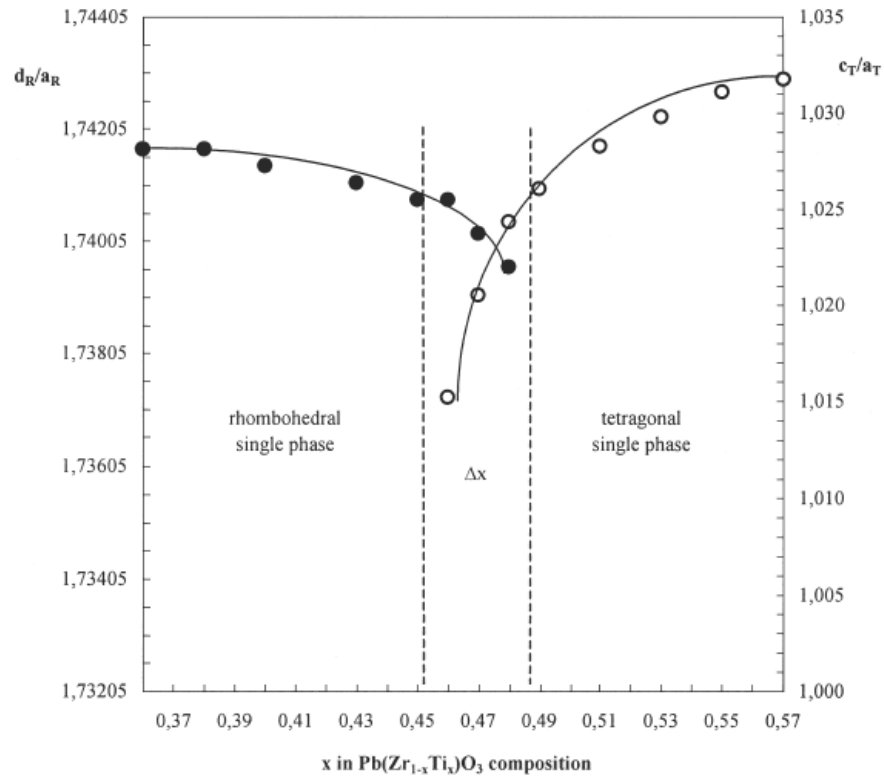


Figure 1.19 - Evolution of the unit cells distortions of the rhombohedral phase, d_R/a_R , and of tetragonal phase, c_T/a_T , with the composition of the PZT ceramics sintered at 1250 °C for 2 h. The tetragonal lattice distortion, c_T/a_T , is decreasing down to $c_T/a_T=1$ (the cubic phase) and the rhombohedral lattice distortion, d_R/a_R , where d_R is the diagonal of the rhombohedron, is decreasing down to $d_R/a_R = \sqrt{3}$ (the cubic phase). Both decreasing behaviours are more pronounced inside the coexistence region [9].

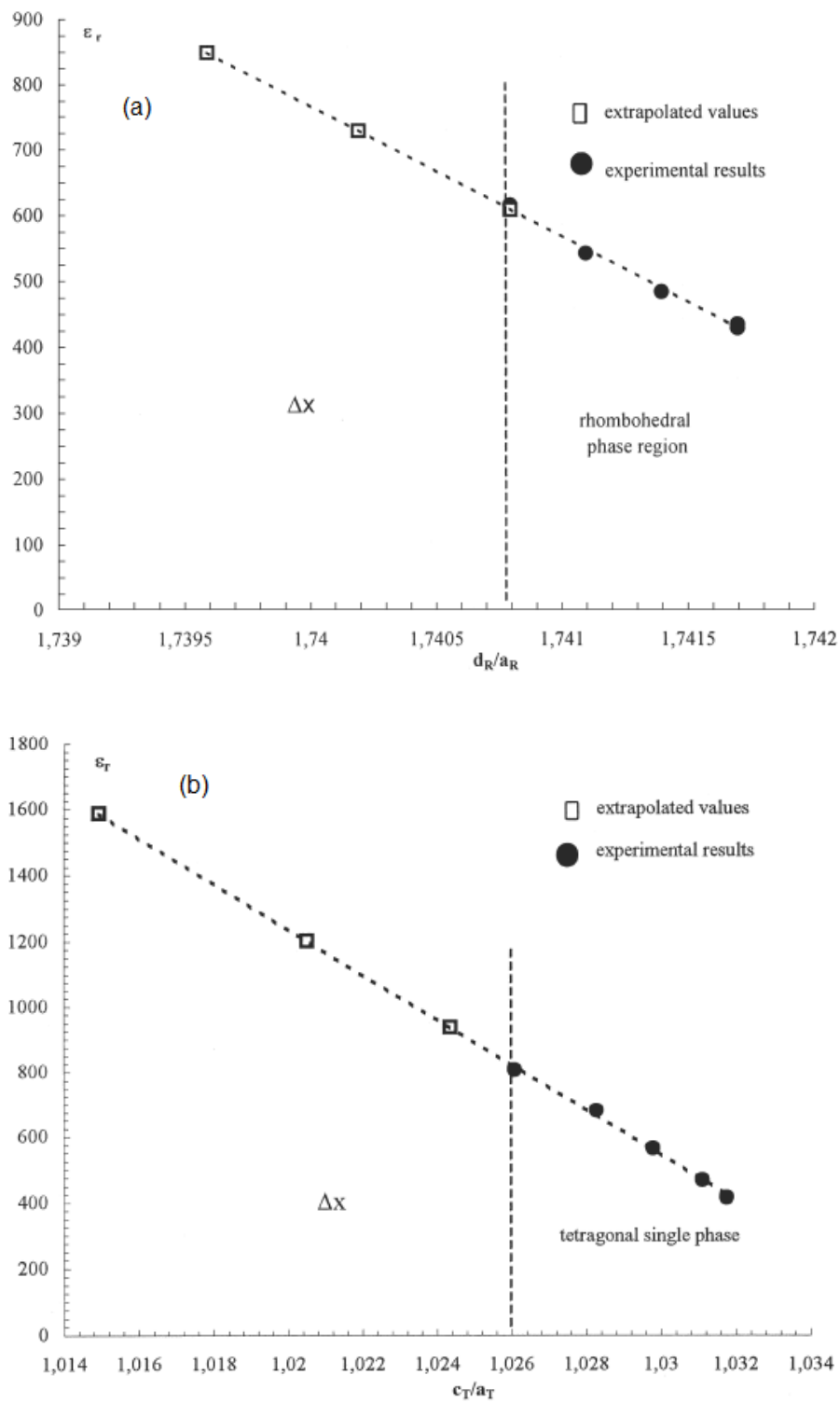


Figure 1.20 - Relation between the dielectric permittivity and the lattice distortion of single phase PZT: (a) rhombohedral phase; (b) tetragonal phase [9].

Recently, Noheda *et al.* [124] found that the MPB region is the field of a monoclinic phase, which was confirmed later by others [125, 126] (Figure 1.21). The maximum in the electro-mechanical properties is explained by the presence of this monoclinic phase, having 24 possible polarization directions which is an advantage for the polarization in the MPB [124]. This could give a solution for the two questions, one concerning the maximum in the electro-mechanical properties (due to the presence of the monoclinic phase) and the other concerning the coexistence of the two phases (there is no coexistence, it is only one phase). Noheda *et al.* [6] also found an abrupt change in the unit cell parameters but a linear volume change with the composition in the MPB (Figure 1.22).

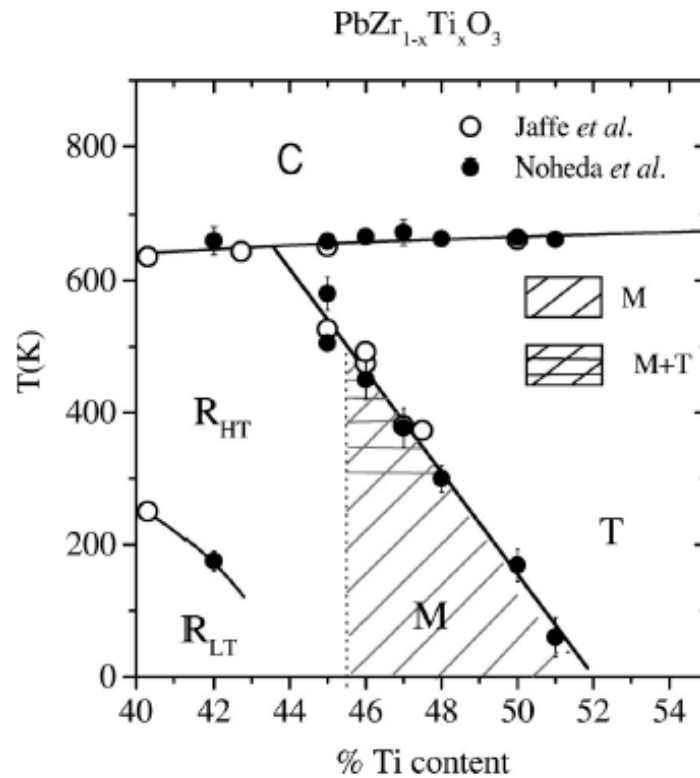


Figure 1.21 - PZT phase diagram around the MPB. The monoclinic region is shaded with diagonal lines. Horizontal lines are superimposed in the region of tetragonal-monoclinic phase coexistence [6, 127].

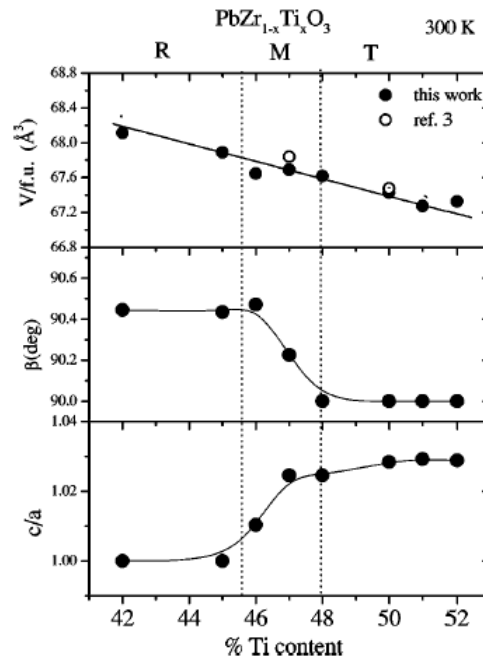


Figure 1.22 - The structural evolution with composition, from the rhombohedral to the tetragonal PZT phases, through the monoclinic phase, as illustrated by the cell volume per formula unit, V (top), the monoclinic angle β (centre) and the lattice strain c/a (bottom) for PZT with $0.42 < x < 0.52$, at 300 K. The cell volumes of the samples are also plotted as open circles at the top of the figure (reproduced from [6]).

1.4.2. Causes for the occurrence of the phase coexistence in the MPB

Some controversy still exists concerning the causes for the occurrence of the phase coexistence in ceramics, the distribution of the coexisting phases and their chemical and structural properties. Benguigui *et al.* [128-130] and Barbulescu *et al.* [131] used the classical thermodynamic theory of solutions to justify the existence of both phases. In their opinion, the two-phases region observed around the MPB of PZT ceramics is a solubility gap. From this model, inside the insolubility interval, only the relative amount of each phase is expected to change according to the lever rule, while the chemical composition, the lattice parameters and the physical properties (dielectric susceptibility, piezoelectric constants) of each phase should remain constant [132]. Among the research work devoted to this subject, Isupov's contribution is one of the most comprehensive. The author formerly considered that the coexistence of the two ferroelectric phases is thermodynamically predictable and tried to state the conditions for that occurrence [133-135]. He then suggested that the tetragonal phase is a stable phase in the composition range

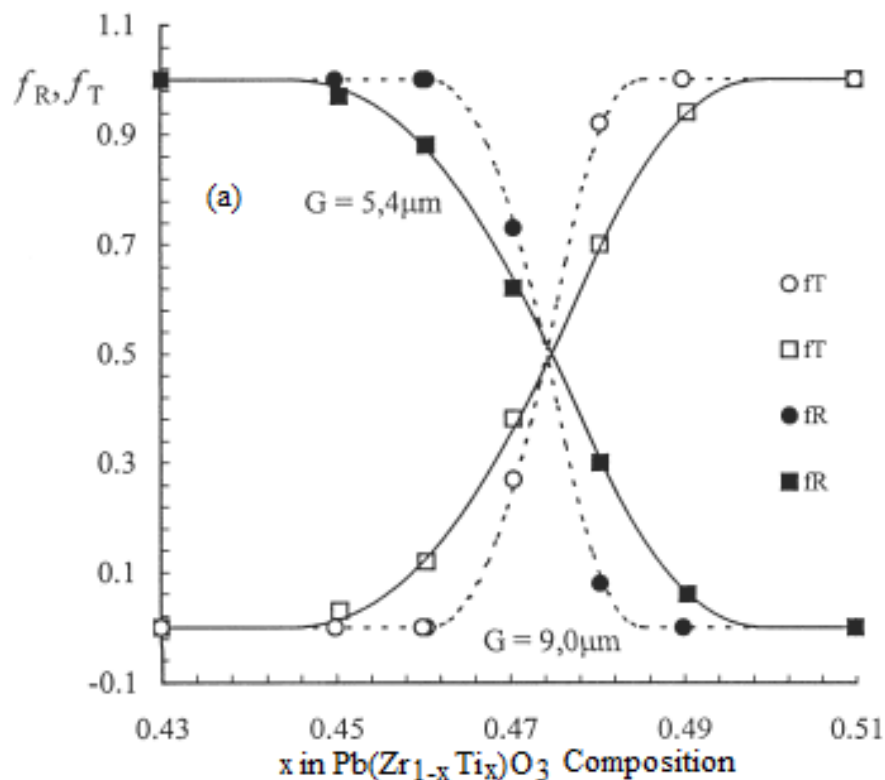
from $x = x_T$ to $x = 1$, while the rhombohedral phase is stable in the $0.08 \leq x \leq x_R$ range (with $x_T < x_R$). The phase coexistence interval would range from x_T to x_R , with one of the phases metastable in relation to the other, in one of the sides of the coexistence interval, and vice-versa in the other side. The presence of the metastable phases resulted from a composition hysteresis around the MPB [136], composition that corresponds to the phase transition considered as a first order phase transition [130]. In this case, inside the phase coexistence interval, the dependence of the lattice parameters of each phase on the composition should be the same as in the single phase regions, which was not experimentally observed. Later, Isupov proposed that the coexistence phase interval depends on the degree of chemical equilibrium of the ceramic and tried to justify the phase coexistence by the presence of chemical heterogeneities in the system [136, 137]. Due to those heterogeneities, associated with composition fluctuations, the coexistence of the tetragonal and the rhombohedral phases is possible in the same grain. Taking a normal distribution of the local Ti:Zr ratio around the mean average composition, \bar{x} , the lattice parameters and the dielectric properties can be related to the mean composition of the coexistence phases, \bar{x}_T and \bar{x}_R , which change slower with the composition than in the monophasic solid solutions. This is different from the phase structure behaviour predicted by the solubility gap and by the composition hysteresis in the first order transition models.

Beyond chemical fluctuations, other factors seem to contribute to the phase coexistence phenomena in ceramics [138, 139]. Wersing *et al.* [138], studying the phase coexistence in PZT prepared from spray dried salt solutions, showed that, even in these 'microscopically homogeneous ceramics', the phase coexistence is still present in a finite compositional range. The authors agreed that compositional fluctuations could stabilise the coexistence of the two phases around the morphotropic transition, although it was not a necessary condition for its occurrence. Emphasis was put on the physical causes for the phase coexistence, namely the reduction of the elastic and the depolarisation energies. Kala [139] and Isupov [137] also recognised that internal stress could favour the coexistence of tetragonal and rhombohedral phases around the MPB.

Experimentally, the coexistence of phases with different composition is not detected above the Curie point [140] and so, it must be considered that above this temperature there is no limited range for the solid solution in PZT system. Therefore, it seems unlikely that upon cooling through the Curie point, the homogeneous solid solution splits into two solid

solutions with different compositions [141, 142]. The temperature is too low to allow the required diffusion of the cations. Based on this fact, Cao and Cross developed a statistical distribution model to describe the molar fraction change in the region where both phases coexist [141, 143]. This model assumes that the two phases occur due to thermal fluctuation quenching during the cooling from the paraelectric to the ferroelectric states. While the solubility gap model reflects the law of mass conservation, this one considers that the phase coexistence region is a statistical distribution of the two phases, where only the MPB is well defined. The former implies a mixing of phases with different chemical compositions, while the later postulates the mixture of phases with the same chemical composition but with distinct structures.

Rosario *et al.* [144] experimentally found a decrease of the width of the phase coexistence (Δx) with the grain size (Figure 1.23). If, with the increasing of the grain size, the width of the MPB decreases, then it is possible to conclude, that, in the limit case of a monocrystal, the MPB will disappear, as was already seen experimentally [91].



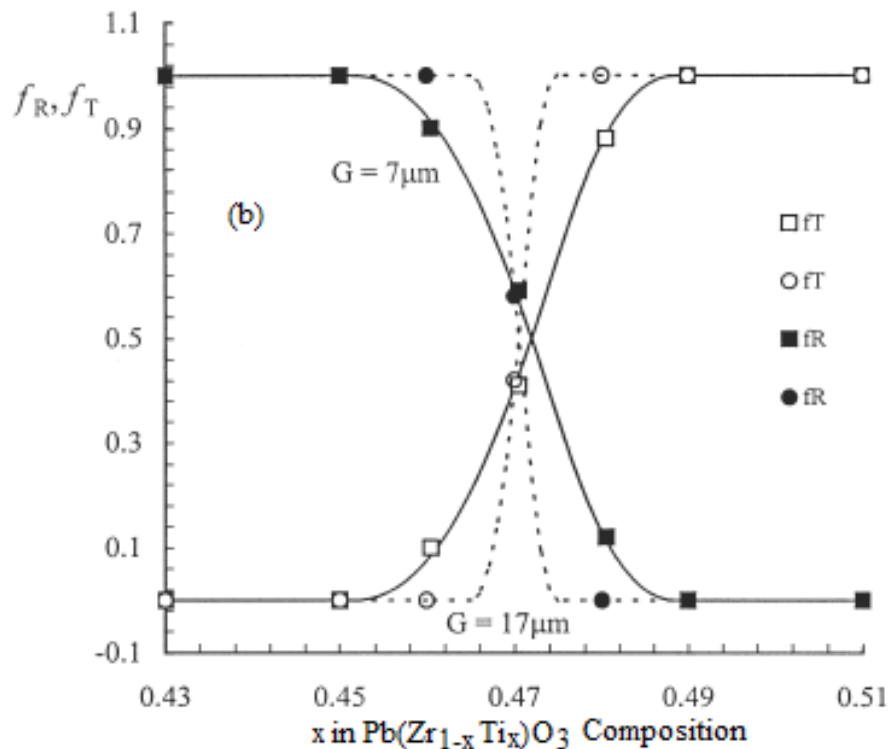


Figure 1.23 - Molar fractions of the rhombohedral and the tetragonal phases, f_R and f_T , respectively, in $\text{Pb}(\text{Zr}_{1-x}\text{Ti}_x)\text{O}_3$ solid solutions. The points correspond to experimental results and the curves are fittings using the statistical model: (a) sintered ceramics at 1150 °C for 2 h (■, □) and 16 h (●, ○), and (b) sintered ceramics at 1250 °C for 2 h (■, □) and 16 h (●, ○) (reproduced from [144]).

1.5. Ferroelectric phase transition

Early research work on ferroelectric phase transitions is summarized in several articles by R. E. Nettleton [145-148]. When the temperature decreases through the Curie point, a ferroelectric crystal undergoes a structural phase transformation from the paraelectric state to the ferroelectric one. If there are two or more ferroelectric phases in a crystal, the Curie point only specifies the upper temperature at which the paraelectric-ferroelectric phase transition occurs [23].

The most important progress in the modern theory of ferroelectric phase transitions is the concept of a soft mode, which was proposed on the basis of lattice dynamics by W. Cochran in the end of the 1950's [149-151]. According to this theory, ferroelectric state stems from the instability of a transverse vibrational mode, referred to as a soft mode or a

ferroelectric mode. Detailed lattice dynamic calculations for several ferroelectric crystals and more rigorous mathematical treatments of the soft mode in ferroelectrics have been reported by Blinc and Zeks [152]. Near T_C the crystalline lattice is also “soft” and can be polarized strongly with a relatively small coercive field. Therefore, the dielectric permittivity of many of useful ferroelectrics is very high in the vicinity of T_C and can reach values as high as 10,000-80,000 at this point. This phenomenon is usually called dielectric anomaly. The “softness” of the lattice at temperatures near T_C makes dielectric properties and other related properties such as elastic, optical and thermal constants, to be temperature dependent in a wide range of temperatures around T_C [23]. In most ferroelectrics, the temperature dependence of the dielectric permittivity above T_C (in the paraelectric phase) can be described by a simple law known as the Curie-Weiss law [22, 23] (Equation 1.7).

The transition from the paraelectric to the ferroelectric state occurs differently in different types of ferroelectric materials. These transitions may be of the first or second order in classical proper ferroelectrics [22]. The order of the phase transition is defined by the discontinuity in partial derivatives of the Gibbs’ free energy, G , at the phase transition temperature [36]. By definition, for an n^{th} -order phase transition, the n^{th} -order derivative of G is a discontinuous function at the transition temperature. Thus, spontaneous polarization and strain change continuously at T_C for a ferroelectric with 2^{nd} -order phase transition and are discontinuous at T_C for a ferroelectric with 1^{st} -order phase transition. It should be mentioned that the slope of the curve of reciprocal permittivity versus temperature below T_C is negative and twice that above T_C for a 2^{nd} -order phase transition, while the ratio of these slopes immediately below T_C to that above T_C is -8 for a 1^{st} -order phase transition [22, 153]. Phenomenological theories (sometimes called thermodynamic theories) are based on the Landau-Ginsburg-Devonshire model [154] and have been also reviewed in the literature (see annexe I) [20, 23]. Figure 1.24 summarizes, schematically, the temperature dependence of the dielectric permittivity and the spontaneous polarization for different ferroelectric phase transitions [153].

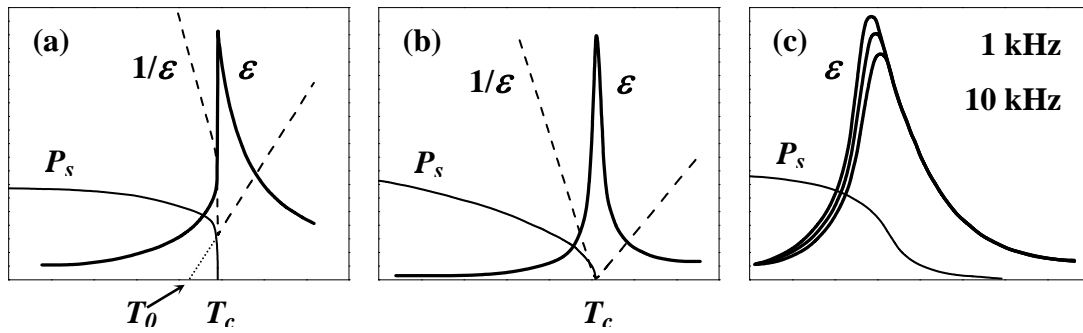


Figure 1.24 - Schematic representations of ferroelectric phase transitions via temperature dependences of the dielectric permittivity ϵ and the spontaneous polarization P_s , for (a) first- (b) second-order ferroelectric and (c) a relaxor ferroelectric [153].

Other ferroelectric materials called relaxors, as exemplified by several perovskite-type compounds [e.g., $\text{Pb}(\text{Mg}_{1/3}\text{Nb}_{2/3})\text{O}_3$] and tungsten-bronze-type compounds [e.g., $(\text{Sr}_{1-x}\text{Ba}_x)\text{Nb}_2\text{O}_6$], can be distinguished from normal ferroelectrics, such as BaTiO_3 and PZT, by the presence of broad, diffuse and dispersive dielectric peaks on cooling over the transition temperature, T_{max} , at which the permittivity is maximum [Figure 1.24(c)] [155]. In relaxor ferroelectrics, the Curie-Weiss law is not completely obeyed in the vicinity of T_{max} . The Curie-Weiss law is obeyed by very few of solid materials and this is the reason for some modifications of the Curie-Weiss equation. One of this was proposed for the materials with diffuse phase transition [156, 157].

Assuming a Gaussian distribution for the compositional fluctuation and the polarization fluctuation, the reciprocal of the permittivity versus temperature obeys a quadratic relation [156]. The quadratic relation was generalised to a form (spin glass model) (for $T > T_c$).

$$\frac{1}{\epsilon} = \frac{1}{\epsilon_{\max}} + R(T - T_c)^\gamma \quad (1.24)$$

where γ is a parameter normally taking values between $1 \leq \gamma \leq 2$ and R is

$$R = \frac{1}{2\epsilon_{\max}\delta^2} \quad (1.25)$$

where ϵ_{\max} is the maximum value of the permittivity and δ is a parameter associated with the degree of disorder in the system [158].

Three different types of phase transitions are of interest in perovskites, starting from the highest symmetry cubic form [34]:

- Simple proper ferroelectric transitions leading to fully ferroelectric, particularly ferroelastic, phases.
- Antiferroelectric transitions close in free energy to the ferroelectric forms, giving rise to interesting dielectric and to improper ferroelastic phases.
- Oxygen octahedron tilting transitions which can occur independently, or in association, with either ferroelectric or antiferroelectric forms.

The more important for their deep influence on the dielectric polarizability and the resultant sequence of polar variants are the simple proper ferroelectric transitions. In the symmetry classification of Megaw [159-161], Tomashpo *et al.* [159-161], Lebedev *et al.* [159-161] and Shuvalov (1970) [4] the high symmetry cubic $m3m$ prototype can give six different polar species (Table 1.3). The directions of the vector of polarization, which are specified with respect to elements of the prototype symmetry, form the domain states of the ferroelectric, giving in each case 6, 8, 12, 24, 24 and 48 polarization directions.

Table 1.3 - Possible ferroelectric phase transitions from the cubic $m3m$ prototype, following the symbolism of Shuvalov [4] and the relation between the symmetry and the maximum polarization permissible in a direction when the sample is poled [30].

Phase and polar axis	Symmetry	Polarization Components	Shuvalov Species	Equivalent directions of polarization	Maximum polarization permissible
Cubic	$m3m$	$P_1^2 = P_2^2 = P_3^2 = 0$	Prototype	0	0
Tetragonal [001]	$4mm$	$P_3^2 \neq 0, P_1^2 = P_2^2 = 0$	$m3m(3)D4F4mm$	6	0.831
Rhombohedral [111]	$3m$	$P_1^2 = P_2^2 = P_3^2 \neq 0$	$m3m(4)D3F3m$	8	0.866
Orthorhombic [110]	$mm2$	$P_1^2 = P_2^2 \neq 0, P_3^2 = 0$	$m3m(6)D2Fmm2$	12	0.912
Monoclinic $\langle ij0 \rangle$ $\langle ijk \rangle$ $\langle ijk \rangle$	m	$P_1^2 \neq P_2^2 \neq 0, P_3^2 = 0$	$m3m(12)A4Fm$	24	-
	m	$P_1^2 = P_2^2 \neq 0, P_3^2 \neq 0$	$m3m(12)A2Fm$	24	-
		$P_1^2 \neq P_2^2, P_3^2 \neq 0$			
Triclinic $\langle ijk \rangle$	1	$P_1^2 \neq P_2^2 \neq P_3^2 \neq 0$	$m3m(24)A1F$	48	-

Clearly, for a polycrystalline ceramic the polarization axes are randomly oriented making more switchable the domain states and easier to align the polarization through the sample. Surprisingly, however, even though permitted by symmetry, there have been no cases reported of transitions into monoclinic or triclinic symmetries in the perovskites (even though such states would be highly advantageous for ceramics), with the unique exception of the PZT [6].

1.6. Soft mode theory for the ferroelectricity

The modern theory of ferroelectricity is based on the lattice dynamics and on the concept of the so-called soft modes [35, 150, 162]. Ferroelectric phase transitions are a special case of structural phase transitions and can thus be interpreted in terms of the stability of the crystal-lattice dynamics. In a structural phase transition, the order parameter (the polarization in the case of a ferroelectric phase transition) may be associated with a lattice vibrational mode which exhibits instability at the transition temperature. For a second-order transition, for example, the frequency spectrum of the lattice vibration related to the order parameter is proportional to $T - T_C$, so that this mode ‘softens’ (its frequency goes to zero) as the material is cooled toward T_C . Freezing of the vibrations at T_C gives rise to a nonzero-order parameter and the corresponding reduction in symmetry. A soft mode is an optical mode and can be studied experimentally by infrared spectroscopy and neutron or Raman scattering [162]. A detailed discussion of the theoretical approach can be found in the book by Lines and Glass [22].

The main technique used to study new structures is x-ray diffraction which provides a very detailed structural characterisation including the observation of phase transitions. Raman spectroscopy has also been widely used for studying structural phase transitions in ferroelectric systems. The lattice dynamics approach and its recent extensions [163] have been very successful in describing qualitatively ferroelectric phase transitions. Whereas the phase transition sequence, the effective charges of ions and the polarization can now be quite accurately calculated for many pure ferroelectrics, predictions of the piezoelectric behaviour based on microscopic theories are still not available.

Raman spectroscopy has been applied for studying the structural features in PZT ceramics [164-167]. Raman scattering is a simple, non-destructive and available

characterisation technique. The understanding of the Raman spectra is useful in the characterisation of PZT-based devices and it has been addressed for the first time only recently [36]. The picture of the microscopic mechanisms responsible for the morphotropic phase boundary behaviour in $\text{Pb}(\text{Zr,Ti})\text{O}_3$ (see section 1.4) has not yet emerged. However, preliminary calculations suggest that the simultaneous competition between long-range order and disorder of Zr and Ti may contribute to the extraordinary properties of this material. In Table 1.4 it is summarised the principal modes of vibration in PbTiO_3 . It can be seen that the introduction of the Zr ion has a little shift of position of the oscillation modes. In the phase transition from tetragonal to rhombohedral structure the principal effects are the oscillation modes $A_2(\text{TO})$ and $A_3(\text{TO})$ which disappear at room temperature. On the other hand, the oscillation modes $A_1(\text{LO})$ and B_1+E change their height, the oscillation mode $A_1(\text{LO})$ being higher in the tetragonal phase and the B_1+E one in the rhombohedral phase; in the MPB region they are equal in height (Figure 1.25). The variation of the different soft modes with the composition in the tetragonal phase is shown in Figure 1.26 [168].

Table 1.4 - Frequencies (in cm^{-1}) of the principal TO and LO phonons for PbTiO_3 [169]. A and B represent a symmetry and anti-symmetry in relation to the principal axis, respectively (one-dimensional representation). Number 1 represents symmetry with respect to a plane which contains the principal axis, E means the identity (bidimensional representation), TO means transversal and LO longitudinal modes [169].

E(TO)	E(LO)	A1(TO)	A1(LO)	B1+E
87.5	128.0	148.5	194.0	289.0
218.5	440.5	359.5	465.0	
505.0	687.0	647.0	795.0	

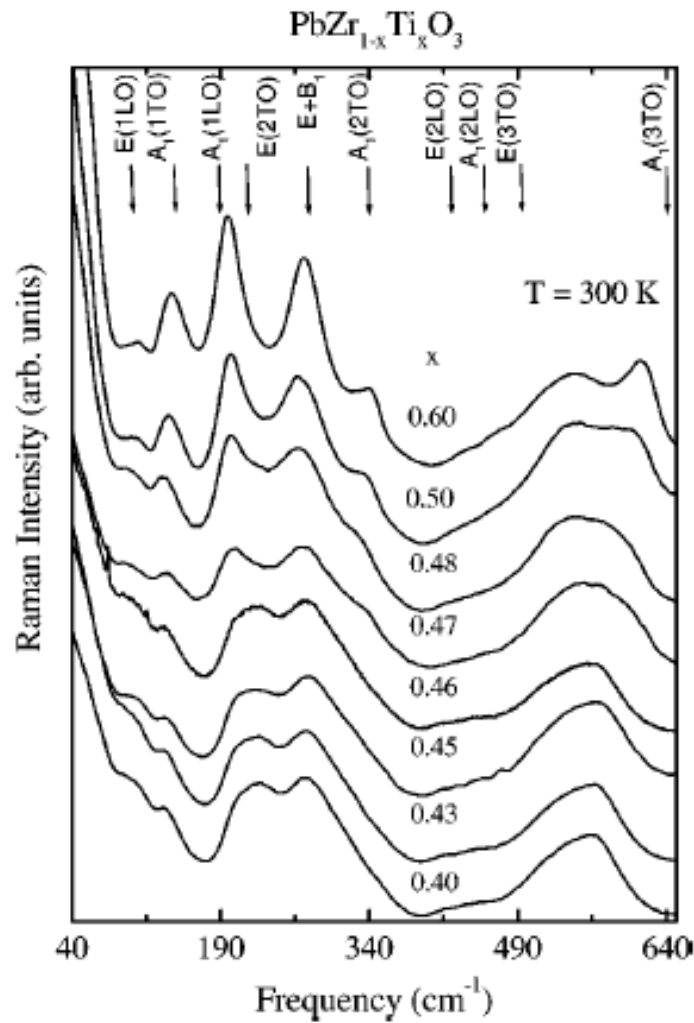


Figure 1.25 - Raman spectra for $\text{PbZr}_{1-x}\text{Ti}_x\text{O}_3$ around the morphotropic phase boundary taken at 300 K. The mode symmetry labelling stands for the tetragonal phase [170].

The recent discovery of a monoclinic ferroelectric phase by Noheda *et al.* [124] put a new light on the understanding of the dielectric and piezoelectric enhancement for compositions in the vicinity of the MPB. In fact, the monoclinic distortion was interpreted as either a condensation along one of the $\langle 110 \rangle$ directions of the local displacements present in the tetragonal phase [6] or as a condensation along one of the $\langle 100 \rangle$ directions of the local displacements present in the rhombohedral phase [87]. This monoclinic phase at low temperatures would be the first example of a ferroelectric material with $P_x^2 = P_y^2 \neq P_z^2$, where $P_x^2, P_y^2, P_z^2 \neq 0$ [124]. Hence, the monoclinic structure can be

considered as a derivative form of both the tetragonal and the rhombohedral phases, representing a link between them [165].

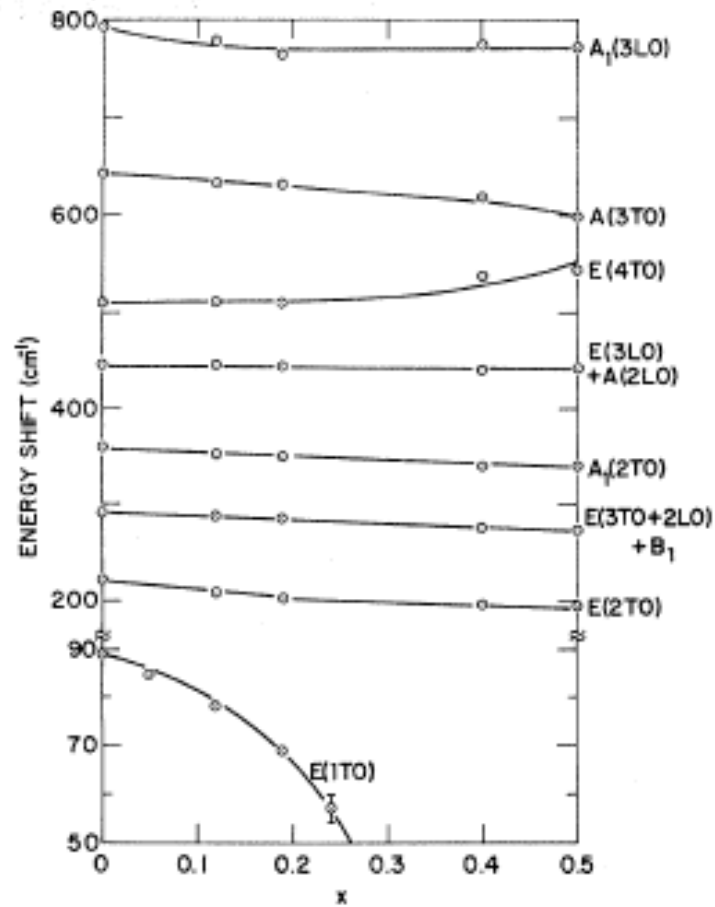


Figure 1.26 - Experimental Raman results, at 23 °C, for the tetragonal phase of the $\text{PbZr}_x\text{Ti}_{1-x}\text{O}_3$ system [171].

CHAPTER 2

Background on PZT single crystals growth by flux and seeded polycrystalline conversion

The purpose of this chapter is to provide a brief description of several methods to grow ferroelectric crystals, in particular, the high-temperature self-flux solution method and seeded polycrystalline conversion (SPC) process.

2.1. Single crystals growth

2.1.1. Methods for growing single crystals

Crystals have fascinated men for thousands of years, whether they are snowflakes, minerals or jewels. For the least 50 years, crystals have fascinated engineers as key material for modern electronics, optoelectronics and other technical fields of application. The formation of crystals in nature, like snowflakes and minerals, as well as the preparation of the crystals in laboratories and factories for technical applications, is called “Crystal Growth”.

The growth of single crystals is both scientifically and technologically important, and the applications of such crystals today range from electronics, to synthetic gemstones. Single crystals reveal the fundamental properties of materials, especially properties with directional dependencies, which make crystals unique as compared to ceramics or glasses. These properties are often key to technological applications, as illustrated in the case of the semiconductor silicon. The electronic properties of silicon underlie the vast majority of electronic devices and today silicon crystals are grown in sizes of up to 30 cm in diameter with carefully controlled purity.

A single crystal is defined by long-range atomic order, extending over many atomic diameters and having a repetitive structure. As a result, crystals have rigidity, fixed shape, and mechanical strength. In crystals, strong connection between the optical, electrical and mechanical responses with the crystal structure is often observed and these features are

used in many current technologies. Beyond utility, the beauty and mystery of crystals are continuing sources of fascination and, in many cases, their growth remains a challenge.

There has been a continuous interest in the development of solid state materials for semiconductor industry, optical communications, medicine, electronic devices and industrial applications in general. Single crystals have played a major role in most of these applications, either in the form of bulk crystals (three dimensional), epitaxial thin films (two dimensional) or fiber crystals (nearly one dimensional) [172, 173].

The most often employed methods for single crystals growth can be divided into two principal groups, the growth from solution (flux) and the growth from a melt.

2.1.2. *Single crystal growth from the melt*

Methods for growing from the melt have been named after those who invented them, like the Czochralski, Bridgman-Stockbarger or Verneuil method. In common, all the methods have the characteristic that a material of approximately the correct composition is melted congruently, i.e., the same crystalline phase is maintained up to before and after melting. The melt is then solidified in a carefully controlled way to cause the formation of a single crystal. In most crystal growth experiments, this solidification is accomplished using a well oriented seed material of the same crystal composition.

Melt growth requires significant understanding of the material phase diagram, the cationic make-up of the desired crystal composition and the high-temperature chemistry of the melt. A lot of work goes into getting this information before a crystal growth technique is selected. This information is often collected by mixing starting materials in the desired proportions and firing them both below and above the melting temperature. This very important and extensive work is necessary to develop the relevant growth information with a given crystal composition.

Growth from the melt requires some conditions:

- 1- The material must melt congruently (no change in composition during melting); for example, Yttrium Iron garnet (YIG) is not grown from melting because it does not melt congruently.

- 2- The material must not decompose before melting; for example SiC is grown from vapour phase (sublimation-condensation) because it decomposes before melting.

3- The material must not undergo a solid state phase transformation between melting point and room temperature. SiO_2 is grown from solution (hydrothermal growth) because of the α - β quartz transition occurring at 573°C.

Some of the advantage characteristics of growing from melt are:

- (a) A fast growth rate (\sim cm/hr), depending on heat transfer and not on mass transfer.
- (b) A large variety of techniques were developed (e.g. crystal pulling and directional and zone solidification).

Unfortunately, some of the most interesting materials have high melting temperatures (1500-2400°C). The melt techniques cannot always be useful because many materials decompose or vaporize at such high temperatures. Also, in some cases the melt may be viscous, so that a glass forms instead of a crystal [174].

2.1.3. *Single crystal growth from solution (flux)*

In solution growth, the chemical components that form the crystal are dissolved in a liquid medium or flux and are allowed to crystallize slowly as the temperature goes down. According to the solubility of the crystal material, different solution growth techniques are employed, like water solution growth at room temperature, flux growth and hydrothermal techniques. In the last case, both high temperature and pressure are needed and the key requirement is a high purity solvent which does not solubilise the crystal.

Flux growth, the most commonly used term for crystal growth from high temperature solutions, is a method which allows the growth of single crystals of a wide range of materials. In this technique, the components of the desired materials are dissolved in a solvent, the flux. The flux growth process is analogous to crystal growth from aqueous solutions, but the solvent solidifies before reaching room temperature. The main advantage of this method is that the crystals are grown below the melting temperature. If the material melts incongruently, or exhibits a phase transition below the melting point, one has to look for growth temperatures lower than those of these phase transitions. Flux growth may be used when the melting temperature is very high and is useful when the vapour pressure at the melting temperature is too high. Thermal strain is also minimized due to the relatively low growth temperature and very slow cooling rates. The main disadvantage of the technique is the low growth rate, because the growth rate of crystals from the flux is generally more than one hundred times smaller than that in the melting growth. Thus,

crystals obtained from the flux method are in general of small size. Crystal extraction from the flux is also quite difficult (it is usually performed with a hammer). A further disadvantage is the unavoidable presence of ions of the flux as impurities in the crystals [93]. The single crystals so produced typically contain defects, such as dendritic structures (especially in regions of the crystals formed during the early stages of growth), planar bands or striations (which were parallel to the growth interface) and twins.

In this work we only reviewed the high-temperature solution or flux growth, because it was used to grow the PZT single crystals.

- *High-temperature solution (HTS) or flux growth*

High-temperature solution growth is one of the oldest processes for crystal preparation. The book by Elwell and Scheel [175] gives a very comprehensive survey and much of the history of the subject. Until quite recently, it was largely used because it was a convenient technique for preparing research specimens [175].

The basic process for making bulk samples is very easy: a suitable solution is cooled slowly. The problems it faces [176] are finding a suitable solvent and a container, achieving the right cooling rate in an uniform manner and, if reproducible results are wanted, introducing a seed crystal with the concomitant difficulties of achieving the correct temperature distribution and stirring conditions. If these problems can be solved without introducing undue complications, the method offers the possibility of growing crystals with high melting points (or which melt incongruently) at reasonable temperatures (i.e. temperatures at which decomposition pressures are reasonably low) in easily constructed apparatus.

The most commonly used fluxes are oxides or fluorides, like PbO, PbF₂, Bi₂O₃, B₂O₃, Na₂O or KF, whose choice depends on the composition of the crystal to be grown. For oxide materials, solvents (or fluxes) based on lead oxide are very popular. The lead ion is so large that it has only a limited solid solubility in most crystals. Lead oxide alone is not a very good solvent and hence lead fluoride is frequently added. This increases the volatilisation of the flux [177, 178] being necessary to close the container to eliminate or reduce the flux loss. Adding a third component to the solvent, like boric oxide, can reduce the volatilisation and modify other properties [179]. Table 2.1 summarizes the desirable characteristics of a flux.

Table 2.1 - The desirable characteristics of a flux for the flux growth technique [179].

<i>Moderate reversible solution (~ 2 mole %)</i>
Reasonable fractional change in solubility with temperature ($\sim 1 \% ^\circ\text{C}^{-1}$)
Low kinematic viscosity ($< 1 \times 10^{-1} \text{ cm}^2 \text{ s}^{-1}$)
Low volatility ($< 10^{-6} \text{ g cm}^{-2} \text{ s}^{-1}$)
Low surface tension ($< 170 \text{ dyn cm}^{-1}$)
Low eutectic temperature (200 °C below growth temperature)
Low crystal dissolution
Residual melt should be easily separated from the crystals
Compatible with crucibles
Pure, cheap and non-toxic

In the growth of crystals from HTS, the material to be crystallized and the flux are put inside a platinum (Pt) crucible (or platinum alloys) sealed with a Pt lid and crystallization takes place when the high temperature solution is allowed to become critically supersaturated by cooling [175, 180, 181]. Supersaturation and supercooling are defined by the phase diagram. Figure 2.1 shows schematically a pseudo-binary system of flux and solute, where three ways to achieve the required supersaturation for crystal growth are represented [182]:

- (1) Crystal growth by slow cooling when the temperature is decreased from *A* to *B* and growth occurs along the arrow to *C* during cooling.
- (2) Crystal growth by flux evaporation when the solvent, or a part of it, is evaporated and the solute concentration increases from *D* to *E* at constant temperature. This method is frequently used for aqueous and organic solutions.
- (3) Crystal growth by vertical temperature gradient transport when the crystal grows in a colder region *G* of the furnace, while the material to be crystallized is continuously replaced from the furnace hotter region *F*, generally by dissolution of the polycrystalline nutrient. Since the growth temperature in each region of the furnace is constant, this steady state method is particularly suitable for the growth of solid solutions.

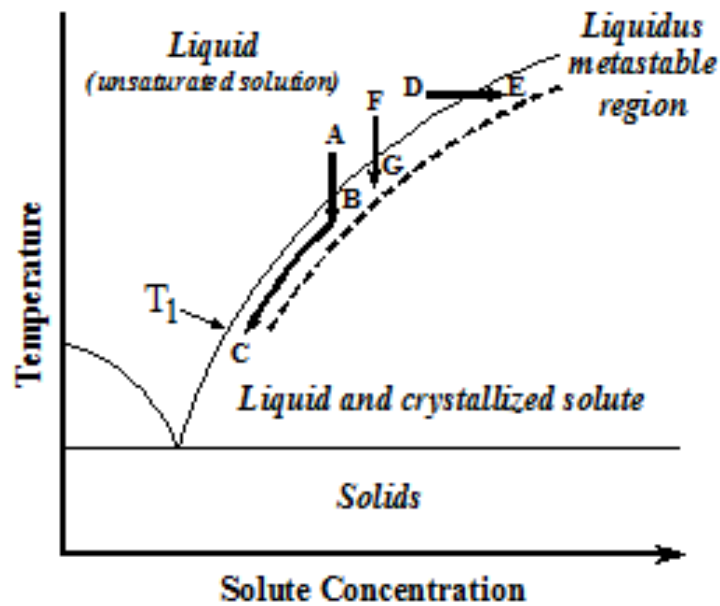


Figure 2.1 - Scheme of a pseudo-binary system of flux and solute [182]. The trajectory ABC, FG and DE are possible thermodynamic paths for the flux and solute during cooling. T_1 indicates the liquidus temperatures lines.

The slow cooling is the most commonly applied method, where the required supersaturation for crystal growth is created by cooling the melt from the point *A* slowly below the liquidus temperature (T_1) into the metastable region (Ostwald-Miers region), as shown in Figure 2.1 [182]. To reach the temperature of spontaneous nucleation (T_n) at point *B*, a larger supersaturation or supercooling ($\Delta T = T_1 - T_n$) than that required for the growth of a nucleus is necessary. Crystals grow at the lowest temperature, which is determined by unavoidable temperature gradients, either at the bottom of the crucible or near the surface of the melt. The crucible is placed in a furnace and then the temperature is increased well above the liquidus temperature of the flux and kept there for a while (soaking time) to achieve complete dissolution of all components. The temperature is then lowered just below the liquidus temperature very slowly to create the supersaturation for nucleation. In some cases, the temperature is increased again somehow to reduce the number of nuclei (cycling). Heterogeneous nucleation is usually obtained at the wall of the platinum crucible which can be reduced by a long soaking period above the liquidus temperature [183]. Growth should be terminated at least before the solution solidifies, usually performed by a faster cooling. The crystals must then be separated from the

solidified flux at high temperature by inverting the crucible on a ceramic within the furnace [184, 185].

The growing interest in the use of ferroelectric and ferromagnetic crystals increased the application of the HTS methods, providing a convenient and powerful method for obtaining samples for research applications. In general, crystal growth from the melt is preferable whenever possible. However, since often only small crystals are needed for investigation or measurements, the difficulty to grow these from HTS is not as strong as from melting techniques. Furthermore, with some experience and with a suitable choice of the flux composition and growth methods, the disadvantages of the HTS growth can be minimized.

2.2. PZT singles crystals

Single crystals of PZT with composition in the morphotropic region are difficult to obtain, because this solution has only a congruent melting point in the pseudo-binary system, which lies outside the MPB region (for ZrO_2 contents less than 14 mol%) [186, 187]. The high volatility of PbO at high temperatures is also another problem to overcome.

The binary phase diagram of PbO-TiO₂ was reported by Roth [187]. This system has an eutectic in both sides of PbTiO₃ and the eutectic temperatures are 838 and 1240 °C (Figure 2.2). From the phase diagram it can be seen that a PbO/TiO₂ mixture of 50 mol % of TiO₂ melts congruently at 1285 °C. Below this temperature, precipitation of PbTiO₃ takes place from the solution. On the other hand, from the binary phase diagram PbO-ZrO₂ (Figure 2.3) it can be seen that a PbO/ZrO₂ mixture with 50 moles % ZrO₂ melts incongruently at 1570 °C and completely melts congruently at 2400 °C. Below this temperature, precipitation of ZrO₂ takes place from solution.

The PbO-ZrO₂-TiO₂ ternary phase diagram (Figure 2.4) shows that it is possible to grow PZT single crystals in the MPB using a PbO flux. However, due to the high melting temperature need to do that, PbO volatilizes and causes ZrO₂ precipitation.

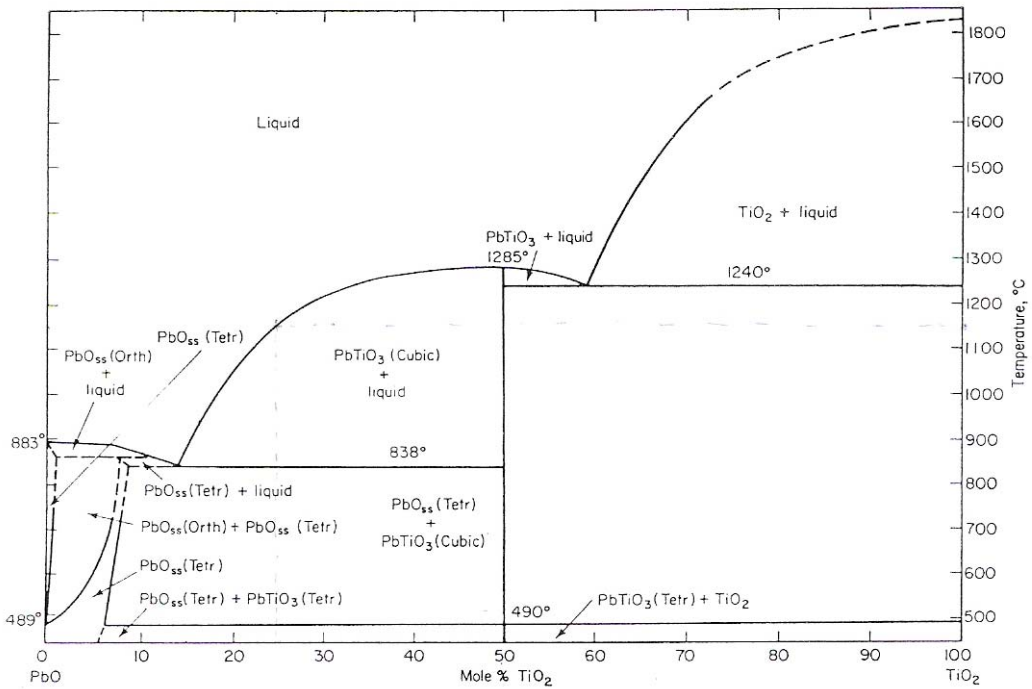


Figure 2.2 - Phase diagram for PbO-TiO₂ [30].

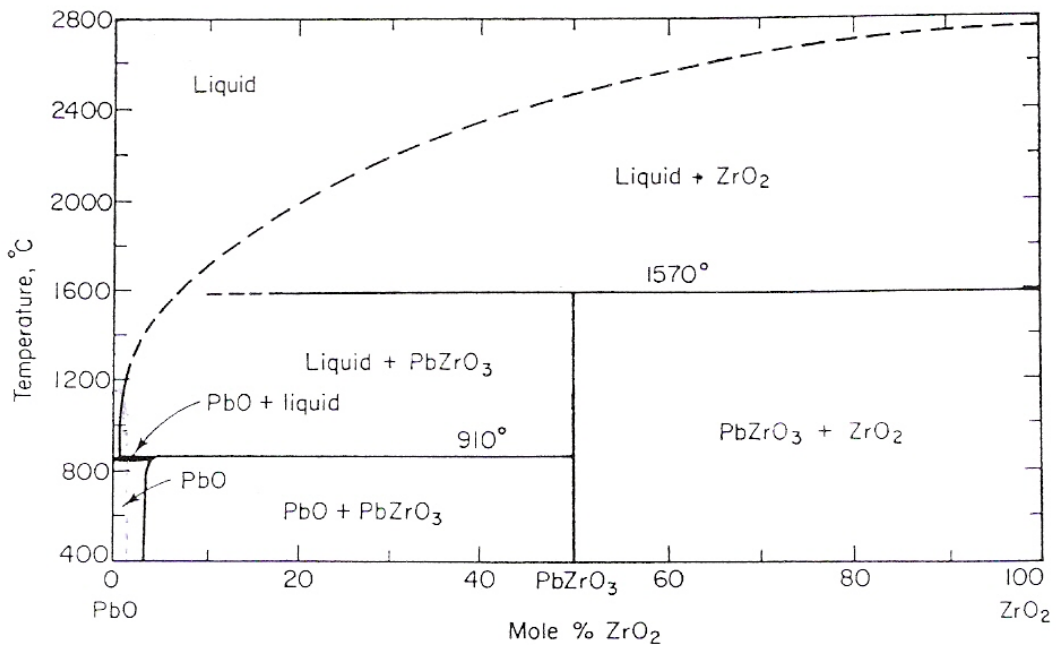


Figure 2.3 - Phase diagram for PbO-ZrO₂ [187].

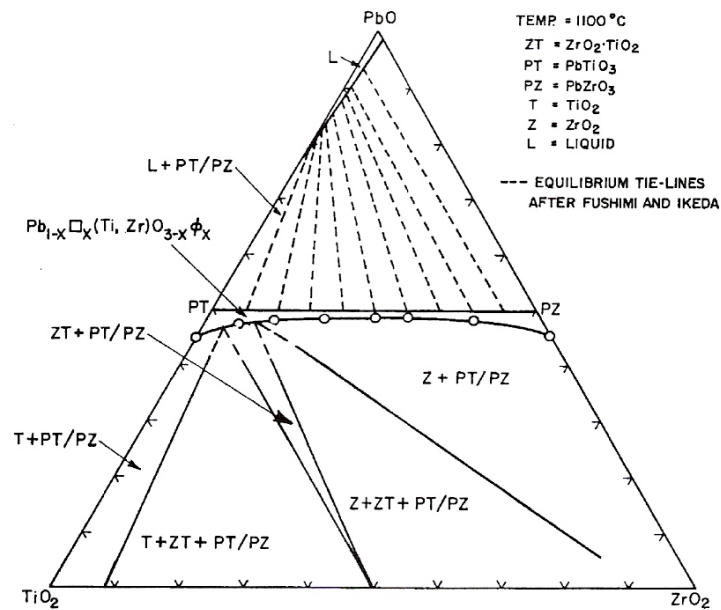


Figure 2.4 - Isotherm of the PbO-ZrO₂-TiO₂ ternary phase diagram at 1100 °C. The tie lines in the PZT + liquid region were determined by Fushimi and Ikeda [187] and by Ikeda *et al.* [188]. The phases present in the lower portion of the diagram were determined by Webster *et al.* [189]. The symbols □ and ϕ denote the lead and oxygen loss, respectively [186].

Due to that, it is not possible to produce single crystals with compositions near the MPB region using the melting growth method, because there is not a congruent melting point at low temperature (lower than 1200 °C). Therefore, some other methods have been used for the growth of PZT single crystals, such as epitaxial growth techniques, like hydrothermal [190-197], sol-gel [198], chemical vapour deposition [120, 199, 200], sputtering [201-203] and flux [49, 79, 204, 205]. The flux method is the most important for this work and, therefore, a historical review is presented about PZT system growth.

The PbZrO₃ single crystal was grown by Jana *et al.* in 1955 [178] using as flux PbF₂ or PbCl₂. A single crystal of PbTiO₃ was grown by Kobayashi in 1958 [206] using as flux PbCl₂ or KF. With PbCl₂, small crystals were obtained, but larger ones were obtained using KF as flux. The first effort to grow PZT single crystals was reported by Sholokhovich and Fesenko in 1960 [207]. These authors grew crystals containing $x \leq 0.12$ of Zr with a flux of *PbO-B₂O₃*, in the molar ratio of 1:1. They reported the lattice parameters for some compositions, with $x \leq 0.07$ of Zr amount.

Ikeda *et al.* in 1962 [188] grew small crystals in the tetragonal part, Ti rich, with Ti (x) content $x \geq 0.7$ using KF and also KF-PbF₂ fluxes. They grew crystals in both Ti and Zr rich ranges of compositions. The same group in 1964 grew PZT single crystals in the rhombohedral and tetragonal rich parts of the phase diagram, Figure 1.11, with $0.40 < x < 0.85$ using a PbO-PbF₂ flux. The crystals obtained were small and therefore inadequate for electric measurements. Optical characterisation was possible and negative birefringence was found in all the crystals [188, 208, 209]. The ternary phase diagram of PbO-TiO₂-ZrO₂ was also explored by Fushimi and Ikeda. Using a quenching method, they found that this system has a congruent melting point only for $x \leq 0.14$ of Zr amount [187]. This result was of great importance because demonstrated the reason why it was so difficult to grow PZT crystals near of the MPB (Figure 2.4).

Tsuzuki *et al.* [210] tested 33 different fluxes to grow PZT crystals and they were successful with 10 of them (Table 2.2). They reported the change of the lattice parameter with the temperature for a crystal with a Zr amount of $x=42$ mol%, grown using the flux KF-PbF₂-Pb₃(PO₄)₂ [210]. This group reported in 1969, using the same flux, the hysteresis loop for a crystal with $x = 0.48$ at room temperature [211]. Later, they have grown crystals with different compositions using the same constituents [212] (Table 2.3).

Table 2.2 - Flux composition and Zr content (x) in grown crystals [210].

<i>Flux</i>	<i>x</i>
PbO-PbMoO ₄ -Li ₂ MoO ₄ (2:3:5)	0.02
Li ₂ MoO ₄ -PbMoO ₄ (1:2)	0.05
PbO- PbCl ₂ (1:4)	0.13
PbMoO ₄	0.17
PbO-PbMoO ₄ -Li ₂ MoO ₄ (3:5:2)	0.20
KF-PbF ₂ (2:3)	0.26
PbO-PbMoO ₄ (2:3)	0.28
Li ₂ MoO ₄ - PbF ₂ (4:1)	0.31
NaF- PbF ₂ (2:3)	0.40
KF-PbF ₂ -Pb ₃ (PO ₄) ₂ (4:5.6:0.4)	0.42

Table 2.3 - Zr content (x) in grown crystals using a $\text{KF-PbF}_2\text{-Pb}_3(\text{PO}_4)_2$ flux [212].

<i>Flux molar ratio</i> $\text{KF-PbF}_2\text{-Pb}_3(\text{PO}_4)_2$	<i>Crystal composition</i> (x)
3:6.6:0.4	0.45
4:5.6:0.4	0.42
5:4.6:0.4	0.30
4:6:0	0.26

Clarke *et al.* [213] used the flux $\text{PbO-PbF}_2\text{-B}_2\text{O}_3$ to grow PZT crystals and later they published a review about the PZT single crystals growth [214]. They found that it is possible to grow PZT crystals using a PbO flux for $1 \leq x \leq 0.84$ and $0.25 \geq x \geq 0$ with reasonable quality [79, 213-216].

Roleder [217-224], Ujma [225], Handerek [226, 227], Dec [228-230], Kugel [231] and Eknadiosiants [232] grew PZT crystals with low concentration of Ti using the $\text{PbO-B}_2\text{O}_3$ flux. Turik [233], Leontev [234, 235], Fesenko [236, 237] and Eremkin *et al.* [90], grew PZT crystals using the same flux ($\text{PbO-B}_2\text{O}_3$) and applying a temperature gradient; this allowed obtaining crystals in all the range of compositions.

Fujii S. *et al.*, in 1991 [204], grew PZT crystals with $x=0.52$ using the flux components PbO-KF-PbCl_2 and PbO-KF-PbF_2 with different proportions of the components. They found that the best results are obtained with the flux PbO-KF-PbCl_2 (2:1:2). Hatanaka and Hasegawa [49], using the same flux, grew PZT ($x=0.30$) crystals with ZrO_2 inclusions and studied the dielectric permittivity with the temperature. We, also grew PZT crystals with compositions $0.65 \geq x \geq 0.40$, without ZrO_2 precipitation, with this PbO-KF-PbCl_2 (2:1:2) flux, which will be reported later in this work [238].

2.2.1. Morphological and optical characterisation of PZT crystals

The morphology of the grown crystals is cubic in the majority of the compositions, except in the end members of the PZ-PT phase diagram, where the crystals are platelike. The grown crystals are transparent, yellow, brown, light red, bluish or black. The colour depends on the flux composition, quality of the crystal and the method used to grow the crystal. The reported transparent crystals were grown using the flux PbO [79, 214, 215], in the rhombohedral region, and the flux $\text{KF-PbF}_2\text{-Pb}_3(\text{PO}_4)_2$, for $x=0.50$ [212].

2.2.2. *Optical properties of PZT crystal*

The principal optical characterisation of a ferroelectric crystal is determined by its birefringence, or double refraction. This effect can only occur if the structure of the material is anisotropic. If the material has a single axis of anisotropy, or optical axis, birefringence can be formalized by assigning two different refractive indices to the material for different polarizations. The birefringence is then defined by

$$\Delta n = n_o - n_e \quad (2.1)$$

where n_o and n_e are the refractive indices for the polarizations perpendicular (ordinary) and parallel (extraordinary) to the axis of anisotropy, respectively.

The reason for the birefringence is the fact that, in anisotropic media, the electric field vector \vec{E} and the dielectric displacement \vec{D} can be nonparallel (namely for the extraordinary polarization), although being linearly related.

Jona *et al.* [178] reported that PbZrO_3 is a crystal which is optically negative (the crystals have a negative birefringence) and they reported the variation of the birefringence with the temperature, which is smaller along the a axis. The optical properties of PbTiO_3 was reported by Kinase *et al.* [239]. In this crystal, the birefringence increases with the temperature, reaches a broad maximum and then decreases as the temperature approaches the Curie point. The intermediate compositions were studied by Fushimi *et al.* [188, 209], who reported the optical properties of several crystals in the tetragonal and rhombohedral phases and the crystals have a negative birefringence. In this work they reported the variation of the birefringence against the temperature for several compositions and they found that the birefringence is higher in the rhombohedral phase compared to the tetragonal one (Figure 2.5). Tsuzuki *et al.* [212] also found a negative birefringence in a crystal with $x=0.5$. Other researchers have reported other optical properties for PZT single crystals, such as refractive index [120], change of the optical properties with the electric field and temperature, to study the phase transitions, and domain structure [219, 235].

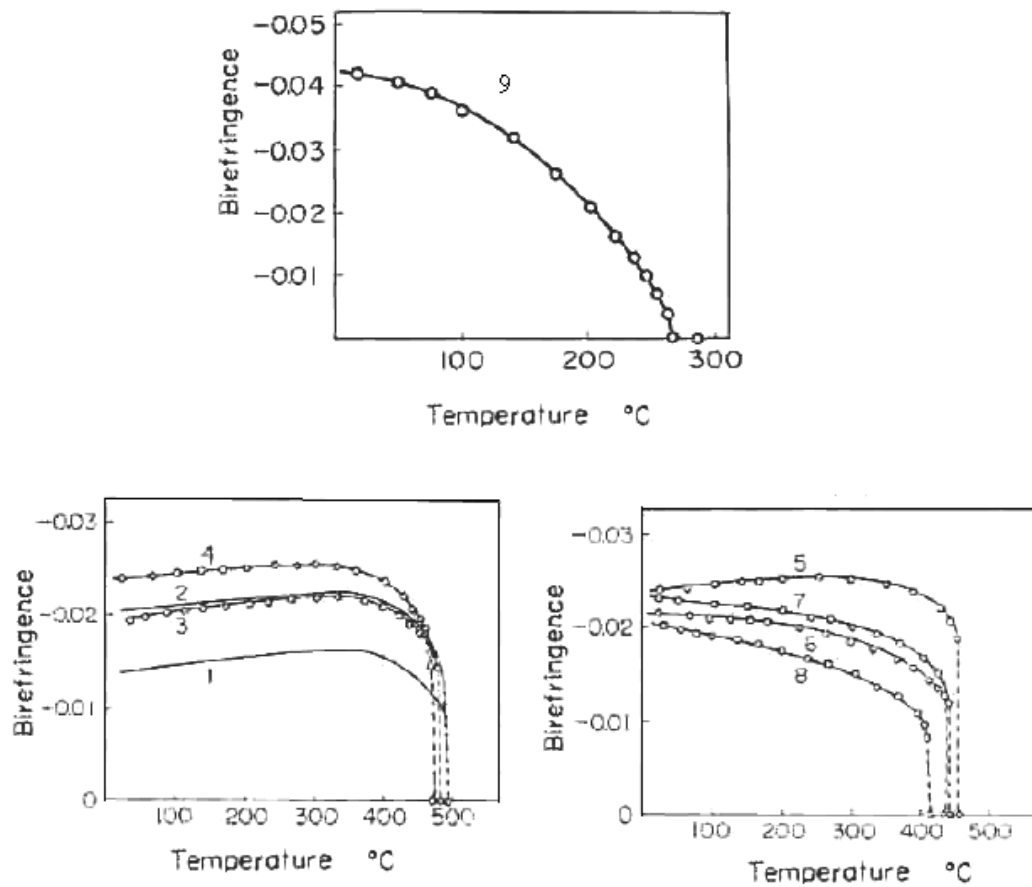


Figure 2.5 - Temperature dependence of PZT birefringence for: 1; $x=0$; 2, $x=0$; 3, $x=0.10$; 4, $x=0.15$; 5, $x=0.20$; 6, $x=0.30$; 7, $x=0.30$; 8, $x=0.40$; 9, $x=0.85$ {Fushimi, 1965 #21495}.

2.2.3. Raman characterisation of the PZT crystals

Raman studies on PT single crystals were performed by Burns *et al.* [168], who grew PbTiO_3 using $\text{PbO-B}_2\text{O}_3$ and studied the variation of the Raman scattering with the frequency and temperature (Figure 2.6). They reported the soft mode from room temperature to 500 °C. Hatanaka *et al.* [205] used Raman spectroscopy to understand the orientation of the domain for a crystal with composition $x=0.059$. The Zr rich part of the phase diagram was studied by different researchers with the main objective of understanding the phase transition [217-222, 231, 240]. Raman characterisation of single crystals near the MPB was never reported.

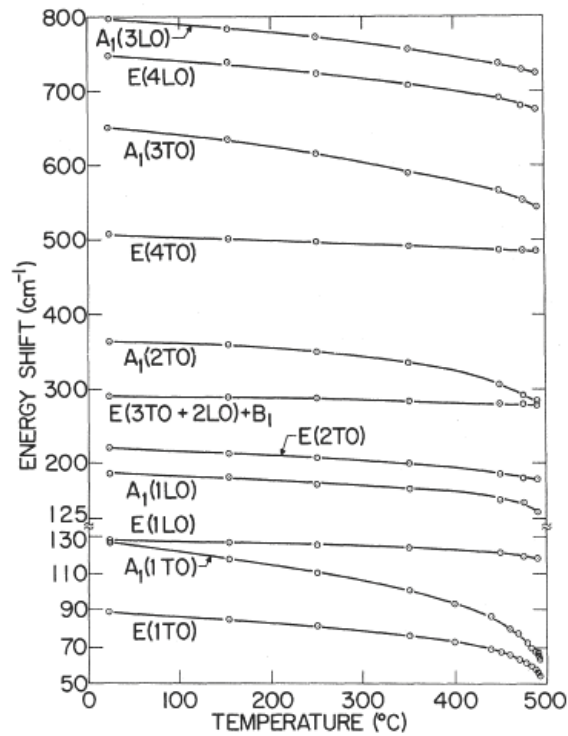


Figure 2.6 - Temperature dependence of the Raman lines for a PbTiO_3 crystal (note that the scale is broken at 125 cm^{-1} to clarify the soft modes) [168].

2.2.4. Electrical and domain characterisation of PZT crystals

For a better understanding of the electrical properties of the PZT system, the phase diagram can be separated into four parts, with similar electric behaviour, which are: $1 > x \geq 0.52$ with an antiferroelectric (orthorhombic structure), and ferroelectric (rhombohedral structure), behaviour $0.52 \geq x > 0$ with a ferroelectric behaviour (tetragonal structure) and the crystals with composition $x = 1$ and $x = 0$, the end members.

- *PbZrO₃ crystal*

Jona *at al.*, in 1955 [178], reported the domain structure of PbZrO_3 using the polarised optical microscopy. The principal characteristic observed in these crystals was the different types of twins in the orthorhombic phase. These twins are:

- Plates with extinction parallel to the twins edges. The twin walls are parallel to a cubic (110) or orthorhombic (111) plane.
- Plates with symmetrical extinction (at 45° to the cubic edges).
- Plates with mixed extinction position (parallel and symmetrical).

(iv) The presence of twinning on a (hk0) plane. This type of twinning was observed less often than types (i) and (iii).

Scott and Burns [93] reported that, in the ferroelectric state, the domain walls intersect the surface along directions which are parallel to the pseudocubic (100) and (010) sides of the platelet. In the antiferroelectric state they found the same result as Jona [178]. On the other hand, Dec [228, 229] observed in the orthorhombic state domains with 60° in the planes (101) and (111).

The PZ crystals have two dielectric transitions, corresponding to crystallographic transitions, and the variation of the dielectric properties with temperature was reported by Scott *et al.* [93], where the phase transition FE↔PE is of the second order type. In the antiferroelectric state, there is a double hysteresis loop which is characteristic of an antiferroelectric material [211]. The presence of small quantities of impurities in the crystal affects the dielectric response [241] and, in some cases, the presence of small quantities of certain impurities is sufficient to suppress the ferroelectric phase [241]. Roleder *et al.* [224] studied the variation of the dielectric permittivity with the temperature and with the frequency and determined the conductivity, activation energy, relaxation time and relaxor behaviour observed in the crystal. Other studies on the PZ crystal were done to observe the variation of the permittivity, the phase transition temperature (T_c), the pyroelectric current and the spontaneous polarization (P_s) with the electric field and hydrostatic pressure. The effect of the variation of lead (Pb) and oxygen (O) ions in the crystal was also analysed [88, 93, 178, 218, 219, 224-231, 241, 242].

- *PbTiO₃ crystal*

Kobayashi [206] reported the domain structure of a PbTiO₃ crystal and the domains are of irregular shape along *c* and *a* axis, but with annealing, the domains become along *c* axis and align together to 90° domains. Fesenko *et al.* [243, 244] studied the domain structure of PT and described large 180° domain configurations and wedge-shaped (or reciprocal domains) which appear in the free surfaces and the 90° domain boundaries at which the condition of zero charge is not fulfilled. In this case, domain boundaries parallel to P_s, were not observed, but only arbitrary zigzag boundaries. They proposed that the high conductivity at the phase transition ($\sigma = 10^{-3} - 10^{-4} \Omega^{-1}\text{cm}^{-1}$) is due to these domain structure peculiarities. In the literature, it is seen many reports on the spontaneous

polarization (P_s), spontaneous deformation (x), piezoelectric coefficients d_{31} and electromechanical coupling coefficient k_{31} , hysteresis loop, and coercive field (E_c), the dielectric permittivity, electro-mechanical coupling factor, elastic compliances and elastic stiffnesses [233, 244-247].

- *PbZr_xTi_{1-x}O₃ crystal with $1 > x \geq 0.52$ (A_O , $F_{R(LT)}$ and $F_{R(HT)}$)*

This region of the phase diagram is the most studied one with single crystals, principally in the range $1 > x \geq 0.85$, probably because in this region it is easier to grow PZT single crystals. On the other hand, in this region the PZT has a complicated phase diagram which is affected by impurities, defects and is influenced by external electric fields and stresses.

Clarke *et al.*, [79] reported the dielectric permittivity of two crystals with $x = 0.97$ and 0.90 . The phase transitions $A_O \leftrightarrow F_{R(HT)}$ and $F_{R(HT)} \leftrightarrow P_C$ are observed at 150 °C and 232 °C, respectively, for the crystal with $x = 0.97$. The phase transitions $F_{R(LT)} \leftrightarrow F_{R(HT)}$ and $F_{R(HT)} \leftrightarrow P_C$ are observed at ~ 95 °C and 267 °C, respectively, for the crystal with $x = 0.90$. The variation of the spontaneous polarization (P_s) with the temperature is reported for the composition $x = 0.91$ and a large anomaly is observed at ~ 90 °C due to the transition $F_{R(LT)} \leftrightarrow F_{R(HT)}$. The polarization (P_s) at room temperature is $44 \mu\text{C}/\text{cm}^2$, which is larger than that observed in ceramics with the same composition, $P_s = 33 \mu\text{C}/\text{cm}^2$. The coercive field (E_c) is $1 \text{ kV}/\text{cm}$, which is lower than that found in ceramics, $E_c = 150 - 200 \text{ kV}/\text{cm}$. The same group reported later the dielectric permittivity for several crystals with $x = 0, 0.925, 0.90$ and 0.88 . The maximum of the dielectric permittivity increases when the quantity of Ti was increased. The difference between the Curie point and the Curie temperature decreases with the amount of Ti, same as found in ceramics (Figure 2.7). It is expected that the phase transition is a first order one for Ti concentrations higher than 0.07 .

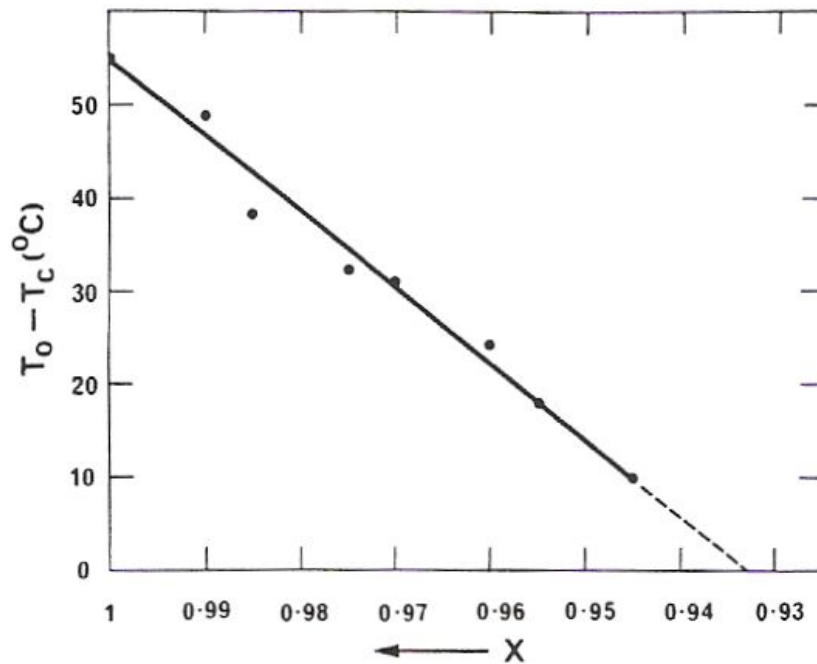


Figure 2.7 - Difference between the transition temperature (T_0) and the Curie temperature (T_c) versus compositions for PZT ceramics [214, 215].

Whatmore *et al.* [247] studied the variation of the dielectric permittivity with the temperature for $x=1, 0.985, 0.971, 0.960, 0.945$ and several thermodynamics parameters such as Pr, C , spontaneous strain (s), T_c and T_0 were calculated. The permittivity reaches a maximum where the variation of the transition temperature with the composition shows an inflection (Figure 2.8). The authors proposed that this inflection may be caused by a tricritical point for $x \sim 0.94$. Roleder *et al.*, [222], using the dependence of the electrostrictive parameters on the composition, concluded that this maximum is due to the presence of a critical point. This effect also appears in ceramics [218].

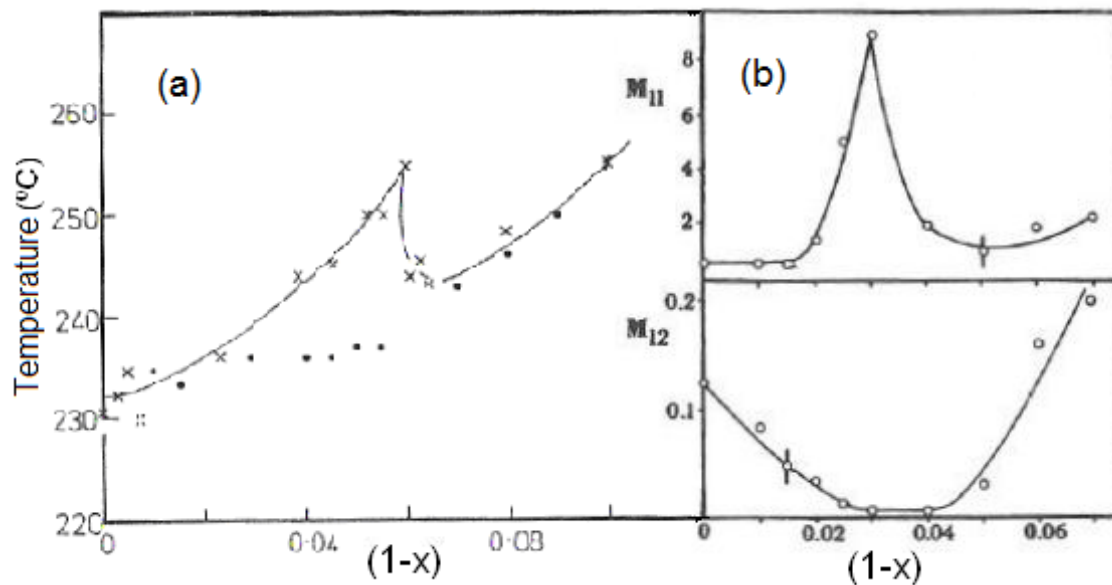


Figure 2.8 - a) Variation of the transition temperature from $F_R \leftrightarrow P_C$ with the composition (using the dielectric permittivity measurement with the temperature (●) ceramic and (×) single crystals) [247]; b) Variation of the electrostrictive parameters ($10^{-4} \text{ m}^4 \text{ C}^{-2} \text{ K}^{-1}$) with the composition $\text{PbZr}_x\text{Ti}_{1-x}\text{O}_3$ [222].

Roleder [217] proposed a phase diagram using the results obtained for the dependence of the dielectric measurements on the electric field and temperature. Leontiev *et al.* [235, 237, 248], using the variation of the optical properties with the temperature of several single crystals, reported a phase diagram for compositions with $x \geq 0.93$ (Figure 2.9). From this phase diagram, it is possible to conclude that the maxima observed by both Roleder [218, 222] and Whatmore [247] are of the same phenomenon, which slightly displaced compositions are probably due to the process used to grow the crystals, to the thermal hysteresis or to the impurities. This maximum corresponds to a tricritical point of the phases $A_{(0)}$, $F_{R(LT)}$ and $F_{R(HT)}$ (Figure 2.9). The domain configuration in this region is probably complicated due to their possible many orientations.

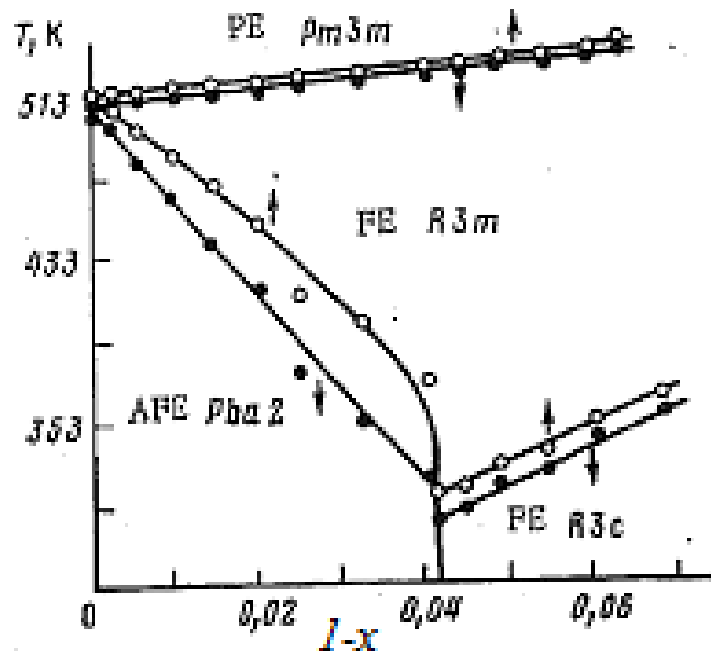


Figure 2.9 - T-x phase diagram for PZT with compositions $x \geq 0.93$ [248]. The double line in each transition is due to thermal hysteresis.

Ekndiosiants *et al.* [232] studied the domain distribution for $x=0.93$ and 0.65 and theoretically determined the possible domain orientations in the PZT, which can be in the rhombohedral structure of 70° walls type of the (011) and 110° walls type of the (001). The 180° domain walls divide the states with antiparallel P_o (in the sections normal to the vector P_o). In the tetragonal structure, normally the domain walls are oriented along (100) or (010) for P_o lying along [001] direction. In the real material they obtained these simple distributions and the interception between them. Figure 2.10 and Figure 2.11 [232] show the most frequent types of domain walls found for $x=0.93$ and 0.65 . The complexity and the number of ferroelectric domain increases with increasing the concentration of $PbTiO_3$, reflecting the accumulation of internal mechanical stresses in such crystals.

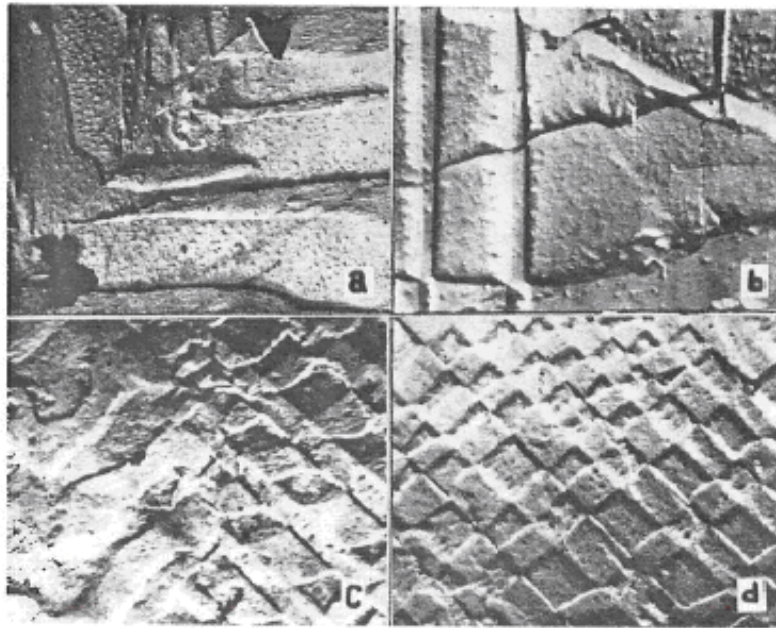


Figure 2.10 - The most frequent types of domain walls found for PZT single crystals with $x=0.93$, a) 70° wall, b) 110° domain wedges and a 180° wall normal to these, c) and d) a series of 70° domain walls intersected by 180° walls normal to these [232].

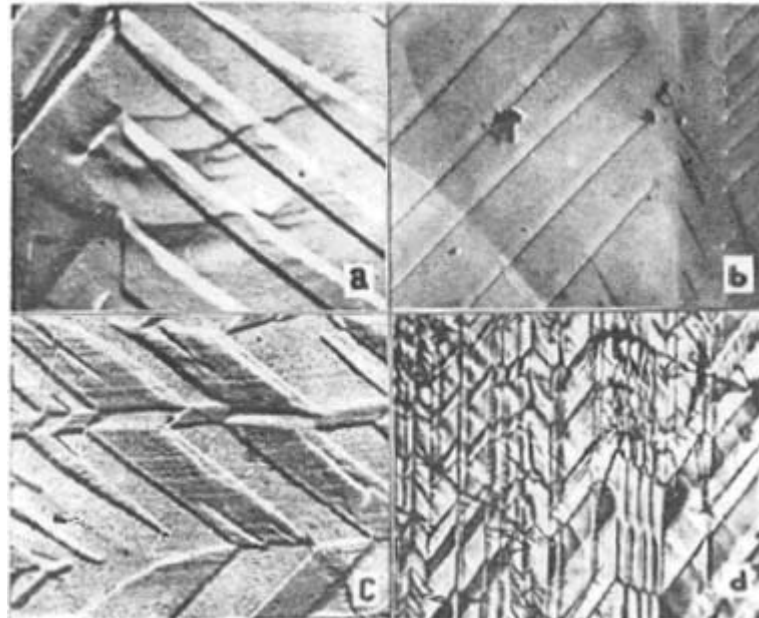


Figure 2.11 - The most frequent types of domain walls found for PZT single crystal with $x=0.65$, a) and b) 70° wedges separated by 110° walls, c) and d) mutual interceptions of 110° and 80° domain wedges [232].

There are other studies in this composition region related to the relaxation time, activation energy of the relaxation and direct current (dc) [249]. The thermodynamic parameters have been determined only with the variation of the dielectric and polarization behaviour with the temperature and time [218-223, 247, 250]. There are only very few studies on the variation of the specific heat with the temperature or of the dielectric permittivity and piezoelectric parameter with the electric field and domains structure [217, 235, 237, 251].

- $PbZr_xTi_{1-x}O_3$ crystal with $0.52 \geq x > 0$ (tetragonal)

Tsuzuki *et al.* [211, 212, 252] grew PZT single crystals in all the range of compositions and reported several physical properties, such as hysteresis loop, domains distribution, optical and dielectric properties for different orientations (clamped and free) of the crystals with $0.4 \leq x \leq 0.5$. The dielectric permittivity has a special behaviour in this range of compositions, the permittivity in the direction of the polar axis, when the crystal is free (ϵ_{33}^T is used for the crystal measurement in the c direction, at 1 kHz), increases quickly with the increase of $PbZrO_3$ (Figure 2.12a). The same behaviour was found for directions

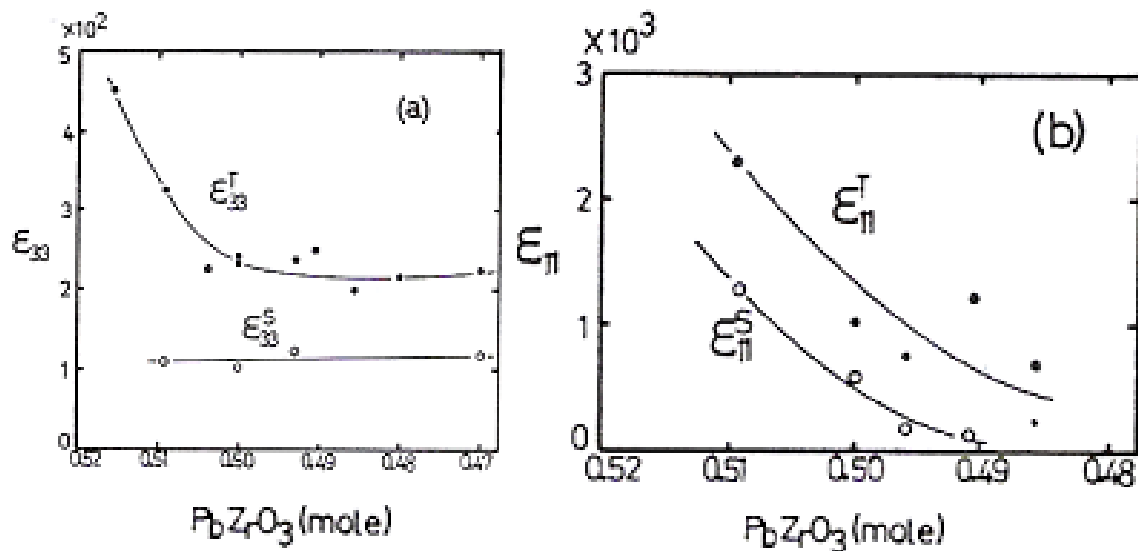


Figure 2.12 - Variation of the permittivity with the composition in tetragonal crystals at room temperature [252]. Where, ϵ_{33} and ϵ_{11} are the permittivity in the direction of the polar axis and perpendicular to it, respectively. The supra-indices T means that the sample was measured free (to 1 kHz) and S that was measured clamped (to 50 MHz).

perpendicular to the polar axis when the crystal is free (ϵ_{11}^T) and clamped (ϵ_{11}^S , the crystal was measured in the a direction, at 50 MHz). On the other hand, for ϵ_{33}^S the dielectric permittivity does not change. The cause for the last difference is that the dielectric response, in the direction of the polar axis, is very dependent on the frequency. The variation of the dielectric permittivity in the different directions with the temperature presents a change of the maximum value among the directions of the polar axis and perpendicular to it near 350 °C (Figure 2.13).

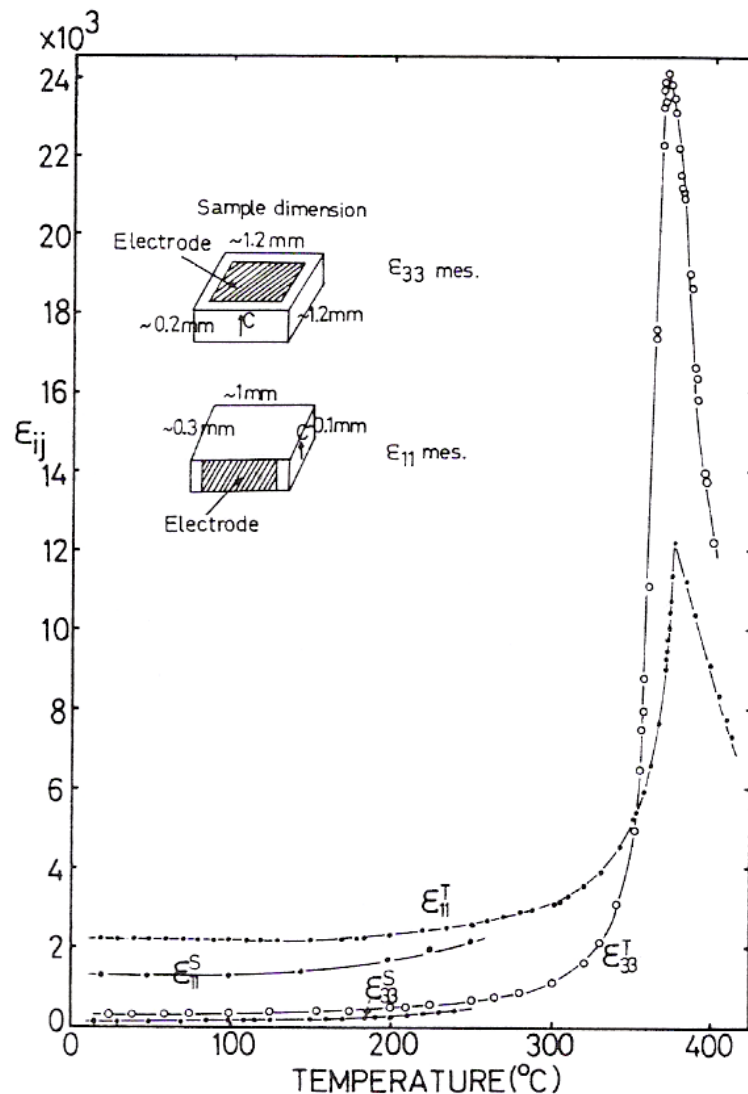


Figure 2.13 - Variation of the permittivity with the temperature in a single domain crystal [252].

The domain structure for a crystal with $x = 0.488$ presents a large domain in the direction of the c axis (polar axis) and, perpendicular to this, there are two small domains

covering the two faces, orientated perpendicular to the axis c in the direction of the large domain (Figure 2.14) [212]. This domain configuration is different from those found in the rhombohedral region [232]. Hatanaka *et al.* [205] investigated the domain configuration for a crystal with $x = 0.06$ (Figure 2.15) and proposed two models for the domain structure (Figure 2.16). The domain configurations given in Figure 2.14 and Figure 2.16 are different. In other proposed model for a PZT single crystal with $x = 0.40$, the domain configuration is even different from these [193].

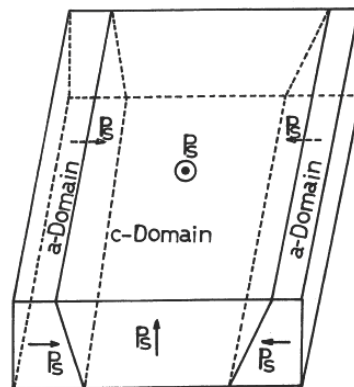


Figure 2.14 - Model for a PZT single crystal with $x = 0.488$. a and c are tetragonal lattice parameters and P_s is the spontaneous polarization [212].

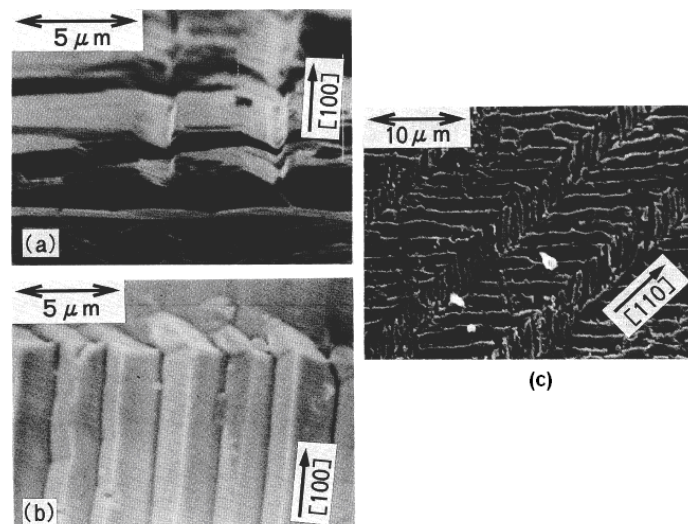


Figure 2.15 - Domain pattern of a single crystal of PZT with $x = 0.06$ [205].

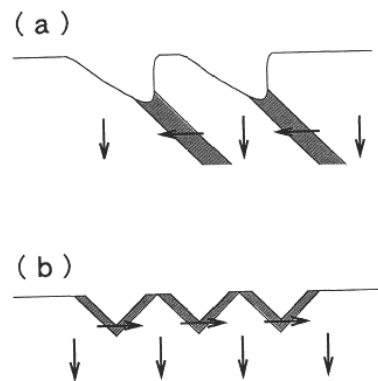


Figure 2.16 - Two possible models for the domain structure shown in Figure 2.15. The arrows indicate spontaneous polarization directions. The black areas are the a-domains and the white areas are the c-domains [205].

In several other studies, the variation of dielectric permittivity with the temperature, spontaneous polarization (P_s), hysteresis loop, coercive field (E_c) and the determination of the electrostrictive coefficients were studied for several crystals in the same region of compositions [49, 211, 252, 253].

2.2.5. Structural characterisation and phase diagram of PZT crystals

Lead zirconate, $PbZrO_3$, was the first antiferroelectric material to be identified by Sawaguchi *et al.* [89, 254], who proposed a structural model consisting of double rows of Pb ions displaced (approximately 0.2 Å) alternately along the $[1\bar{1}0]_p$ and $[\bar{1}10]_p$ directions, as shown in Figure 1.10. This picture of the cation displacements was later verified by Jona *et al.* [255]. More recently, the structure of $PbZrO_3$ single crystals has been investigated and confirmed by using XRD and TEM [78, 88, 214, 215, 241].

The temperature dependences of the pseudocubic lattice parameters and the interaxial angles are shown in Figure 2.17. Pure $PbZrO_3$ exhibits three phases: one antiferroelectric orthorhombic (A_O) phase, between room temperature and 230 °C, another ferroelectric rhombohedral (F_R) phase, until 233°C, and another paraelectric cubic phase above this temperature. The interaxial angles increase progressively and have a strong anomaly in the ferroelectric phase transition (Figure 2.17).

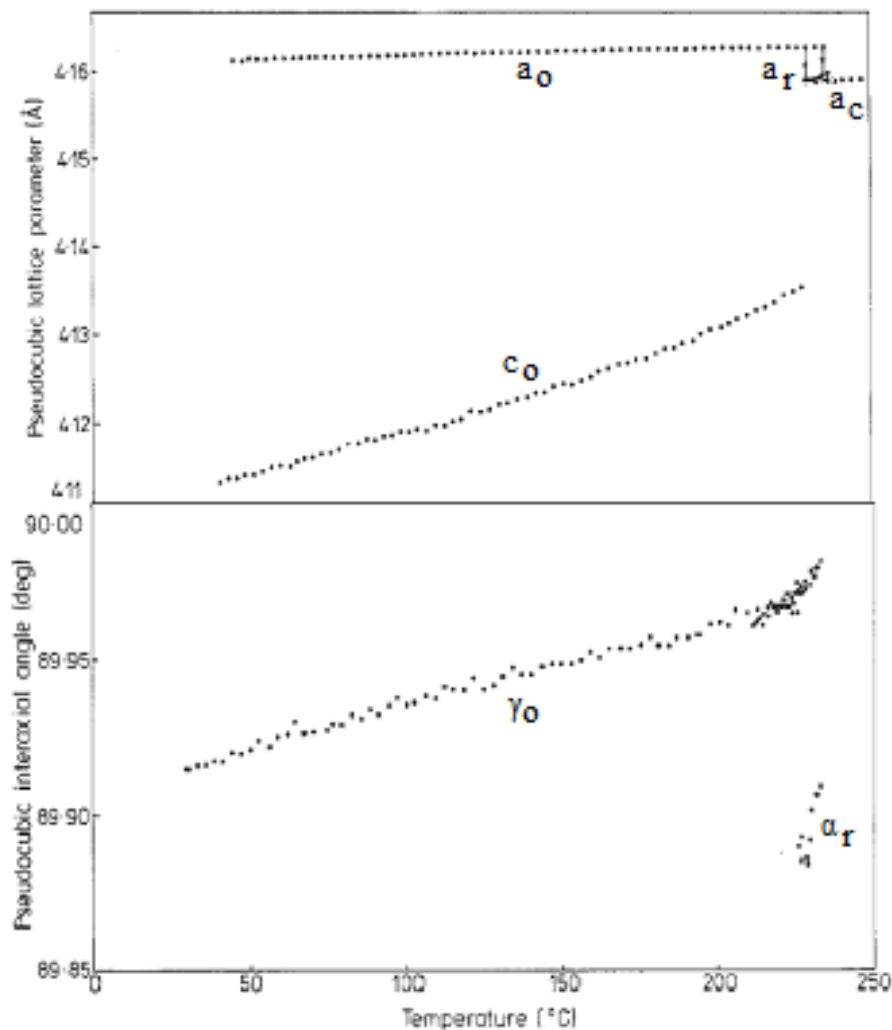


Figure 2.17 - Temperature dependence of the pseudocubic axial lengths and the pseudocubic interaxial angles in PbZrO_3 [241]. Here a_o , a_r , a_c denote parameters of the orthorhombic, rhombohedral and cubic unit cell, respectively. The parameter α_r is the rhombohedral angle and γ_o is the orthorhombic angle.

With the addition of a small PbTiO_3 amount to PZ the unit cell parameter decreases and near $x = 0.96$ the crystal has a phase transition from orthorhombic to rhombohedral, as shown in Figure 2.18 [216]. Many other studies have also been done to construct a refined phase diagram for this region (Figure 2.9) [235, 237, 248]. For contents of PbTiO_3 higher than 0.04, it appears the rhombohedral phase, which can be rhombohedral at low and high temperatures, being the difference between them a rotation of the oxygen octahedrons. In Figure 2.19, it is shown the variation of the pseudocubic subcell parameter (a) and the rhombohedral angle (α) versus the temperature [216]. The transition from the paraelectric

to the ferroelectric phase is related with an anomaly in the pseudocubic subcell parameter (a) and the same anomaly is also observed in the rhombohedral angle (α).

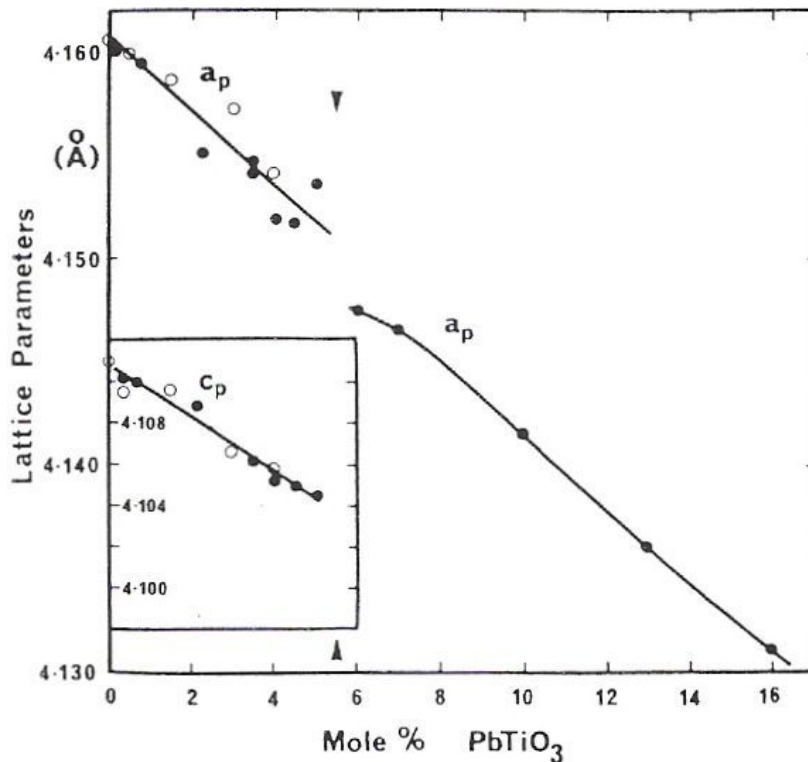


Figure 2.18 - Composition dependence of the lattice parameters near the PZ end member, at room temperature, for ceramic samples [216]. The arrows indicate the boundary between the orthorhombic A_O and Rhombohedral $F_{R(LT)}$ phases.

Eremkin *et al.* [90] reported the unit-cell parameters for PZT single crystals in all the range of compositions (Figure 2.20). This group reported the phase diagram also for all the range of compositions as shown in Figure 2.21. [90, 91, 256]. They reported that the anomalies in the lattice parameters during the transition $F_{R(LT)} \leftrightarrow F_{R(HT)}$, for the composition $x = 0.64$ were not detected [90, 91]. In Figure 2.21 it is also shown the ceramic phase diagram (dotted line), where the transition temperatures from the ferroelectric to the paraelectric state in the single crystal are higher than in the ceramic. The difference between the transition temperature in ceramic and single crystals was attributed to the presence of internal stresses in ceramics that decrease the transition temperature [90, 91]. On the other hand, they proposed that the MPB in pure single crystals does not exist.

However, the presence of impurities can lead to the observation of the MPB in single crystals [90, 91].

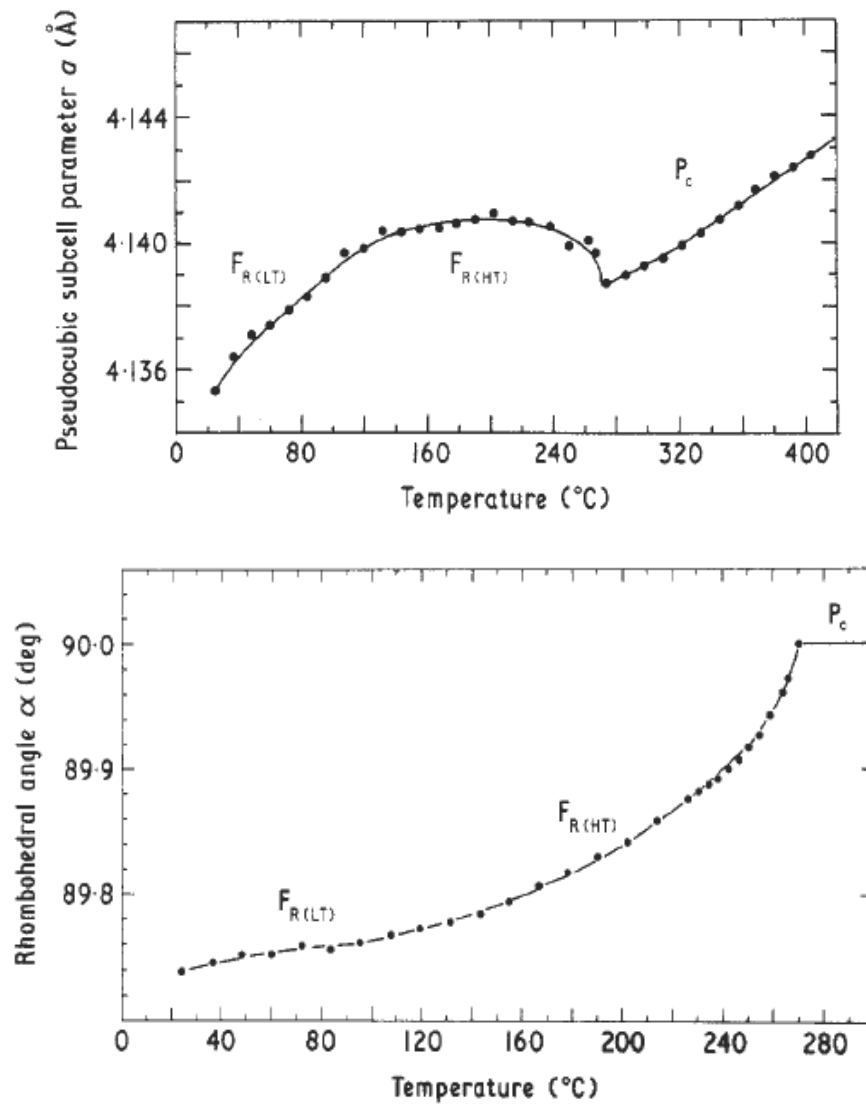


Figure 2.19 - PZT single crystal with $x = 0.90$. (a) Plot of pseudocubic subcell parameter a versus temperature. (b) Plot of rhombohedral angle α against temperature. The transition temperature T_0 is taken at the point where α becomes 90° [213].

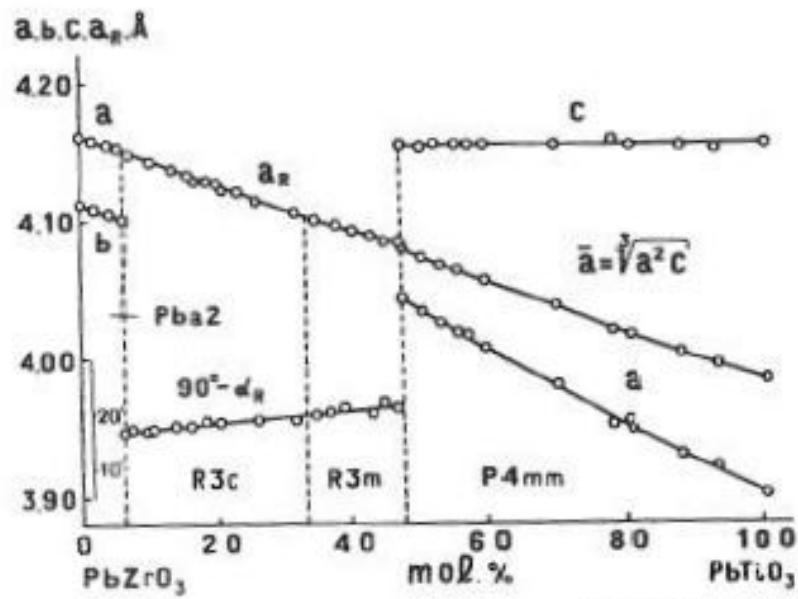


Figure 2.20 - Composition dependence of the unit-cell parameters in PZT single crystals at T = 293 K [90].

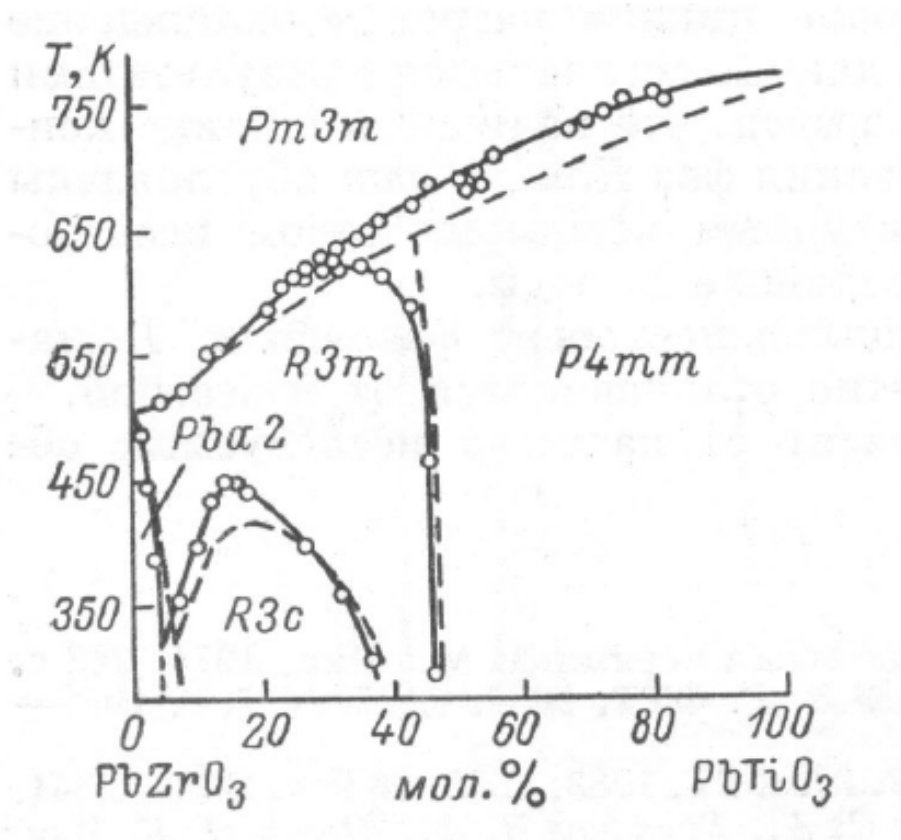


Figure 2.21 - PZT single crystals phase diagram. The dotted line is for ceramics [90, 91, 256].

There are several other studies on the structure and phase diagram of PZT investigations on the dependence of the transitions with the electric field, hydrostatic pressure and temperature [207, 210, 217, 235-237, 250]. Similar results were obtained by Foster *et al.* [120], who grew single crystals using the epitaxial method. In their work, they reported the remanent polarization (P_r), coercive field (E_c), dielectric permittivity and resistance against the composition. The results are in agreement with the results obtained in ceramics [120]. About the structure of PZT, they showed that some aspects of the phase diagram, either in single crystals or in ceramics, need to be further investigated, such as: i) the line of the transition $F_{R(LT)} \leftrightarrow F_{R(HT)}$, not defined for low temperatures; ii) the line of the transition $F_{R(HT)} \leftrightarrow F_{P4mm}$ in single crystals; iii) the dependence of the electromechanical and the structural characteristics with the electric field near the MPB in single crystals; iv) the domain distribution around the MPB also needs to be further studied in a comparative form.

2.3. The seeded polycrystalline conversion (SPC) and templated grain growth (TGG) processes

The seeded polycrystalline conversion (SPC) and templated grain growth (TGG) processes are normally used to grow crystals (seed) inside a polycrystalline matrix. Both processes induce exaggerated grain growth around the used seed appearing larger grains than the mean grain size.

Early works on TGG and SPC include several patents for producing single crystals from polycrystalline precursors as well as textured ceramics [257-259]. TGG process can be applied either for the growth of large single crystals with a small amount of crystals (e.g., templates) distributed and oriented (or not) in a fine-grained matrix (Table 2.4) [260]. The principal use of TGG process is for obtaining textured ceramics using anisometric template crystals, which are oriented using a tape casting, slip casting, extrusion, uniaxial pressing or other technique. On the other hand, the SPC process is used to grow a crystal embedded inside or on the top of a polycrystalline matrix. The faces of the crystal are polished for a better contact with the polycrystalline matrix. In most cases, single crystals or textured ceramics are obtained by a homoepitaxial process, where the matrix powder has the same composition and crystal structure as the template material. In this case, both the crystal and

the matrix grow by a simple Ostwald ripening-type process (i.e., the large grains grow at the expenses of the finer matrix grains) [261, 262]. Alternatively, the heteroepitaxial process is when the template material has a different composition, but the same crystal structure or the lattice matches with the matrix material, e.g. $\text{Pb}(\text{Mg}_{1/3}\text{Nb}_{2/3})\text{O}_3$ - PbTiO_3 or BaTiO_3 single crystals from a SrTiO_3 template [263, 264]. The lattice matching ensures that the nucleation of the growing phase occurs on the template surface and then further heating drives densification and subsequently grain growth in the same way as in the homoepitaxial case. It is frequently found that these processes (TGG and SPC) are used indistinctively due to their similarities. In Table 2.4 it is resumed the practical conditions used in the TGG and SPC processes.

Table 2.4 - Resume of the practical conditions used in the TGG and SPC processes.

parameters	Solid state crystal growth processes	
	Templated grain growth (TGG)	Seeded polycrystalline conversion (SPC)
Number of seeded crystals	~ 5 wt% of the powder	1 crystal
Average seeded size	20 - 100 μm	0.2 - 4 mm
Matrix average particle size	lower than 1 μm	
Orientation of the crystal	Can or not be oriented	
Presence of liquid phase	Yes	
Uniaxial pressing	10 - 100 MPa	
Cold isostatic pressing (CIP)	150 - 400 MPa (it is not always applied)	
Hot pressed (HP)	20 - 40 MPa (it is not always applied)	
Sintering time	From 1 h to several hours	

The principal characteristic of the template is the thermal stability during all the process [265]. The template particles must have a good lattices match with the desired final composition, sufficient stability and an appropriate driving force for growth [260]. In the TGG process it is desired anisometric template particles which help the orientation of the particles and the development of the final texture. On the other hand, the matrix powder particles are of equal importance to be successful in the templated grain growth. In the

homoepitaxial case, the matrix powder is already in the final phase form and it is important that its size is finer than the template particles after densification and it must be sintered to high density (*e.g.*, > 95% theoretical density) [266]. It is convenient to introduce a second phase, having a melting point lower than the matrix phase. Upon annealing the second phase forms a liquid phase throughout the polycrystalline matrix and around the seed. The presence of the second phase in the matrix and around the growing single crystal has been shown to aid in the growth of the single crystal.

In general, the TGG and SPC processes occur in three stages [267-269]: densification, rapid radial growth of individual template particles until template impingement, and slower growth by template thickening, as schematically shown in Figure 2.22 [260]. Because the pores restrain the boundary motion, a significant template growth can not occur during densification, being generally limited until the matrix density is $\geq 90\%$ of the theoretical density (TD), as observed by Messing *et al.* [269-271] and Watanabe *et al.* [272] in Al_2O_3 and $\text{Bi}_4\text{Ti}_3\text{O}_{12}$ ceramics, respectively. During heating, template particles grow at the expense of the finer ones. The thermodynamic driving

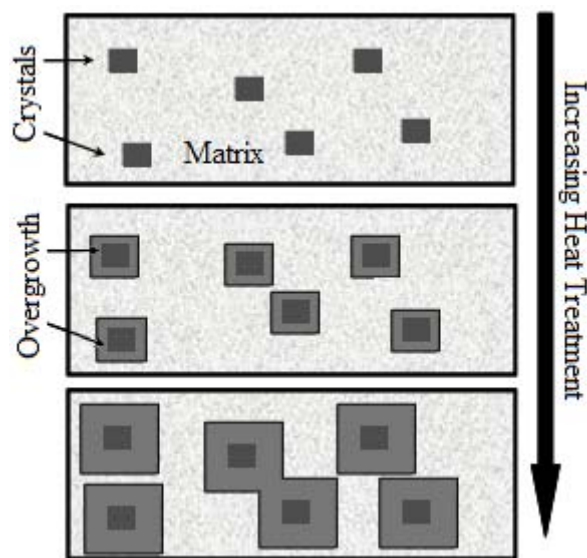


Figure 2.22 - Schematic of the stages for the TGG process {Hong, 1999 #23932}.

force for the migration of the template boundary into the polycrystalline matrix during the thermal processing appears from the difference in the surface free energies between the advancing crystal plane and the matrix grains [260]. A large matrix grain growth during sintering can reduce the thermodynamic driving force enough so that the template growth

stops. Therefore, the finer the matrix grain size, the higher the driving force for these processes (TGG and SPC).

In almost all the cases, the kinetics of boundary migration is increased by intentionally introducing a liquid phase at the grain boundaries to reduce the stress around the templates and to increase the mobility of the grain boundary, thus facilitating the densification and grain growth [260, 266]. Because a small amount of liquid is present during growth, template growth occurs by dissolution of the polycrystalline matrix grains and deposition on the lowest energy surface in the system that is the template major face.

In summary, TGG and SPC offers significant opportunities for reducing the cost of single-crystal-like materials [260] and to increase the average size of polycrystalline materials. Being based on a conventional powder processing and sintering, large grain size ceramics, frequently highly oriented or single crystal can be achieved at a significantly lower cost as compared to other techniques commercially available.

2.3.1. *Templated grain growth (TGG) in PZT*

Single-crystal materials have many industrial and scientific applications; however, growing large single crystals is often difficult, time-consuming, and expensive. Some single crystals are especially hard to grow. For example, lead zirconate titanate (PZT) is a widely used piezoelectric and ferroelectric material that is available as an isotropic, polycrystalline ceramic. PZT single crystals are not commercially available due to the difficulty to grow these crystals in all the range of compositions. Recently, the interest in the study of PZT single-crystal-like materials has been increased, as a way to optimize their piezoelectric properties, approaching them to those of single crystals [191, 273-275]. The best PZT single-crystal-like materials have been obtained in thin film using epitaxial methods [120, 193, 194, 253, 263-265, 276].

Sekiya *et al.* [273] used a tape casting method to develop an array of PZT orientated crystals, obtained by the usual PbO flux method. The grown crystals exhibited a size distribution with a peak at around 80 μm , while the starting crystals were around 10 μm in size [277, 278]. Later, Liu *et al.* [191], demonstrated the formation of single-crystal-like materials that contained preferentially oriented arrays of lead zirconate titanate (PZT) cube-shaped particles by self-assembly. Hydrothermally synthesized PZT particles with a bulk composition of $\text{Zr/Ti} = 70/30$ were used to make microcrystal arrays.

At the moment, none has been able to obtain a really PZT textured ceramics using the TGG method and only a few efforts have been reported in the literature [274, 275]. Muramatsu *et al.* [274, 275] made textured PZT ceramics with $\langle 111 \rangle$ orientation, prepared by TGG using platelike $\text{Ba}_6\text{Ti}_{17}\text{O}_{40}$ hetero-templated grains. The effects of the matrix composition (x value) on the texture development were examined. The template grains gave $\langle 111 \rangle$ -texture in Ti-rich PZT ($0 \leq x \leq 0.5$) but not in Zr-rich PZT ($1 \geq x \geq 0.7$). The matrix composition determined the extent of reaction between PZT and $\text{Ba}_6\text{Ti}_{17}\text{O}_{40}$ (B6T17), which hindered the texture development because of the disappearance of template grains at high temperatures. The final grain size is not reported.

CHAPTER 3

Materials processing and experimental techniques

This chapter details the experimental work on the synthesis and processing of PZT powders, the sample preparation procedures and the conditions of ceramics sintering, the single crystals growth and finally the technique and conditions for the characterisation of their structure, microstructure and electrical behaviour.

3.1. Ceramics preparation

The PZT ceramics studied in this work had the compositions of $\text{Pb}(\text{Zr}_x\text{Ti}_{1-x})\text{O}_3$, with $0.40 \leq x \leq 0.65$ corresponding to the region around the MPB.

3.1.1. Synthesis of PZT powders

The PZT powders were prepared using the reagents PbCO_3 (Merck, > 99%), TiO_2 (Merck, > 99%) and ZrO_2 (Aldrich, > 99%). The powders were mixed for 3 h in a planetary ball milling, in teflon jars with alcohol medium and zirconia balls. The slurries were dried at 120°C for 24 h, calcined at 900°C for 2 h and grounded in an agate mortar. The calcined powders were then grounded for 16 h and dried again at 120°C for 24 h.

3.1.2. Preparation of frits

A set of frits was used to promote grain growth in the ceramics. The used compositions are shown in Table 3.1. The glassy phases were prepared from reagent-grade PbO (Alfa-Aesar, 99.9%), SiO_2 (BDH, 99.9%) and MgO (Merck, > 99%). The powders were mixed for 3 h in a planetary ball milling (Restch, USA) using teflon jars with alcohol medium and zirconia balls. The slurries were dried at 120°C for 24 h. After drying, the mixtures were placed in an alumina crucible and melted at 900 °C during 30 min in an electric furnace. Once the melting was completed, the crucible was removed from the furnace and the molten glass was poured into cold distilled water. After drying, the glass was grounded in an agate mortar and then sieved through a 230 mesh screen.

Using the frits in the Table 3.1 and PZT powder of the composition $\text{Pb}(\text{Zr}_{0.525}\text{Ti}_{0.475})\text{O}_3$, mixtures were prepared in the desired composition, grounded in alcohol medium for 16 h and dried at 120°C for 24 h.

Table 3.1 - Frits used to promote grain growth in the ceramics.

Frit composition (% molar)	Used weights in the ceramics (%)
96%.PbO - 4%.SiO ₂	3, 5, 8
92%.PbO - 8%.SiO ₂	3, 5
84%.PbO - 16%.SiO ₂	3
100%.PbO	3
91%.PbO + 8%.MgO	3
72%.PbO + 7%.MgO + 21%.SiO ₂	3

3.1.3. *Pressing and sintering of PZT ceramics*

Green compact discs were pressed from the prepared powder in a uniaxial die with diameter of 10 mm (Carver laboratory press Group). The effect of the compaction pressure on the green density for this type of powder preparation was already reported [279] and the optimum pressure applied was 460 MPa.

The green compacted ceramics were placed in a covered alumina crucible and sintered at various temperatures, between 800°C and 1250°C, for different sintering times, 1 to 16 h. The atmosphere was enriched in PbO by using PbZrO_3 powder with 3 wt% excess of PbO. The sintering was carried out in a tubular furnace (Termolab LAD) with a thermal controller (Eurotherm 2404) under stationary air atmosphere, using a heating rate of 10 °C/min until the maximum temperature.

The specimen weight loss and the linear shrinkage were determined. The green density was calculated from the weight and dimensions of the compacted sample. The sintered density of specimens was determined by the Archimedes' method, using water as fluid. The sample was previously immersed in boiling water to drive off the air in the open pores. In this way water absorption can also be measured.

The results of the density will be expressed in terms of their relative values to $\rho=8.0 \text{ g/cm}^3$, the theoretical density of PZT52, in order to assess the porosity of the samples. All the ceramics had $63\pm 1\%$ of relative green density. The number after the designation “PZT” means the amount of Zr (in mol %) in the system $\text{Pb}(\text{Zr}_x\text{Ti}_{1-x})\text{O}_3$; for example, PZT52 means the composition $\text{Pb}(\text{Zr}_{0.52}\text{Ti}_{0.48})\text{O}_3$, only for the composition $\text{Pb}(\text{Zr}_{0.525}\text{Ti}_{0.475})\text{O}_3$ the designation is PZT525.

3.2. Preparation of PZT single crystal

3.2.1. Crystals growth from flux

PZT single crystals were grown using the high-temperature self-flux solution method already described (section 2.1.3) [175, 180, 182]. In Figure 3.1 it is shown a flux diagram of the materials preparation and their experimental details. In this diagram it is summarized all the principal issues to obtain the PZT single crystals.

The PZT studied in this work had the composition $\text{Pb}(\text{Zr}_{0.525}\text{Ti}_{0.475})\text{O}_3$, which is in the MPB region. The preparation of the PZT powders was already described in section 3.1.1. The flux PbO-KF-PbCl_2 , in molar ratio of (2:1:2) [49], was then added to the PZT using different flux amount. It was prepared using PbO (Alfa Aesar, > 99%), KF (Merck, > 99%) and PbCl_2 (Alfa Aesar, > 99%). The powders were mixed for 3 h in a planetary ball milling, in teflon jars, with alcohol medium and zirconia balls. The slurry was dried at 120°C for 24 h. This flux has a melting point around 650°C . The melting point may be conveniently reduced by adding other components to the flux, e.g., B_2O_3 , resulting in a more stable flux with crystals nucleating in an optimum homogeneous and viscous medium [280]. It was added 4 wt% of B_2O_3 (Merck, > 99%).

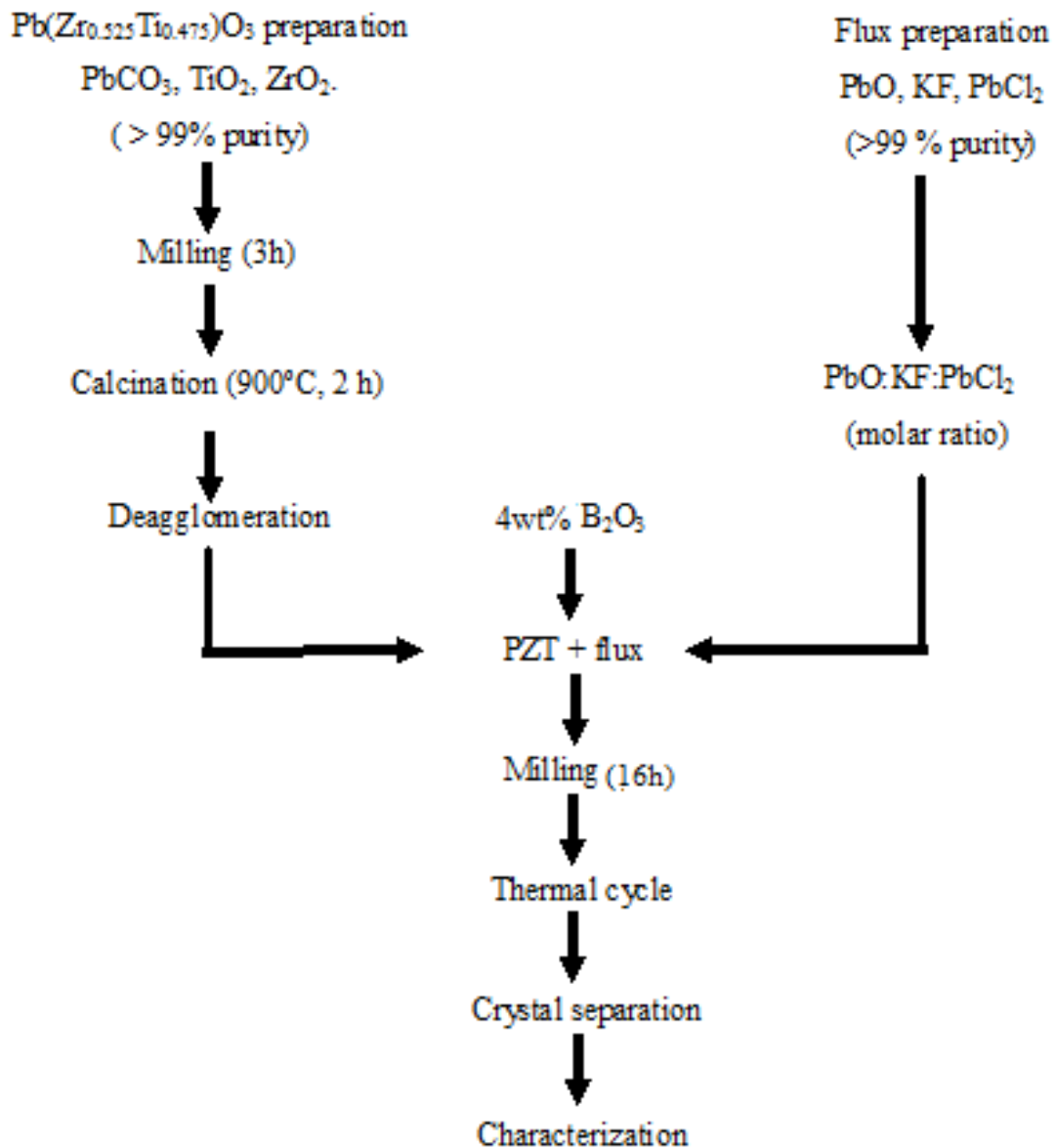


Figure 3.1 - Flux diagram of the single crystals preparation and some experimental details.

The mixture of PZT and flux was put in a platinum crucible of 50 cm³, with percentage of flux in relation to the PZT between 40 to 65 wt %. The total mass of the flux and PZT was 20 g. The platinum crucible was then covered by a larger alumina crucible, sealed with alumina cement to minimize the evaporation of lead oxide (Figure 3.2). The crucible was placed inside a vertical electric furnace with a very small vertical temperature gradient, equipped with a thermocouple located on the top, as schematically illustrated in Figure 3.2(a).

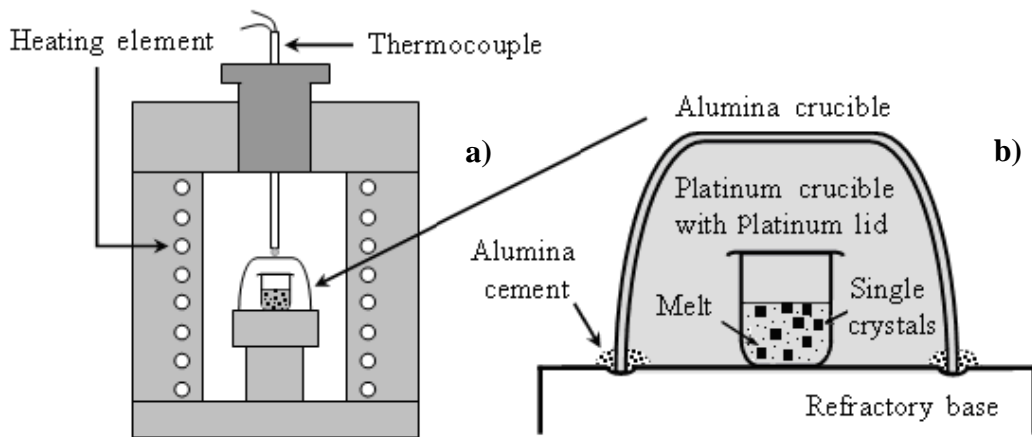


Figure 3.2 - a) Schematic diagram of the furnace used for the growth of PZT single crystals and b) the double crucible arrangement used to prevent the evaporation of the flux at high temperatures [3].

The different thermal profiles in Table 3.2 were tested in an attempt to achieve large single crystals without second phases. The weight losses fluctuated between 18% and 32% of the initial powder amount (flux plus PZT). Figure 3.3a) shows an example of the heat treatment condition M6 (Table 3.2) and Figure 3.3b) shows an optical photograph of the grown crystals inside the flux. To evaluate the weight loss, the platinum crucible was weighed before and after the thermal treatment.

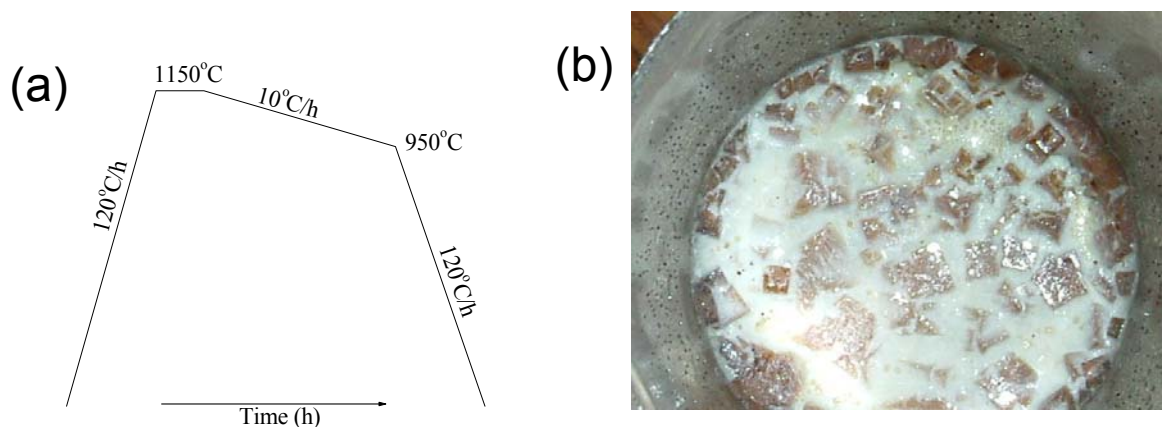


Figure 3.3 - a) The heat treatment curve for the M6 condition and b) optical photograph of the grown crystals inside the flux (2x2 cm).

Table 3.2 - Conditions used for the growth of the single crystals, the corresponding weight losses and the obtained crystals composition in terms of x in $\text{Pb}(\text{Zr}_x\text{Ti}_{1-x})\text{O}_3$. The cooling rate is related to cooling from the crystal growth temperature to 950 °C.

Methods	Temperature (°C)	Holding time (h)	Cooling rate (°C/h)	Flux amount (wt%)	Weight loss (wt%)	Composition Range x	Second phase
M1	1200	5	5	40	24	0.40 - 0.60	Yes
M2	1200	5	10	40	22	0.40 - 0.60	Yes
M3	1200	5	20	40	18	0.40 - 0.60	Yes
M4	1150	5	10	40	20	0.40 - 0.60	No
M5	1150	5	10	60	28	0.40 - 0.60	No
M6	1150	10	10	60	32	0.40 - 0.60	No
M7	1100	10	10	60	19	0.40 - 0.60	No
M8	1150	5	10	65	15	-	Yes
M9	1150	5	10	40	4	-	Yes
M10	1150	5	10	60	25	0.40 - 0.60	Yes
M11	1150	5	10	60	31	0.40 - 0.60	Yes

In Figure 3.4, it is shown all the tested flux compositions used to grow the PZT crystals using the PbO-KF-PbCl_2 system [204]. The composition M1-8 was used in this work, although it was previously used to grow PZT crystals in all the range of compositions [91]. The compositions marked with M9 to M11 were used for the first time here (table in Figure 3.4). It was added 4% (w/w) of B_2O_3 in all the compositions, except in M8, where a ratio of $\text{PbO}:\text{B}_2\text{O}_3$ of 6:1 was used.

The grown PZT single crystals were separated from the flux by heating up to ~ 1000 °C the crucible into the furnace in an inverted position and collecting the flux on an alumina crucible, during 20 min, followed by slowly cooling. This process moves the flux of the crystals, the flux is deposited on the ceramic and the crystals remain in the crucible. The crystals and the residual flux were taken off from the crucible mechanically as a solidified

mass and then the crystals were separated from the glass by leaching in hot HNO_3 to dissolve the residual flux while the crystals are not dissolved. This step took 6h in maximum because after long periods the acid starts to attack the single crystals. Finally, the PZT crystals were leached in hot water for 24 hours to dissolve the nitric salt and then annealed at $750\text{ }^\circ\text{C}$ for 1 hour.

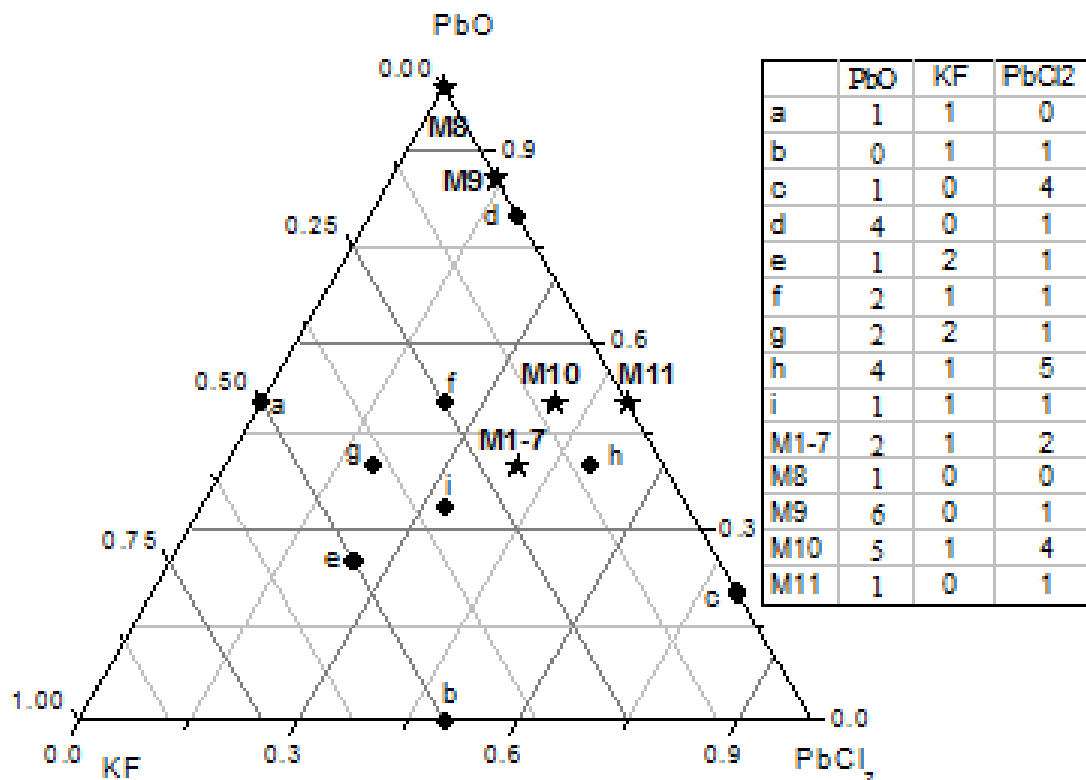


Figure 3.4 - Ternary PbO-KF-PbCl₂ diagram where the symbols represent tested compositions. In the table it was summarized all the compositions used to grow the PZT crystals using the PbO-KF-PbCl₂ system. In this work only were tested the compositions designed by M1-11. The numbers in the column mean the molar ratio for each compound.

3.3. Seeded polycrystalline conversion (SPC) method

The procedure of seeded polycrystalline conversion (SPC) method was used to stimulate the crystal growth by putting 5 wt% of single crystals in a ceramic matrix. For the present investigation, a PZT powder was firstly synthesized via solid state reaction

using an identical method and similar reagents to those previously described in section 3.1. The mobility of the grain boundaries at the sintering temperatures was enhanced using a liquid phase, selected among those presented in Table 3.1. In Table 3.3 it is shown the liquid phases compositions used in this work in the form of a frit and mixed with the PZT powder.

Table 3.3 - Liquid phase, amount of liquid phase, temperature and sintering time used to promote the crystal/grain growth by the seeded polycrystalline conversion method.

Frit composition in (mol)	Used weight (%)	Time in (h)
		1200 (°C)
7PbO:0.7MgO	3	4
7PbO:0.7MgO:2SiO ₂	3	2

The PZT powder and the frit were mixed and grounded for 16 h in a planetary ball milling (Restch, USA) using teflon jars with alcohol medium and zirconia balls. The slurry was dried at 120°C for 24 h. Then, 5 wt% of single crystals, with approximately size of 30x30x30 µm, were added and carefully hand mixed in an agate mortar. The samples were compacted unidirectionally and then isostatically at 200 MPa. The thermal treatments and the reagents used were identical to those previously described in section 3.1.3. The samples were sintering at 1200°C with different holding time (Table 3.3).

3.4. Electroding and surface preparation

Both the electrical and microscopic characterisation of ceramic and single crystals needed a certain degree of surface polishing. The samples (ceramics or single crystals) were first inserted in an epoxy resin (araldite) and then polished by using several abrasives in the following order: a) silicon carbide papers, b) diamond pastes (15, 6, 3, 1 and 0.25 µm) and c) a colloidal-silica aqueous suspension (~ 0.05 µm). Submicron polishing was performed only when required, namely for domain studies by atomic force microscopy (AFM), scanning electron microscope (SEM) and electron probe microanalysis (EPMA). After polishing, samples were removed, or not, depending on the experiment, from the resin and cleaned in an ultrasonic machine (Branson 1510) with ethanol and dried at 120 °C for several hours. The polished ceramics were chemically etched by using a solution of

1 vol.% of hydrofluoric acid (HF 5%), 10 vol.% of hydrochloric acid (HCl 37%) and 89 vol.% of water for different etching times, from 10 to 60 second, depending on the sintering conditions, in order to reveal the grain boundaries.

For electrical characterisation, the single crystals were polished, a flat surface normal to the ab -plane (Figure 3.5) for measurements along the $[001]$ direction (c -axis direction determined by XRD) using a disc grinder (Gatan 623). The final area of the crystal polished surfaces used in this study varied from $2 \times 2 \text{ mm}^2$ to $0.4 \times 0.4 \text{ mm}^2$, while the final thickness was 100 to 200 μm . Gold electrodes were then sputtered (in ceramic and crystals) onto the central area of the parallel polished faces using a *Polaron E5000* vacuum sputtering system. A grid with a hole size between 200 μm and 2 mm of diameter was used to apply electrodes on the single crystals. The grid was put on the top of the crystal using an optical microscope and then carefully placed inside the sputtering machine where gold electrodes were sputtered Figure 3.5. In the ceramics, the hole size was of 6 mm in diameter, Figure 3.5.

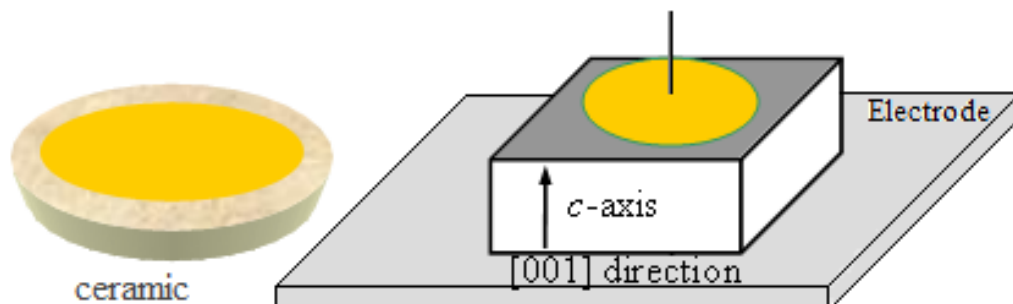


Figure 3.5 - Schematic representations of ceramics and crystals configurations for electrical measurements. The crystal was polished perpendicular to the $[001]$ direction.

For ferroelectric domain observations via a piezoelectric force microscopy (PFM), the single crystals were polished similarly to the method previously described. After polishing, the crystals were annealed at 750 $^{\circ}\text{C}$ for 1 hour to eliminate stresses and domain deformations on the crystal surface and cooled at 30 $^{\circ}\text{C}/\text{h}$. Then, the whole area of the bottom face of the crystals was electroded by sputtering gold layer.

3.5. Phase identification and microstructure characterisation

3.5.1. X-ray diffraction (XRD) of powders

The phase analyses were performed on the calcined powders and the sintered samples (in powder state) using a X-ray diffractometer (Rikagu/New) with monochromatic CuK α radiation. The detection range was from 20 to 60 degrees, with a step of 0.05° and a speed of 2°/min. Identification of crystalline phases was carried out by comparison of XRD patterns with JCPDS database.

3.5.2. X-ray diffraction (XRD) of single crystals

The single crystals were mounted on a glass fibre using FOMBLIN Y perfluoropolyether vacuum oil (LVAC 25/6) from Aldrich [281]. Data were collected at 180(2) K on a Nonius Kappa charge-coupled device (CCD) area-detector diffractometer (Mo K α graphite-monochromated radiation, $\lambda = 0.7107 \text{ \AA}$), equipped with an Oxford Cryosystems cryostream and controlled by the Collect software package [282]. Thanks to the high symmetry of the materials, a full sphere of reflections could be collected. Images were processed using the software packages Denzo and Scalepack with P1 symmetry [283]. Intensity data were corrected for Lorentz polarization and background effects and also for absorption using the empirical method employed in Sortav [284, 285]. Analyses of the systematic absences using the XPREP interface, suggested a number of feasible Niggli reduced unit cells in combination with various space groups.

Structures were solved using the Patterson synthesis algorithm implemented in SHELXS-97 [286], which permitted direct location of the crystallographic position corresponding to the heaviest atoms. Refinement was performed with full-matrix least squares on F^2 using SHELXL-97 [287], which ultimately permitted the location of the crystallographically independent oxygen atom. The data provided by EPMA were used for the chemical compositions.

3.5.3. *Scanning electron microscopy (SEM) and electron energy dispersive spectrometer (EDS)*

For scanning electron microscopy (SEM) observations the samples were polished as discussed in section 3.4, although some observations were alternatively done over fractured samples.

The polished and etched samples were glued in a special sample holder using a conductive carbon paste and dried for 24 hours at 120 °C. Then, the samples were covered with a thin layer of carbon in order to improve the quality of the image. The carbon deposition process was performed using an *Emitech* K950 carbon deposition chamber equipped with a turbo pump. SEM observations were performed using a field emission scanning electron microscope *Hitachi* S4100 and the images were obtained using an electron acceleration field of 25 kV and a filament emission current of 10 μ A.

The chemical composition was analyzed by a Jobin Yvon (*Jy70 Plus*) energy dispersive spectrometer (EDS) attached to the SEM. A map of the chemical composition was produced with an energy dispersive spectroscopy analyser (*Bruker Quantax*) attached to a SEM *Hitachi Su-70 (S-4100)*. The *Bruker Quantax* spectroscopy analyser had an absolute sensibility of the order of 0.1 pg. The precision and accuracy of the spectroscopy is limited by the sample preparation, properties of the sample and the elements to be analysed, but in normal circumstances the error is low, 3 to 5 mol%.

3.5.4. *Electron probe microanalysis (EPMA)*

Electron probe microanalysis (EPMA) is an analytical technique used to establish the chemical composition of small areas on specimens. EPMA is one of several particle-beam techniques. Particular to this technique, although not unique, is the bombardment of the specimen with a beam of accelerated electrons. The electron beam is focused on the surface of a specimen using a series of electromagnetic lenses, and these energetic electrons produce characteristic X-rays within a small volume (typically between 1 and 9 μm^3) of the specimen. The characteristic X-rays are detected and the intensities are measured to determine the concentrations of each chemical element. All elements (except hydrogen, helium and lithium) can be detected because each element has a specific set of emitted X-rays. This analytical technique has a high spatial resolution and sensitivity and

individual analyses are reasonably short in time, requiring only a minute or two in most of the cases.

Electron probe microanalysis (EPMA), CAMECA, model Camebox SX50 was used to determine chemical compositions of polished crystals and ceramics.

3.5.5. *Transmission electron microscopy (TEM)*

In this work, a transmission electron microscope (HRTEM) Hitachi H9000-NA Instrument, operating at 300 keV, was used to perform selected area diffraction (SAD) and energy dispersive X-ray (EDX) analyses in single crystals. The samples for TEM were prepared from the milled single crystal dispersed in ethanol and deposited on a grid.

3.6. *Electric characterisation*

3.6.1. *Measurement of dielectric properties*

Dielectric properties were measured using a HP4284A precision LCR Meter in the frequency range of 1 kHz - 1 MHz, with the temperature controlled by an Eurotherm (2404) controller. The samples were polished to obtain parallel faces for electrical characterisation. Gold layers were sputtered onto the parallel faces as presented in section 3.5. An appropriate holding sample was used to measure the single crystals due to the small size of the crystals. In Figure 3.6 it is shown a draw of this sample holder. This hold allows measuring small crystals without the problem of loss or breaking the crystal.

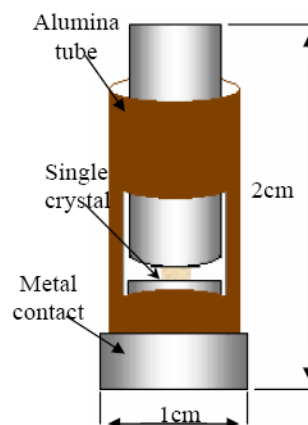


Figure 3.6 - Draw of the sample holder used for the electric measurements.

3.6.2. *Pyroelectric characterisation*

The specimens were poled in a mineral silicone oil bath at 120°C with a dc field of 25 kV/cm applied for 10 min. Then, the specimens were cooled to room temperature with the applied electric field. The samples were short-circuited for 24 hours to remove conduction charges. The current was measured using a programmable electrometer (Keithley 617) and the temperature was controlled by a Eurotherm controller (2404). The data acquisition and the experiment control were carried out using a computer with a GPIB interface (National Instruments).

3.6.3. *Piezoelectric characterisation*

Piezoelectric measurements of an *ac* electric field induced strain (converse piezoelectric effect) at low frequencies (from 500 Hz to 5 kHz) were performed using an interferometric technique described elsewhere [288]. The longitudinal piezoelectric coefficient d_{33} was calculated from the slope of the straight line between the strain and the electric field.

A double-beam (Mach-Zender) laser interferometer with an active stabilization of the working point was used to measure the d_{33} piezoelectric coefficient of the single crystals. In this case, the probing beam reflects from both the front and the back faces of the sample and the bending contribution to the measured vibrational piezoelectric response is automatically eliminated by the optical arrangement [288]. Figure 3.7 shows the schematic diagram of the setup for the assembly single crystal-araldite holder used in this measurement with a double-beam laser interferometer.

For piezoelectric measurements, the crystals were previously embedded in araldite (due to the small thickness) and polished in both the front and back faces. Gold electrodes were sputtered onto the whole area of the parallel polished faces resulting in mirror-like reflection, and the crystals were poled at room temperature with an electric field of $E_p = 40$ kV/cm for piezoelectric characterisation. The frequency dependence of the d_{33} coefficient and phase of the poled crystals was measured at room temperature using an *ac* voltage of $V_{ac} = 100$ V ($E_{ac} \approx 3$ kV/cm) in the frequency range from 500 Hz to 5 kHz.

The behaviour of the d_{33} coefficient for different *dc* poling fields was also measured at room temperature as follows: first, a *dc* poling field is applied to the crystal during 1 min, and then the poling field is removed and a weak *ac* voltage ($V_{ac} = 100$ V) is applied for piezoelectric deformation, which is measured using a lock-in amplifier (Perkin-Elmer

7265). This process is repeated increasing (and decreasing) the *dc* poling field in steps of ~ 3 kV/cm in both directions for each crystal.

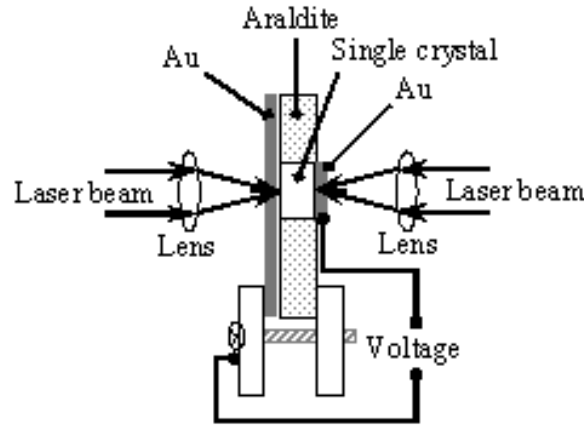


Figure 3.7 - Scheme of the setup for the assembly single crystal-araldite holder used for the elimination of bending motion in the single crystals [288]. For this measure it was used a double-beam laser interferometer.

3.6.4. *Hysteresis loop*

To confirm the anisotropy of the ferroelectric properties of the studied single crystals, the polarization-electric field (P-E) hysteresis loops were measured at room temperature along the *c*-axis or in the *ab*-plane (parallel to [110] direction) using a modified Sawyer-Tower circuit (Figure 3.8) [30]. An alternating voltage is applied on the ferroelectric sample (C_x) connected to the horizontal plates of an oscilloscope; hence, the quantity plotted on the horizontal axis of the oscilloscope (V_x) is proportional to the electric field across the sample (E), which can be calculated considering the sample thickness (t) and the following expression,

$$E = \frac{V}{t} \quad (3.1)$$

C_O is a linear capacitor with a large capacitance of $\sim 1 \mu\text{F}$ that is connected in series with the ferroelectric material C_x in such a way that most of the voltage drops across the sample. The voltage across the linear capacitor C_O (V_Y) is therefore proportional to the polarization (P) of the ferroelectric material, which is calculated taking into account the area of the electrodes (A), using the following expression [30]

$$P = \frac{C_o V_Y}{A} \quad (3.2)$$

The spontaneous (P_S), the remanent polarizations (P_r) and the coercive field (E_C) of the studied material can be computed from the recorded hysteresis loop and the value of the relative permittivity (ϵ_r) can be calculated from the slope of the P-E linear behaviour on the saturation,

$$P = \epsilon_r \epsilon_o E \quad (3.3)$$

Electric fields as high as ~ 45 kV/cm were applied to the samples at the frequency of 50 Hz. During P-E hysteresis measurements, the samples were submerged in silicone oil, an insulating liquid, to prevent arcing. The hysteresis loop was visualized and recorded using a digital oscilloscope (*LeCroy* LT322) and the acquired data were saved on a floppy disk. Once again, because of the small transverse size of the samples, a correction for the stray capacitance (parasite capacity) of the sample holder and connecting wires was necessary to separate the P-E hysteresis loop of the sample from the linear contribution due to the stray capacitance.

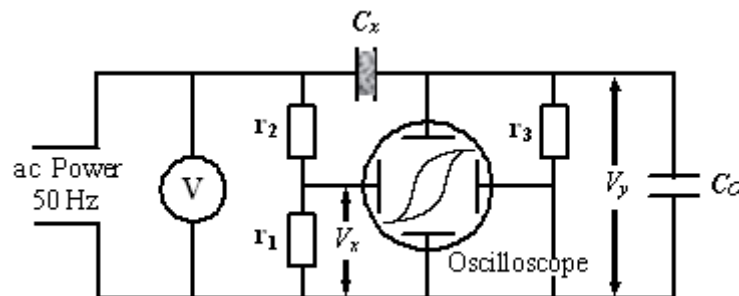


Figure 3.8 - Modified Sawyer-Tower circuit used for the P-E hysteresis loop measurements in single crystals and ceramics [30].

3.6.5. Piezoresponse scanning force microscopy

The quantitative piezoelectric characterisation of the ferroelectric materials at the nanoscale is extremely important and with the advent of piezoresponse scanning force microscopy, the investigation of nanoscale piezoelectric phenomena has not only become possible, but also indispensable [289]. The three-dimensional piezoresponse force microscopy (PFM) enables the visualization of the domains and their polarization

directions and it is based on the detection of bias-induced local surface deformation [290]. The tip is brought into the contact with the surface, and the piezoelectric response of the surface is detected as the first-harmonic component of the bias-induced tip deflection $d=d_0+A\cos(\omega t+\varphi)$. The phase φ yields information on the polarization direction below the tip, as shown in Figure 3.9.

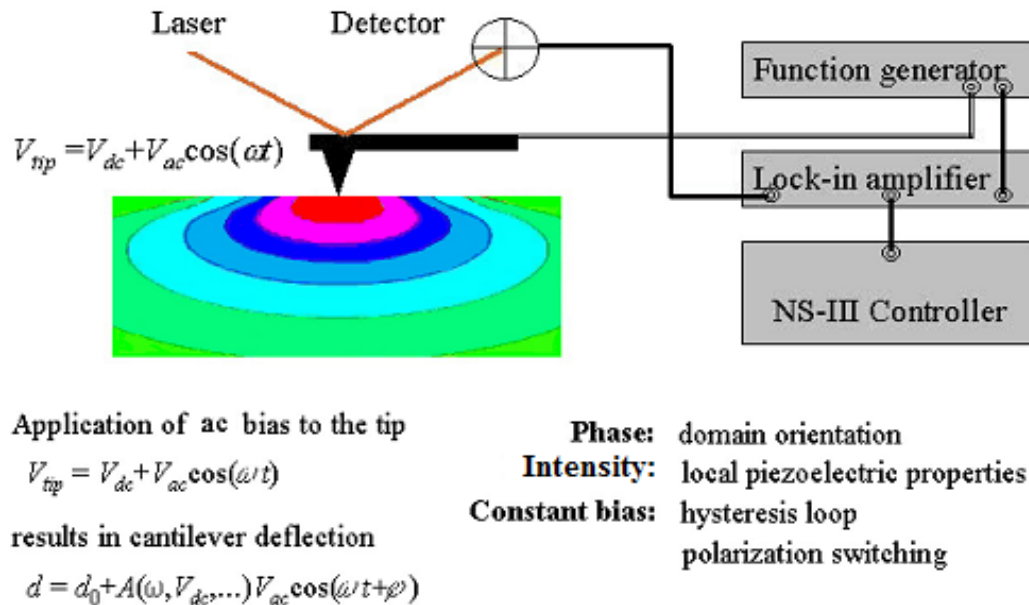


Figure 3.9 - Schema of the piezoresponse force microscope.

For negative domains (polarization vector pointing to the free surface), the application of a positive tip bias results in the expansion of the sample and the surface oscillations are in phase with the tip voltage, $\varphi=0$. For positive domains, $\varphi=180^\circ$. The amplitude, A , defines the local electromechanical response and depends on the geometry of the tip-surface system and material properties. An AFM system, consisting of a commercial *Multimode* atomic force microscope equipped with a Digital Instrument *Nanoscope IIIa* scanning probe microscope controller and a hard silicon conducting tip, was used to examine the domain structure of PZT sample. The force constant and resonance frequency of the tip were about $k \sim 40$ N/m and $\omega/2\pi \sim 340$ kHz, respectively [291]. A small ac electric field of variable magnitude and frequency 50 kHz was applied between the tip and the bottom electrode to induce local vibration. The AFM tip signals (both amplitude and phase), originating from the induced vibration of the film, were detected by a lock-in

amplifier. The amplitude of the tip vibration signal (A) is proportional to the piezoelectric coefficient, whereas the phase difference between the tip vibration signal and the small ac field indicates the polarization orientation (see Figure 3.9). Finally, the topography and domain images were processed using WSxMbeta6_0 software.

3.7. Raman scattering

Raman scattering measurements were performed from 173 to 673 K. The Raman spectra were recorded in a triple subtractive Jobin Yvon T64000 Raman spectrometer equipped with a liquid-nitrogen-cooled charge-coupled device (CCD) detector. The emission line at 514.5 nm from the Ar⁺ ion laser was focused on the sample under the microscope, with the width of the analyzed spot being about 1 μm . The power of the incident beam on the sample was about 5 mW. The time of acquisition was adjusted according to the intensity of the Raman scattering. The wavenumber values reported from the spectra are accurate to within 2 cm^{-1} . The spectra were recorded at several points in order to ascertain the homogeneity of the crystal (PZT52). These spectra were plotted in the figures presented in this study.

CHAPTER 4

Growth and characterisation of $PbZr_xTi_{1-x}O_3$ single crystals

In this chapter, the specific experimental conditions to obtain and characterize $PbZr_xTi_{1-x}O_3$ (PZT) single crystals are analyzed and discussed. In the several subsections of this chapter the quality of the crystals is analysed based on the X-ray diffraction and topography analyses and the domain configuration, the dielectric, ferroelectric and piezoelectric properties are evaluated.

4.1. Obtention of PZT single crystals

4.1.1. Single crystal growth and optimization of the conditions

The single crystals growth was previously explained in chapter 3 (section 3.2). The materials and experimental details are summarized in Figure 3.1. In the PZT crystal growth process was used several methods and different experimental conditions (see Table 3.2). Under M2 condition (1200 °C, 5h, 10°C/h of cooling) it was obtained single crystals with a 1.0x0.5x0.1mm shape, as shown in Figure 4.1a. However, these crystals show second phase in the form of dark particles (Figure 4.1b). XRD technique revealed the composition of the dark particles to be ZrO_2 . A possible explanation for the presence of ZrO_2 precipitates comes from a partial dissolution of PZT in the flux, resulting in a Ti-rich PZT phase and the ZrO_2 precipitate with the volatilization of the corresponding PbO, since the holding temperature is high [49, 193]. PbO might also be dissolved in the flux; however, we did not carry a systematic study to corroborate this hypothesis. In the M1 condition (1200 °C, 5h, 5°C/h of cooling) the crystal size is larger than in the M2 condition, but the amount of ZrO_2 precipitate is higher. In both cases, the volatilization of PbO or its dissolution in the flux can be slowed down by decreasing the holding temperature or by increasing the cooling rate. Therefore, in the M3 condition the cooling rate was increased (1200 °C, 5h, 20°C/h of cooling). In this case, the crystal size and the precipitated ZrO_2 both decreased. Increasing the flux volume from 40 to 60 wt% the crystal size increases up to 3 - 4 mm; nevertheless it remains the ZrO_2 precipitate. A similar result is obtained when

the holding time is decreased to 1 hour. In the M4 condition the holding temperature is decreased from 1200 °C to 1150 °C. The result of the temperature decrease is a lower amount of ZrO_2 precipitate (ZrO_2 peak in the XRD spectrum of Figure 4.2), but it remained the problem of the existence of this second phase.

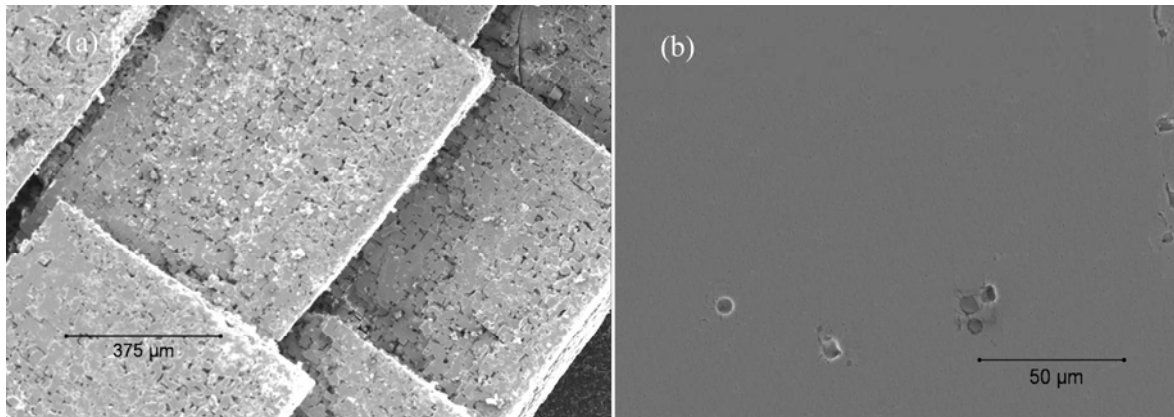


Figure 4.1 - SEM micrographs of the single crystals grown under the M2 condition: a) unpolished crystals and b) polished crystal.

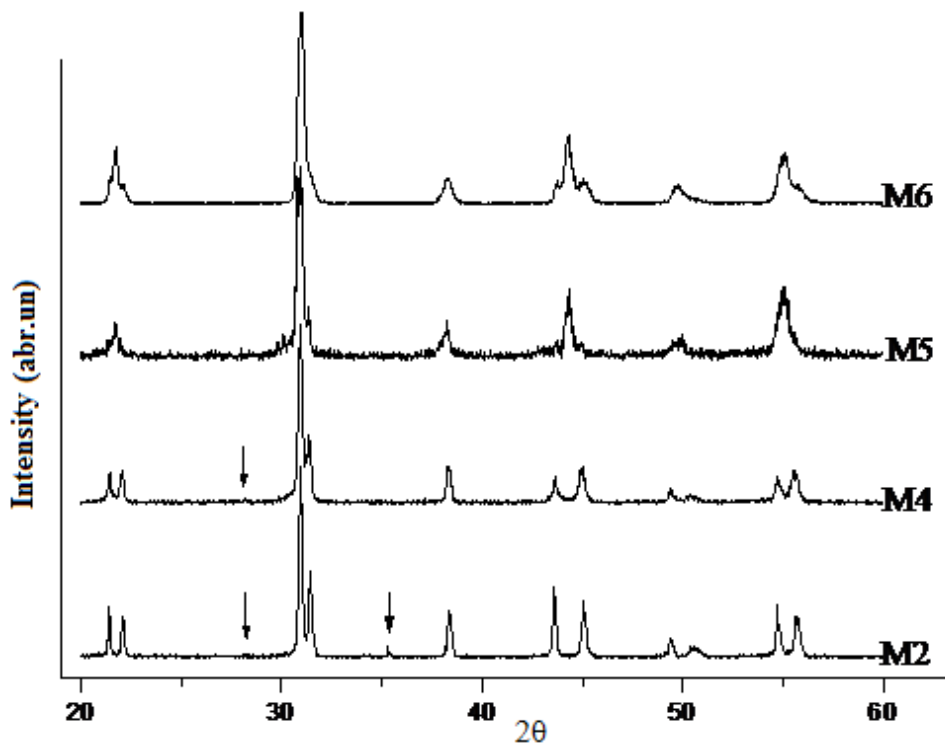


Figure 4.2 - XRD patterns of milled crystals. The arrows indicate the position of the ZrO_2 peaks.

In this flux method, it is expected that a recrystallization process takes place. Time and space (steric condition) are required to develop the process. Perhaps the precipitation of ZrO_2 is observed due to the lack of time or space for the formation of a Zr-rich PZT phase. Under condition M5 (1150 °C, 5h, 10°C/h of cooling), the amount of flux is increased in order to increase the available space for recrystallization, resulting in the elimination of the ZrO_2 phase, as shown in Figure 4.2. However, in this condition XRD reveals a low crystallinity of the sample, which implies the necessity of longer holding times for the recrystallization to proceed. On the M6 condition (1150 °C, 10h, 10°C/h of cooling), where the holding time is twice the M5 holding time, the crystallinity of the obtained crystals is improved (Figure 4.2), again without the second phase. Under conditions M5 and M6 the crystals have sizes between 1-3 mm, good enough for electrical characterisation (Figure 4.3). Consequently, these are the best conditions to obtain PZT single crystals with chemical composition in the MPB region. With the decreasing of the holding temperature (M7 condition) from 1150 °C to 1100 °C the crystals size decreases and the quantity of flux in the crucible increases (see Figure 4.4).

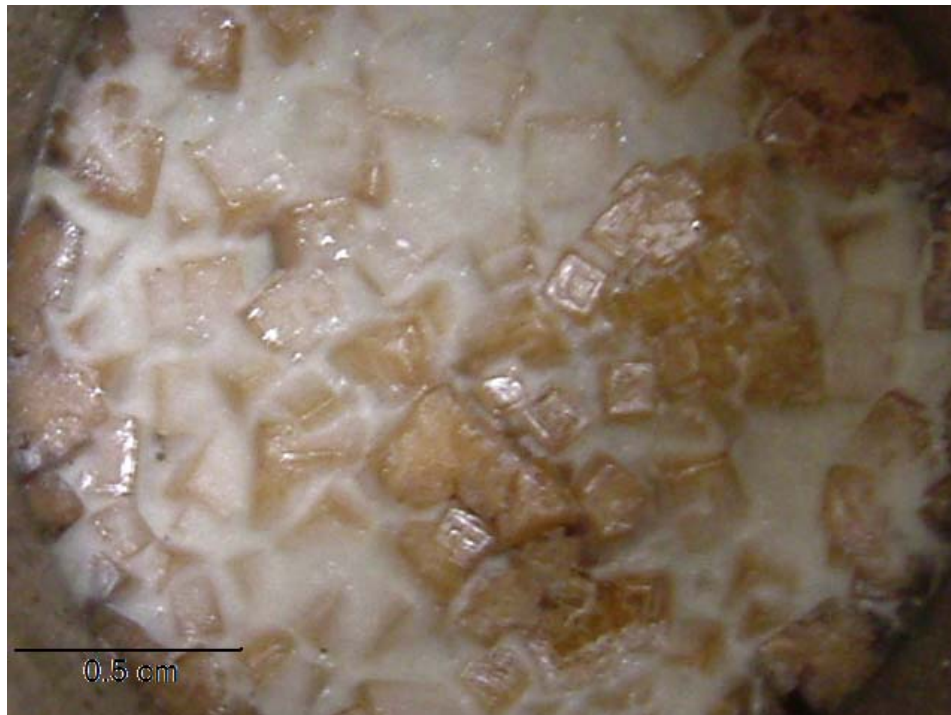


Figure 4.3 - Photograph of the grown crystals inside the flux, typical for the M5 and M6 batches.

The analysis of the XRD patterns of all the crystals, obtained under the M6 condition revealed the presence of two phases: the tetragonal, with the chemical composition in the titanium rich part, $x \approx 0.49$, and the rhombohedral, with the chemical composition in the zirconium rich part, $x \approx 0.55$. The tetragonal phase ($\text{PbZr}_{0.49}\text{Ti}_{0.51}\text{O}_3$) and the rhombohedral ($\text{PbZr}_{0.55}\text{Ti}_{0.45}\text{O}_3$) correspond to 33 mol% and 67 mol% of the total amount, respectively. With these proportions, the general composition of the sample corresponds to $x = 0.52$, *i.e.*, the initial composition, which indicates that there was not a precipitation of ZrO_2 under this condition.



Figure 4.4 – a) Photograph of the crystals grown by M7 and M4 methods and b) SEM images of the crystal obtained by the M7 method.

In order to optimize the composition of the flux, in the ternary PbO - KF - $PbCl_2$ phase diagram (Figure 3.4), it was tested three new flux compositions M9, M10 and M11, as shown in Table 3.2). In all these cases, the crystals show a second phase. Therefore, the composition of the flux and the temperature profile were optimized for the crystal grown in this system. The main problem to solve is the reduction of the number of formed nuclei in the initial stage. The formation of a large number of nuclei in the initial stage decreases the crystal size and complicates the separation process of the crystals from the flux.

4.1.2. *Morphology of the grown crystals*

The morphologies analyzed are referred to the conditions M2 and M6 because the other conditions show similar results. During the cooling process, supersaturation is created and two separate phenomena take place: crystal nucleation and crystal growth. For a constant precursor solution, the crystal size decreases as the number of formed nuclei increases. In the present system, the dependence of the nucleation and growth rates on the cooling process has not been reported yet. The combination of temperature and time profiles (Figure 3.3a) provides adequate conditions for PZT crystal nucleation and growth near the MPB; however, large and good quality PZT crystals were not achieved.

The crystals grown at 1150 °C (or below) crystallize under a cubic shape, as shown in Figure 4.4. Crystals grown at 1150 °C with 60 wt% of flux also crystallize under a cubic shape, but it is common to appear twined crystals (see Figure 4.5a). Twined crystals are more frequent above 1150 °C, where crystals with spiral growth are also obtained (Figure 4.5b and c). The normal colour of the crystals is brownish-red and after a thermal treatment, they became black or transparent, with black spots inside the crystals.



Figure 4.5 - Typical crystals shape (from M1 to M6) a) crystal with twinning b) and c) a spiral. Figures size (3x3 mm).

The final morphology of the crystals is predominantly determined by the temperature and flux fraction. In all the thermal conditions, a large number of small crystals are obtained. This could be understood assuming that the initial supersaturation is higher and thus, the nucleation rate enhances, giving rise to a larger number of nuclei. The large number of nuclei is only reduced upon increasing the flux fraction and using a sawtooth thermal cycles. The shape of the crystals is cubic around the MPB. Both in the Zr and Ti rich regions crystals with platelets-like shapes were grown for compositions with more than 90% of Zr or Ti [9].

4.2. X-ray diffraction and chemical characterisation

This section of the X-ray diffraction and chemical characterisation is divided in three parts, each corresponding to a region of different structural phase: the rhombohedral, the tetragonal and the morphotropic region.

4.2.1. Rhombohedral single crystals

Figure 4.6 shows two of the selected single crystals used in this work, which differ in shape and colour. In Figure 4.6a it is shown the crystal named PZT60, which has a parallelepiped shape (*ca.* 0.25x1x1.5mm) and is black. The electrode used for electrical measurements is visible on the top. The crystal in Figure 4.6b (PZT65) has a cubic shape (*ca.* 1x1x1 mm) and is brownish-red in colour. After polishing and annealing at 950°C for 20 min, it became transparent with some black spots.

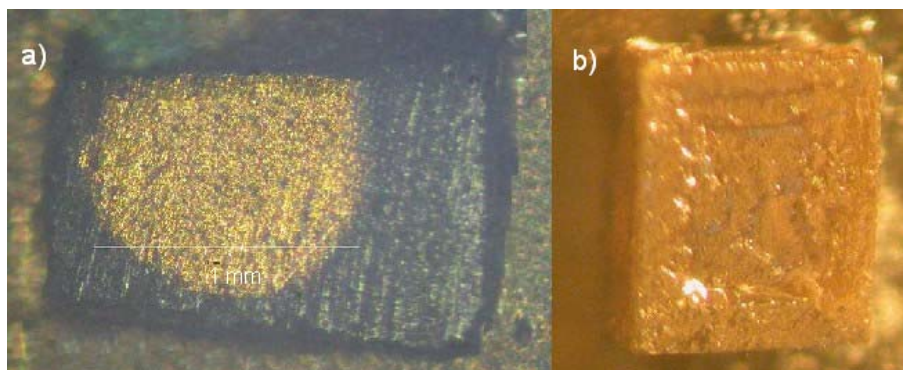


Figure 4.6 - Single crystals: (a) PZT60 and (b) PZT65.

Single-crystal X-ray diffraction studies in a portion of these two crystals revealed that both crystallize in the rhombohedral phase (non-centrosymmetric $R3m$ space group), as shown in Table 4.1 and Table 4.2. The use of a small portion of each crystal decreases the number of defects and minimizes the X-ray absorption, which affect the reflection intensities. The details of PZT60 and PZT65 crystal structure are typical for this family of compounds (Figure 4.7).

Table 4.1 - Crystal and structure refinement data for PZT60 and PZT65 compounds.

Crystal	PZT60	PZT65
Formula	$\text{PbTi}_{0.40}\text{Zr}_{0.60}\text{O}_3$	$\text{PbTi}_{0.35}\text{Zr}_{0.65}\text{O}_3$
Formula weight	329.08	331.25
Crystal system	Rhombohedral	Rhombohedral
Space group	$R3m$	$R3m$
$a/\text{\AA}$	4.0900(5)	4.0989(5)
$b/\text{\AA}$	4.0900(5)	4.0989(5)
$c/\text{\AA}$	4.0900(5)	4.0989(5)
α°	89.845(17)	90.083(17)
β°	89.845(17)	90.083(17)
γ°	89.845(17)	90.083(17)
Volume/ \AA^3	68.417(14)	68.865(15)
Z	1	1
$D_c/\text{Mg m}^{-3}$	7.987	7.987
$\mu(\text{Mo-K}\alpha)/\text{mm}^{-1}$	64.638	64.262
F(000)	139	140
Analysed crystal size/mm	0.07×0.07×0.05	0.07×0.05×0.05
Crystal type	Black block	Black block
θ range	4.98 to 26.86	4.97 to 26.82
Index ranges	$-4 \leq h \leq 5$ $-5 \leq k \leq 5$ $-4 \leq l \leq 5$	$-4 \leq h \leq 5$ $-5 \leq k \leq 5$ $-4 \leq l \leq 5$

Reflections collected	600	574
Independent reflections	125 ($R_{\text{int}} = 0.0868$)	121 ($R_{\text{int}} = 0.0787$)
Completeness to $\theta = 26.86^\circ$	100.0%	100.0%
Final R indices [$I > 2\sigma(I)$] ^{a,b}	$R1 = 0.0282$ $wR2 = 0.0698$	$R1 = 0.0410$ $wR2 = 0.1026$
Final R indices (all data) ^{a,b}	$R1 = 0.0282$ $wR2 = 0.0698$	$R1 = 0.0410$ $wR2 = 0.1026$
Weighting scheme ^c	$m = 0$ $n = 3.3702$	$m = 0.0502$ $n = 5.8506$
Largest diff. peak and hole	1.136 and -1.669 \AA^{-3}	3.491 and -1.349 \AA^{-3}

$${}^a R1 = \sum \frac{\|F_o| - |F_c|\|}{\sum |F_o|}; \quad {}^b wR2 = \sqrt{\frac{\sum [w(F_o^2 - F_c^2)^2]}{\sum [w(F_o^2)^2]}}$$

$${}^c w = 1 / \left[\sigma^2(F_o^2) + (mP)^2 + nP \right] \text{ where } P = (F_o^2 + 2F_c^2) / 3$$

Where F_o and F_c are observed and calculated Fourier structure factors

Table 4.2 - Fractional atomic coordinates and equivalent U_{eq} (\AA^2) for PZT60 and PZT65 compounds.^a

Atom	x	y	z	U_{eq}
PZT60				
Pb(1)	0.0062	0.0062	0.0062	0.018
Ti(1)	-0.5222	-0.5222	-0.5222	0.011
Zr(1)	-0.5222	-0.5222	-0.5222	0.011
O(1)	-0.5540	-1.0420	-0.5540	0.021
PZT65				
Pb(1)	-0.3719	-0.3719	-0.3719	0.015
Ti(1)	1.1370	1.1370	1.1370	0.031
Zr(1)	1.1370	1.1370	1.1370	0.031
O(1)	1.1110	1.6230	1.2410	0.049

^a U_{eq} is defined as one third of the trace of the orthogonalized U_{ij} tensor

Information on the crystallographic data collection and structure refinement details for the two structures is summarized in Table 4.1. Fractional atomic coordinates and U_{eq} isotropic displacement parameters for the two structures are provided in Table 4.2. Further crystallographic information may be obtained in the deposit from Fachinformationszentrum Karlsruhe, 76344, Eggenstein-Leopoldshafen, Germany (e-mail: crysdata@fiz-karlsruhe.de), quoting the depository numbers CSD-417960 and 417961 for PZT60 and PZT65, respectively.

Table 4.1 shows the unit cell volume of both crystals. The unit cell volume of the PZT65 is larger than that of PZT60 which is expected because the increase of the Zr amount increases the unit cell volume. This implies different chemical compositions, which was confirmed by EPMA but not by EDS (Table 4.3). The chemical composition was determined using EPMA and EDS techniques, five small regions were arbitrarily selected and the concentration of each element was determined. The statistical average and the standard deviation are reported, in Table 4.3.

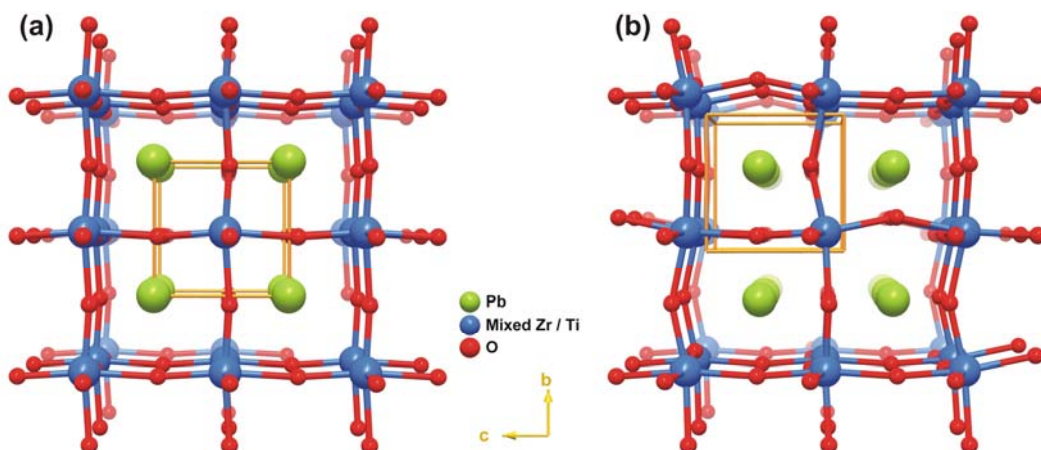


Figure 4.7 - Schematic representation of the crystal of (a) PZT60 and of (b) PZT65 viewed in the perspective along the $[100]$ crystallographic direction. In the PZT65 structure, only one crystallographic position of the disordered oxygen atom is shown for clarity.

Using the volumes of the unit cells, it is possible to obtain the values of the chemical composition (x). Frantti *et al.* [125, 167, 292] showed a graph of the variation of the volume of the unit cells (V) with the PZT composition and we took that graph and have also incorporated other results of single crystals [78, 250], ceramics [6, 87, 126, 127, 293-

300] and thin films [301, 302] (Figure 4.8). The results can be fitted by a linear expression of the type:

$$V = 72.069 - 0.093 \times [Ti(\%)] \quad (4.1)$$

where [Ti(%)] is the amount of titanium expressed in mol %. We cannot use the values of volume (V) reported in Table 4.1 in the Equation 4.1, because they are measured at 180 K and those reported in Figure 4.8 are measured at room temperature. Therefore, we need to know the unit cell volume of PZT at room temperature. X-ray diffraction carried out on a portion of PZT65 at room temperature revealed that it crystallizes in the rhombohedral phase, the same as the one obtained at 180 K (non-centrosymmetric $R3m$ space group).

The change in volume between 180 K and RT, $\Delta V \approx 0.148 \text{ \AA}^3$, is lower than the error for the determination of the chemical composition using the linear dependence of Figure 4.8. For this reason, it was used the volume determined at 180 K to assess the chemical composition of the crystals. Using the unit cell volumes at 180 K (Table 4.1) and inserting them in Equation 4.1, the conclusion is that $x \approx 0.62$ for PZT60 and $x \approx 0.67$ for PZT65. These values are in good agreement with those determined by EPMA, particularly in view of all the approximations used to derive them. These last two values are given in Table 4.3 under the designation of “XRD”.

Table 4.3 - Chemical composition values (x) of two PZT crystals determined by different methods: electron dispersive spectroscopy (EDS), electron probe micro-analysis (EPMA), “Tc” obtained from the variation of the Curie point T_c with the composition, and by X-ray diffraction technique (XRD). The last row shows the sensitivity of the methods (S), indicated by the difference of zirconium concentration (x) between the two crystals.

Crystal	EDS	EPMA	XRD	T_c
PZT60	0.64 ± 0.04	0.60 ± 0.03	0.62 ± 0.02	0.62 ± 0.04
PZT65	0.64 ± 0.04	0.65 ± 0.03	0.67 ± 0.02	0.62 ± 0.04
S	0	0.05	0.05	0

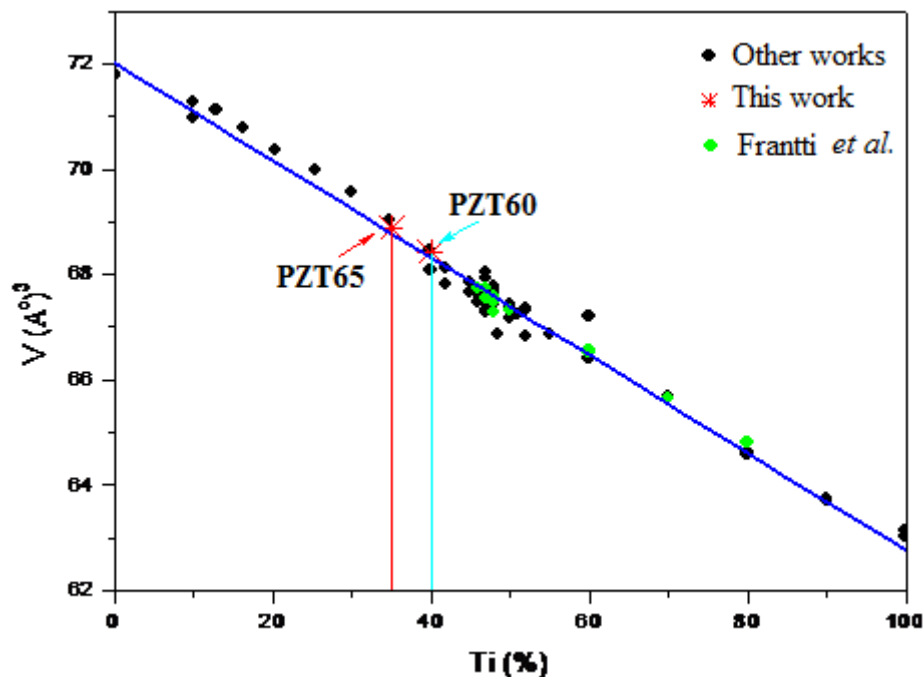


Figure 4.8 - Titanium content dependence of the unit cell volume of PZT solid solutions at room temperature. The original dependence was reported by Frantti *et al.* [125, 167, 292] and the results of other works have been added [6, 78, 87, 126, 127, 250, 293-300]. The volumes of the PZT60 and PZT65 single crystals are also given (XRD results, see Table 4.1).

An usual way to check the chemical composition of PZT materials is by analyzing the paraelectric–ferroelectric transition temperature, obtained from the variation of the permittivity with temperature in the PZ-PT phase diagram. Figure 4.9 shows the temperature dependence of the dielectric permittivity of both crystals, measured at different frequencies. The insert in Figure 4.9a shows the frequency dependence of the permittivity near and during the transition temperature. The analysis is more complicated because the transition temperature, T_c , changes with the frequency. In the frequency range of 100 Hz to 1MHz, the variation of T_c for the PZT60 single crystal is ΔT_c (PZT60) ≈ 9 °C and for PZT65 is ΔT_c (PZT65) ≈ 3 °C. Using the average value of T_c for each crystal, it is possible to estimate the chemical composition. Figure 4.10 shows that the chemical compositions obtained using this method are the same for both crystals due to the large experimental error associated with this procedure (Table 4.3).

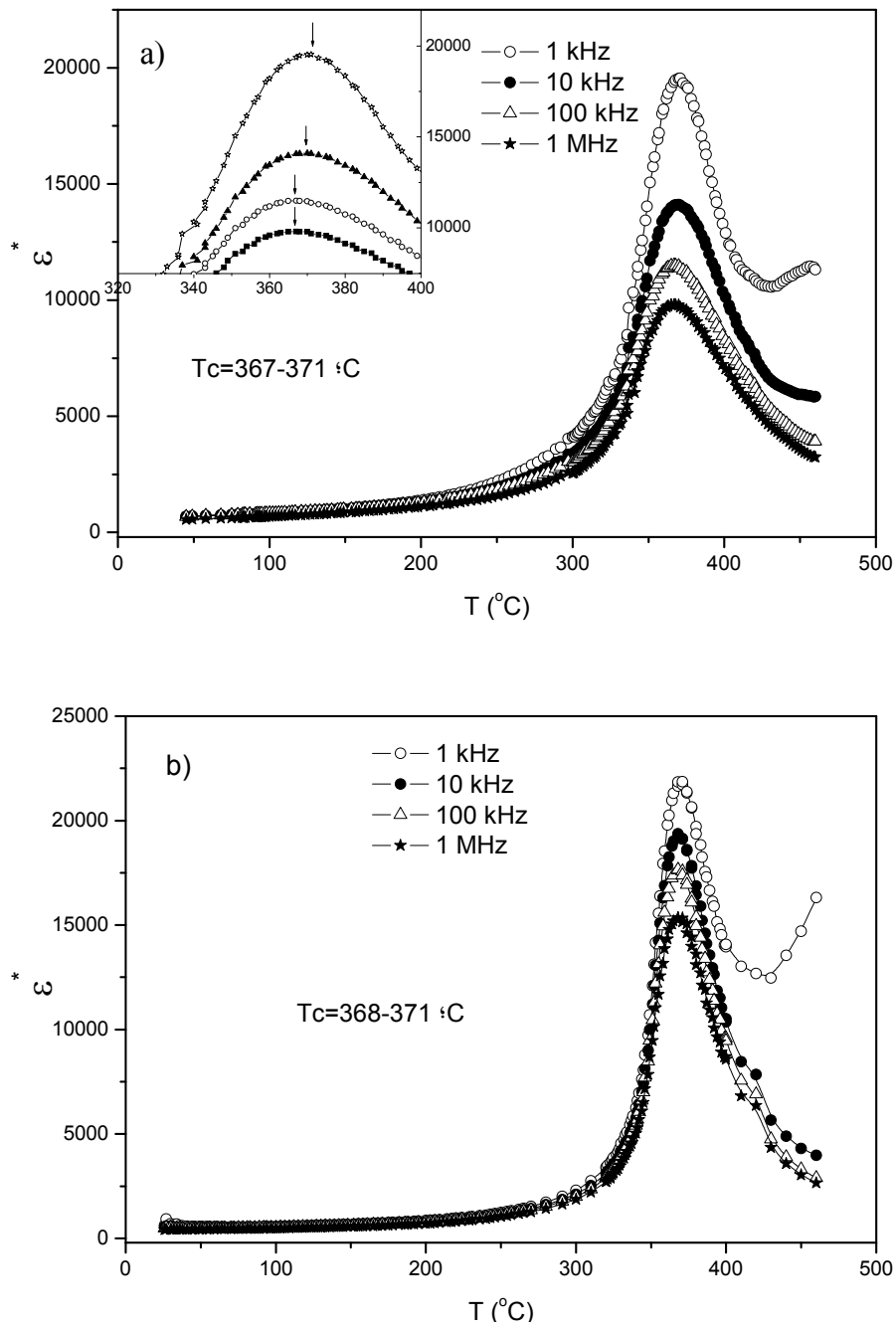


Figure 4.9 - Temperature dependence of the dielectric permittivity of a) PZT60 and b) PZT65 at different frequencies. The inserts show the frequency dependence of the dielectric permittivity peak in a).

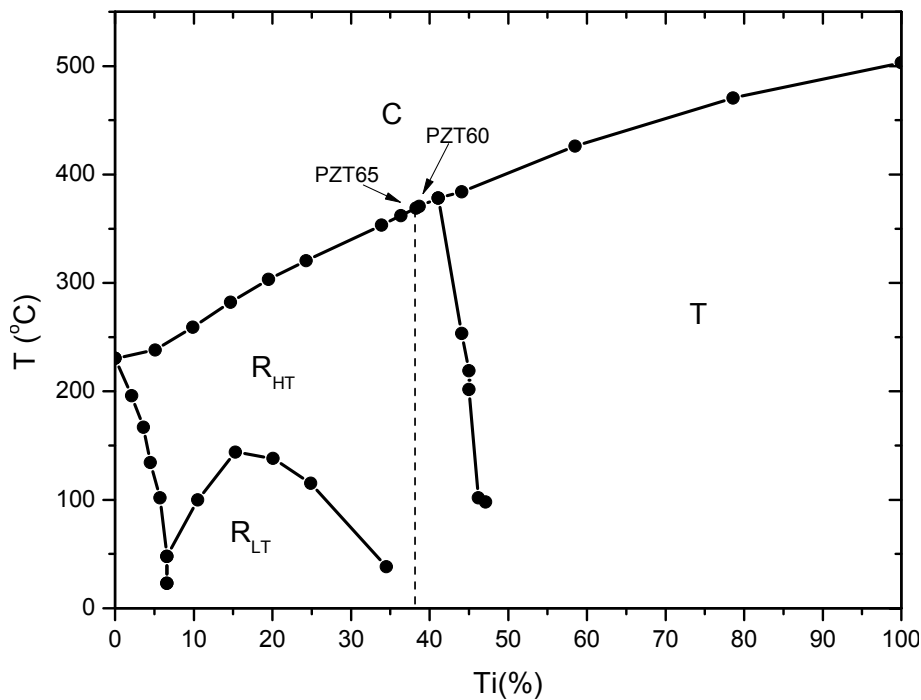


Figure 4.10 - The PZ-PT phase diagram [30]. C indicates a cubic phase, T, a tetragonal phase, R_{HT} a high temperature rhombohedral phase and R_{LT} a low temperature rhombohedral phase. The vertical line represents the compositional position of the crystals using the transition temperature (T_c).

Another problem coming up when the permittivity curves are used is the presence of thermal hysteresis (Figure 4.11), i.e., the permittivity curve on cooling is not coincident with that on heating, near and during the phase transition. Since hysteresis could be caused by a non-equilibrium measuring process, we heated the PZT65 crystal to a pre-defined temperature and held it there for 20 min before measuring the permittivity. The chosen temperatures (below and above the transition temperature) were far from the transition temperature, but still in the range of the observed hysteresis, in order to avoid resonance problems from the transition itself. The same procedure was followed during the cooling. In Figure 4.11(b) the full circles and the stars correspond to these measurements. It can be seen that they match the curves obtained during the heating and cooling runs. Therefore, this process was not repeated for PZT60. Once again, we stress how difficult can be the analysis of the permittivity versus temperature curves with the purpose of finding the chemical composition of the single crystals.

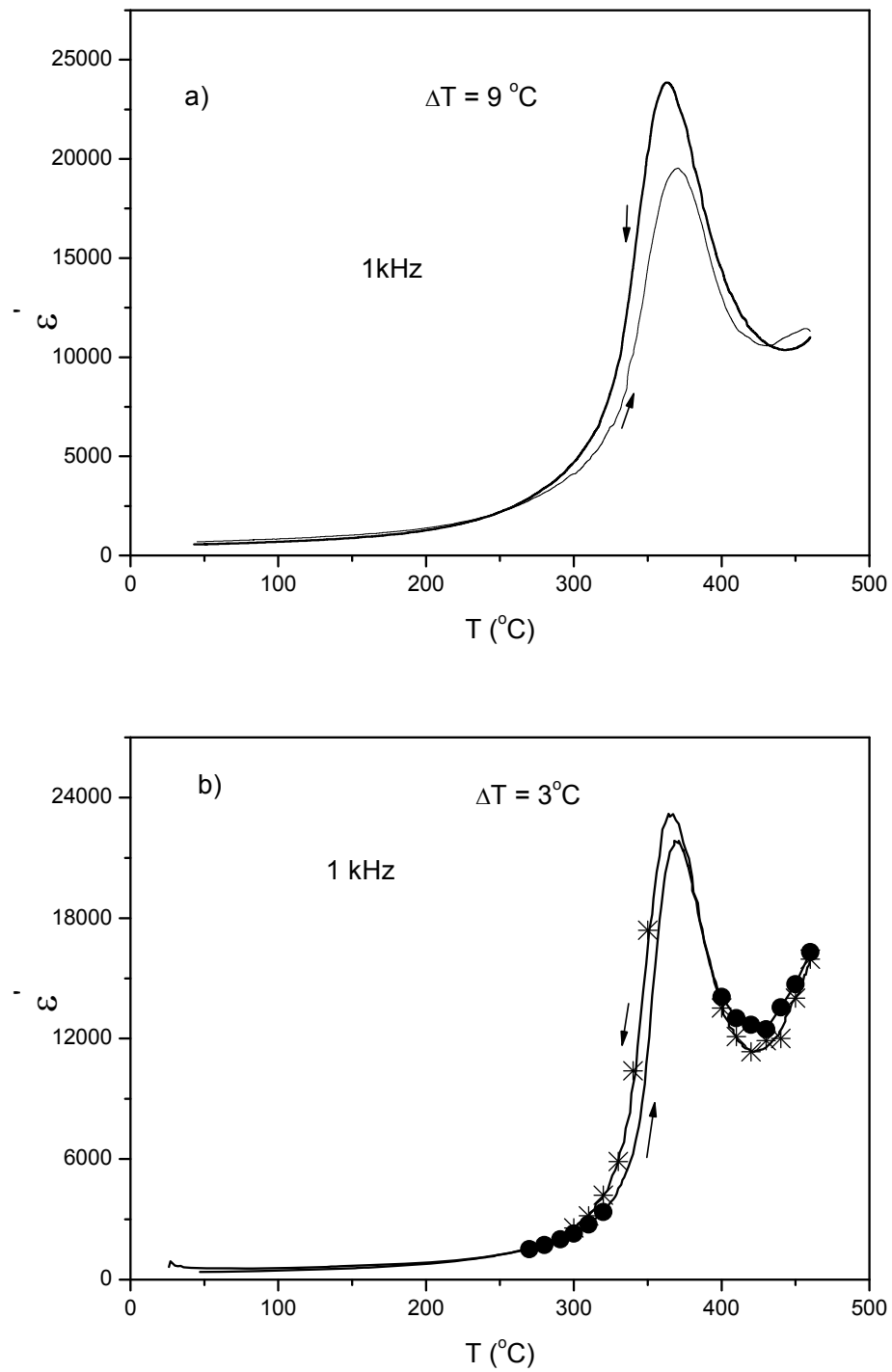


Figure 4.11 - Dependence of the dielectric permittivity with the temperature during the heating and the cooling at 1 kHz for a) PZT60 and b) PZT65 single crystals. The dielectric values take after 20 minutes of stabilization at this temperature is represent by full circles (heating) and stars (cooling).

Although the thermal hysteresis of PZT65 slightly affects the temperature shift, $\Delta T \approx 3^\circ\text{C}$, the effect is stronger for PZT60, with $\Delta T \approx 9^\circ\text{C}$. This could be due to chemical impurities in the crystals (introduced during the grown process), defects, oxygen vacancies, or to relaxation processes among other effects. Figure 4.12 shows the dielectric losses for both crystals as a function of temperature. It is noted that they are larger than in the case of ceramic samples [303]. The dielectric losses are higher for PZT60 than for the PZT65. This is in good correspondence with the temperature shift, ΔT , and with the colour of the crystals. As mentioned above, the PZT60 crystal is black, which is probably an indication of the presence of impurities, cracks, or other defects, while PZT65 is transparent.

In Figure 4.12(b), a small peak is observed in the lower temperature range ($\sim 27^\circ\text{C}$) and a peak in the permittivity curve is also seen in this temperature range. Due to experimental difficulties, we were unable to measure the dielectric characteristics at lower temperatures to obtain a better view of this peak. Nevertheless, its appearance, only in PZT65, might be an indication of another phase transition. In the PZ-PT diagram (Figure 4.10), there is a phase field below the paraelectric-ferroelectric phase transition on the rhombohedral side. This field is related to a transition from a high temperature rhombohedral phase to a low temperature rhombohedral one [189]. In literature, the high temperature rhombohedral phase shows a $R3m$ space group, while the low temperature rhombohedral phase shows a $R3c$ space group [30, 191]. However, the XRD analysis performed at 180 K and 285 K clearly showed the presence of the $R3m$ space group in both crystals. Therefore, it seems that the peaks in the permittivity and dielectric losses do not correspond to a phase transition.

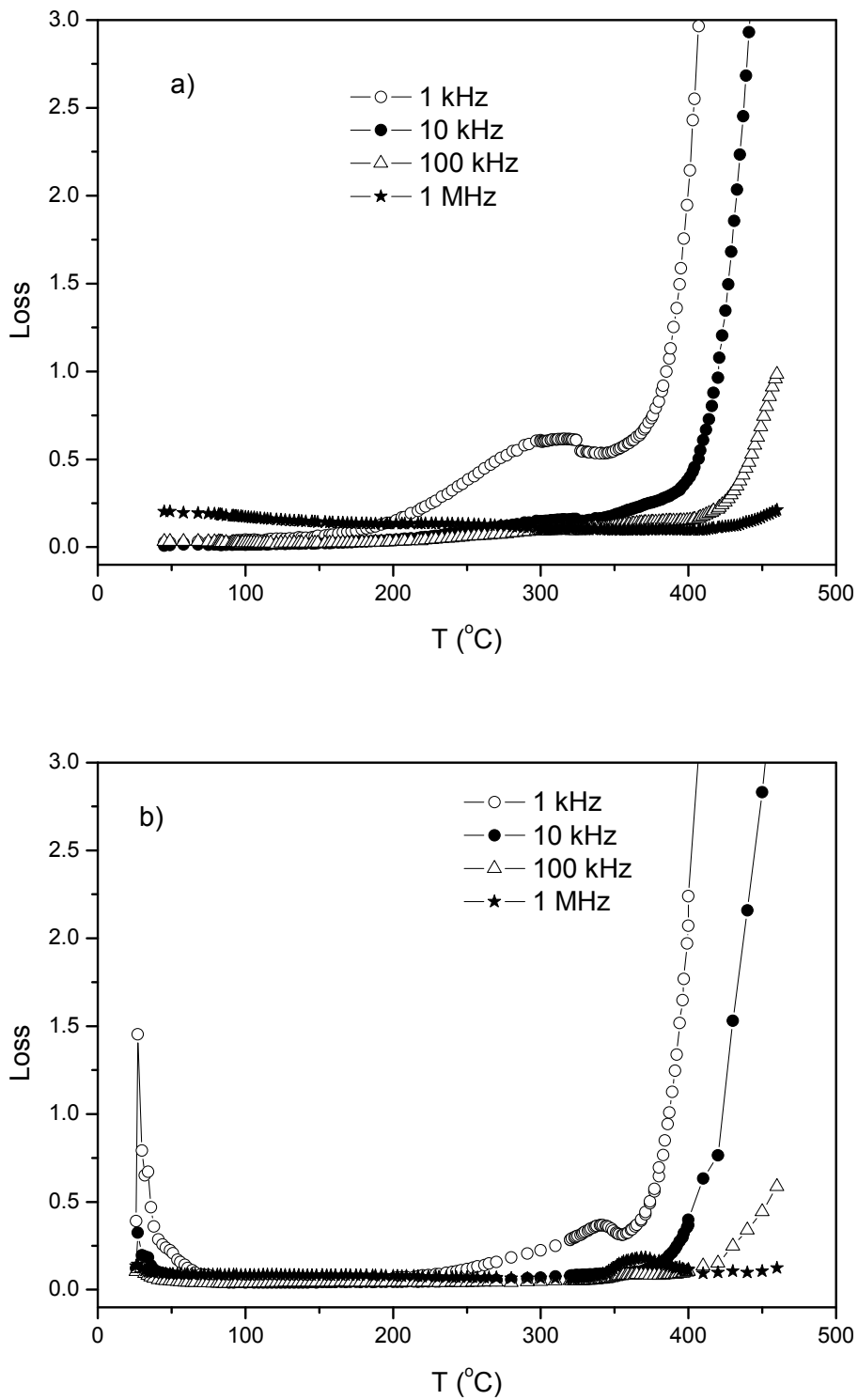


Figure 4.12 - Temperature dependence of the dielectric losses (heating ramp) of a) PZT60 and b) PZT65.

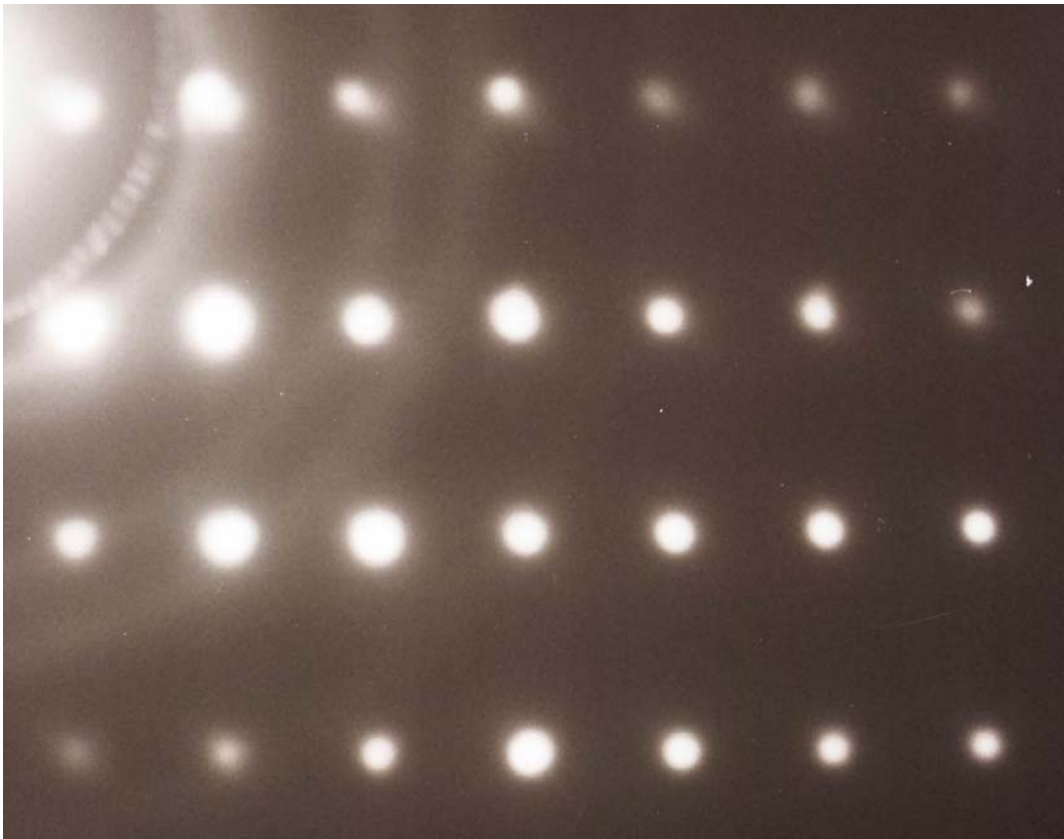


Figure 4.13 - Electron diffraction pattern at room temperature of the PZT65 crystal observed in the $\langle 110 \rangle$ direction

Electron diffraction was carried out at room temperature in the crystal with the low temperature peak (PZT65), as shown in Figure 4.13, and in 6 determinations it is not detected planes of the R3c spacial group. At this moment, we have no suitable explanation for the appearance of these peaks at low temperature (~ 27 °C). On the other hand, it was found in PZT single crystals with $x \leq 0.64$ that the R3c phase is not present at room temperature [90]. Based on that, we can conclude that the low temperature rhombohedral phase is not present at $x \approx 0.65 \pm 0.03$. Using this information, it is possible to give a new phase diagram for the PZT system (Figure 4.14). Other phase diagrams, from high temperature down to 0 K, are proposed by other authors [304-306], but these phase diagrams are not observed in PZT single crystals.

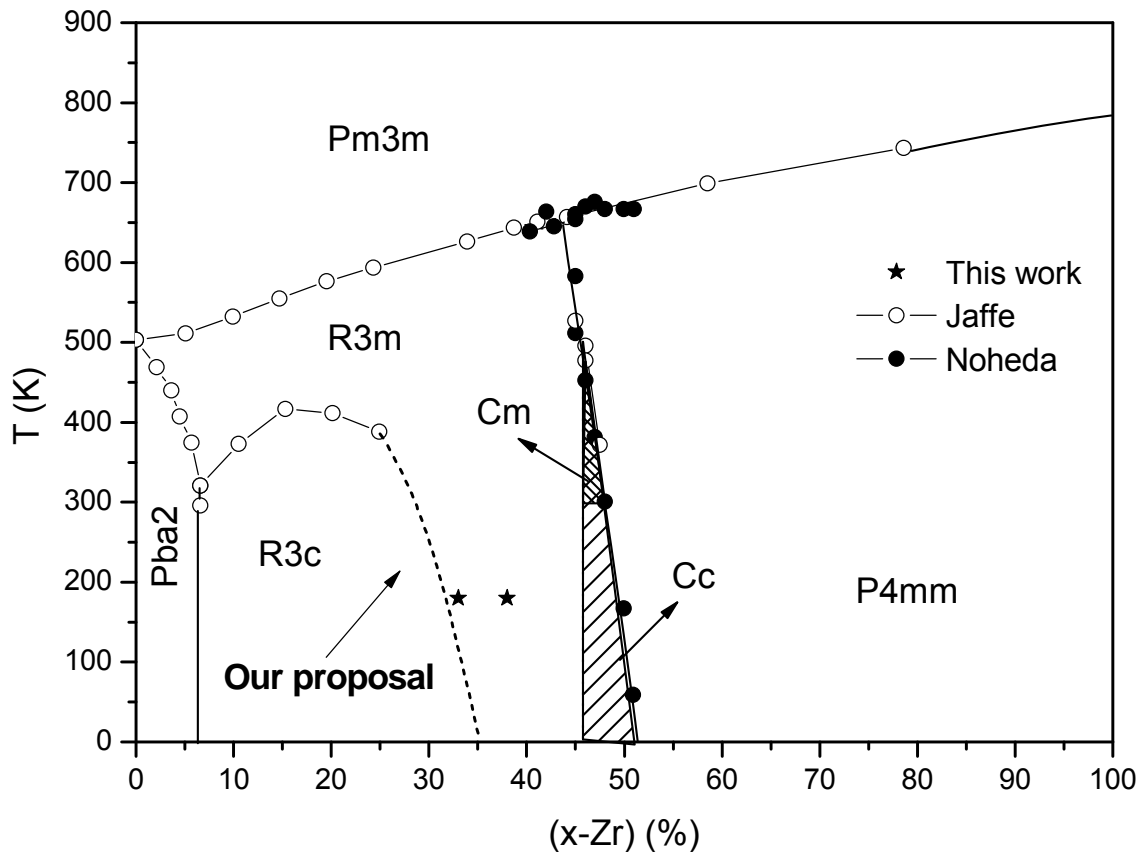


Figure 4.14 - Phase diagram of the $\text{PbZr}_x\text{Ti}_{1-x}\text{O}_3$ system extend down to 0 K. The black stars represent the PZT single crystals prepared in this work and measured at 180 K.

4.2.2. *Tetragonal single crystals*

In this region we used two single-crystals, both with yellowish dark colour and cubic shapes (2x2x2 mm) and (1x1x1 mm) before polishing. These crystals will be called PZT46 and PZT42, respectively. After polishing and annealing at 950°C for 20 min, they become transparent with some black spots. Figure 4.15 shows the optical photograph of the PZT46 crystal, broken during the electrical measurement process.

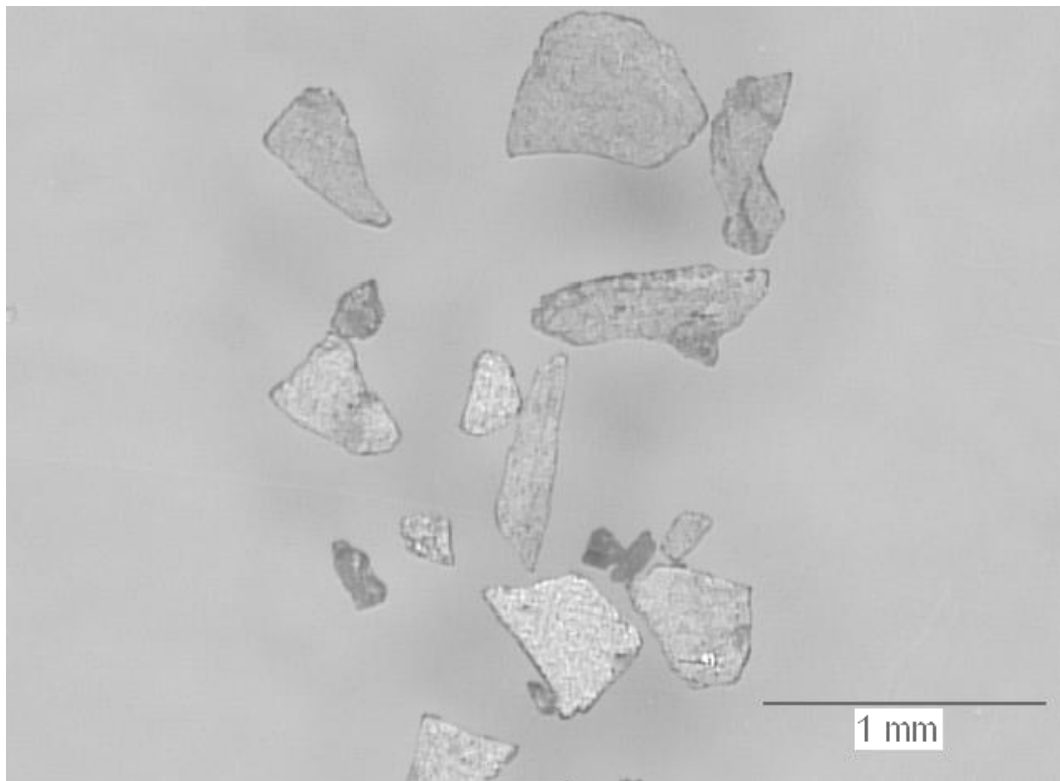


Figure 4.15 - Optical photograph of the PZT46 crystal, broken during the measurement process.

XRD patterns for both crystals show that they belong to the tetragonal lattice with a space group $P4mm$, in agreement with their chemical composition (Table 4.4).

Table 4.4 - Crystal structure and indexed data of PZT46 and PZT42 crystals.

Sample	PZT46	PZT42
Crystal system, Bravais lattice	Tetragonal P	Tetragonal P
a = b	4.0055(5) Å	3.9988(6) Å
c	4.1655(5) Å	4.1500(7) Å
$\alpha = \beta = \gamma$	90°	90°
Volume	66.830(7) Å ³	66.360(3) Å ³
Number of reflections	247	788

The chemical composition obtained by EDS and EPMA are shown in Table 4.5, together with the estimated values from XRD obtained by interpolation of the volume with the chemical composition (Figure 4.16b), as explained in the last section. Checking the ferroelectric-paraelectric transition temperature (T_c), obtained from the variation of the permittivity with temperature (Figure 4.17) (~ 429 °C for the PZT42 and ~ 409 °C for the PZT 46) and using the PZ-PT phase diagram (Figure 4.16a) we could estimate the chemical composition for these crystals. The results of the chemical composition using the last method are shown in Table 4.5 with the designation of T_c . Although it is difficult to determine the chemical composition of single-crystals of PZT by this method [307], the obtained results are in good agreement with those determined by EDS and EPMA.

Table 4.5 - Chemical composition (values for x , the amount of Zr in the PZT) of the crystals determined by the different methods: XRD means that was obtained by X-ray diffraction, EDS by Electron energy dispersive spectrometer, EPMA by Electron probe microanalysis and T_c by the transition temperature.

Crystal	XRD	EDS	EPMA	T_c
PZT46	0.44 ± 0.02	0.46 ± 0.04	0.46 ± 0.03	0.47 ± 0.04
PZT42	0.38 ± 0.02	0.41 ± 0.04	0.42 ± 0.03	0.42 ± 0.04
S	0.05	0.05	0.04	0.05

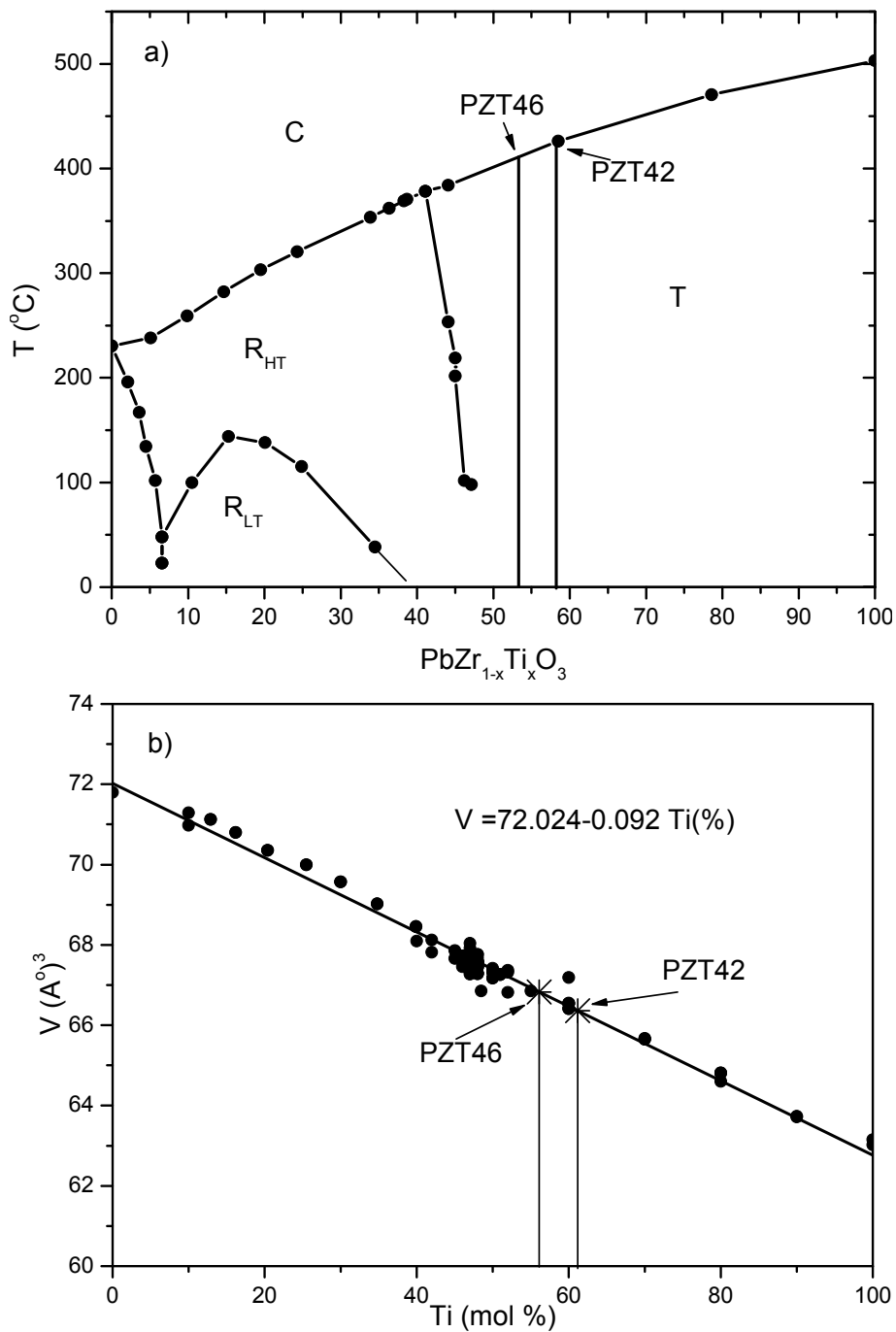


Figure 4.16 – a) The PZ-PT phase diagram [30]. C indicates a cubic phase, T, a tetragonal phase, R_{HT} a high temperature rhombohedral phase and R_{LT} a low temperature rhombohedral phase. b) Variation of the unit cell volume as a function of the Ti (%) in PZT solid solutions at room temperature. The vertical lines represent the compositional position of the crystals using a) the transition temperature (T_c) b) unit cell volume.

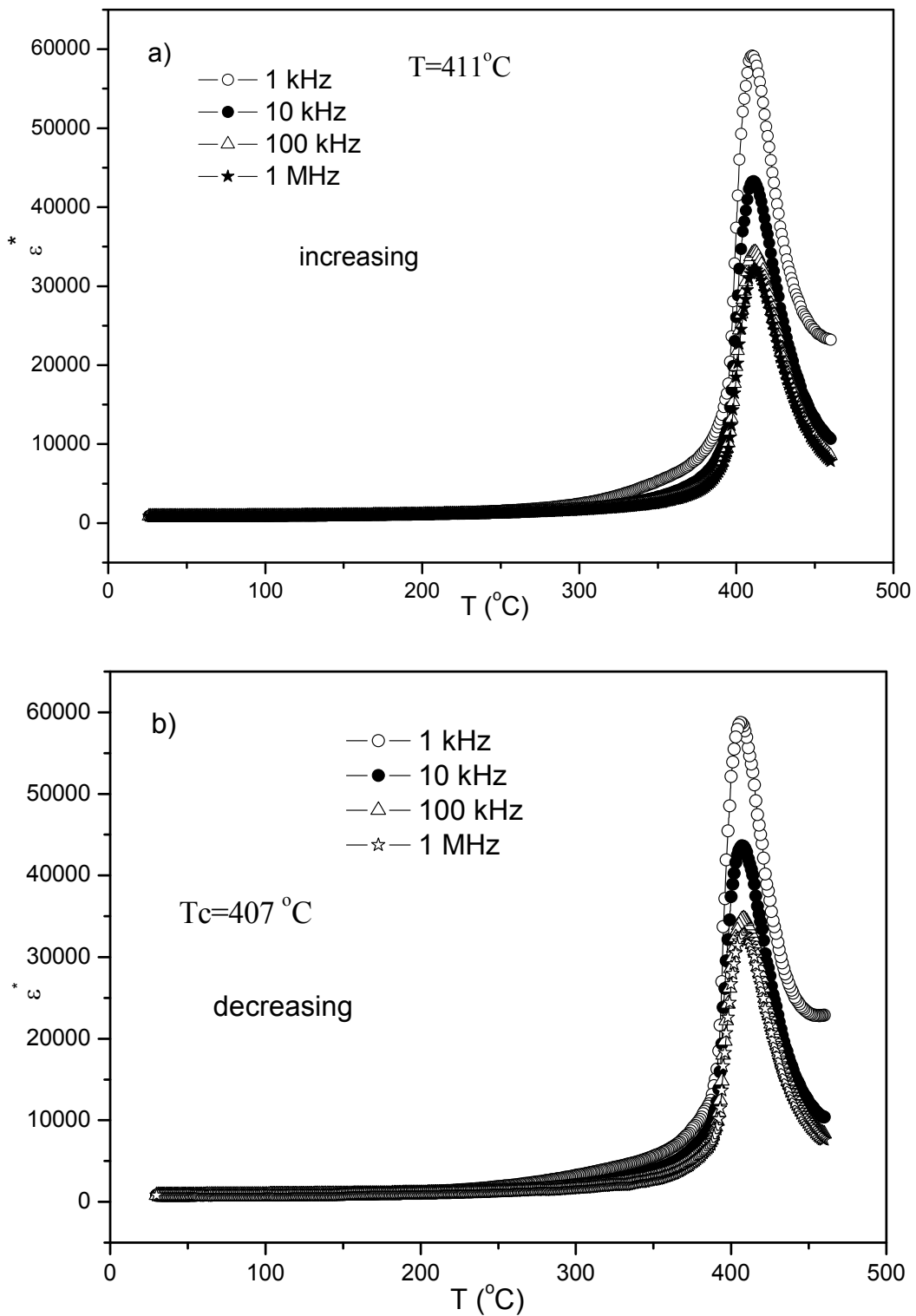


Figure 4.17 - Temperature dependence of the dielectric permittivity of the PZT46 crystal during a) heating ramp and b) cooling ramp.

4.2.3. *Single crystals with chemical compositions near the MPB*

The single crystal used in this subsection was the one designated as PZT52. This crystal had a cubic shape (1x1x1 mm) and was brownish-red in colour. After polishing and annealing at 950°C for 20 min, it became black in colour. Figure 4.18 shows the optical photograph of a portion of the PZT52 crystal, broken during the electrical measurements. Three crystals with the same composition were obtained and the dielectric and crystallographic characteristic of them were similar; because of this, we present the characterisation of only one of them. The properties of this crystal are compared with the rhombohedral and tetragonal ones.

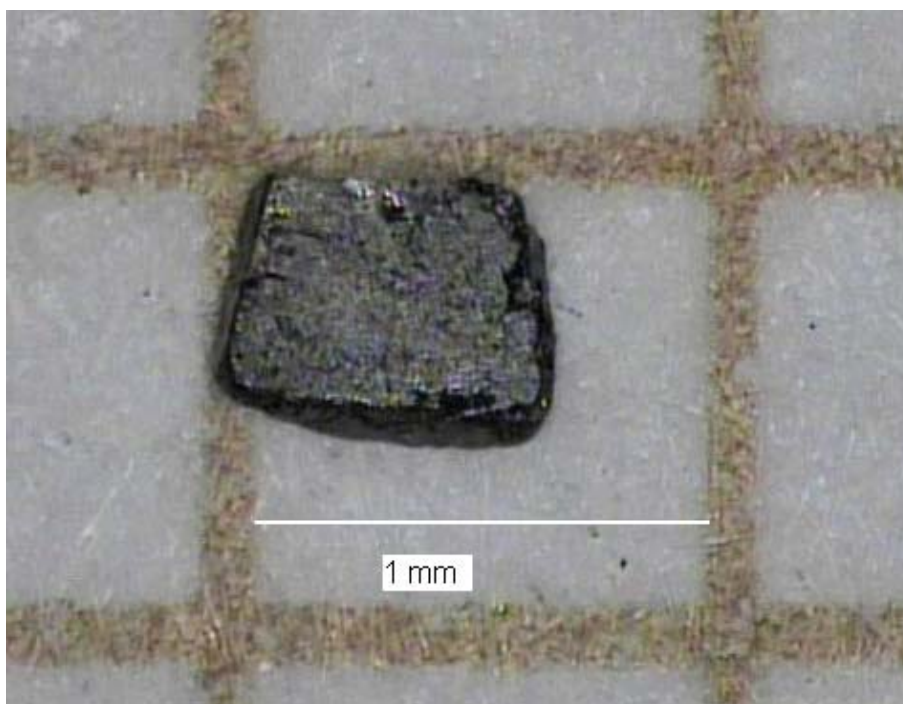


Figure 4.18 - Optical photograph of the PZT52 crystal, broken during the measurements.

Single-crystal X-ray diffraction studies in a small portion of these crystals at 180 K revealed that these materials crystallize in a cubic phase, within the spacial group $P\bar{4}3m$, as shown in Table 4.6 together with the rhombohedral and the tetragonal ones. The cubic structure of this crystal is contradictory with ferroelectric properties. More detail on this structure is given later using Raman spectroscopy. The X-ray diffraction studies at 285 K

do not resolve the structure due the increase of the thermal vibrations and due the proximity of this structure to the cubic one.

Table 4.6 - Crystal and structure of all the single crystals characterized by XRD in this work (cubic, rhombohedral and tetragonal).

Sample	PZT65 (R)	PZT60 (R)	PZT52 (MPB)	PZT46 (T)	PZT42 (T)
Crystal system	(Trigonal) Rhombohedral	(Trigonal) Rhombohedral	Cubic	Tetragonal	Tetragonal
Space group	R 3 m	R 3 m	$P\bar{4}3m$	P4mm	P4mm
a = b (Å)	4.0989(5)	4.0900(5)	4.0814(5)	4.0055(5)	3.9988(6)
c (Å)	4.0989(5)	4.0900(5)	4.0814(5)	4.1655(5)	4.1500(7)
$\alpha = \beta = \gamma$	90.083(17)°	89.845(17)°	90°	90°	90°
Volume (Å ³)	68.87(2)	68.417(14)	67.987(14)	66.830(7)	66.360(3)
Calculated density (Mg/m ³)	7.852	7.903	7.953	8.04	8.06

The chemical composition was determined using the same procedure as in the previous cases, with EPMA and EDS techniques. The values are given in Table 4.7, together with the chemical composition of the crystals with rhombohedral and tetragonal structures. The reported errors correspond to the local difference of chemical composition inside the crystal (see section 4.2.1). Other indirect methods to access the chemical composition (x) are possible, like using the volumes of the unit cells (subsection 4.3.1) [125, 167, 292]. Figure 4.19 shows the variation in volume of the unit cells (V) with the PZT composition and we have also incorporated our results. The results of the chemical compositions, determined using the unit cell volume, are presented in Table 4.7 under the designation of XRD.

Table 4.7 - Chemical compositions of the crystals determined by several methods: XRD means that they were obtained by X-ray diffraction, EDS by Electron energy dispersive spectrometer, EPMA by Electron probe microanalysis and Tc by the transition temperature.

Crystal	XRD	EPMA	EDS	Tc
PZT65 (R)	0.66 ± 0.02	0.65 ± 0.03	0.64 ± 0.04	0.63 ± 0.05
PZT60 (R)	0.61 ± 0.02	0.60 ± 0.03	0.64 ± 0.04	0.63 ± 0.05
PZT52 (MPB)	0.56 ± 0.02	0.52 ± 0.03	0.53 ± 0.04	0.61 ± 0.05
PZT46 (T)	0.44 ± 0.02	0.46 ± 0.03	0.44 ± 0.03	0.47 ± 0.04
PZT42 (T)	0.39 ± 0.02	0.42 ± 0.03	0.38 ± 0.03	0.42 ± 0.04

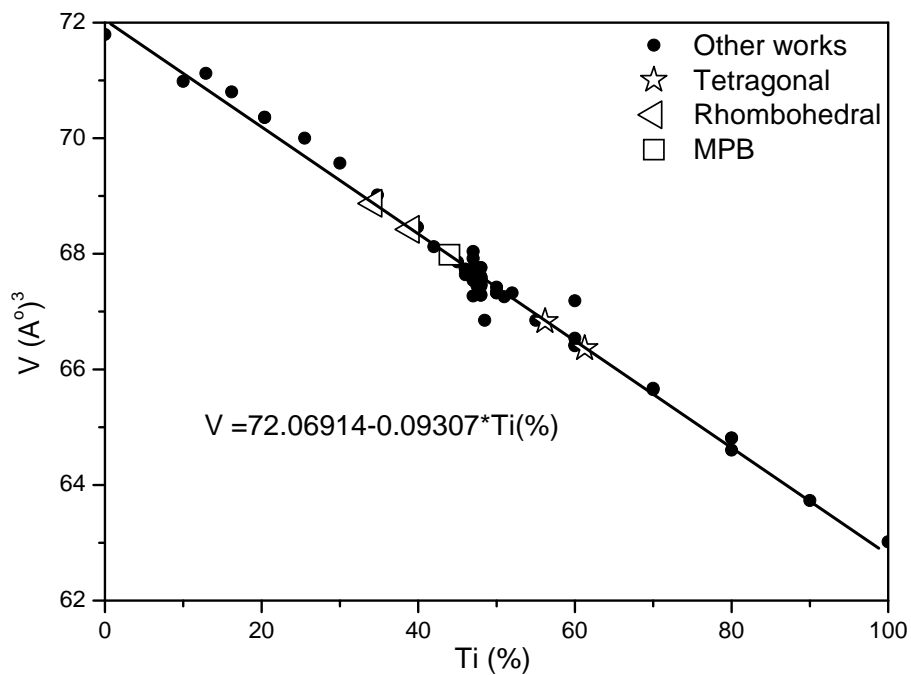


Figure 4.19 - Variation of the unit cell volume (see Table 4.6) as a function of the Ti (%) in the PZT solid solutions at room temperature.

Figure 4.20 shows the dielectric temperature dependence of the PZT52 single crystals, at different frequencies. From this figure it is observed a large permittivity peak and that the

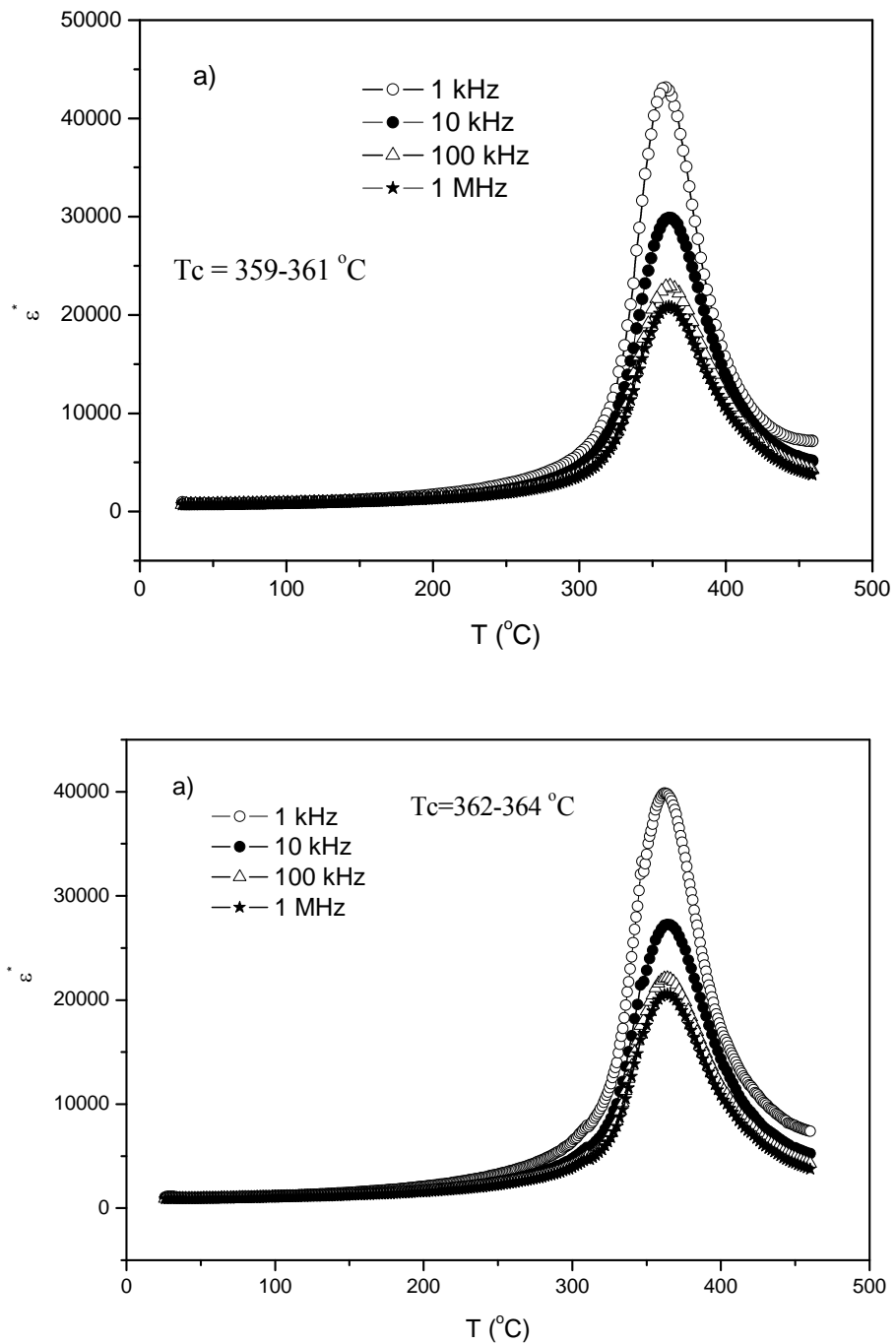


Figure 4.20 - Temperature dependence of the dielectric permittivity of PZT52 single crystal a) heating and b) cooling.

maximum decreases with the increase of the frequency and it stabilizes for high frequency. Figure 4.21 shows the chemical compositions obtained using this method and it is necessary to consider the large experimental error of this procedure (Table 4.7). The chemical compositions obtained using the paraelectric–ferroelectric transition temperatures are given in Table 4.7 under the designation of “ T_c ”.

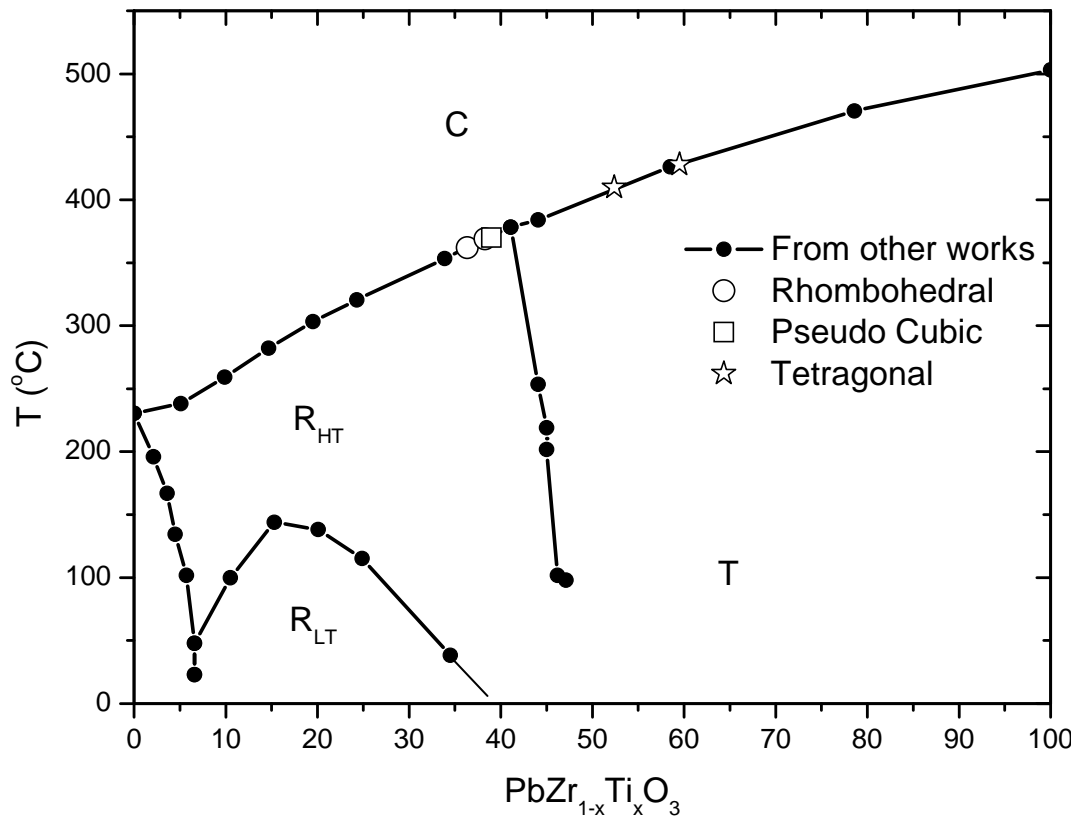


Figure 4.21 – The PZ-PT phase diagram [30] with the indication of the composition of the single crystals. C indicates cubic phase, T tetragonal phase, R_{HT} high temperature rhombohedral phase, and R_{LT} low temperature rhombohedral phase.

The chemical composition for this crystal (PZT52) obtained from these different methods is significantly different from one to another (Table 4.7). Several causes can justify it. Considering that the EPMA technique is a direct and more exact technique to determine the chemical composition among the other ones used in this work, then the low value obtained by T_c can be due to a decrease of the transition temperature. The last supposition is not explicitly reported in the literature but in the Sawaguchi work [94] it was reported a phase diagram obtained from paraelectric–ferroelectric transition temperature and it is

observed an anomaly near the MPB (Figure 4.22a). After, Jaffe *et al.* [30] reported the phase diagram for the PZ-PT system, and this anomaly disappeared from the phase diagrams (Figure 4.22b).

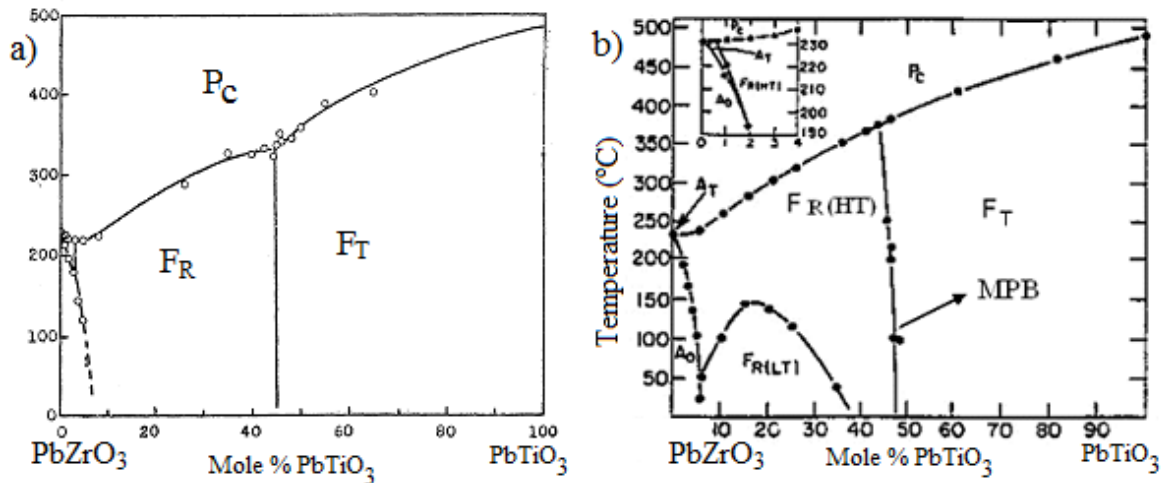


Figure 4.22 - a) PZ-PT phase diagram after Sawaguchi [94] and b) after Jaffe *et al.* [30]. P_c indicates paraelectric cubic phase, F_T ferroelectric tetragonal phase and F_R ferroelectric rhombohedral phase.

Another effect to note is the presence of a small peak in the dielectric losses near room temperature (Figure 4.23). This peak is present both in the increase and decrease of the temperature runs, which means that this is not a transient process due to disorder or instability in the crystal. This peak appears in the dielectric losses of the three crystals with the same composition, $\sim 52\%$ of Zr content. It could be associated with the phase transition from rhombohedral to tetragonal or caused by the presence of an intermediate phase (*e.g.*, mixture of phases or a monoclinic phase). In this work it was not found any mixture of phases or a monoclinic phase in the single crystals. For a better understanding of this peak the Raman Spectrometry was also used to characterize the pseudo cubic crystal.

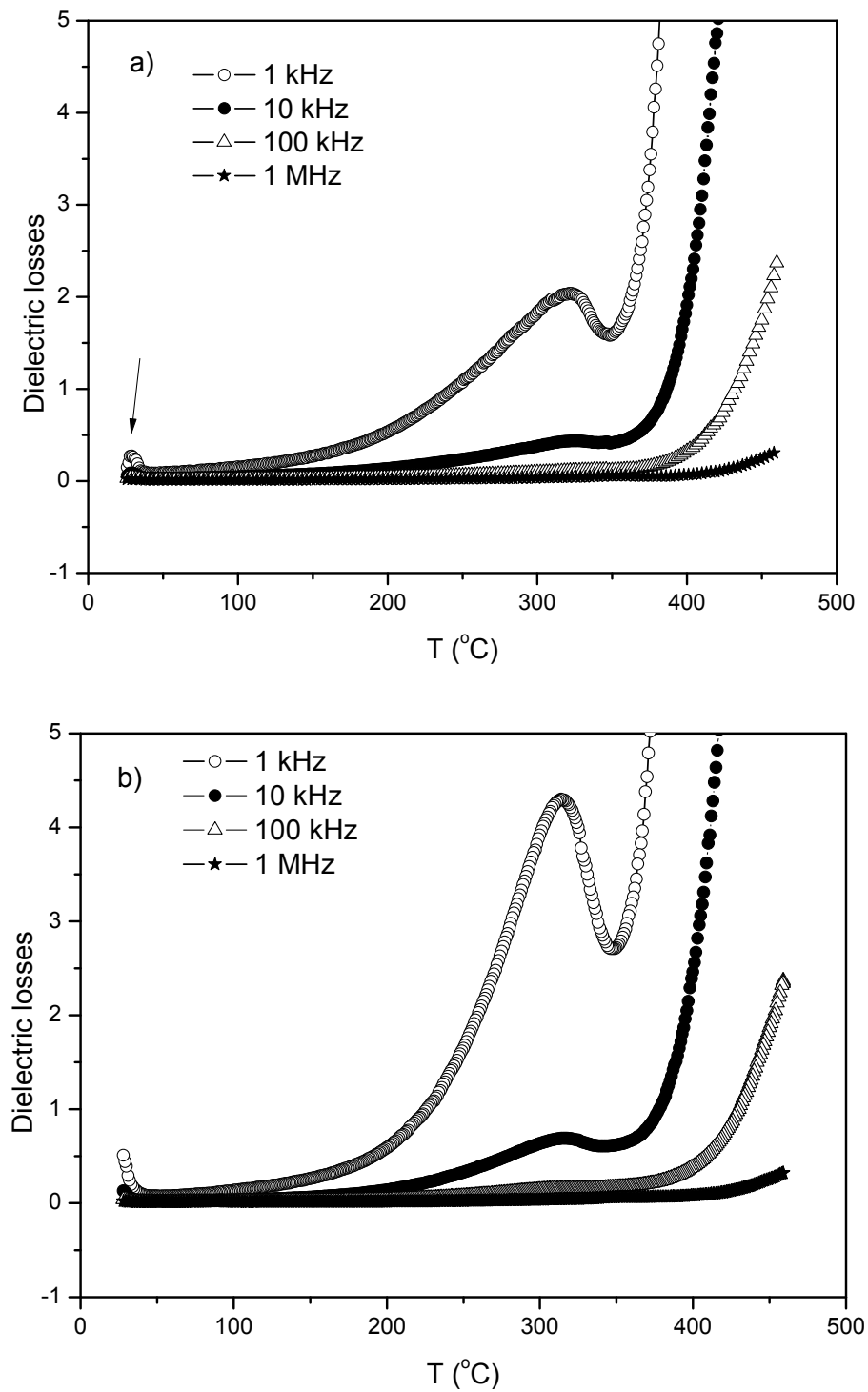


Figure 4.23 - Temperature dependence of the dielectric losses of PZT52 single crystal a) heating ramp and b) cooling ramp.

4.3. Raman study of the PZT52 single crystal

4.3.1. Room temperature analysis

The normal vibrations that can be observed in a Raman spectrum are determined by the crystal symmetry and it can be studied all the scattering geometry by using the polarized scattering experiments. As pictorially represented in Figure 4.24, two backscattering geometries were used in order to obtain the relevant information about the phase transition, $A_1(ZXX)Z$ and $B_2(ZXY)Z$, depending on the polarization configuration, where X and Y represent two orthogonal directions parallel to the experimental stage and perpendicular to the Z direction. A normal backscattering is obtained when the direction of the incident and scattered light is normal to the PZT sample or parallel to the $[001]$ direction (out-of-plane direction), as schematically shown in Figure 4.24. In this scattering geometry, the propagation direction of the relevant phonon ($A_1(\text{LO})$ and $E(\text{TO})$ modes) is along the Z direction which is parallel to the principal $[001]$ polar axis. In our case $X \parallel a$, $Y \parallel b$ and $Z \parallel c$, where a , b and c are the unit cell parameters.

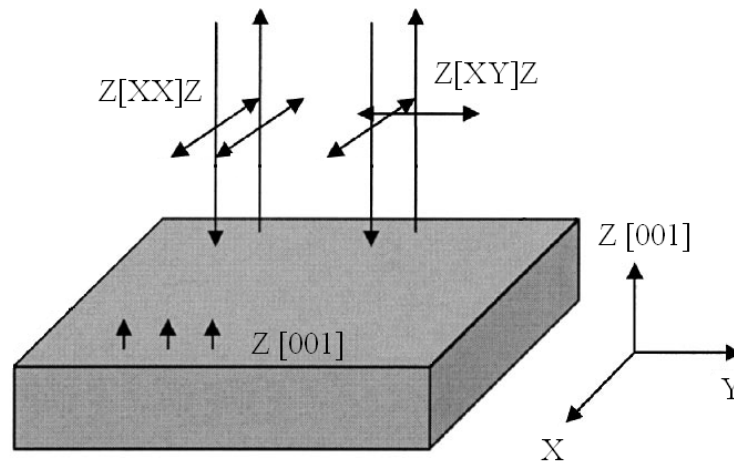


Figure 4.24 - Backscattering geometries used in polarized Raman scattering study of $[001]$ -oriented PZT52 single crystal.

Figure 4.25a) shows the room-temperature polarized spectra of the $[001]$ -oriented PZT 52/48 single crystal, obtained using parallel and cross polarizations ($Z(\text{XX})Z$ and $Z(\text{XY})Z$). The two spectra are quite similar; however, there is a pronounced difference in the scattering intensity. This difference can be attributed to the polarized $Z(\text{XY})Z$

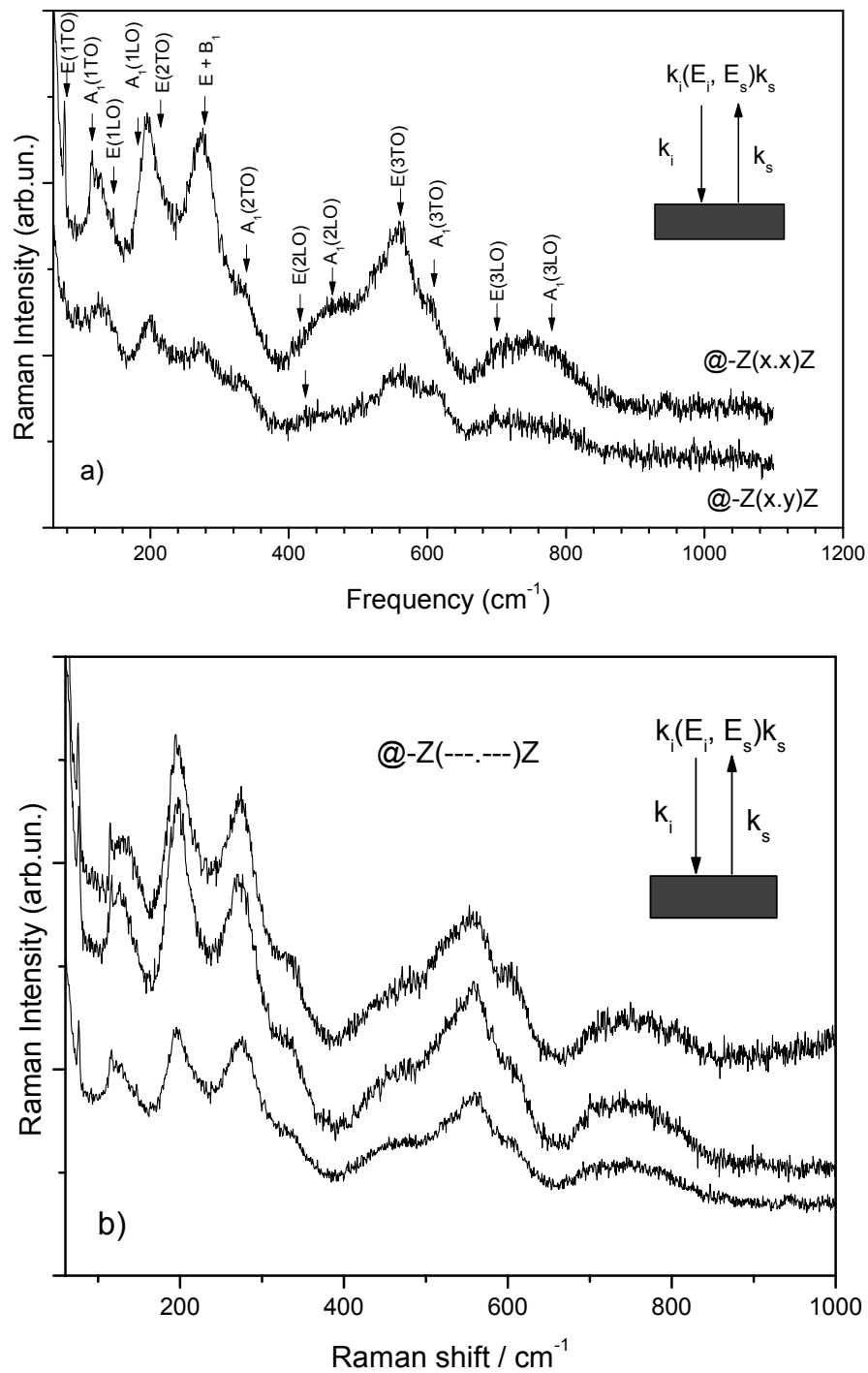


Figure 4.25 - Raman spectra of PZT52 at room temperature: a) measurement at different polarized configurations in the same position of the crystal; b) unpolarized Raman spectra obtained at different positions of the crystal. K_i and K_s are the directions of the wave vector incident and scattering, E_i and E_s are the direction of polarization of the electric field incident and scattering, respectively.

configuration, where several modes have low contribution to the intensity of the spectra. It is necessary to emphasize that all the peaks are present in both polarized configurations, which can be due to a small inclination of the crystal from the [001] direction or to the presence of a deformation in the crystal. Such deformation (distortion) from a perfect crystal could be due to defects (impurities, vacancies, twins) or to the presence of non-180° oriented domains, as will be observed in the AFM studies. When the laser is focused on more than one domain, having a non-180° domain wall, it is found that the polarized Raman spectrum is a mixture of modes. The above mentioned effect can be produced when we are in the presence of small domains, as in ceramics. Considering this feature and taking into account the mode assignment carried out by others [171, 308-310], it is possible to assign the position of the peaks, as shown in Figure 4.25a). The positions of different Raman peaks at room temperature in PZT are also shown in Table 4.8.

The chemical composition may be estimated comparing the Raman spectra shown in Figure 4.25a) with the published work [308, 309]. In Sousa Filho *et al.* work, the $A_1(2TO)$ mode is present for Zr contents lower than 53 molar % [308]. The peak size of the 52% and 50% molar Zr compositions are comparable with our $A_1(2TO)$. On the other hand, the peaks $E(2TO)$ and $E+B_1$ show relative height similar to the obtained by Sousa Filho *et al.* [308], for the 52% and 50 % molar Zr compositions. Based on the last observation, it is possible to estimate the chemical composition of the PZT crystals. It is reported between 50% to 52% molar of the Zr content, in agreement with the obtained by EPMA technique.

The structure obtained by XRD at 180 K is not coincident with the Raman analysis at room temperature, in the sense that the presence of Raman activity means that the structure analysed is not cubic. The presence of the mode $A_1(2TO)$ in our spectra (also detected by others in ceramics and thin films), is a clear signature of the presence of the tetragonal phase [308-310]. Based on the above analysis, we can conclude that the PZT crystal with 52% of Zr content show tetragonal symmetry at room temperature.

In Figure 4.25b) it is shown the room-temperature unpolarized spectra of the [001]-oriented PZT52 single crystal, obtained in different points of the crystal. The spectra are also very similar, which means that the sample is homogeneous in structure and composition. Six points were analyzed in the crystal, but, for simplicity, only three are shown in this figure.

Table 4.8 - Wavenumber (in cm^{-1}) and symmetry of the different Raman peaks in PZT52 measured at room temperature.

	Mode (E)		Mode (A_1)		Mode (E + B_1)
Modes	E(1TO)	E(1LO)	A_1 (1TO)	A_1 (1LO)	E(3TO+2LO)+ B_1
Wavenumber	78	135	120	195	273
Modes	E(2TO)	E(3LO)	A_1 (2TO)	A_1 (2LO)	
Wavenumber	218	427	337	461	
Modes	E(4TO)	E(4LO)	A_1 (3TO)	A_1 (3LO)	
Wavenumber	557	708	608	765	

4.3.2. Variation of the Raman spectra with temperature

The temperature dependence of the Raman spectra was carried out in the PZT52 crystal, in the temperature range of 153 K to 673 K (Figure 4.26). In order to better understand the experimental data reported in Figure 4.26, it was performed a smoothing with a fast Fourier transform (FFT) filter tool, allowing the reduction of the noise significantly. Once the noise is reduced, it is possible to obtain a clear image of all the peaks shown in Figure 4.26. In this experiment it was used a new cooling apparatus, which decreases the sensibility of the measurement. The decrease in the resolution of the spectrum does not allow the use of the A_1 (2TO) mode directly. Alternatively, we used the intensity of the peaks A_1 (1LO)+E(2TO) and E+ B_1 in order to estimate the phase transition. As it will be analyzed later, the A_1 (1LO)+E(2TO) and E+ B_1 + A_1 (2TO) peaks change intensity, being A_1 (1LO)+E(2TO) more intense than E+ B_1 + A_1 (2TO) in the tetragonal phase, while the opposite is observed in the rhombohedral one [308]. This means that the transition temperature from rhombohedral to tetragonal is observed at ~ 183 K (Figure 4.26b). In Figure 4.27 it is plotted the relative intensities of these peaks, obtained by fitting the maxima in the Raman spectra in Figure 4.26b, around 180 K. It can be observed the anomaly at $\sim 183 \pm 5$ K, which confirms the phase transition.

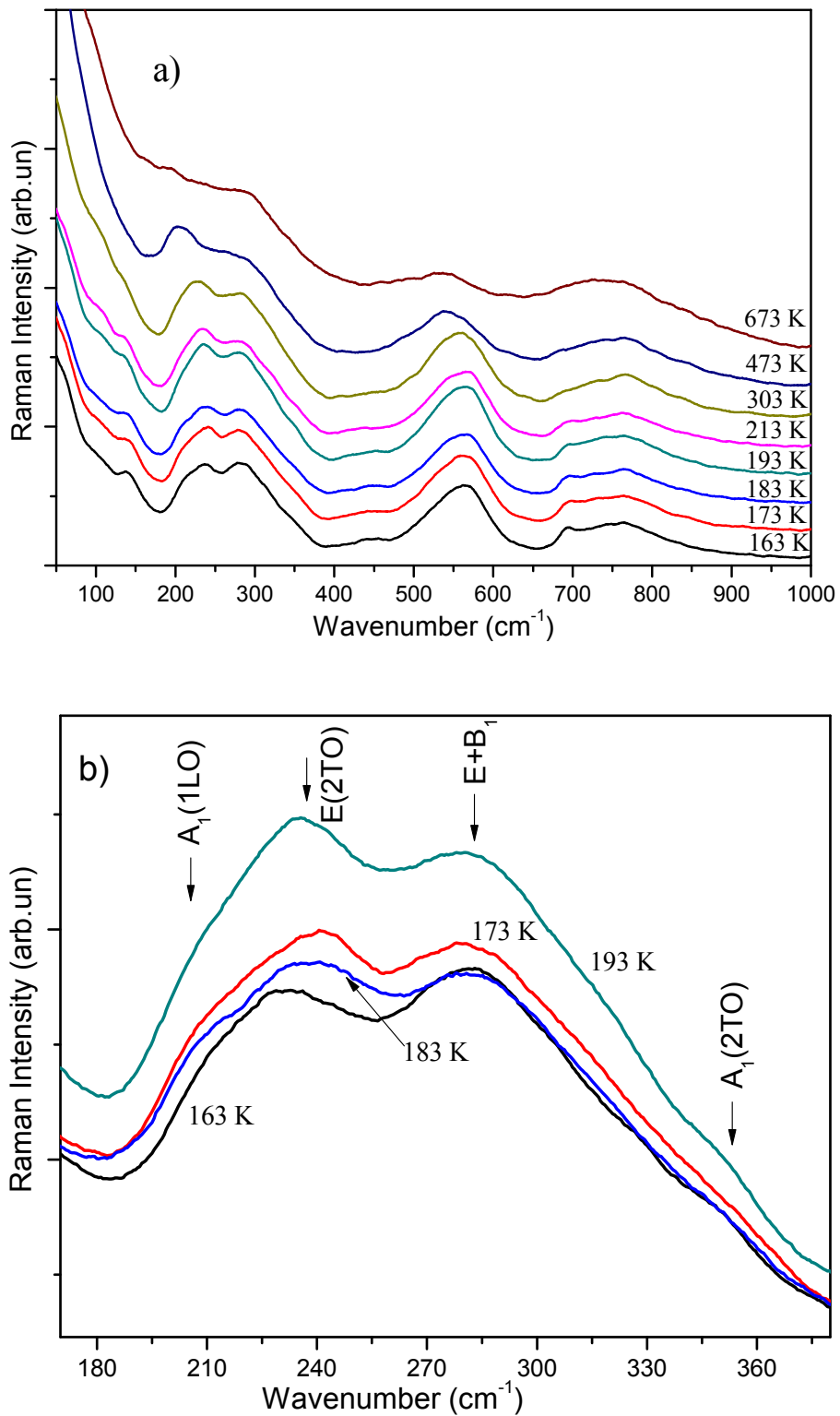


Figure 4.26 - a) Raman spectra for PZT52 for different temperatures and b) Amplification around the transition temperature (180 K).

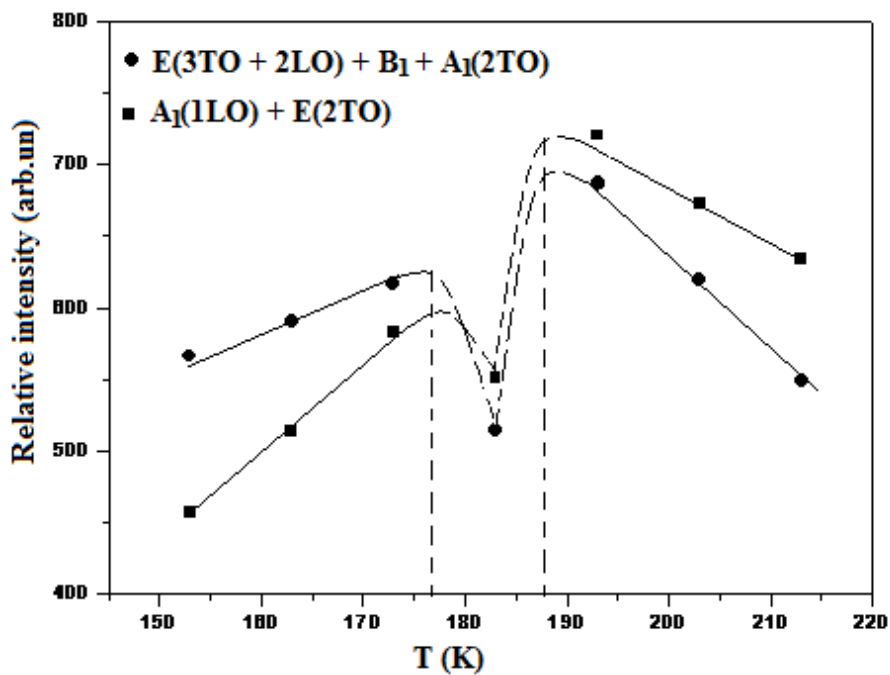


Figure 4.27 - Height of the Raman spectra peaks in Figure 4.26(b).

The XRD at 180 K found that the crystal PZT52 has a cubic structure. As we see now, this temperature coincides approximately with the transition temperature of the tetragonal-rhombohedral phases. It is worth to mention that the tetragonal distortion decreases and the system is closer to a cubic structure at this point. In contrast, the rhombohedral distortion increases when the composition approaches to the MPB or, at least, it remains constant, as reported in ceramics, single crystals and thin films [6, 125, 311]. The rhombohedral distortion must remain constant or decrease as it is found in Soares *et al.* [308], because if the distortion increases, the phase transition has an abrupt change in the microstructure (first order transition) as found by Noheda *et al.* [308]. In fact, the change of the spacial group $R3m$ to the $P4mm$ one is a first order phase transition with an increase in the symmetry and must loose vibrational modes.

The variation of the frequency of the vibration modes with temperature is shown in Figure 4.28. The spectrum for each temperature was fitted using procedures involving available software packages [312]. The intensity values of the phonon modes, for the different temperatures, were obtained using the Igor Pro software packages [312], according to Lorentzian or oscillators functions. The initial approximation for the Raman modes position was the one given by others (Figure 4.26a) [171, 308, 309]. The spectrum

was systematically fitted by the sum of Lorentzian and oscillators functions, obtaining therefore the observed deconvolution of the Raman bands, as shown in Figure 4.29.

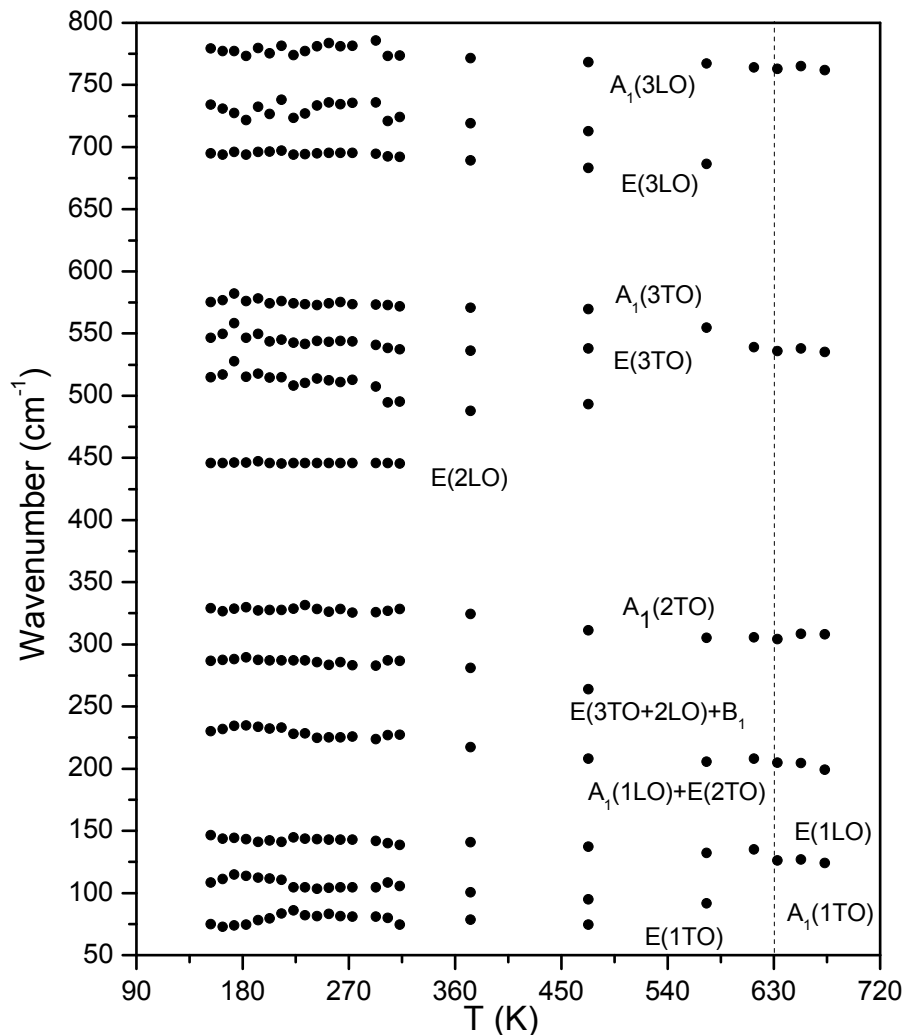


Figure 4.28 - Dependence of the Raman wavenumber with temperature.

In Figure 4.28 it is observed that the vibrational $A_1(2TO)$ mode can be fitted in all the analyzed temperature range. This mode, as previously discussed, does not clearly appear at temperatures below 173 K. Using the spectrum deconvolution, it can be revealed. The last analysis is not in contradiction with the previous conclusion for the determination of the phase transition, because for the phase transition it was used the difference of intensities between the peaks $E(2TO)$ and $E+B_1$ (Figure 4.26b). In fact, the $A_1(2TO)$ mode is only observed in the tetragonal phase.

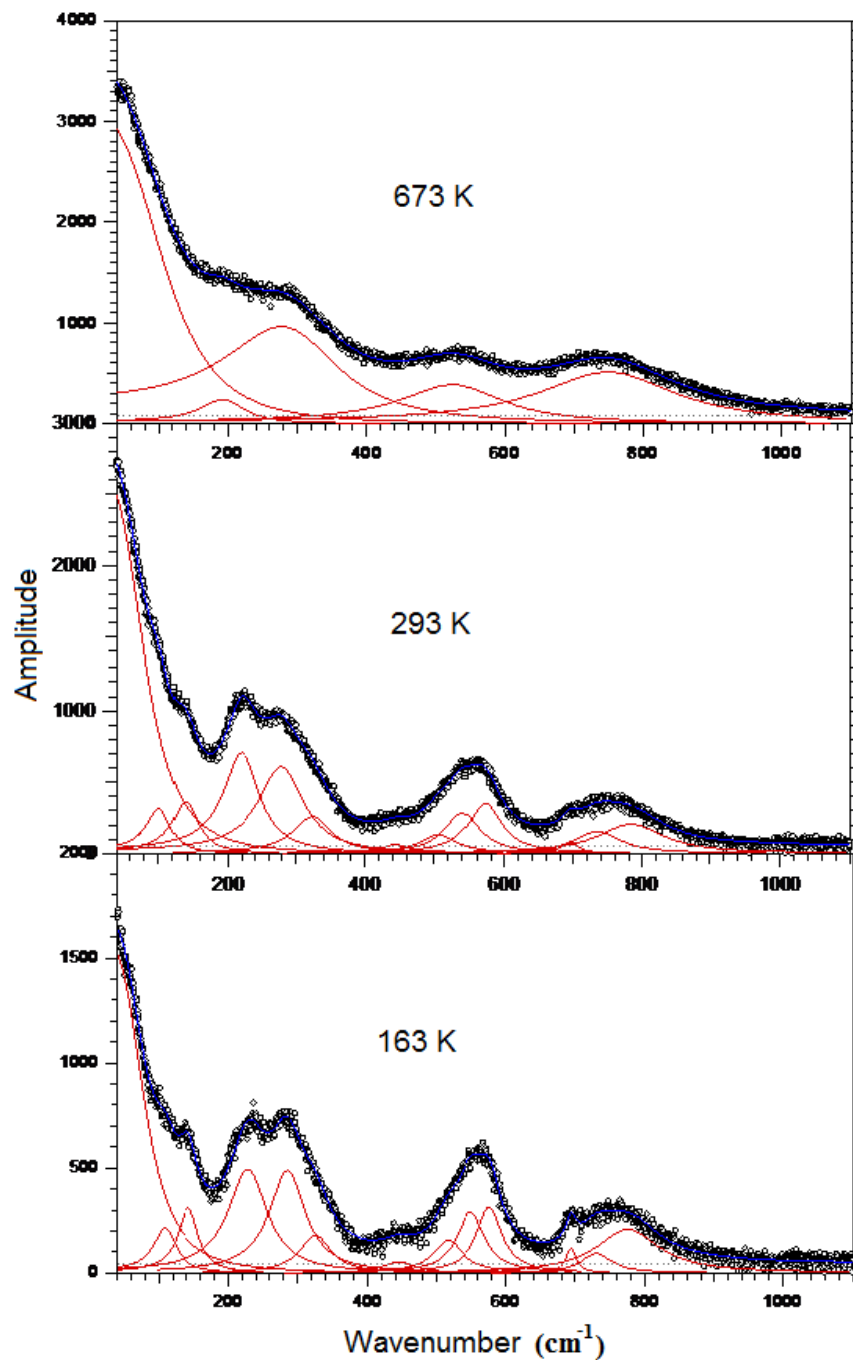


Figure 4.29 - Fitting of the Raman spectra, using a set of oscillators, of PZT52 for different temperatures.

Figure 4.28 shows an anomaly near room temperature in all the vibrational modes and also the suppression of the E(2LO) mode. This is the temperature range where it is found a peak in the dielectric measurements, clearly observed in the dielectric losses curve (Figure 4.23). Probably, the room temperature dielectric losses peak is associated with the anomaly

in the Raman modes and the hidden of the E(2LO) mode (by overlapping with other modes). In section 5.1 it is explained that the inflexion in the dielectric measurement at room temperature are not associate with a phase transition. Using the last result of the Raman spectrum, it is possible to reduce the number of hypothesis used to explain the dielectric losses peak.

In the literature this transition is associated to a disorder in the oxygen octahedral framework, which might decouple the long-range polar order during the cooling process, resulting in fluctuations of the polarization [313]. The decoupling of the long-range polar order affects the interaction among the molecular orbitals, resulting in a variation of the vibration modes [314]. The last comment is a possible hypothesis that could explain the presence of an anomaly in the dielectric and Raman measurements.

The dashed vertical line in Figure 4.28) corresponds to the transition temperature from the ferroelectric to the paraelectric state. At temperatures higher than the transition temperature (T_c), it is found several modes. Theses modes should not appear because in this region the structure is cubic. The observation of vibrational modes in a cubic structure can be explained by the presence of distortions in the crystallographic network, which can be originated by defects (vacancy, interstitials) and impurities (atom donor or acceptor).

In this study it is not observed any vibrational mode corresponding to the monoclinic phase. The monoclinic phase was observed in PZT ceramics or in thin films [6] but not in single crystals. Using this information, it is possible to give a new approximation for the phase diagram reported in Figure 4.14, as shown in Figure 4.30. The proposed phase diagram, down to 0 K, does not show the morphotropic phase region. The black region in the MPB is due to the presence of a crystalline structure near to cubic. The temperature difference inside this region is approximately 10 K as observed in Figure 4.27. The black region is represented in the diagram although we do not know the exact position of the boundaries due to the reduced number of crystals analysed. In Figure 4.31 it is shown the transition region observed by dielectric measurements (1 MHz for PZT52). In this figure, in the temperature range between 170 K and 190 K, it takes place the transition at $\sim 180\text{K}$ shown before. The dielectric measurements at low temperature were not frequently more used because the experimental difficult of this measurement provokes the apparition of high dispersion in the dielectric data (Figure 4.31).

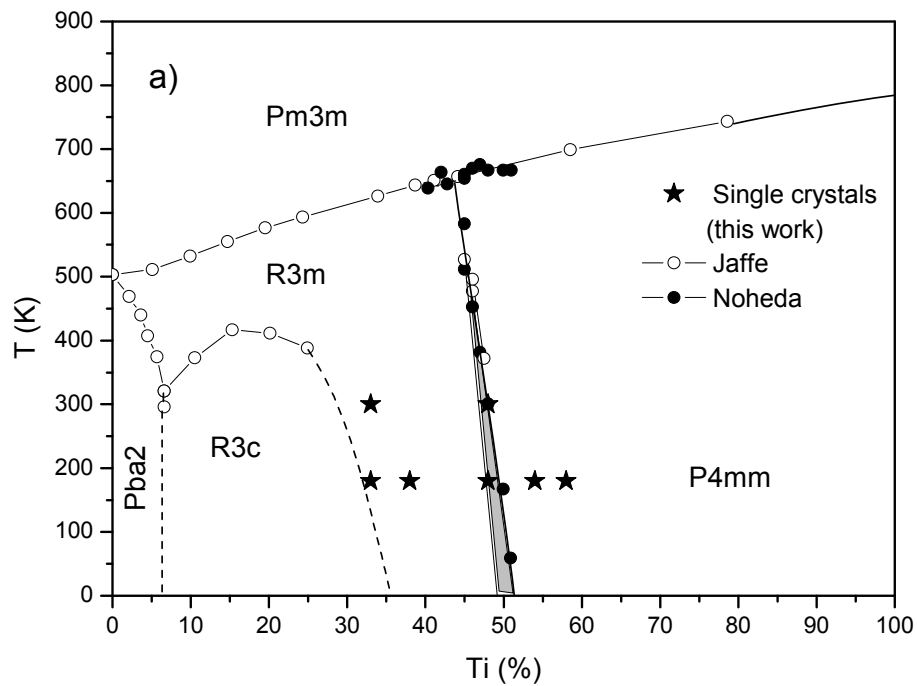


Figure 4.30 - Phase diagram of the $\text{PbZr}_{x-1}\text{Ti}_x\text{O}_3$ system extended to 0 K. The black stars represent the measurement of the PZT single crystals.

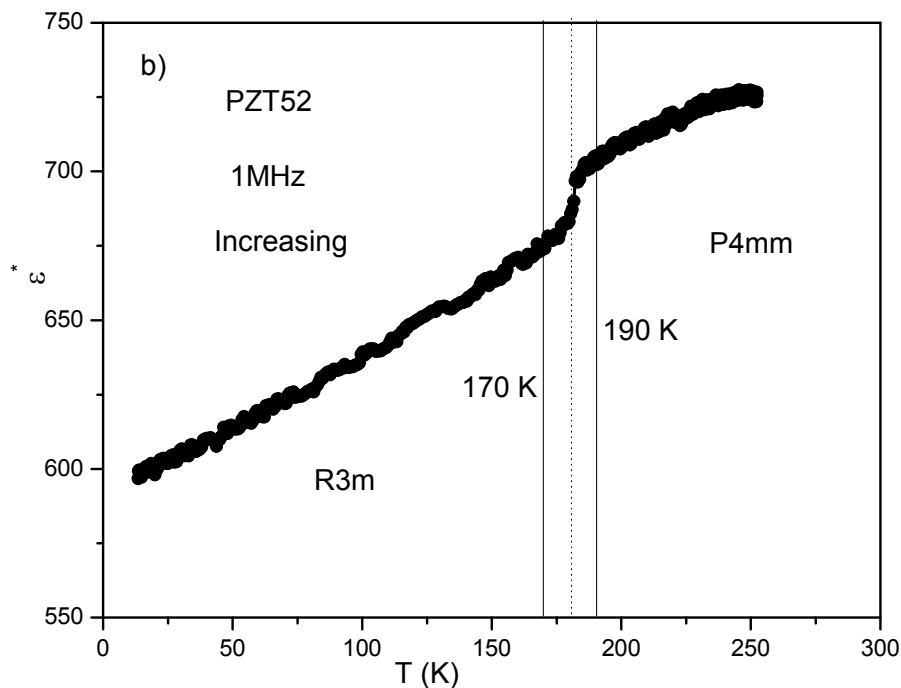


Figure 4.31 - Temperature dependence of the dielectric permittivity for the PZT52. The curve was obtained during heating measurements, taken at 1 MHz. The step observed around 180 K is due to the phase transition between the rhombohedral phases at lower temperature, R3m, and the tetragonal one at higher temperature, P4mm.

4.4. Dielectric, ferroelectric and piezoelectric properties

4.4.1. Dielectric characterisation

A detailed study of the dielectric, ferroelectric and piezoelectric characterisations was performed in PZT single crystals. The temperature dependence of the dielectric permittivity upon cooling and heating at several frequencies (from 100 Hz to 1 MHz) was measured along the [001] direction.

- *Rhombohedral Crystals*

From the point of view of the thermodynamics of the system, it is important to obtain the principal parameters for each phase, which help to characterize the material. The Curie-Weiss constant (C), the parameter (γ), the degree of diffuse transition (δ), the maximum of the permittivity (ϵ_{max}), the Curie temperature (T_c) and the Curie-Weiss temperature (T_0) were determined using Equation 1.7 and are summarized in Table 4.9, for the rhombohedral crystals PZT60, PZT65 and for a $x = 0.60$ ceramic for comparison.

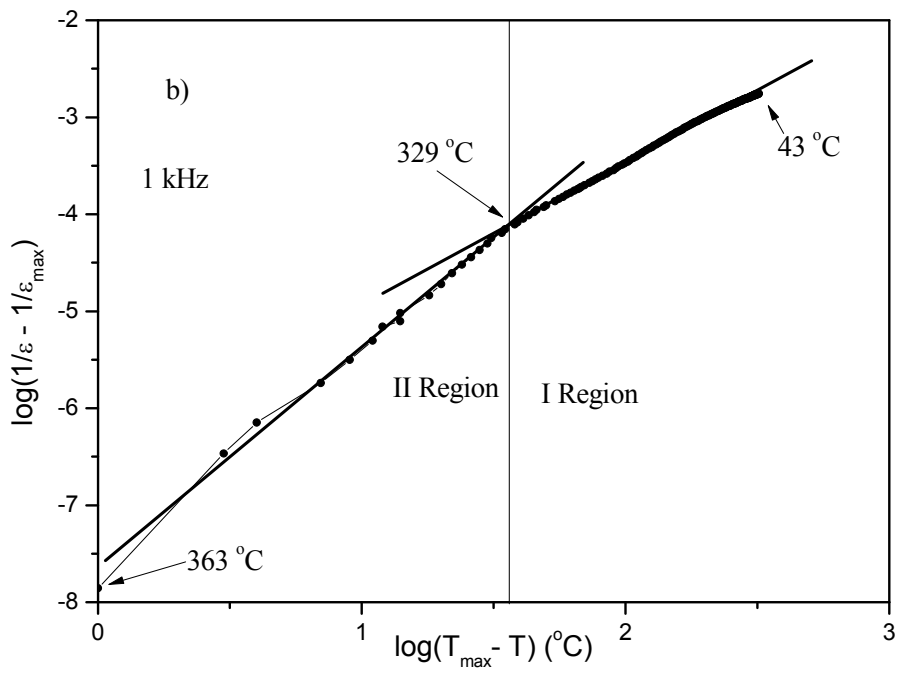
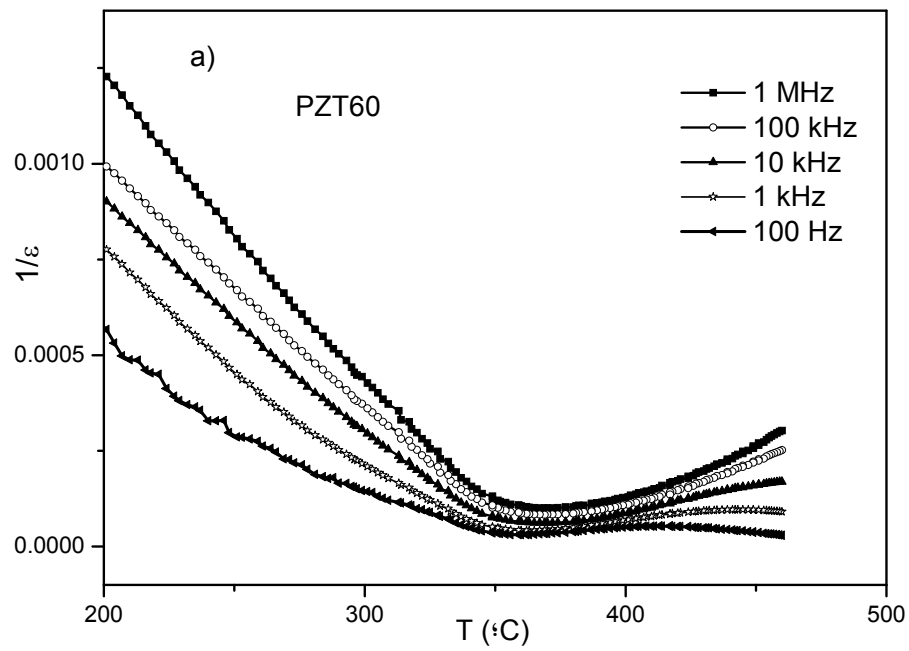
In both crystals and ceramics a divergence of the Curie-Weiss law is observed from the temperature dependence of the inverse of the dielectric permittivity, mainly at low frequencies and high temperatures. In Figure 4.32a it is only shown the case of the PZT60 single crystal and similar behaviours are observed for PZT65 single crystal and the PZT60 ceramic. Commonly, it is used Equation 1.24 to explain the divergence from the Curie-Weiss law, particularly in ferroelectrics with a diffuse phase transition and relaxor behaviour [158]. Using this equation and representing the variation of the $\log\left(\frac{1}{\epsilon} - \frac{1}{\epsilon_{max}}\right)$

with $\log(T_{max} - T)$ in the ferroelectric region ($T < T_c$), it is observed two regions, I and II, which are indicated in Figure 4.32b. In Table 4.9 it is observed that the parameter γ have values between 1 and 2, which is expected by the model, and the δ values are typical for a diffuse phase transition. The obtained values of δ for $T > T_c$ are larger than $T < T_c$. A large value for the parameter δ means a large diffuse transition, but the dielectric curves of this material have not these large diffuse character. The large values of δ must be induced by other effect, which provokes the appearance of two slopes for $T < T_c$ (Figure 4.32b). The constant C in the regions III (Figure 4.32c) is larger than the one expected for the Curie

constant. On the other hand, the values obtained for the region I for all parameters are in correspondence with the normal values reported for ferroelectric materials. This means that region I obeys the Curie-Weiss law, which signifies that we are not in the presence of a diffuse phase transition. We are in the presence of a normal ferroelectric-paraelectric phase transition, which is affected by a process thermally activated that changes the value of the dielectric parameters similarly to a diffuse phase transition.

Table 4.9 - Values of the different parameters for Equations 1.7 and 1.24.

General parameters				$\varepsilon = \frac{C}{T - T_0}$				$\frac{1}{\varepsilon} - \frac{1}{\varepsilon_{\max}} = \frac{1}{2\varepsilon_{\max}} \delta^2 (T - T_c)^\gamma$					
				$T < T_c$		$T > T_c$		$T < T_c$			$T > T_c$		
Sample	f(Hz)	ε_{\max}	T_{\max} (°C)	C ($\times 10^5$)	T_0 (°C)	C ($\times 10^5$)	T_0 (°C)	δ	C ($\times 10^5$)	γ	δ	C (10^5)	γ
PZT65	1M	15685	367	1.13	357	2.49	371	3.70	4.29	1.25	16.67	87.2	1.74
	100k	17608	367	1.16	355	2.63	370	3.70	4.82	1.25	16.67	97.8	1.74
	10k	19737	367	1.22	354	3.49	363	3.84	5.82	1.29	12.50	61.6	1.66
	1k	23183	367	1.43	354	4.09	370	4.00	7.42	1.32	10.00	46.4	1.41
PZT60	1M	9938	369	1.31	358	6.09	318	6.66	8.82	1.34	33.33	220.8	1.80
	100k	11994	369	1.61	359	6.41	327	5.55	7.38	1.25	24.00	138.2	1.77
	10k	16163	369	1.72	359	6.84	338	5.55	9.96	1.32	20.00	129.3	1.67
	1k	23862	363	2.83	359	10.0	330	7.69	28.22	1.48	14.28	97.3	1.52
PZT60 Ceramic	1M	13376	373	1.88	375	2.95	366	5.00	6.68	1.23	16.67	74.3	1.72
	100k	13997	373	1.98	377	2.89	368	5.00	6.99	1.24	20.00	111.9	1.77
	10k	15023	373	1.94	374	3.70	360	5.00	7.51	1.26	16.67	83.4	1.74
	1k	18188	372	2.66	379	4.08	345	5.55	11.20	1.32	-	-	-



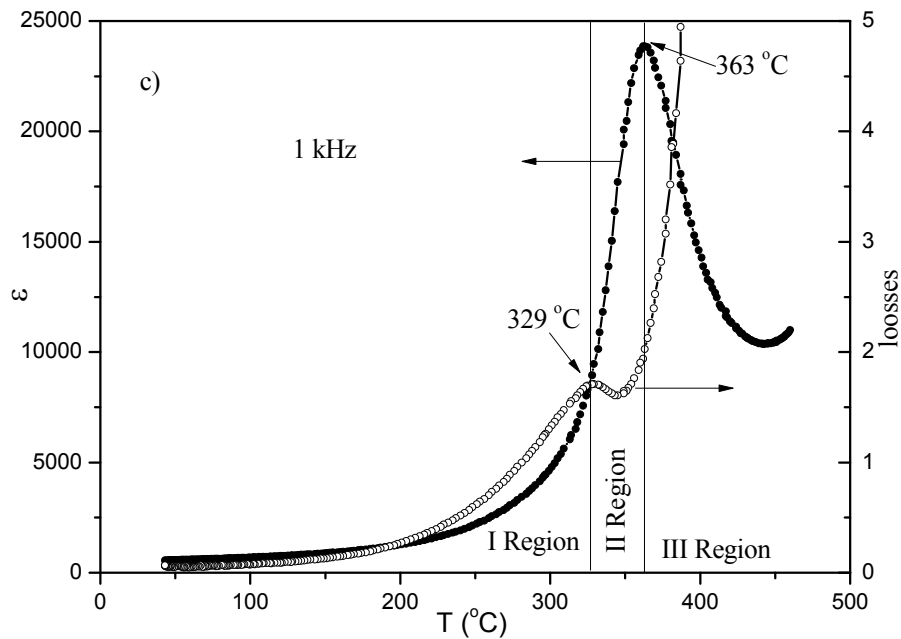


Figure 4.32 - a) $1/\epsilon$ vs temperature curves for PZT60 at various frequencies, b) the $\log\left(\frac{1}{\epsilon} - \frac{1}{\epsilon_{\max}}\right)$ vs $\log(T_{\max} - T)$ curve (1 kHz) in the ferroelectric region and c) ϵ and the losses vs temperature.

In order to understand why there is a non-linearity of the dielectric constant (referred to the inverse of the Curie-Weiss law) at high temperature and low frequency, it was plotted in Figure 4.32c the permittivity and the dielectric losses in function of the temperature. The region II in Figure 4.32b is coincident with the maximum of the dielectric losses. The discrepancies in region II with respect to the Curie-Weiss law is due to a process conductive which is thermally activated. The conductivity in PZT crystals can be due to defects in the crystals introduced during the crystal growth process. It was also found high conductivity at low frequency in ceramic, which increases with the temperature and meaning that the conductivity may not only occur due to impurities introduced during crystals growth. The conductivity can be due to lead volatilization, which produces defects in the material. Furthermore and as already referred, the EDS analyses in several points of the crystals do not reveal the presence of impurities reinforcing the previous hypothesis of lead volatilization.

- *Tetragonal single crystals*

The temperature dependence of the dielectric permittivity of the tetragonal crystals is shown in Figure 4.17, for PZT46, and in Figure 4.33, for PZT42.

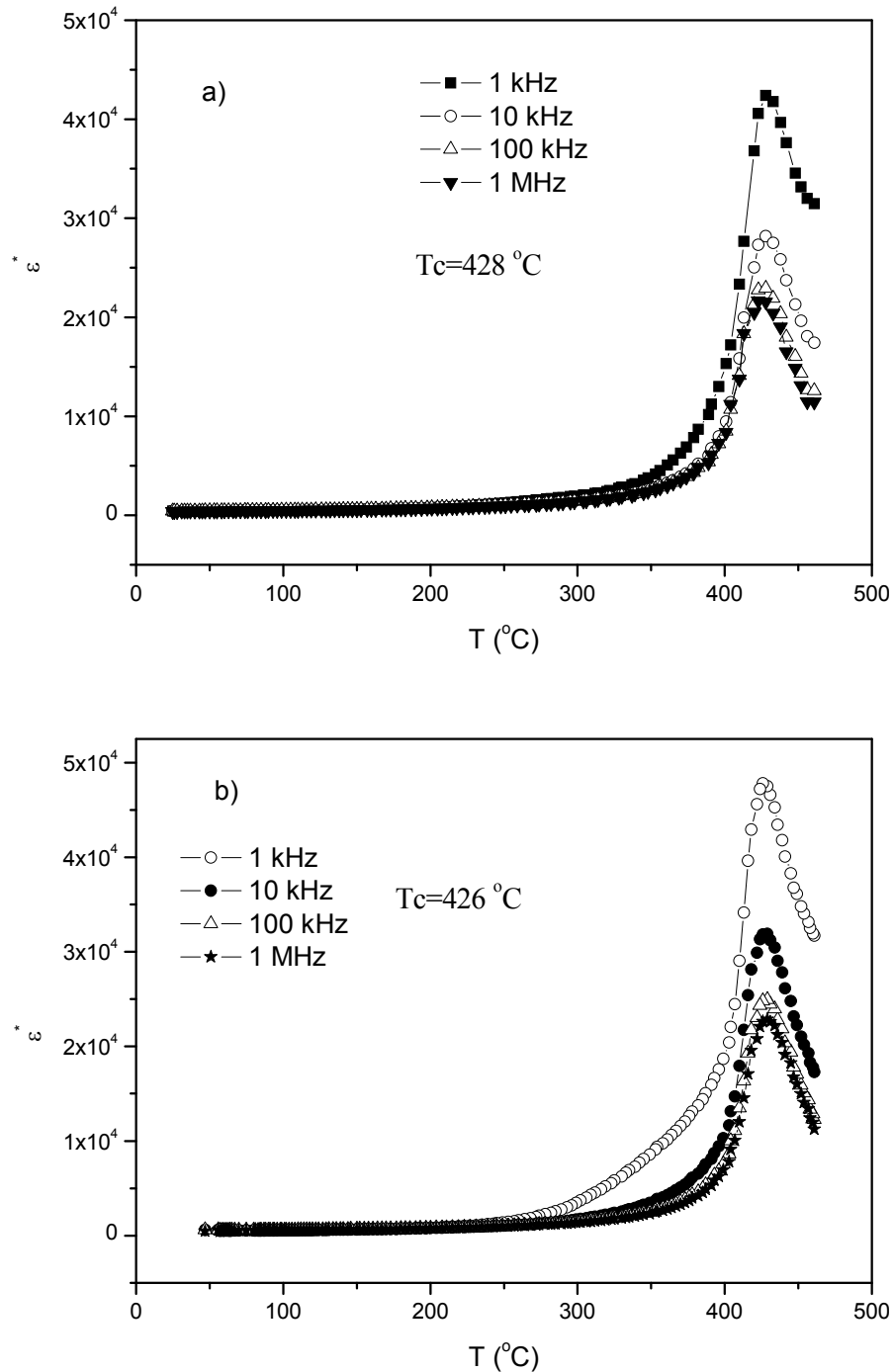


Figure 4.33 - Temperature dependence of the dielectric permittivity of the PZT42 crystal on a) heating and on b) cooling conditions.

A small shift is observed in the dielectric permittivity between heating and cooling runs (thermal hysteresis). This effect increases when the frequency is decreased. This shift can be associated with charge movement in the crystals.

The variation of the permittivity with the temperature in heating and cooling conditions, at different frequencies, for the PZT46 crystal is shown in the Figure 4.17. The values of the dielectric permittivity in the transition temperature for this single-crystal (59 000 at 1 kHz and 32000 at 1 MHz) are higher than those reported in the ceramics (normally lower than 25000). On the other hand, these values are higher than those obtained in the rhombohedral single-crystals [307]. The values of the permittivity of these crystals obtained at room temperature (between 600 and 900) are comparable with those obtained in ceramics for the same composition (between 800 and 1100). A process of dispersion in the dielectric permittivity is observed between 300°C and 400°C similar to the one observed in the rhombohedral phase. The dielectric behaviour of the PZT46 crystal shows high losses in the transition temperature as shown in the Figure 4.34. These high losses are associated to conductive charges which are thermally activated for temperature around 300°C, that it was said can be oxygen or lead vacancies motion.

The Curie-Weiss constant (C) and the Curie-Weiss temperature (T_0) (Equation 1.7 and 1.24) at 1MHz, in heating and cooling conditions for these five crystals are summarized in Table 4.10. The T_0 values obtained using the Curie-Weiss law for temperatures $T < T_c$ and $T > T_c$ are different. The parameter δ represents the diffuse degree of the ferroelectric phase transition and in this case approximately coincident to the wide of the region II (Figure 4.32). Table 4.10, the value of T_0 in the region $T > T_c$, for PZT42 is not present due to a low number of points. The values of the Curie constant (C) have a maximum with the composition for $T < T_c$ and for $T > T_c$ (Figure 4.35), but these maxima are not coincident. The maximum for $T < T_c$ is near the composition reported by Amin *et al.* [315] and it was fitted using a Gaussian distribution (Equation 4.2) and the parameters are presented in Figure 4.35.

$$C = C_o + a_1 * e^{-\frac{a_2}{2}(x - a_3)^2} \quad (4.2)$$

where C_o , a_1 , a_2 , a_3 are constants and x is the Zr concentration.

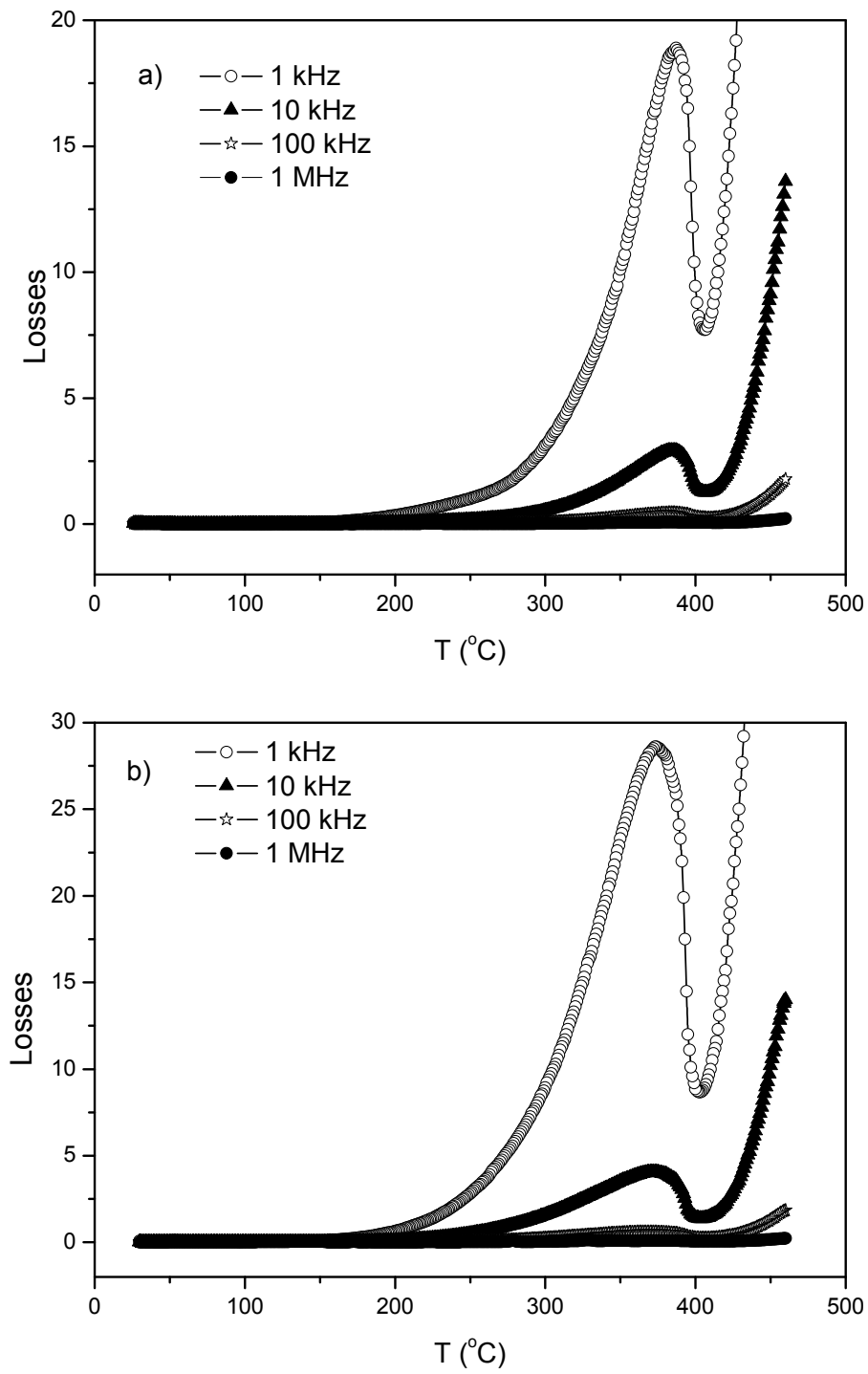


Figure 4.34 - Temperature dependence of the dielectric losses of the PZT46 crystal on a) heating and b) cooling conditions.

Table 4.10 - Values for the different parameters in Equations 1.7 and 1.24 for the five crystals so far presented. In the case of crystal PZT42, it was not possible to calculate C and T_0 , for $T > T_c$, due to the low number of experimental point obtained in this region.

General parameters 1MHz			$\varepsilon = \frac{C}{T - T_0}$				$\frac{1}{\varepsilon} - \frac{1}{\varepsilon_{\max}} = \frac{1}{2\varepsilon_{\max}} \delta^2 (T - T_c)^\gamma$					
Crystal	ε_{\max}	T_{\max} (°C)	$T < T_c$		$T > T_c$		$T < T_c$			$T > T_c$		
			C ($\times 10^5$)	T_0 (°C)	C ($\times 10^5$)	T_0 (°C)	δ	C ($\times 10^5$)	γ	δ	C ($\times 10^5$)	γ
PZT65	15685	367	1.13	357	2.49	371	3.70	4.29	1.25	16.67	87.2	1.74
PZT60	9938	369	1.31	358	6.09	318	6.66	8.82	1.34	33.33	220.8	1.80
PZT52	20826	361	1.82	350	3.09	374	2.77	3.19	1.06	20.00	166.6	1.79
PZT46	32828	408	3.98	407	1.58	409	1.29	1.09	0.88	12.50	102.6	1.72
PZT42	22871	429	1.67	421	-	-	2.85	3.72	1.12	20.00	182.9	1.85

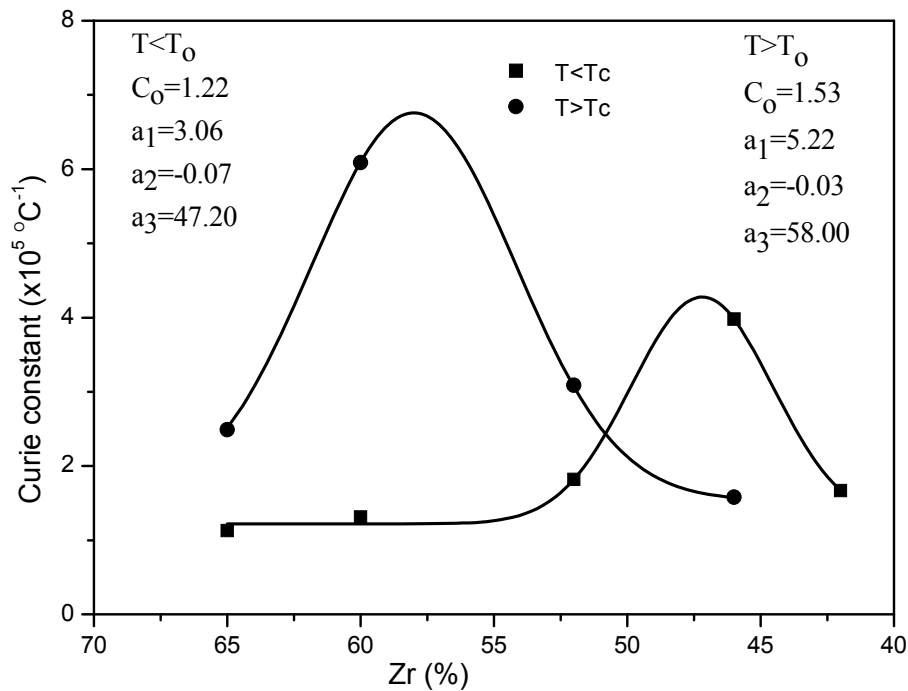


Figure 4.35 - The Curie constant (C) for PZT single crystal versus composition. The solid curve is Gaussian distribution used to fit the data (see Equation 4.2)

4.4.2. Hysteresis loop measurement in a pseudo cubic crystal

The P-E hysteresis loop was measured at room temperature along the c -axis ([001] direction) in order to confirm the ferroelectric properties in PZT52 single crystals. Figure

4.36 shows a hysteresis loop in the c -direction. The values for the spontaneous polarization ($P_S \approx 40 \mu\text{C}/\text{cm}^2$) and the coercive field ($E_C \approx 39 \text{ kV}/\text{cm}$) were estimated from this curve. This observation of the hysteresis loop confirms the ferroelectric character of this composition, *i.e.*, it cannot belong to the cubic symmetry at room temperature, as initially indicated by XRD analysis.

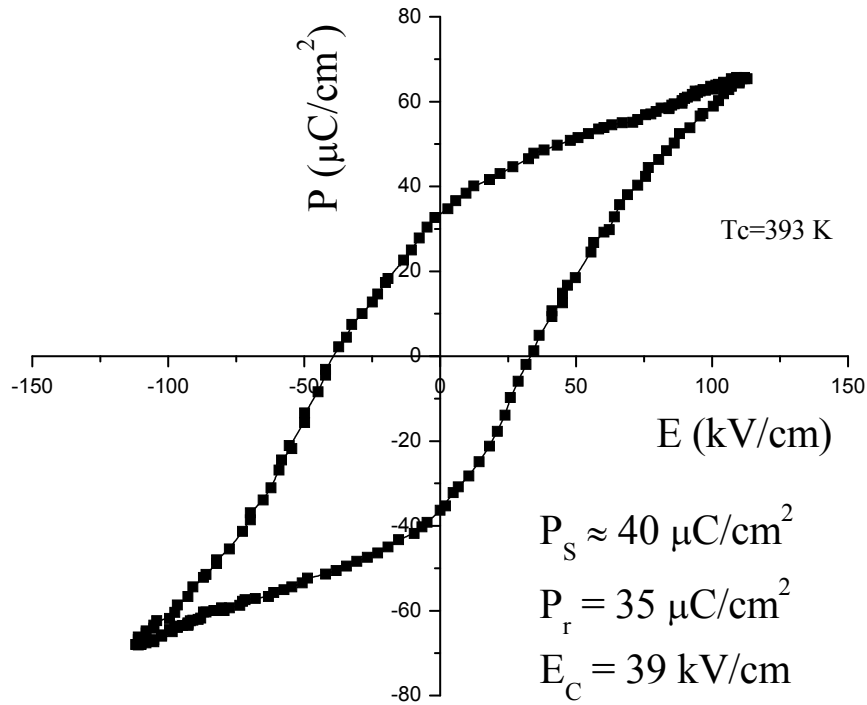


Figure 4.36 - Room temperature P-E hysteresis loop measured along the [001] (c -axis) direction in PZT52 single crystal.

4.4.3. Piezoelectric characterisation

The principal property of the PZT system is the high piezoelectric response. In this study it is present the preliminary results of the piezoelectric characterisation of the PZT52 crystal, which was performed along the c -axis ([001] direction). The PZT52 crystal was previously poled at $E_P = 40 \text{ kV}/\text{cm}$, as described in section 3.6.3. Figure 4.37 shows the frequency (f) dependence of the d_{33} coefficient and the phase measured using an ac voltage of $V_{ac} = 100 \text{ V}$ ($E_{ac} \approx 3 \text{ kV}/\text{cm}$) in the frequency range from 500 Hz to 5 kHz.

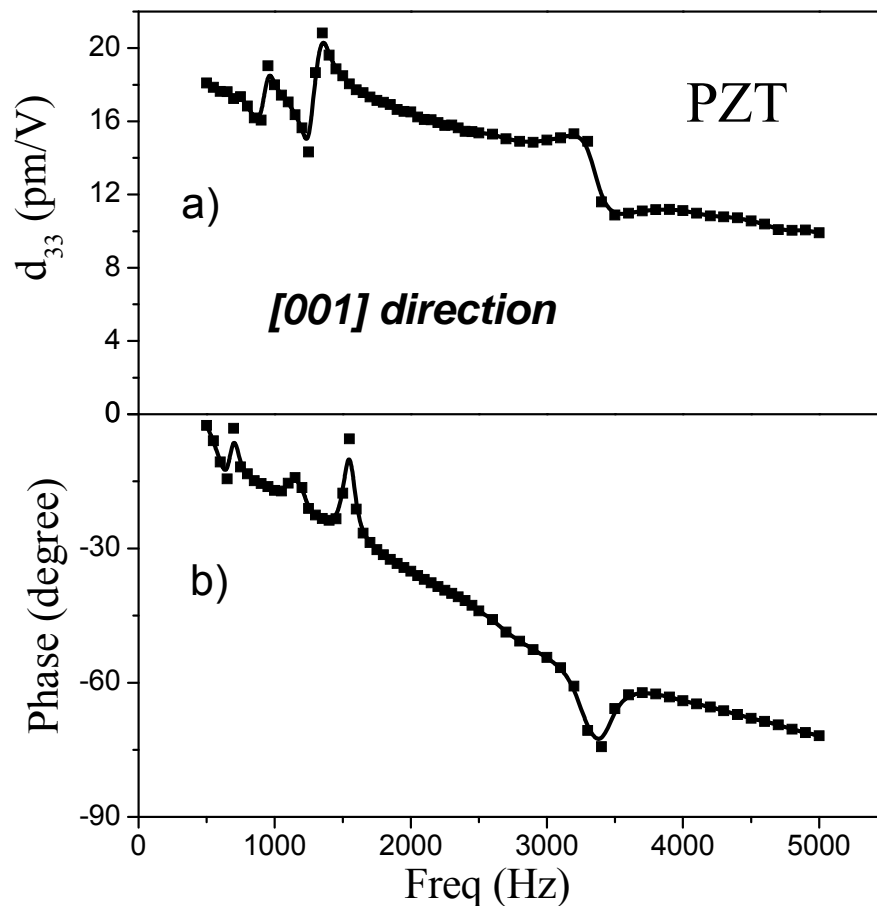


Figure 4.37 - Frequency dependence of: a) the piezoelectric coefficient d_{33} and b) the phase, measured along the [001] direction of the PZT52 single crystal using an ac voltage of $V_{ac} = 100$ V ($E_{ac} \approx 3$ kV/cm).

Frequency dispersions of the d_{33} are observed in the analyzed frequency range, with four clear mechanical resonances at 0.7, 1.15, 1.55 and 3.4 kHz. Moreover, the peak with frequency of 3.4 kHz has a vibrational displacement in opposite direction to the other peaks, which means that this peak can not be a harmonic of the other ones. The piezoelectric resonance peaks common vibration modes appear in a piezoelectric resonator (e.g., length, radial, thickness or shear modes) at higher frequencies (> 50 kHz). Thus, it is believed that the resonances, as well as the frequency dispersion observed in our experiments, can be associated to the clamping of the small PZT crystal by the araldite, used in the piezoelectric measurements (see section 3.6.3 and Figure 4.38). The PZT crystal, together with the araldite, constitute a piezoelectric composite with a total impedance depending on the individual parameters of both materials. This results in a

different equivalent circuit, where mechanical resonance may occur at lower frequencies (probably, flexural vibrations) [3]. Figure 4.38 represents a schematic view of a clamped crystal inside the araldite. When an *ac* electric field is applied, a flexural vibration may appear in the crystal.

The large number of the resonance frequencies can be related to an incorrect orientation of the crystal in the [001] direction, which provokes the presence of shear and other modes in the crystal. The last effect can be more complicated due to the clamping of the crystal in the araldite.

Based on the above-mentioned arguments, from the zero extrapolation ($f \rightarrow 0$) of the PZT crystals d_{33} coefficient is estimated to be ≈ 20 pm/V along the [001] direction, being this value approximately the same as the d_{33} coefficient in a *dc* mode. This value is lower than the one obtained in ceramics, normally around 220 pm/V [23, 316]. A reason for this discrepancy can be associated to the 72 hours delay between the crystal poling and the piezoelectric measurement, which can depolarize the crystal. On the other hand, the crystal was poled at 40 kV/cm, which is a low electric field to saturate this crystal.

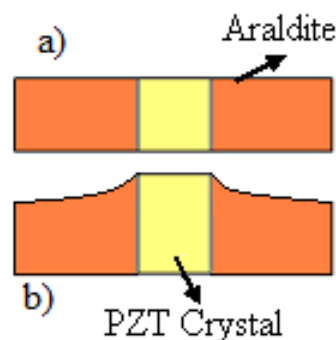


Figure 4.38 - Diagram of a clamped crystal inside the araldite (a) and the flexural vibration of the crystal (b).

The crystal was poled again at $E_p = 40$ kV/cm and the values of the d_{33} coefficients were measured again (Figure 4.39). They were larger than those previously obtained (Figure 4.37), decreasing quickly as the number of cycles (*ac*) increases. The crystal polarization relaxes with time, resulting in a decrease of the d_{33} coefficient down to 20 pm/V after 72 hours of poling. When the crystal is poled at 70 kV/cm, the values of the d_{33} coefficient decrease faster than when it is poled at 40 kV/cm. The d_{33} coefficient values are

close in both cases, for a number of cycles of over 10^6 (Figure 4.39), and the decrease is not stabilized even after this number of cycles. This can be related to that this crystal has mobile charges (electrons) which block the external effect of the polarization.

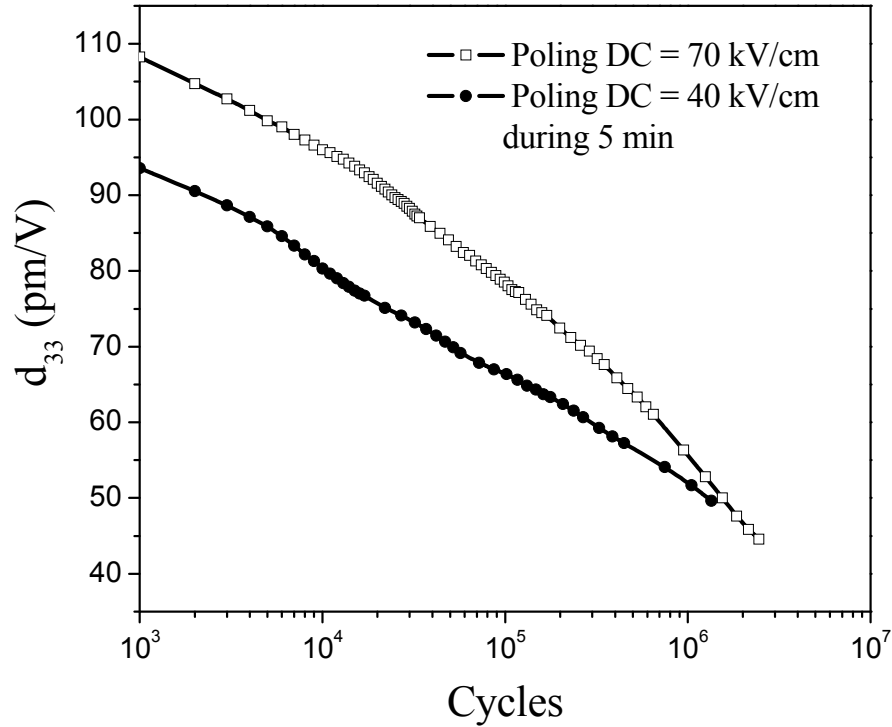


Figure 4.39 - Dependence of the piezoelectric coefficient d_{33} with the number of cycles, measured at 1 kHz and along the [001] direction in PZT52 crystal.

Low values of d_{33} are frequently found in thin films and this effect is explained by the clamping of the PZT thin film to the substrate. In Kholkin *et al.* work [288] for the case of an ideal clamping, where the transverse strain is completely constrained by the substrate, the following expression [317] is valid for the effective d_{33} coefficient measured by the converse piezoelectric effect:

$$\frac{(d_{33})_{eff}}{d_{33}} = 1 - 2 \left(\frac{d_{31}}{d_{33}} \right) \frac{c_{13}^E}{c_{11}^E + c_{12}^E} \quad (4.3)$$

where d_{33} and d_{31} stand for the longitudinal and transverse piezoelectric coefficients of the free (unclamped) material, respectively, and c_{ij}^E are the elastic compliances of the film. Since for PZT (compositions near the morphotropic phase boundary), $d_{31}/d_{33} \approx -0.4$ [30]

and c_{13}^E is negative, the effective piezoelectric coefficient ($(d_{33})_{\text{eff}}$) can be significantly smaller than that of the free material [318]. This probably explains why the piezoelectric coefficients reported for PZT films [121, 318, 319] are typically smaller than those observed in bulk ceramics of the same compositions. We believe that same explanation is possible give to our result.

Figure 4.40 shows the behaviour of the d_{33} coefficient after applying a dc poling field (piezoelectric hysteresis loop). It was obtained by poling the PZT crystal along the [001] direction and then measuring the d_{33} coefficient using a low ac voltage $V_{ac} = 100$ V at 1 kHz, as described in section 3.9.3. The hysteretic behaviour of the calculated d_{33} coefficient with the dc poling field is confirmed. The electric field value at which d_{33} vanishes should be close to the conventional coercive field (39 kV/cm measurement using hysteresis loop). This is because approximately at this point half of the ferroelectric domains that were previously oriented along the poling field direction have switched back to their original states (180° domains) due to the poling in the opposite direction.

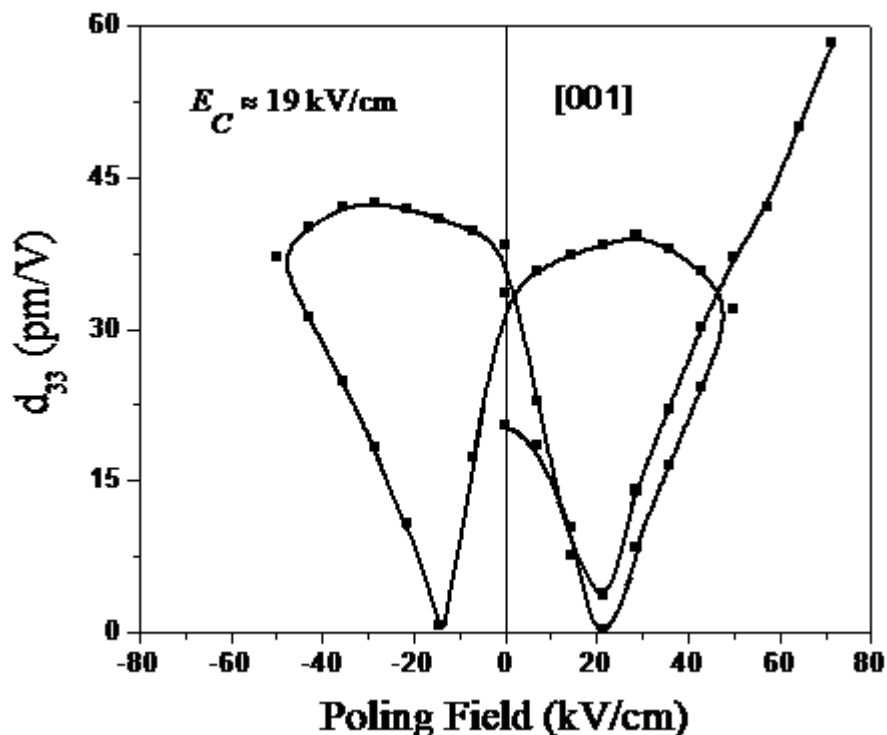


Figure 4.40 - Dependence of the piezoelectric coefficient d_{33} of the clamped crystal with the dc poling field, measured at 1 kHz and along the [001] direction in PZT52.

Therefore, the net polarization of the crystal tends to zero and the crystal is

piezoelectrically inactive (*i.e.*, the effects from the individual domains cancel each other and no piezoelectricity is observed). The coercive field estimated from this experiment is $E_C \approx 19$ kV/cm, which disagrees with the result of the P-E hysteresis measurements (see Figure 4.36), where E_C is twice the value here obtained (≈ 39 kV/cm). The large difference can probably be associated with the crystal clamping inside the araldite because the measured in Figure 4.36 the sample are not clamping.

4.4.4. *Piezoelectric force microscopy: distribution of domains.*

The domain distribution obtained by piezoelectric force microscopy (PFM) was studied on the five single crystals as described in section 3.6. The crystals have the following characteristics: one of the crystals has rhombohedral structure ($x \approx 0.54$), others have pseudo-cubic structure (compositions at the MPB, $x \approx 0.53$ and 0.52) and two have tetragonal structure ($x \approx 0.42$ and 0.35). These crystals were selected within the composition range of the crystals previously analyzed by XRD and dielectric measurements.

- *Tetragonal crystals*

Figure 4.41a shows the out-of-plane (OPP) PFM image, of the PZT35 single crystal, with line parallel black and white domains with size of several microns. As can be observed in Figure 4.41b the histogram distribution of the PFM signal has almost full negative domains. In the PFM experiments the voltage was applied on the bottom electrode and the tip was grounded. In this case, negative measurement means a positive orientation of the polarization, called positive self polarization effect, well known in PZT films [320]. The measurements made in different points of the sample give the same results: no positive domains were found. Therefore the presence of positive polarization in all the crystals can be related with superficial charges which provoke this effect. The histogram of distribution of the polarization (Figure 4.41) is constituted by two peaks corresponding to two of the main domain orientations. The first peak corresponds to the orientation of domains with in-plane polarization parallel to the crystal surface and the second peak corresponds to domains with polarization perpendicular to the surface and pointing out of the surface.

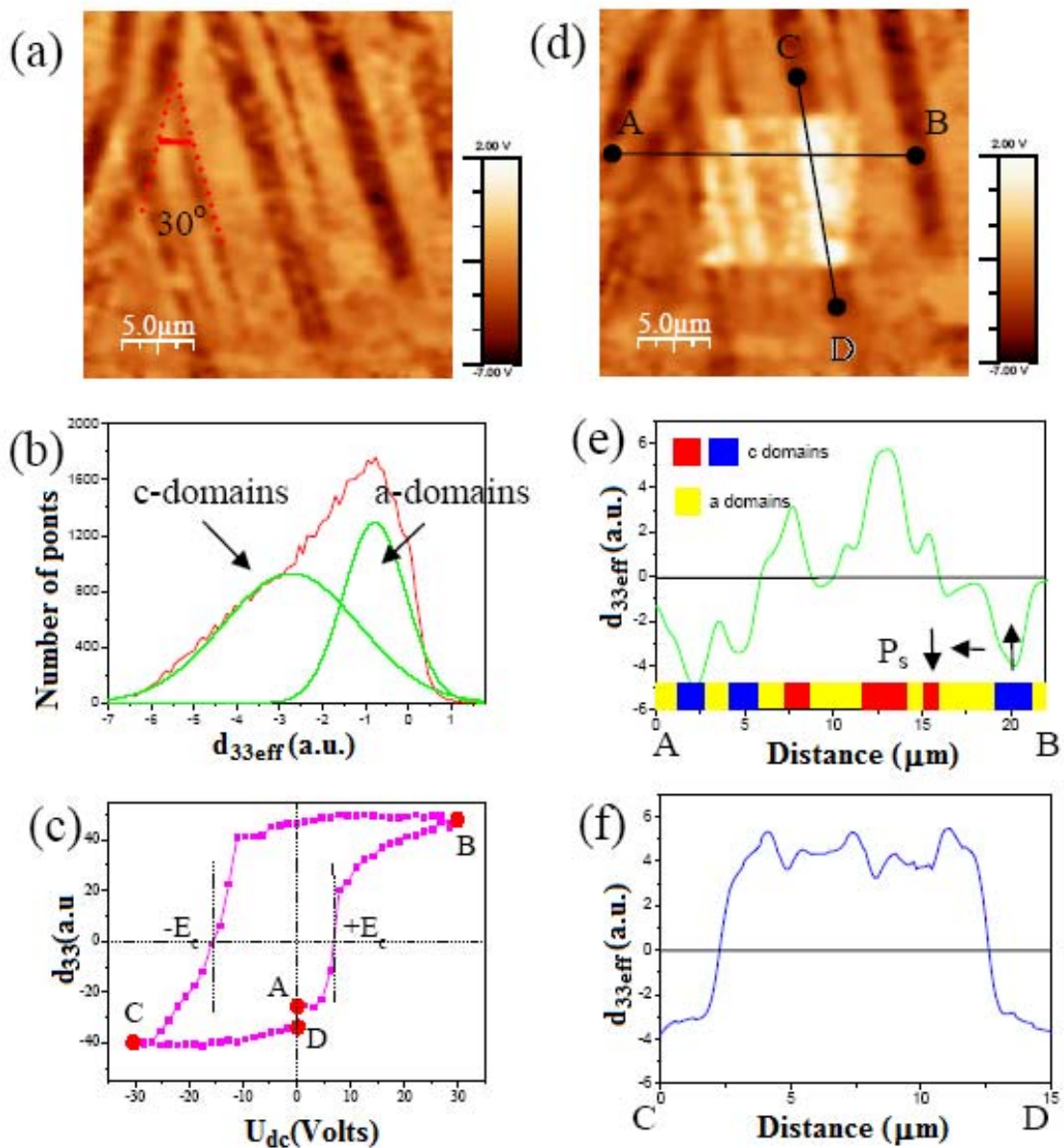


Figure 4.41 - PFM images of the 100-oriented PZT single crystal (PZT35): (a) before poling; (b) histogram of PFM image before poling; (c) local hysteresis loop; (d) after poling with $V_{dc} = +30$ V applied to the tip; (e) and (f) cross-sections of the PFM images after poling, along the AB and the CD lines in (d).

When a dc electric field higher than the coercive field is applied between the tip and the bottom electrode, it can be observed a local switching of the polarization corresponding to the voltage direction. Local hysteresis loop is shown in Figure 4.41c. It can be noticed that the beginning (negative level, point A) and the end of the hysteresis loop (point D) have

the same sign. But after poling a positive signal is present (point B). The coercive voltages for the positive and the negative switching are different. This can be due to the presence of additional potential at the sample surface originated by the presence of negative domains. Figure 4.41e and Figure 4.41f show the polarization orientation along of the line AB and CD respectively, in Figure 4.41d.

In Figure 4.42a it is shown the topographic images of the 100-oriented PZT35 single crystal and the angle formed by the domains in the plane. The angle of 80° is not usual in tetragonal structures and may be related to reciprocal domains. The cross section profile along AB line (Figure 4.42b) show the polarization orientation along this line and the peak represents the change of orientation of a domain to another one. The angle formed by each peak is correlated to the angle of the domain pattern which is related to the PZT unit cell parameters according to the following relation:

$$\begin{aligned} c/a &= \text{ctg}(\alpha/2 - \pi/4) \\ c/a &= \text{ctg}(177.3^\circ/2 - 45) = 1.048 \end{aligned} \quad (4.4)$$

This value for c/a corresponds to a Zr content in the range of $x = 0.40 - 0.30$ [125], which correlates well with the chemical characterisation of this crystal $x=0.35$ [307]. The angle used in the calculation (177.3°) was taken from Figure 4.42b.

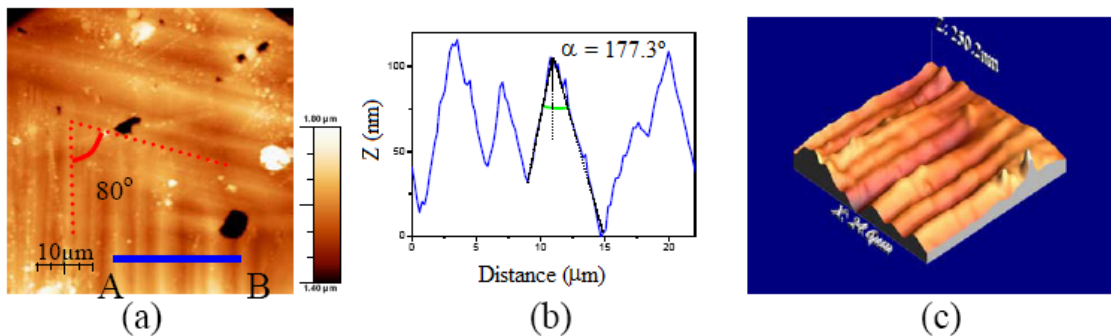


Figure 4.42 - (a) and (c) topographic images of the 100-oriented PZT35 single crystal and (b) cross section profile along the AB line.

It is possible to reconstruct the domain structure of the sample based on the out-of-plane polarization (OPP) and the two perpendicular in-plane polarization (IPP) images of the PFM obtained in the same region of the crystal (Figure 4.43). Figure 4.43a and Figure 4.43e show the OPP images in two perpendicular directions of the same crystal region. These images have the same contrast, which is possible because these two orientations

differ only in the rotation of the sample about the z axis (perpendicular to the surface). A rotation of the sample around the z axis does not affect the projection of the polarization along this direction and therefore the OPP image does not change. In Figure 4.43a and Figure 4.43e it is observed mixed domains with negative and zero signals. Negative signal means an orientation of the polarization out-of-plane to the sample surface. A zero signal means orientation of the polarization in-plane. From the OPP images it is not possible to determine the polarization orientation in plane.

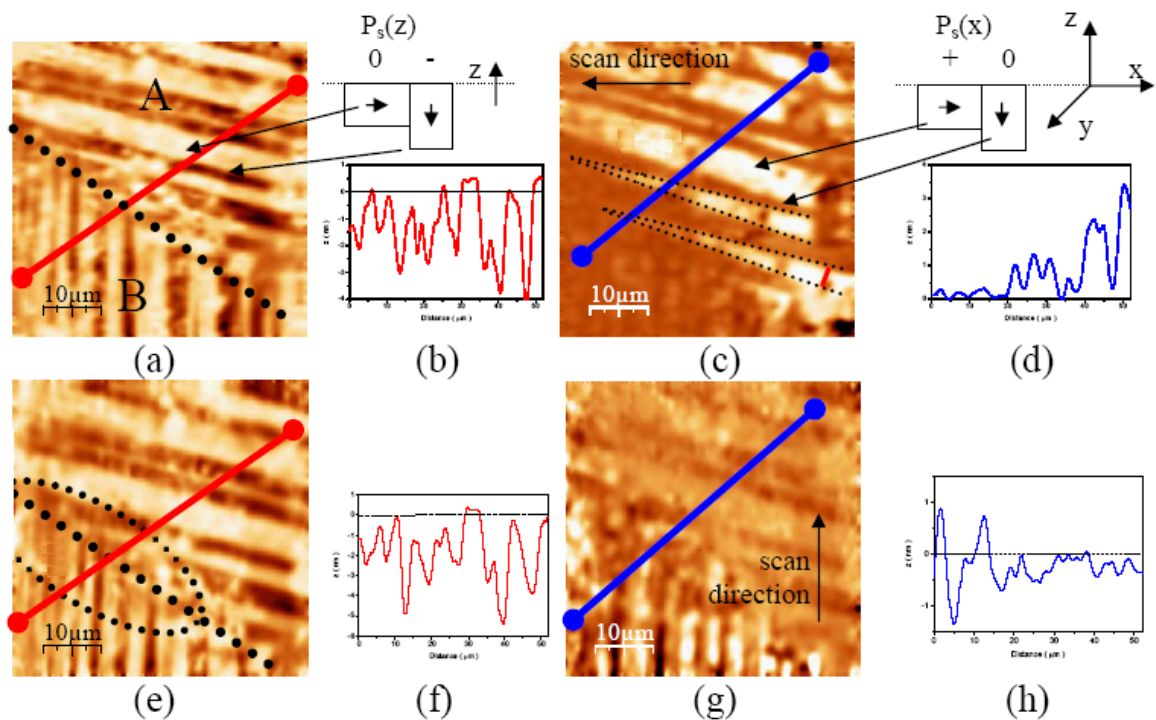


Figure 4.43 - PFM images of 100-oriented PZT35 single crystal: (a) and (e) out-of-plane polarization (OPP) images; (c) and (g) in-plane polarization (IPP) images; (b), (d), (f) and (h) cross-sections along the corresponding PFM images. (a), (c) and (e), (g) are rotated 90° about z axis.

The polarization orientation in plane is obtained from the IPP images (Figure 4.43c and g). These IPP images are obtained for two perpendicular directions by rotation of the sample around the z axis. They are different from the OPP images and between themselves. Using the information from the OPP and IPP images, it is possible to observe that the searched area consists of two main parts (A and B). These parts have different domain structure orientation. The OPP images for A and B show the same domain

behaviour. This suggests periodic domains with zero intensity and negative contrast with sizes between 2-5 μm (Figure 4.43). The IPP images have one part without contrast and the other part is contrasted (Figure 4.43c), which is opposite to the correspondent images for the perpendicular orientation (Figure 4.43g).

This means that these images reflect in-plane components of the piezoelectric effect from two perpendicular (x and y) directions. Part B of Figure 4.43c and part A of Figure 4.43g have weak contrast, close to zero and for these orientations it can be determined the projections of the polarizations. Part A of Figure 4.43c and part B of Figure 4.43g show correlated (opposite) contrast. From this analysis, it is reconstructed the domain structure of this crystal, which is shown in the Figure 4.44. This is related to the tetragonal symmetry of the crystal. Based on Hatanaka *et al.* work [205], the PFM images can be explained by a domain structure with boundaries in the (101) plane, as shown in Figure 4.44. This model can describe the step surface structure and the PFM images (OPP and IPP) and can also explain the preferential domain orientation in the positive direction. From this model with tetragonal twinning in the (101) plane, only two orientations of polarization are possible (OPP images): positive and zero or negative and zero (zero polarization means that this is oriented in-plane and do not has contribution in the out-of-plane polarization). In our case only the first variant was observed.

The boundary area between the A and B parts (Figure 4.43e - dotted line) contains relatively small domains (smaller than 1 μm). The decrease in the domain size can be associated to the higher stress in this area resulting from the contact of two different non-coherent domain systems (A and B). This is also related with the non-orthogonal orientation of the crystal (crystal polish surface and crystallography plane).

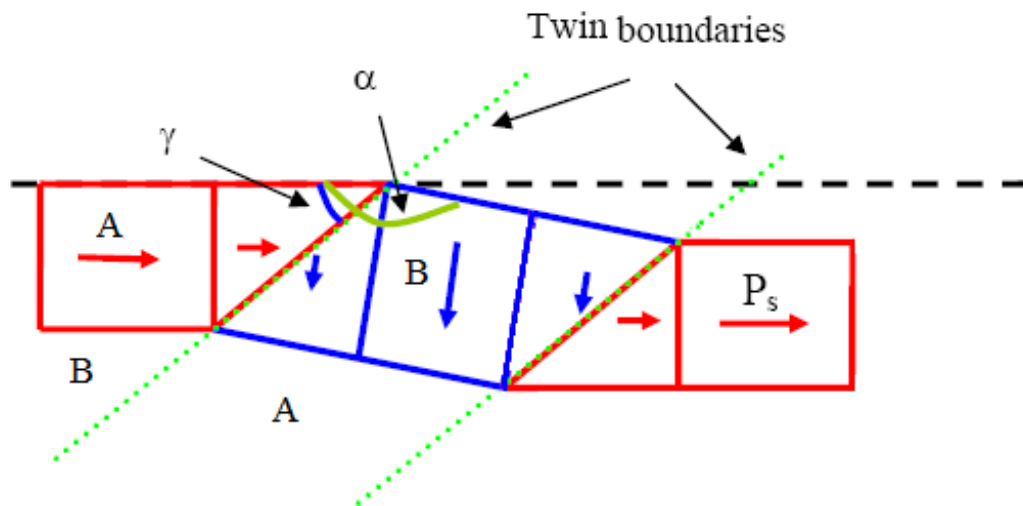


Figure 4.44 - Schematic model of the domain structure of the tetragonal PZT35 single crystals based on the PFM images of Figure 4.43. The arrows inside the domains represent the spontaneous polarization.

The increase of the Zr content in the PZT composition (in the tetragonal field of the phase diagram) increases the number of domains (decreases the domain size). In Figure 4.45 it is shown the local PFM topography images of the 100-oriented PZT42 single crystal, using different resolutions. Small 90° domains are observed in the topography images with sizes much smaller than $1\mu\text{m}$. In Figure 4.46 it is shown the deflection of the topography (dz/dx), in-plane and out-of-plane of the same region of PZT42 single crystal. The OPP and IPP images confirm the topography results (Figure 4.46) and they are coincident (domain distribution) with the results obtained for the sample PZT35. The main difference is in the number and size of the domains. The model presented in the Figure 4.44 can be used for the PZT42.

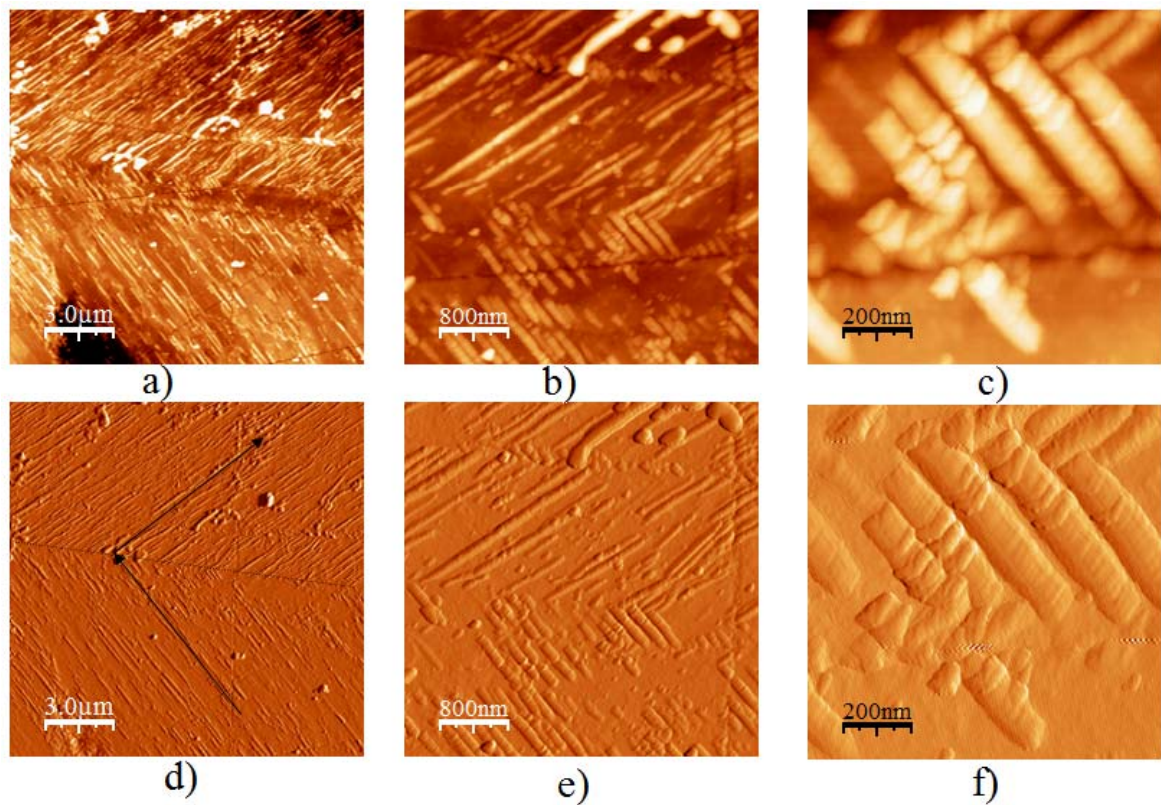


Figure 4.45 - Local PFM topography images of 100-oriented PZT42 single crystal (a, b, c) and deflection of the topography (d, e, f) for different zooms.

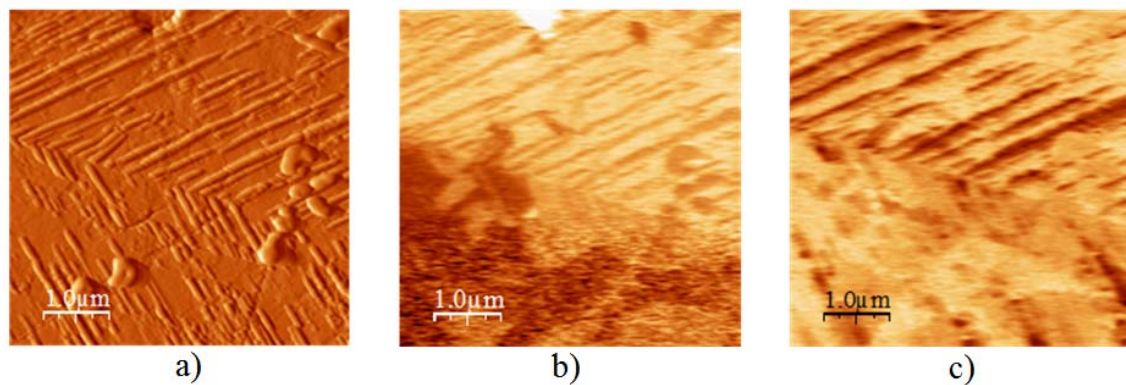


Figure 4.46 - Local PFM images of [100] - oriented PZT42 single crystal: a) topography deflection, b) in-plane and c) out-of-plane.

- *Pseudo-cubic crystals*

In the pseudo-cubic crystal, in the MPB part of the phase diagram it is the domain structure not clear. In Figure 4.47 it is shown some AFM images of a PZT53 single crystal taken in different points of the crystal. The out-of-plane piezoresponse before poling does

not show a domain structure. This suggests that either the crystal is not ferroelectric or it is single domain. The best method to determine if a crystal is ferroelectric is by measuring the hysteresis loop. Figure 4.48 shows the local hysteresis loop (piezoresponse) for the crystal with 52% of Zr content. The presence of a loop means that this crystal is ferroelectric as already expected from the previous dielectric characterization of an equivalent crystal (PZT52). In the dielectric measurements it was observed the transition temperature from ferroelectric to paraelectric which confirms that this crystal is ferroelectric (Figure 4.20) and a Raman spectrum typical of a tetragonal structure was obtained in this composition at room temperature.

In Figure 4.49 it is shown the PFM images of the [001-oriented PZT52 single crystal. The out-of-plane piezoresponse after poling ($V_{dc} = -30$ V applied to the tip on an area of $2 \times 2 \mu\text{m}^2$) is shown in Figure 4.49a. The form of the polarization indicates an instability of the domain structure [320]. This can be due to the instability of the unit cell caused by the low tetragonal distortion of the structure at this composition. The low distortion means weak interaction forces of short and long range, which hinders the domains formation. On the other hand, low electric fields induce large polarization in the crystal, which relaxes quickly decreasing the polarization in logarithmical form with time similar as it is observed in rhombohedral crystal (PZT54).

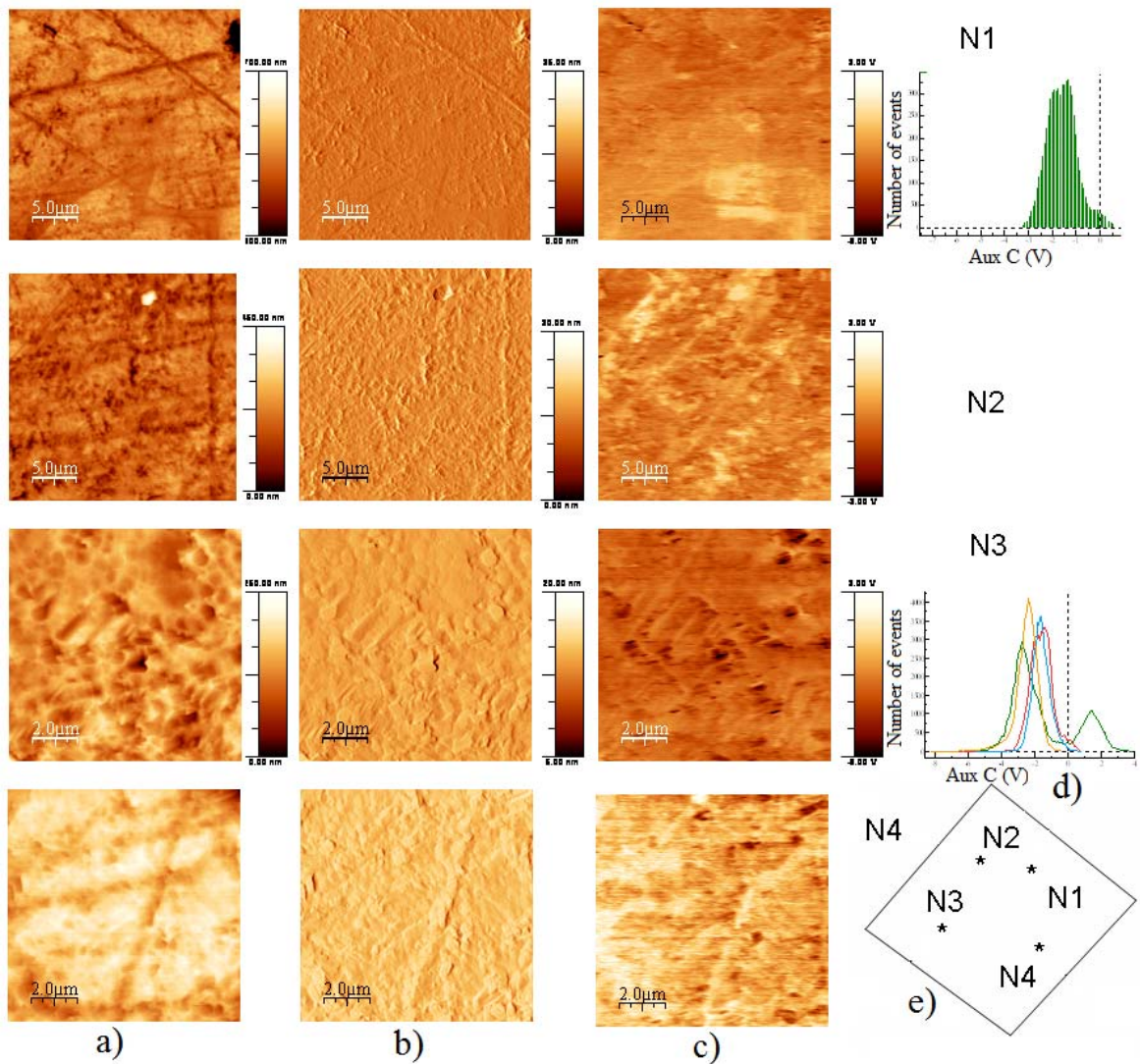


Figure 4.47 - AFM images of the PZT53 single crystal ([001]-oriented): (a) topography, (b) deflection (dz/dx), (c) PFM out-of-plane piezoresponse before poling, (d) histogram of PFM image before poling and (e) measurement position on the single crystal. As can be seen, there is not clear observation of the domain structure of this sample.

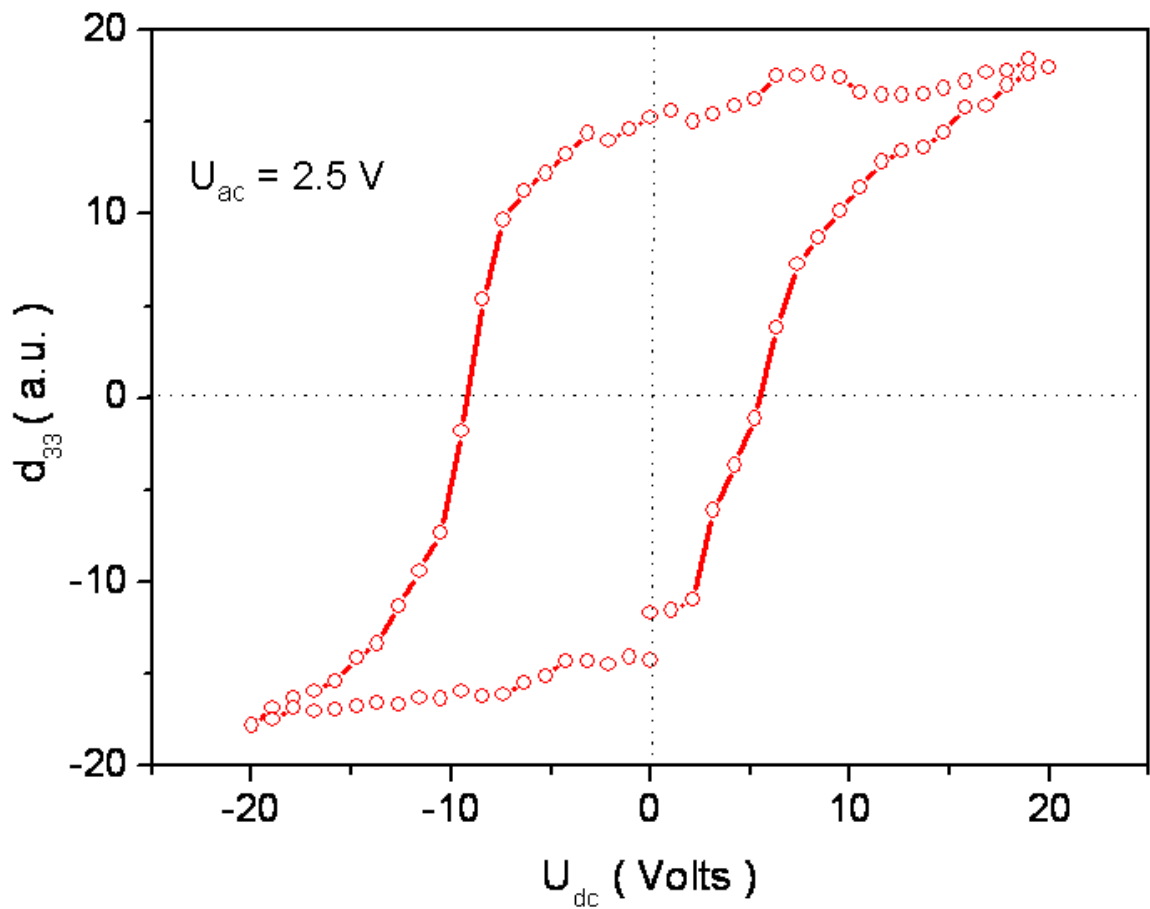


Figure 4.48 - Local hysteresis loop (piezoresponse) of the [001]-oriented PZT52 single crystal.

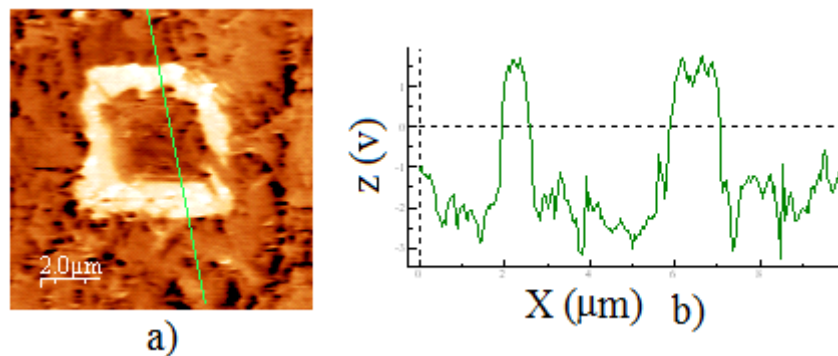


Figure 4.49 - PFM images of the [001]-oriented PZT52 single crystal: (a) out-of-plane piezoresponse after poling at $V_{dc} = -30$ V applied to the tip, on an area of $2 \times 2 \mu\text{m}^2$; (b) cross-sections linear profile of the PFM images, after poling.

- *Rhombohedral crystal*

In the rhombohedral part of the phase diagram it can be seen large domains of several microns (Figure 4.50). In this figure it is shown the PFM images of a single crystal with 54% of Zr amount (PZT54).

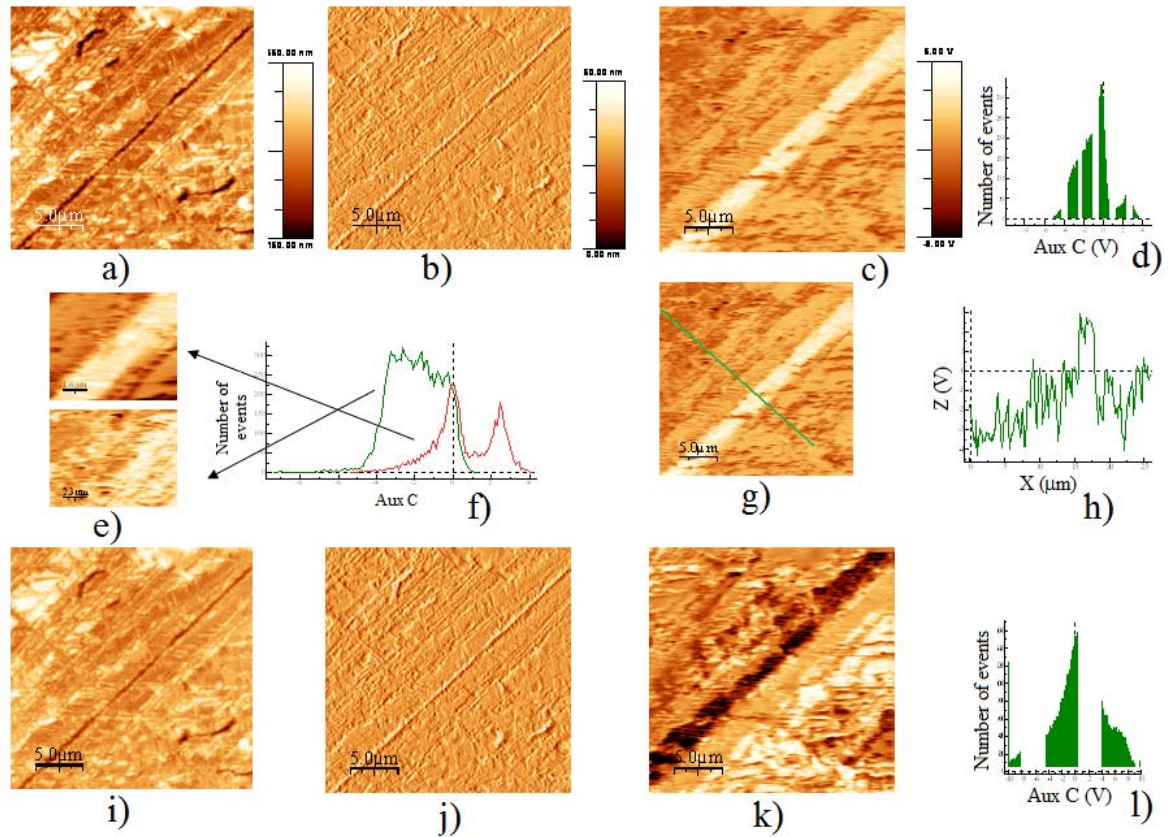


Figure 4.50 - PFM images of the PZT54 single crystal ([001]-oriented). The images (a) and (i) shows the topography, (b) and (j) the deflection (dz/dx), (c), (e) and (g) are out-of-plane, (k) in-plane, (d) and (l) represent the histogram of PFM image before poling and (f) and (h) the cross-sections of the PFM images after poling along the lines.

A small area ($2 \times 2 \mu\text{m}^2$) of this sample was polarized with a dc voltage of $V_{dc} = -30 \text{ V}$ and the out-of-plane piezoresponse was measured for several times, from 0 to 2475 minutes (Figure 4.51). A decrease of the polarization with time is observed (Figure 4.51c). The decrease of the polarization with time was also observed in the tetragonal field and it is larger in pseudo-cubic field, when the composition is $\sim 52 \%$ Zr content.

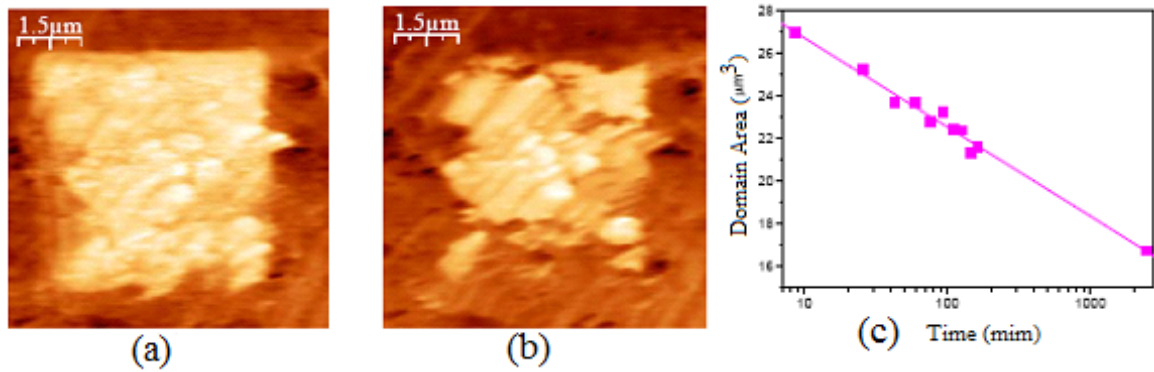


Figure 4.51 - Out-of-plane piezoresponse of the PFM images of the 001-oriented PZT54 single crystal: (a) after poling at $V_{dc} = -30$ V applied to the tip on area $2 \times 2 \mu\text{m}^2$; (b) after 41 h and c) polarization with time.

In general, in the rhombohedral region we have not enough information to conclude about the changes on the domain distribution with the compositions, but in the tetragonal region, including the MPB, it is possible to give a first approximation about that evolution: the number of domains increases when the compositions approach that of the MPB, in such a way that they are not observed anymore for the MPB composition.

4.5. Thermodynamics of the systems

In chapter I it was discussed the importance of the evaluation of the coefficients of the thermodynamic energy function (Equation I.8, all the equations used in this section are given in the Appendix I) α_{11} , α_{12} , α_{111} , α_{112} and α_{123} , which are determined using the experimental data from χ_{11} and χ_{33} together with any pair of other measured parameters (for example, piezoelectric and polarization, strain and polarization, parameters). It is possible to obtain all the parameters by fitting the experimental data with the appropriate equations [117-119, 321-323]. In practice, Equation I.30 is used in the paraelectric part and the Equations I.31 and the inverse of I.28 in the ferroelectric part of the susceptibility. These equations are dependent on the structure and the measurement direction of the crystal. Equations I.30, I.31 and the inverse of I.28 were fitted to the experimental data of the susceptibility and the parameters were determined for the minimum of error between the fitting function and experimental data.

In Figure 4.52a it is shown the temperature dependence of the dielectric permittivity together with the fitting curve in the [001] direction for a rhombohedral crystal, PZT60. In this case the fitting was carried out in all, paraelectric and ferroelectric, range and the parameters are not fixed. Appreciable differences are observed between the experimental data and the fitted curve. Therefore the analyzed interval was to the range of temperature where the Curie-Weiss law is obeyed and the parameters of the Curie-Weiss law (T_c , T_0 and C) are determined using the temperature dependence of the inverse of the dielectric permittivity (Figure 4.52b).

The values of the parameters T_c , C and T_0 can be obtained using the Curie-Weiss law. This reduces the number of parameters to evaluate and select in the interval to fit. This method was used in the first part of our calculation (T_c , C and T_0 were fixed), but to optimize the fit these parameters were not fixed. In Figure 4.53 it is shown the new fitting curve. As expected, it is observed a good fitting of the experimental results in a large interval of the temperature, but there is no matching near T_c . This is due to the assumption that only α_1 was dependent on the temperature or because this function does not obey this system. The previous method was used to determine the parameters of all the crystals and they are resumed in 4.11.

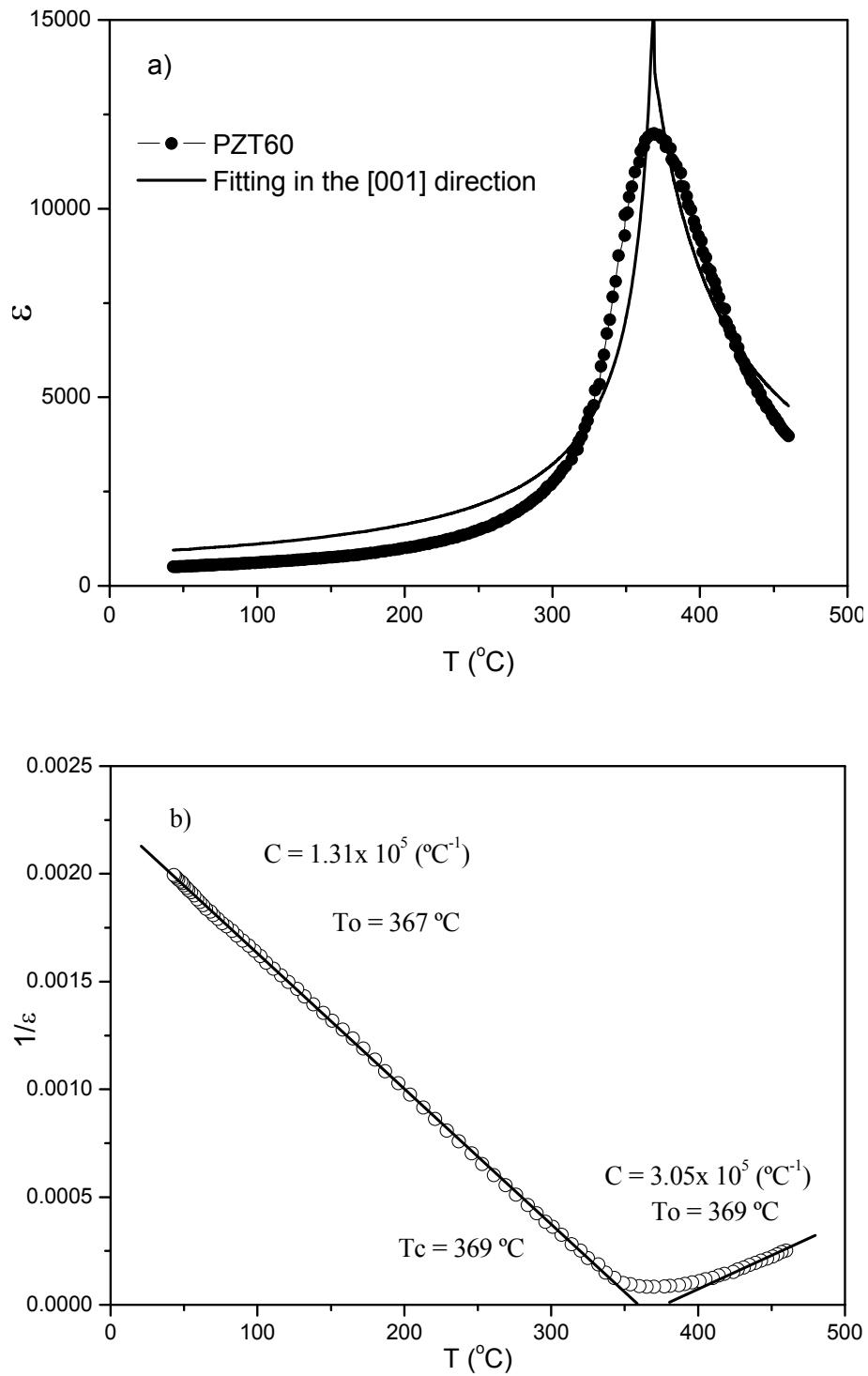


Figure 4.52 - a) temperature dependence of the dielectric permittivity together with the fitting curve (Equation I.30 and the inverse of Equation I.28) and b) temperature dependence of the inverse of the dielectric permittivity (during cooling, at 100kHz).

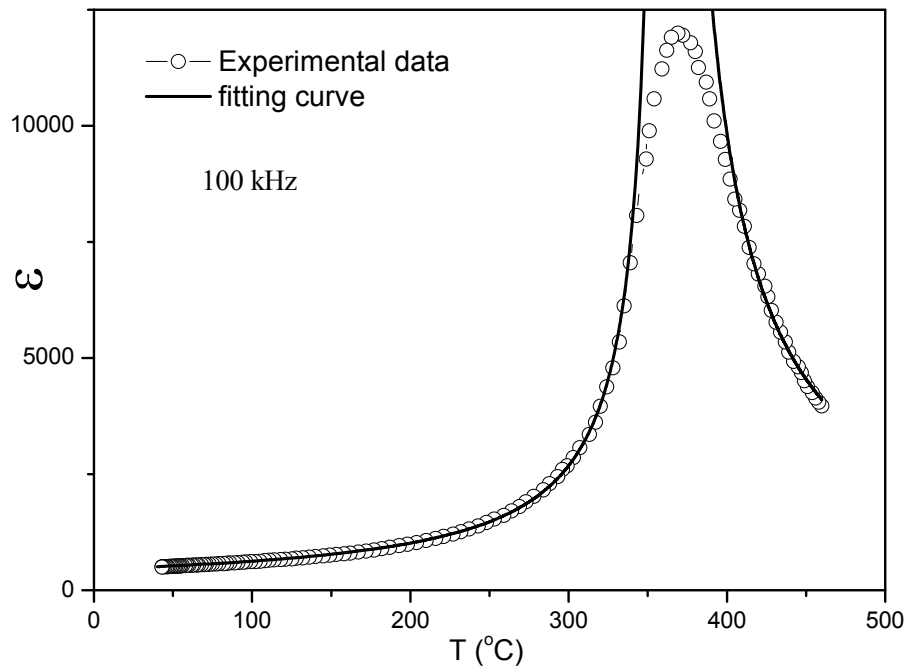


Figure 4.53 - Temperature dependence of the dielectric permittivity together with the new fitting curve in PZT60.

Table 4.11 - Parameters obtained by fitting the experimental data of the dielectric permittivity using Equations I.30, I.31 and the inverse of I.28. The values of α_1 and the polarization (P_s) were calculated at T_c and at room temperature (30°C). The values were obtained in the $[001]$ direction and 100kHz.

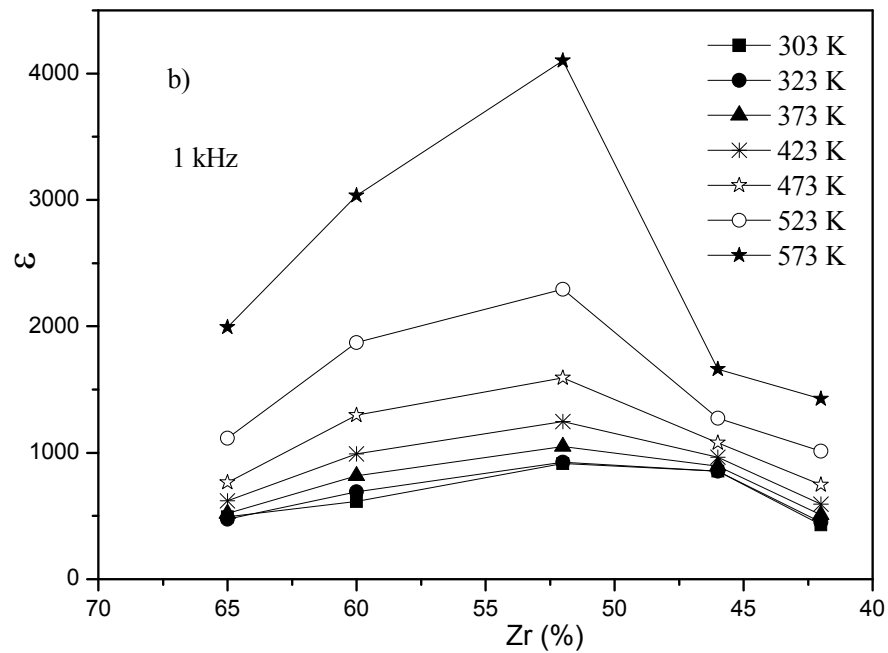
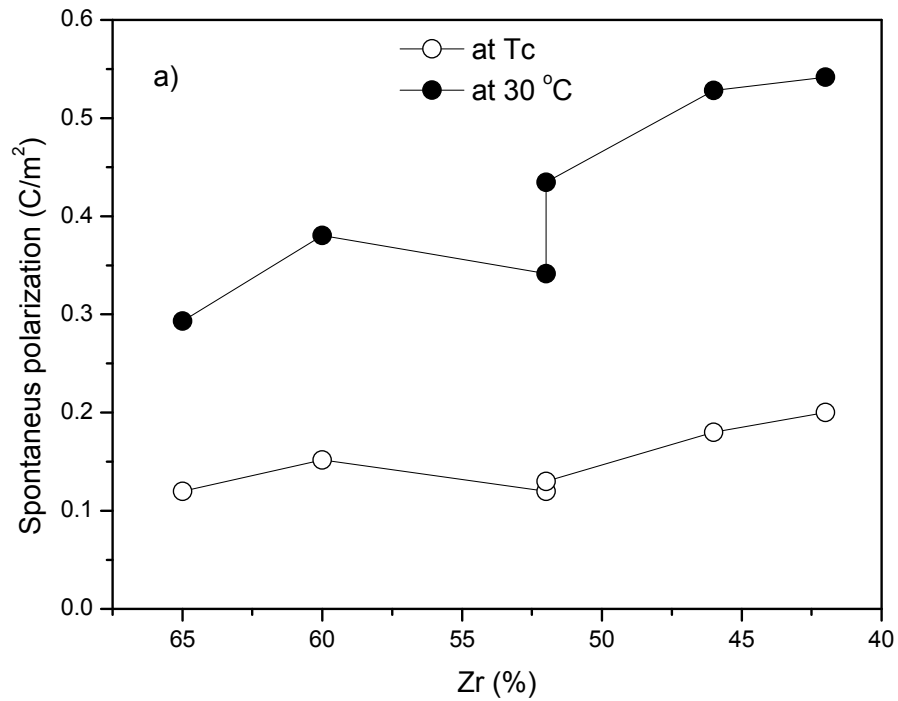
			Rhombohedral phase ϵ_{33}								$T < T_c$		$T > T_c$	
Cristal	ϵ_{\max}	$T_{\max} \equiv T_c$ ($^\circ\text{C}$)	T_0 ($^\circ\text{C}$)	P_0 (C/m^2)	$P(30^\circ\text{C})$ (C/m^2)	$C \times 10^5$ ($^\circ\text{C}^{-1}$)	$\alpha_1(30^\circ\text{C}) \times 10^8$ ($^\circ\text{C}$)	$\alpha_1(T_c) \times 10^9$ ($^\circ\text{C}$)	ζ $\times 10^9$	ξ $\times 10^{12}$	T_0 ($^\circ\text{C}$)	$C \times 10^5$ ($^\circ\text{C}^{-1}$)		
PZT65	15700	367	363	0.12	0.29	1.13	-1.66	1.99	-0.06	10.30	367	2.64		
PZT60	9900	369	367	0.15	0.38	1.31	-1.45	0.86	-1.54	0.84	369	3.05		
PZT52	20800	361	359	0.12	0.34	1.82	-1.02	0.62	-2.90	3.66	361	3.96		
			Tetragonal Phase ϵ_{33}								$T < T_c$		$T > T_c$	
Cristal	ϵ_{\max}	$T_{\max} \equiv T_c$ ($^\circ\text{C}$)	T_0 ($^\circ\text{C}$)	P_0 (C/m^2)	$P(30^\circ\text{C})$ (C/m^2)	$C \times 10^5$ ($^\circ\text{C}^{-1}$)	$\alpha_1(30^\circ\text{C}) \times 10^8$ ($^\circ\text{C}$)	$\alpha_1(T_c) \times 10^6$ ($^\circ\text{C}$)	α_{11} $\times 10^7$	α_{111} $\times 10^9$	T_0 ($^\circ\text{C}$)	$C \times 10^5$ ($^\circ\text{C}^{-1}$)		
PZT52	20800	361	354	0.13	0.43	1.97	-1.02	0.31	-8.29	0.73	361	3.96		
PZT46	32800	408	406	0.18	0.52	2.33	-0.56	0.30	-2.84	1.03	408	3.92		
PZT42	22900	429	426	0.20	0.54	1.87	-1.19	0.90	-6.02	1.09	429	3.58		

The composition dependence of the calculated spontaneous polarization is plotted in Figure 4.54a, for $T = T_c$ and for $T = 30^\circ\text{C}$. For both temperatures, in the tetragonal field, it is

observed an increase of the polarization with the increase in the Ti content. In the rhombohedral part, it is not found a similar behaviour. The presence of two points in the composition with 52 % of Zr content is because, for this composition, it was calculated using two model, the rhombohedral and the tetragonal one. It was predicted by several works that no maximum is found in the polarization in the MPB [117-119, 321-323], despite the maximum found in the dielectric measurements (Figure 4.54b) or in other electro-mechanical properties (see chapter 1). PZT is a system in which the polarization is originated by the displacement of a group of ions in respect to an electrostatic equilibrium in the unit cell of the material. The displacement of these ions are related to the unit cell distortion, where low distortions (with respect to a cubic structure) correspond to low displacements of the ions and vice-versa [324]. The unit cell distortion in the tetragonal field decreases with the increase of the Zr content, which decreases the spontaneous polarization in the material. This explains the decrease of the polarization in the tetragonal field upon increasing the Zr content in Figure 4.54a. In the rhombohedral field one would expect a similar behaviour of the polarization but a clear behaviour is not observed. The presence of a local minimum in the polarization is possible in the centre of the MPB but it is not clear too Figure 4.54a. In our work is believed that low electric fields or mechanical stress can change the symmetry of the crystal near the centre of the MPB. This change in symmetry (between tetragonal and rhombohedral or monoclinic) with a low electric field or small stress can occur because it exists instability of the tetragonal structure [122] due to the decrease of the unit cell distortion [9]. This deformation can increase the dielectric and piezoelectric properties but not the polarization. The coexistence of phases or the monoclinic phase in the vicinity of the MPB in polycrystalline materials can be explained by internal effects (internal stress or deformations).

The composition dependence of the Curie constant is shown in Figure 4.54c. A maximum is observed near the centre of the MPB in both cases (determinations from the paraelectric and the ferroelectric regions). The values obtained from the paraelectric region are slightly higher than those from the ferroelectric region as already seen in Figure 4.35. These values are not in concordance with the ones determined using the inverse of the Curie-Weiss law (Figure 4.35), although a maximum was also here observed. The difference between these results is because the model introduces several parameters of superior order in the free energy equation, which affects the obtained result in relationship

with the Curie-Weiss law. These values are in agreement with those determined by others [325]. The other parameters presented in Table 4.11 are in agreement with the literature [325, 326].



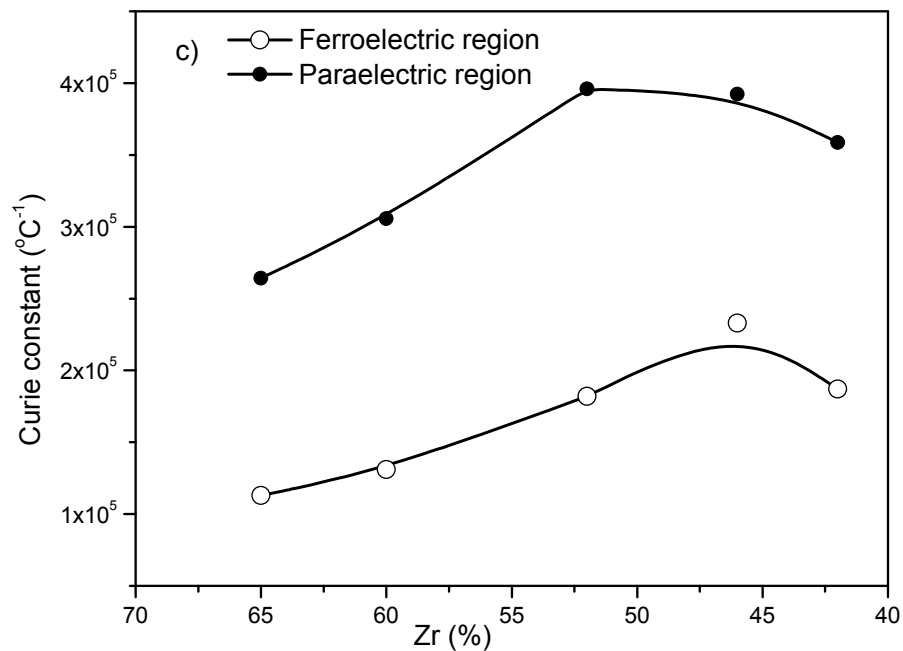
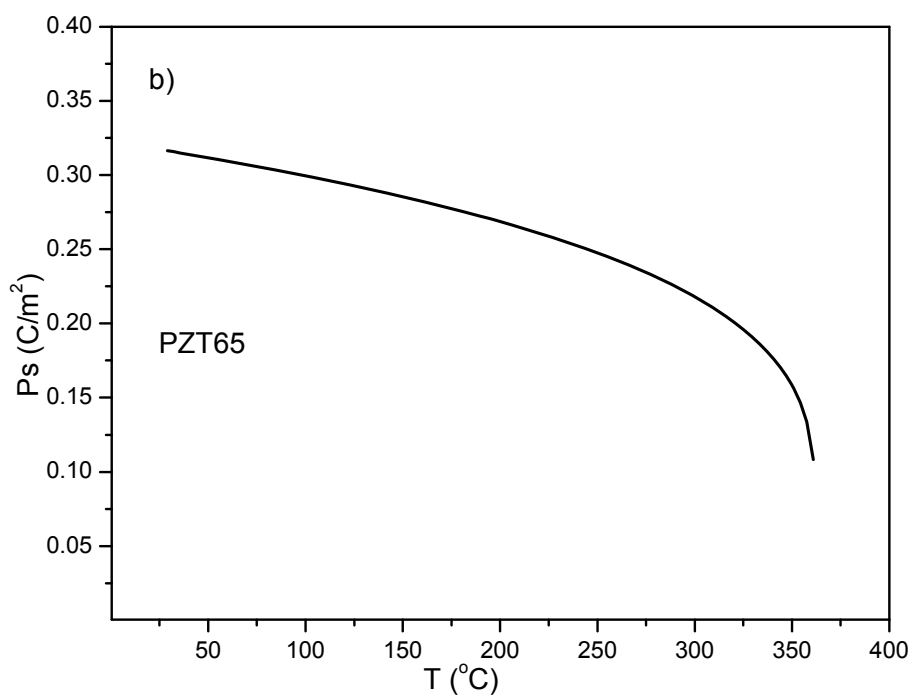
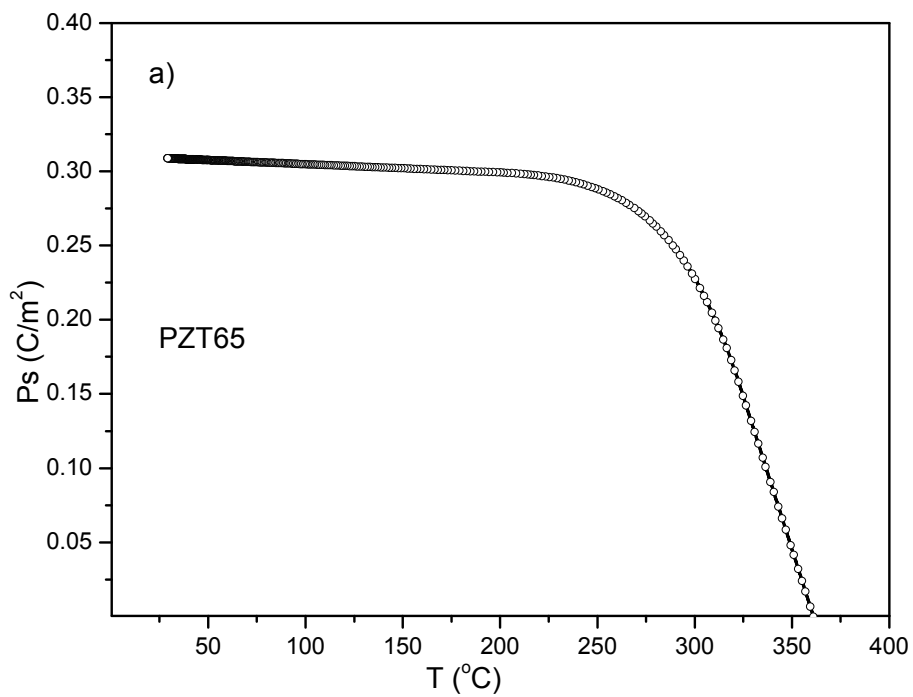


Figure 4.54 - Composition dependence of: a) calculated spontaneous polarization, b) dielectric permittivity and c) Curie constant, obtained by fit the data using the thermodynamic equations in the [001] direction.

The values of the parameters α_{11} , α_{12} , α_{111} , α_{112} and α_{123} (Appendix I), for the crystals with rhombohedral structure, were not obtained. It is possible to determine the spontaneous polarization with the temperature by the pyroelectric current (Equation 1.13) and the results for the PZT65 are presented in Figure 4.55a. The spontaneous polarization can be also calculated from the thermodynamic model (Equation I.45) using the determined values of T_c , T_o and P_o (Table 4.11) as represented for the PZT65 in Figure 4.55b. P_s can also be calculated using the Equation I.51 and obtained the value of P_o from the hysteresis loop, the values of the parameter of T_c and T_o can be obtained from Table 4.11 (Figure 4.55b). It is observed that a difference exists between these results for P_s . This difference may come from the different experimental techniques used to calculate P_s , *i.e.*, the pyroelectric current (Figure 4.55a), permittivity (Figure 4.55b) and hysteresis loop (Figure 4.55c). The contribution of conductive charges to the depolarization of the crystal can also contribute to the differences or simply because the Formula I.51 does not describe correctly the polarization in the rhombohedral PZT crystal. Other thermodynamic coefficients can be determined and they are presented in the Appendix II.



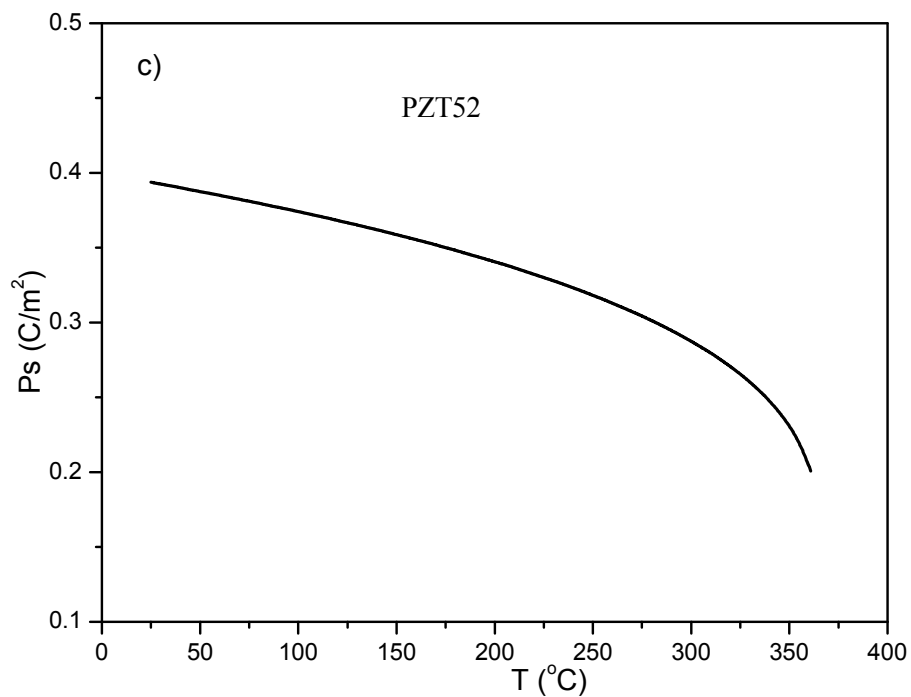


Figure 4.55 - Temperature dependence of the spontaneous polarization: a) calculated from the pyroelectric current and b) calculated from the thermodynamic model for the PZT65 and c) calculated from the hysteresis loop of the PZT52.

CHAPTER 5

Processing and characterisation of $PbZr_xTi_{1-x}O_3$ ceramics

The main purpose of this chapter is the study of the processing and characterisation of PZT ceramics, namely the relation between the grain size distribution, the dielectric properties and the composition effect. Samples with compositions around the MPB were obtained using different sintering times. The effect of the sample composition and sintering conditions (Temperature and time) on the dielectric properties was analysed. The domain structure was determined for samples with compositions in the centre of the MPB and with different grain sizes. Several glassy phases were deliberately introduced in the PZT composition. The main objectives of introducing the liquid phase were to increase the densification, to decrease the sintering temperature and to promote the grain growth. Additionally, less usual methods such as seeded polycrystalline conversion method (SPC) has been tempted in order to obtain large grains or single crystals inside of a polycrystalline ceramic matrix [327, 328].

The experimental results are discussed in separated sections as follows. Firstly, the characterisation of PZT ceramics without liquid phase (dielectric and domain distribution characterisation) will be presented. In the second part, it will be analyzed the effect of the initial processing parameters and the introduction of different liquid phases on the final density of PZT ceramic with several compositions around the MPB. Then, the microstructure evolution is analyzed and correlated with the processing parameters and dielectric measurements. Finally, the seed crystals were introduced in the ceramic and the effect on the sintered microstructure were analyzed using SEM.

5.1. PZT ceramics without a liquid phase

The ceramics analyzed in this section were prepared using the method described in chapter 3, without a liquid phase. In Table 5.1 it is resumed the density (ρ) and the average grain size (\bar{G}) of the ceramic sintered in this work.

Table 5.1 - Relative density (ρ) and average grain size (\bar{G}) for the ceramics prepared using different composition and sintering times. The sintering temperature was 1250 °C, during 2 or 16 h, for all the samples.

Samples		PZT60	PZT57	PZT55	PZT54	PZT53	PZT525	PZT52	PZT51	PZT49	PZT47	PZT43
2h	$\rho(\%)$	93	95	94	96	95	96	94	95	96	94	96
	$\bar{G}(\mu\text{m})$	7	7	7	7	7	7	7	7	7	7	7
16h	$\rho(\%)$	-	-	-	98	98	96	98	-	-	-	-
	$\bar{G}(\mu\text{m})$	-	-	-	17	17	14	17	-	-	-	-

The density and the average grain size are not dependent on the composition, in the analyzed interval. On the other hand they are dependent on the sintering time.

5.1.1. Dielectric characterisation

In Figure 5.1 it is shown the dielectric permittivity as a function of the temperature for several compositions of PZT ceramics sintered at 1250 °C, 2h: in a) on heating from room temperature up to 460 °C and in b) on cooling from room temperature down to 20 K. The frequency used in the measurement was 250 kHz. The dielectric permittivity reaches a maximum at T_c , near the composition of 52.5% of Zr content [23].

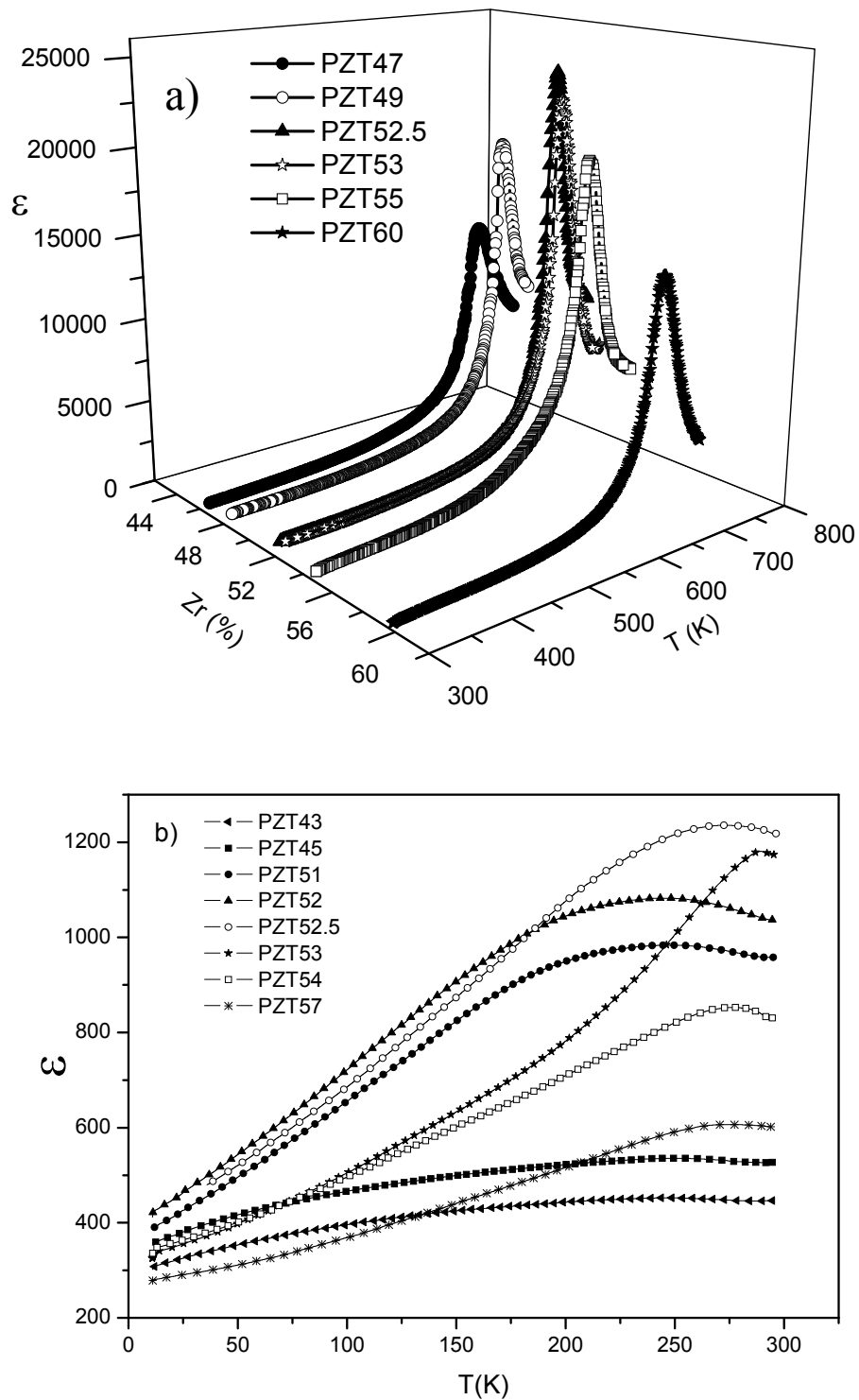
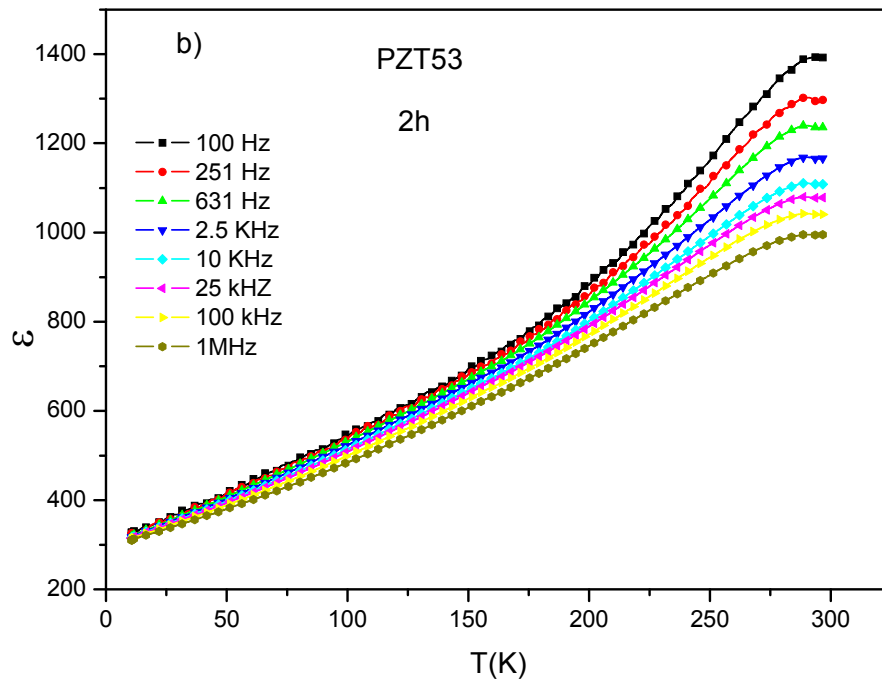
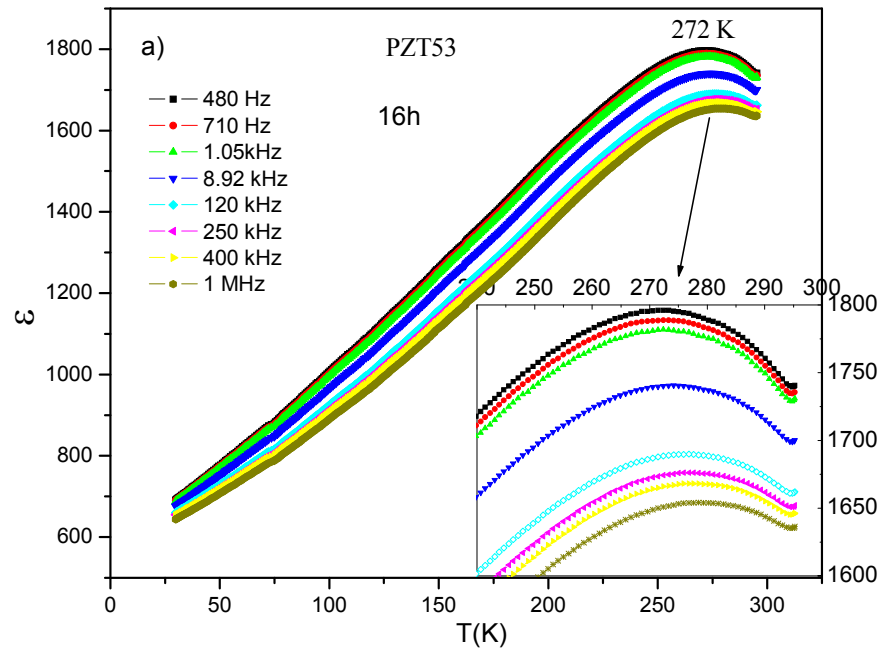


Figure 5.1 - Dielectric permittivity as a function of the temperature for several compositions, where the number in the label means the amount (%) of Zr: a) on heating and b) on cooling (samples sintered at 1250 °C, 2 h; measurements at 250 kHz).

The dielectric permittivity increases with the sintering time Figure 5.2. Figure 5.2a) shows the dielectric permittivity measured during cooling as a function of the temperature for the PZT53 ceramic sintered at 1250 °C, 16 h. In Figure 5.2b) it is shown the same composition but with 2 h of sintering time and in Figure 5.2c) it is compared the dielectric permittivity, at 250 kHz, of samples sintered for 2 and 16 h. Differences in dielectric properties may come from an effect of the grain size [9, 109, 113], among other features. The samples sintered for 2 and 16 h (see Table 5.1) have a medium grain size of 7 and 17 μm , respectively, and a significant difference is observed in the dielectric permittivity (Figure 5.2c). Other effect observed in these measurements is the presence of an inflection near room temperature for both samples which also appears in other compositions around the MPB (Figure 5.1b)). It is not associated to any structural phase transition. As mentioned in Dai *et al.* [313] work, this transition is associated (in the rhombohedral part, with Zr concentrations higher than 55 %) with a coupling between the polarization and the random octahedral strains due to a disorder in the oxygen octahedron rotations. These strains may decouple the long-range polar order on cooling, resulting in fluctuation effects in the polarization characterized by a dielectric dispersion [313]. In Herbiet *et al.* [329] work, this inflexion corresponds to a relaxation which is attributed to domain walls vibrations. The same explanation is proposed by Zhang *et al.* [330]. They found a large contribution of the domain walls when weak external electric fields are applied at room temperature. In any case, this peak is a relaxor type effect, because it depends on the frequency (Figure 5.2a) and b)), in accordance with other authors [331]. This effect could be related with the transition found in single crystals (section 4.2). The exact cause for this inflexion is difficult to conclude. It can be a mixture of effects, domain contribution, defects, charge movement and disorder in the oxygen octahedrons. The understanding of the real cause of this behaviour needs more experimental work (measurement of the dielectric impedance at high frequency between 1MHz to 1GHz, pyroelectric characterisation in the temperature range between 200K to 350K, Raman scattering and piezoelectric measurement in this temperature interval, among other). In this work these characterisations were not performed because we have not access to these techniques at low temperature.



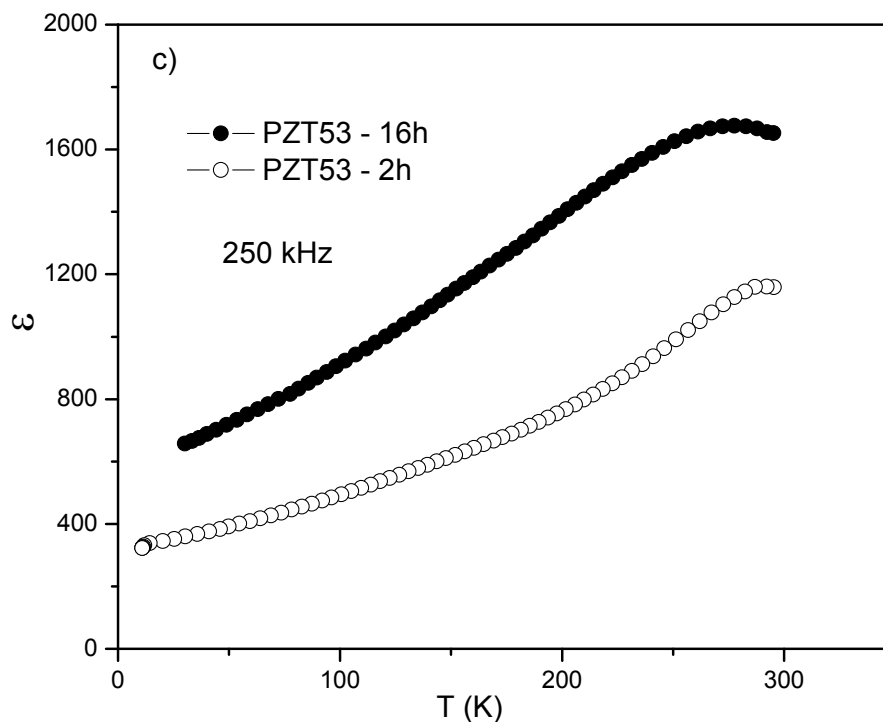


Figure 5.2 - Dielectric permittivity as a function of the temperature for the PZT53 ceramic (measured during cooling) sintering at 1250 °C, during: a) 16 h and b) 2 h, both for several frequencies, and c) 2 and 16 h, for 250 kHz. The insert in a) is a magnification of the results near room temperature.

The dependence of the permittivity with the composition of ceramics in the range of temperatures of 10K to 633K, together with the values extrapolated to 0 K, is shown in Figure 5.3. It is possible to observe a maximum in the centre, in the morphotropic phase region, for all the temperatures from 10 K to 450 K and that this maximum shifts for the Zr rich part with the increasing of the temperature. Taking into consideration the previous works on crystallography [6, 126, 294, 332], in the MPB there are four spacial groups: the monoclinic of low temperature (Cc), the monoclinic of high temperature (Cm), the tetragonal (P4mm) and the cubic (Pm3m) in the paraelectric state. Among the various theories developed to explain the high values of the electro-mechanical properties in the MPB, that of Noheda *et al.* [333] correlates those high values to the presence of the monoclinic phase. Looking at Figure 5.3, the maximum is still present at 450 K, temperature at which the monoclinic phase was not detected in literature [6]. This indicates that the large electro-mechanical properties in the MPB cannot be attributed to this phase.

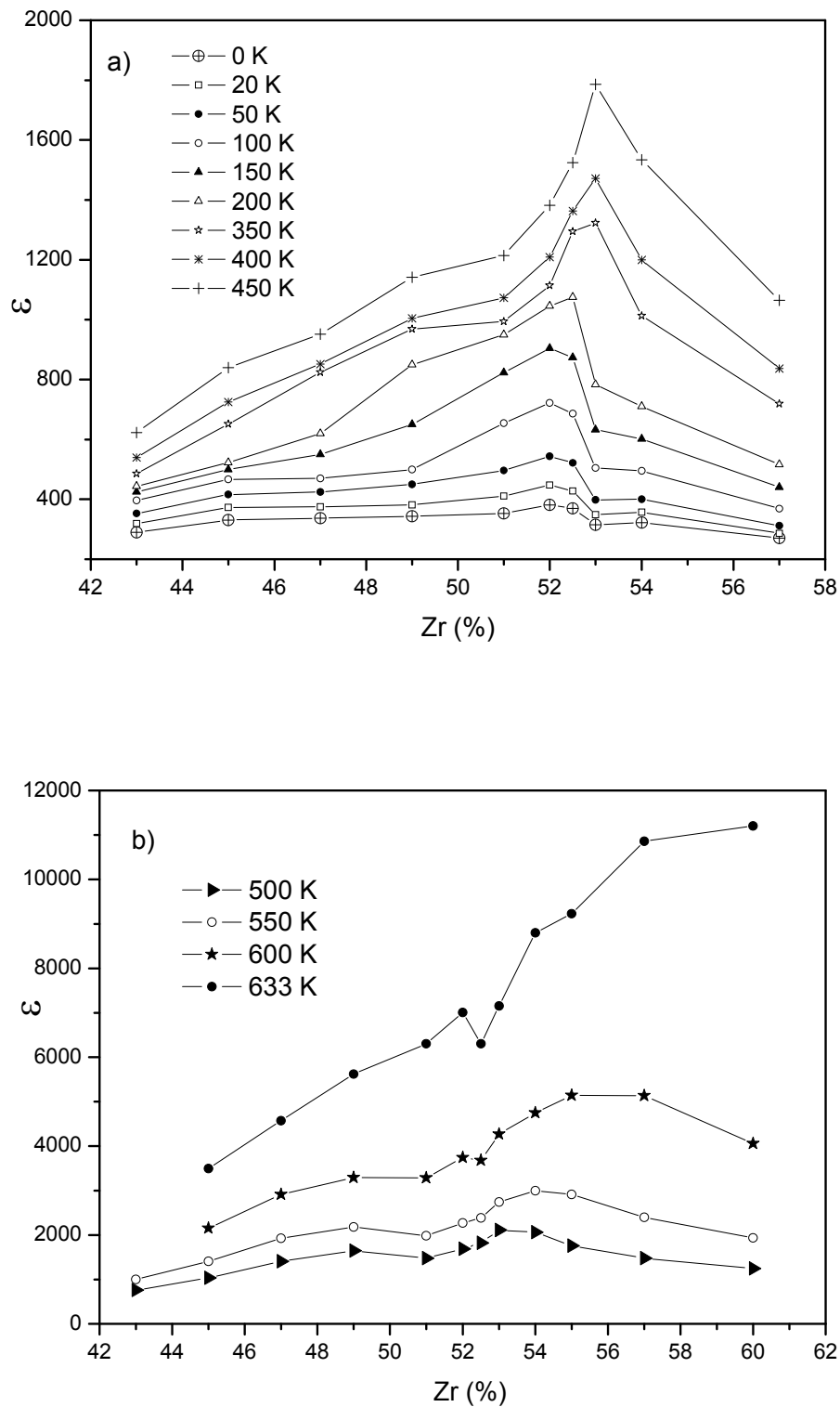


Figure 5.3 - Dielectric permittivity vs Zr concentration in ceramics for several temperatures (at 250 kHz). The values for 0K were extrapolated from the dielectric measurement at low temperature from Figure 5.2a.

A monotonous increase of the permittivity and other properties when the composition is approaching the MPB (Figure 5.3 and Figure 1.13 and Figure 1.15) [30] are already observed in PZT for compositions out of that region and, therefore, this increase can not be related with the MPB. A decrease of the unit cell distortion was observed in the rhombohedral and tetragonal phases when the composition is approaching the centre of the MPB. Probably the decrease of the distortion is responsible for the increase of the electro-mechanical properties in the PZT system. A decrease of the unit cell distortion can increase the domain movement, as can be found in the tetragonal part of the phase diagram [330].

In a previous work, it was reported the dependence of the dielectric permittivity with the concentration of Zr in PZT ceramics at room temperature for the tetragonal and rhombohedral phases and extrapolated to the morphotropic region [9]. The empiric conclusion of the authors was that the mixture of phases (coexistence model) has not a positive influence in the high values of the permittivity in the MPB. The values of the permittivity in the tetragonal phase are slightly greater compared with the values obtained for the rhombohedral phase. The extrapolation of the dielectric permittivity to the morphotropic region has a significantly greater increment in the tetragonal phase than in the rhombohedral one. These results were confirmed later by others authors [123].

Taking the values of the Ti concentration corresponding to the maximum of the permittivity at different temperatures, in Figure 5.3a), and representing them in Figure 5.4, together with the structural data of Noheda *et al.* [6] and Jaffe *et al.* [30], the following observations may be done: (i) the behaviour of the maximum of the temperature with the composition is close to the phase diagram reported by others [6]. (ii) This maximum in the dielectric properties with the composition (Figure 5.3a)) could be related to the change on the molar fractions of the rhombohedral and tetragonal phases (lever rule), but this rule cannot explain the maximum for temperatures higher than 450 K (Figure 5.3b)), since the mixture of phases is not present anymore. (iii) A possible explanation for this line can be given by the decrease of the unit cell distortions [123], since both in the rhombohedral and tetragonal regions the distortions come to a minimum in this composition range [10], i.e., the structures are near a cubic cell. The decreasing of the distortion increases the domain mobility and therefore weak electric fields can activate the domain response.

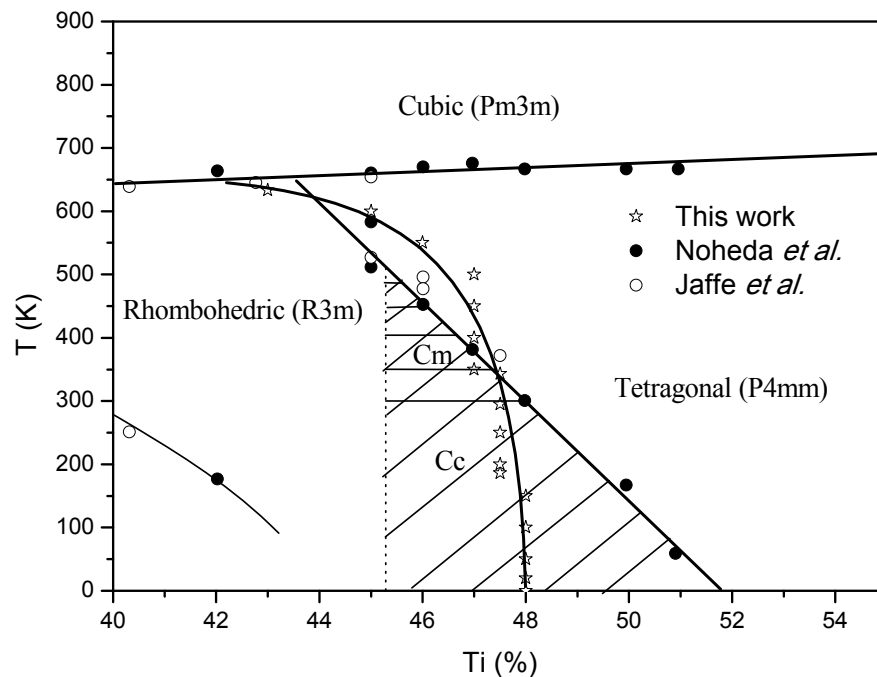


Figure 5.4 - Phase diagram for the PZT system from Noheda *et al.* [6] and Jaffe *et al.* [30], together with our results taken from the values of the observed maxima in Figure 5.3. Cc represents the monoclinic phase of low temperature and Cm the monoclinic phase of high temperature.

5.1.2. Piezoelectric response and distribution of domains

The piezoelectric properties depend strongly on the ferroelectric domain structure. Piezoelectricity-related constants (d_{ij}) were found to increase with decreasing the domain size [334] and it has been also pointed out that 90° domain wall motion may be responsible for the enhancement of the piezoelectric properties [334, 335].

In polycrystalline ferroelectric materials, the domain structure is affected by the microstructure. Extensive studies have been made on the observation of domain structures, particularly in thin films, using various techniques such as chemical etching [205, 336], transmission electron microscopy [337, 338] and scanning force microscopy (SFM) [290, 339].

Chemical etching has been widely used in the observation of domain structures in ferroelectrics owing to the observation by Hooton and Merz [340] that crystal planes of barium titanate have differential etching rates when etched in hydrochloric acid depending of the polarization direction. At room temperature, barium titanate has a tetragonal

structure and is polarized along the c -axis, (the polar axis). Domains polarized along the normal of the polished surface of the grains (outward to the normal) have the highest etching rate and domains polarized opposite to the normal, $[00\bar{1}]$ direction, have the lowest etching rate. All other orientations have intermediate etching rates. The difference in etching rate gives rise to topographical contrast, revealing the domain structure. For example, Devries and Burke [341], Arlt and Sasko [342] and Hu *et al.* [343] have investigated domain structures of chemically etched polycrystalline barium titanate using SEM.

In Figure 5.5 to Figure 5.7 are shown SEM micrographs of chemically etched PZT ceramics (see section 3.4) with 52.5 molar percent of Zr. A difference in the etching rate gives rise to topographical contrast. Based on the resemblance of the observed patterns with the domains in barium titanate reported by Arlt and Sasko [342] and within PZT ceramics and single crystals reported by others [232, 344-346], we assume that the topographic difference is due to the domain structure in the PZT grains.

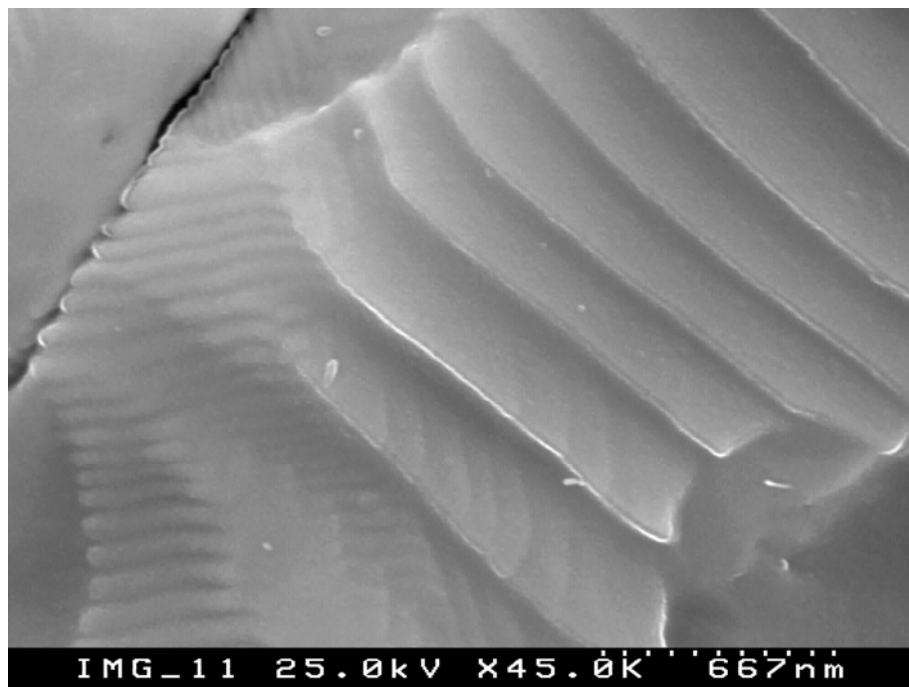


Figure 5.5 - Micrograph of PZT525 ceramic sintered at 1200 °C, during 2h. This is a photograph of a fracture surface chemically etched.

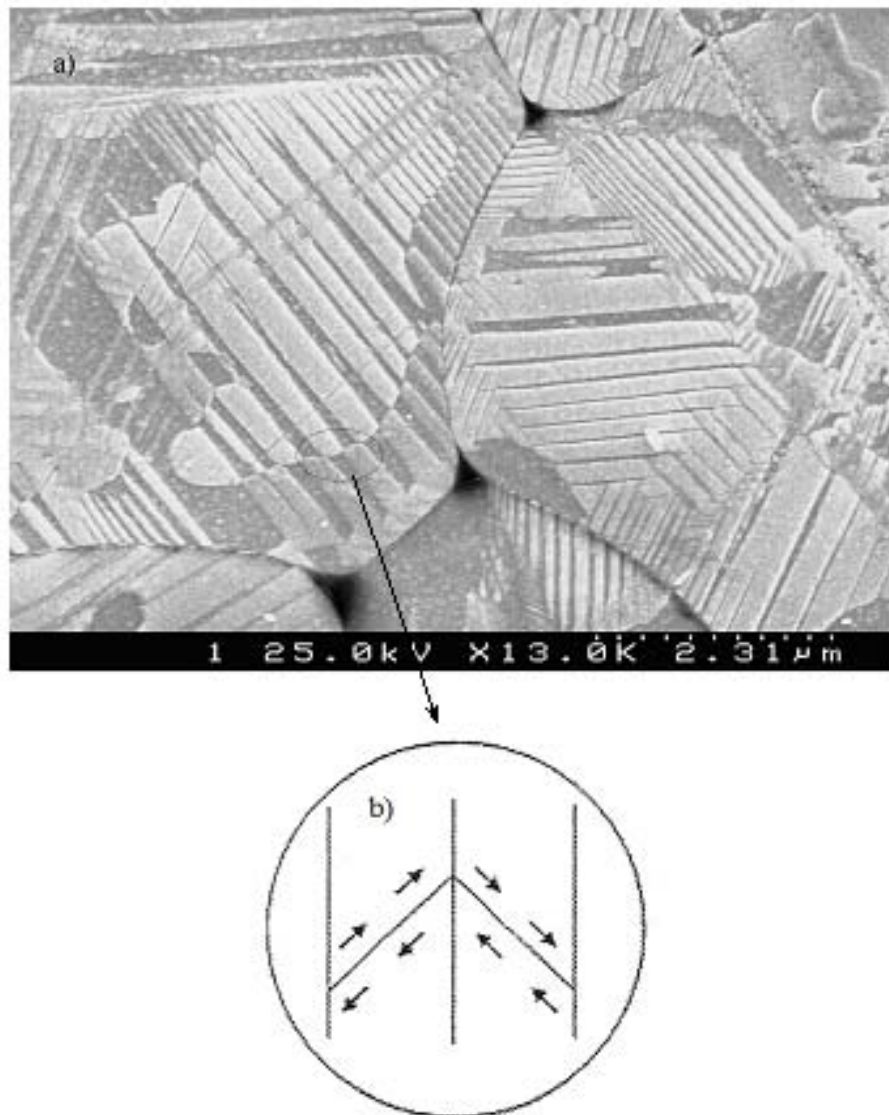


Figure 5.6 - a) Micrograph of the polished PZT525 ceramic sintered at 1200 °C, during 5h; b) schema of typical domain boundaries of the magnified circle region in a).

It is observed the characteristic domain patterns in unpoled PZT fracture surface (Figure 5.5) and in polished surfaces (Figure 5.6 and Figure 5.7). It was found that a band structure (herringbone pattern), composed of 90° domains, predominates and several variants are observed simultaneously in each grain [1]. The domain width varies from approximately 100 to 300 nm. We have not measured domains directly, but rather the actual topographic features resulting from differential etching rates associated with the different domain orientations. The domain wall orientations were also not directly determined, but it is possible to determine them performing a stereographic analysis on the herringbone pattern

observed in the crystallites (Figure 5.7a), as determined by Saldaña [345] and Tsurekawa [344]. Assuming that domain walls have a specific crystallographic orientation, we can confirm that the banded structure is composed by 90° domains and the domain walls are oriented parallel to $\{110\}$ planes and the grain in Figure 5.7a is polished perpendicular to the $\langle 001 \rangle$ directions. It is supposed that each grain is a crystallite (single crystal) and monophasic.

In the literature it is reported that the domain size decreases with decreasing the grain size [347-349]. We verified such trend for the PZT55 composition. Figure 5.7 shows the domain structure in two grains, one of $6 \mu\text{m}$ and another of $17 \mu\text{m}$, as examples. It was analysed the domain features (domain size and domain density) for three grain sizes, as summarized in Table 5. 2. In Figure 5. 8 it is shown the dependence of the average domain size (d) with the average grain size (G). This dependence is not parabolic, $d \propto G^{1/2}$, as reported by Kittel [350] and Arlt [39] for $BaTiO_3$, or later by Cao and Randall [351] for PZT ceramics. Cao and Randall [351] also found that, for grain sizes lower than $1 \mu\text{m}$, the domain densities were higher than the values predicted by using the parabolic relation. In this work, we obtained the relation $d \propto G^{1/3}$.

Table 5. 2 - Average grain size (G), number of analysed grains (# grains), total number of domains (# domains), average domain size (d) and domains density (# domains/ μm^2) per grain.

G (μm)	# grains	# domains	Average domain size (d)	Domains density (# domains/ μm^2)
6	5	500	100	3.54
9	6	340	120	0.89
17	7	280	140	0.18

Near the grain boundaries, the domain size can be not altered relatively to the bulk or the domains size can be decrease as observed in Figure 5.6a). The domains near the grain boundaries normally form twinning, which is a consequence of the stress between the grains. A slight deformation of the lattice cell leads to a slight deformation of the crystallite which is built up of the deformed lattice cells. This deformation, however, is more or less

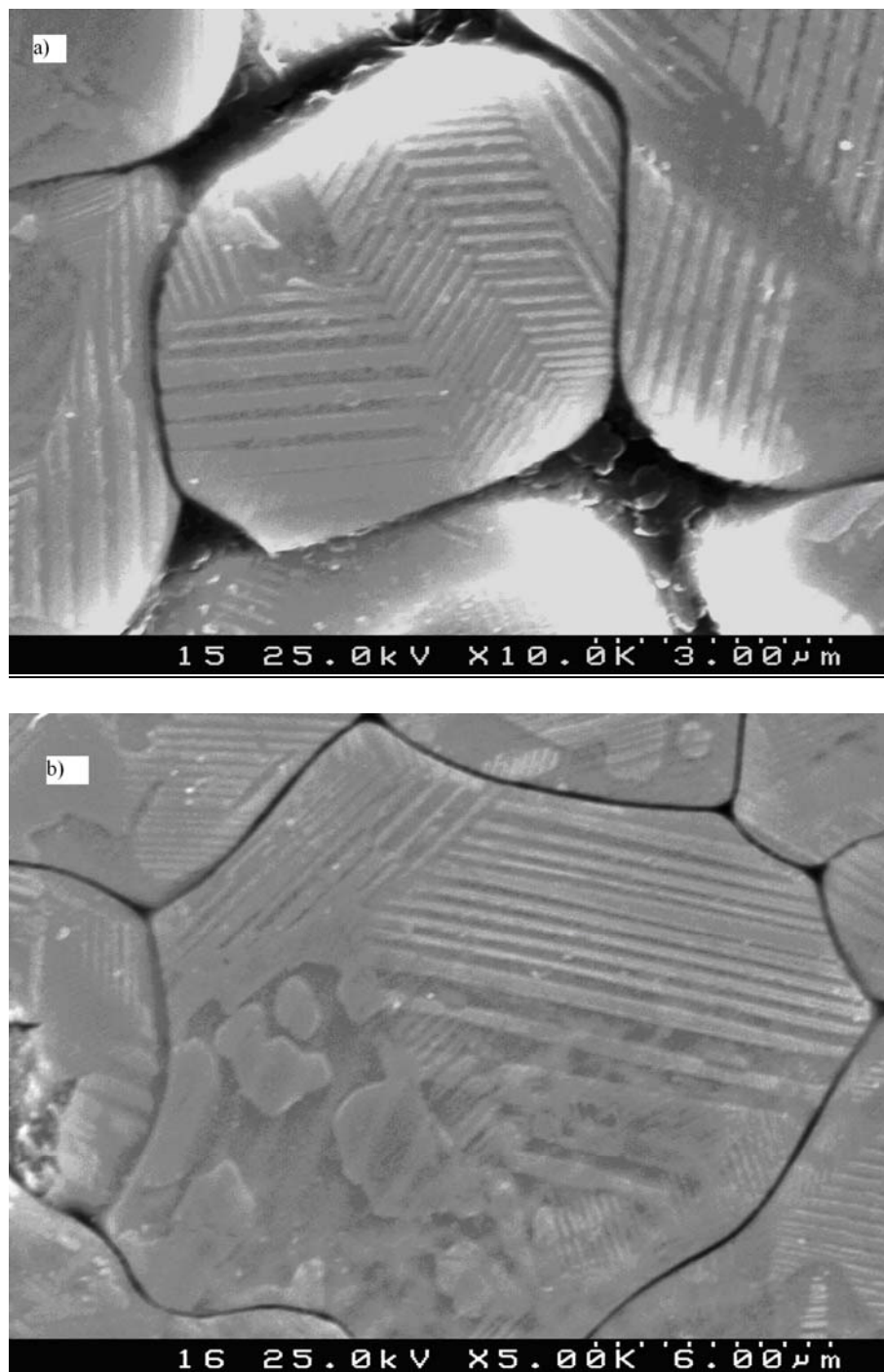


Figure 5.7 - Micrograph for PZT55 ceramic sintered at 1200 °C during 2h. a) Illustrates a 6 μm grain and b) illustrates a 17 μm grain.

obstructed by the surroundings of the crystallite producing stresses in the grains. A single crystal is free and can therefore, in principle, deform like the lattice cell and it does not

need twins, from the mechanical point of view. On the other hand, a grain in a ceramic is clamped by its neighbours in all the directions. It can be equally deformed by cooperative motion of the adjacent grains. To maintain the shape it requires either high stresses or mechanical twinning, which at least preserves the gross shape of the grain. In addition to these conditions of the boundaries, heterogeneous stresses, caused by mutual interactions between adjacent grains or by heterogeneous composition, heterogeneous cooling through the phase transition, composition dependence phase transition temperatures and other irregularities will cause additional irregular twinning.

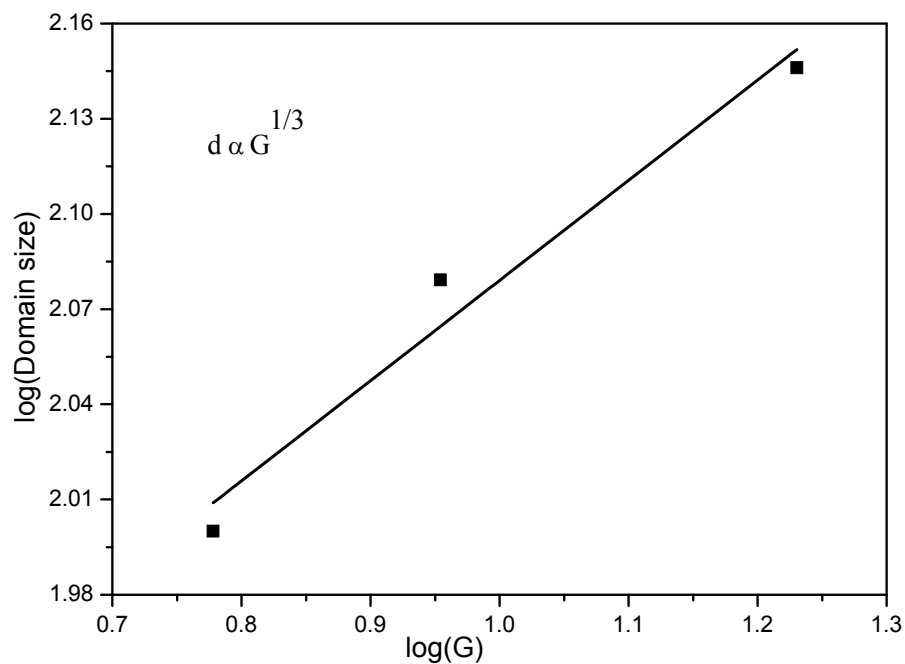


Figure 5. 8 - Dependence of Average grain size (G) with the Average domain size (d).

One of the characteristic features of the domain configuration in PZT ceramics is the band structure of 90° domains (Figure 5.7), where the domain walls are oriented parallel to the $\{110\}$ planes. These relations have been summarized in the spatial domain configuration of Figure 5.9 [342, 345].

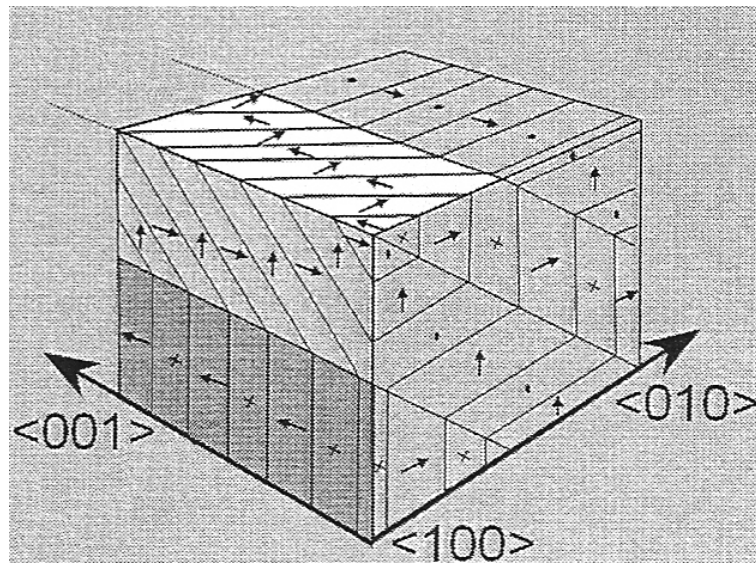


Figure 5.9 - Spatial domain configuration in PZT ceramics. In white, it is shown the herringbone pattern frequently observed in the form of a banded structure [342, 345].

The best procedure used to study the domain distribution is the exploring of the domains image with AFM and PFM techniques. In this work it was used an AFM to visualize the domain pattern in PZT samples. Figure 5.10 and Figure 5.11 show the topography and the out-of-plane piezoresponse of two samples sintered at 1200 °C with different holding time, 2 and 16 h, respectively. In the topographic image it is observed a similar result to that obtained using chemical etching. The herringbone pattern is frequently observed here too, in the form of a band structure (Figure 5.10a and Figure 5.11a). The out-of-plane piezoresponse images clearly show that these structures are 90° oriented but we cannot say, which is the real orientation of each domain, because the in-plane images do not have a good quality. However, the last result confirms the results obtained using chemically etched (that the surfaces structures in SEM image are domains Figure 5.7).

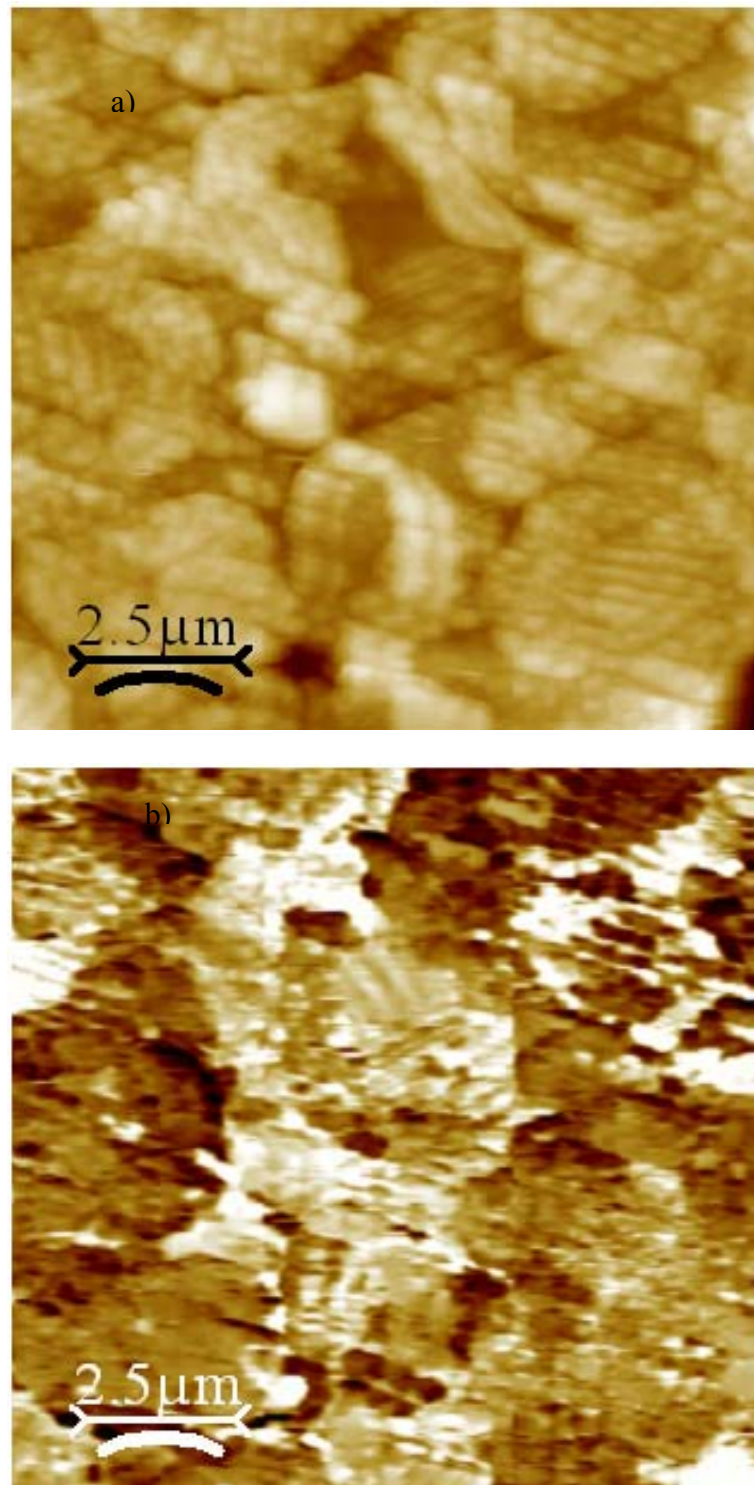


Figure 5.10 - AFM images of the PZT525 ceramic sintered at 1200 °C, during 2h: a) topography of the grain and b) the out-of-plane piezoresponse.

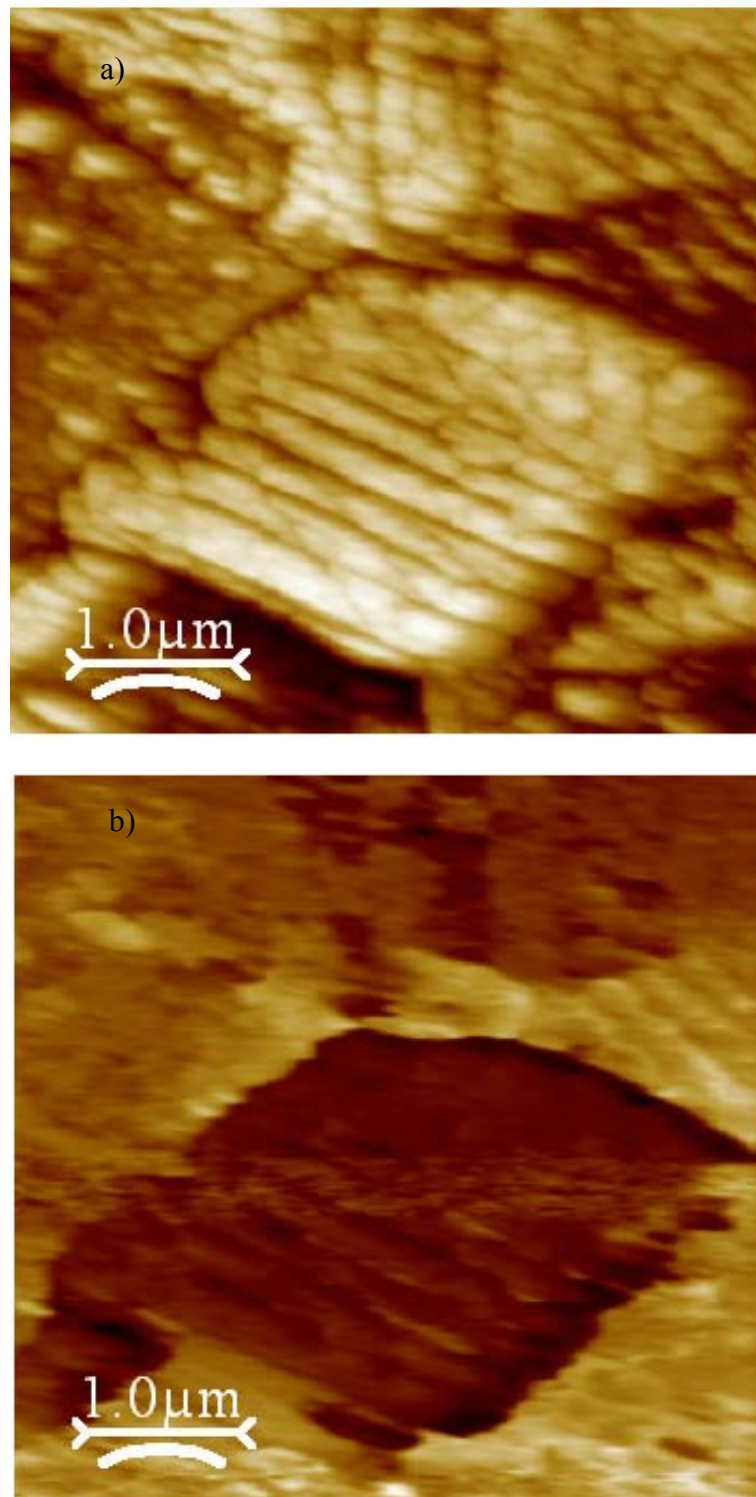


Figure 5.11 - AFM image of the PZT525 ceramic sintered at 1200 °C, during 16h: a) topography of the grain and b) out of plane piezoresponse.

5.2. Ceramic processing and X-ray characterisation

5.2.1. Densification results

The PZT ceramics in the sintering studies had the composition of $\text{Pb}(\text{Zr}_{0.525}\text{Ti}_{0.475})\text{O}_3$, corresponding to the MPB. Firstly, different frits were added to the ceramic to promote a liquid phase at the sintering temperatures with the following compositions: 96%PbO + 4%SiO₂, 92%PbO + 8%SiO₂ and 84%PbO + 16%SiO₂ (w/w). The last two being near the eutectic points in the binary phase diagram (Figure 5.12). It was used 3%, 5% and 8% (w/w) of these compositions in the ceramic. The liquid phases based on the PbO-SiO₂ binary system were selected because they could present the following advantages: they are PbO-rich, which in principle could compensate losses of PbO from the PZT phase; it has never been reported that silica is dissolved in the PZT lattice, which is important to maintain the efficiency of this additive during all the sintering process and to keep the original electrical characteristics; and liquid phases are formed at temperatures as low as 720°C with a low SiO₂ content, ~ 8 wt%, (Figure 5.12).

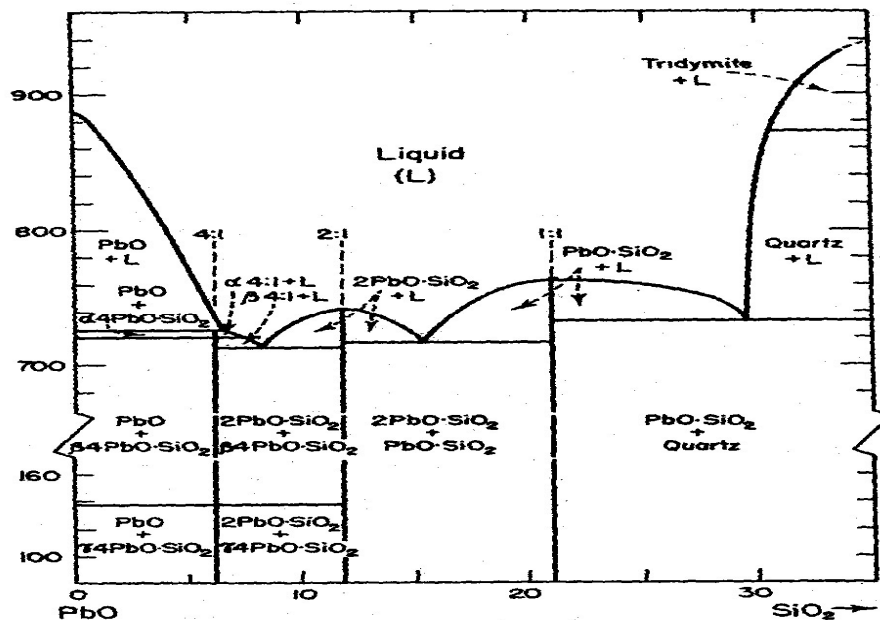


Figure 5.12 – The PbO-SiO₂ phase diagram [352].

The densifications as a function of the sintering temperature for several ceramics obtained using different liquid phases and holding times are shown in Figure 5.13. The

densities are given in percentage of the theoretical density (8 g/cm^3). It is observed an appreciable densification already at 800°C , $\rho = 80 - 86 \%$ (the starting density is 67%), for all the compositions. The values of the density at 800°C are attributed to the effect of the glassy phases, since for pure PZT temperatures higher than $\sim 1100^\circ\text{C}$ are necessary to attain this level of relative density [112, 353]. The quick decrease of the density of PZT with 3% of PbO for temperatures higher than 900°C is a consequence of the weight losses due to the volatilization of PbO (Figure 5.13a). The last effect was not observed when an excess of 2.5 wt% of PbO was added to the ceramic during the calcination; but when the PbO was added in a glassy form these large losses were observed.

The increasing of SiO_2 in the frit decreases the temperature at which the density achieves the maximum, but the effective density value decreases (Figure 5.13a). On the other hand, the increasing of the frit content decreases the temperature at which the density achieves the maximum, but decreases the density value for frit contents higher than 5% (Figure 5.13a). The dependence of the density with sintering time is shown in Figure 5.13b). The density is only slightly affected by the sintering time.

The variation of the relative weight losses of PZT ceramic samples with the sintering temperature for 2 hour of holding time is shown in Figure 5.14a for some of those compositions. The weight losses increase with the increasing of SiO_2 content and with the glass percent in the ceramic, as shown in Figure 5.14a. The effect of the holding time for constant temperatures of 1000°C and 1100°C is shown in Figure 5.14b and, similarly to the previous Figure 5.14a, it is observed that the weight losses increase with the SiO_2 content and with the glass amount in the ceramic. The losses are responsible for the decreasing of the density when more SiO_2 is added and the temperature is increased (Figure 5.15). It is observed that in the samples with high SiO_2 content the increase of the fluidity of the liquid phase may be the cause for the increase of the weight losses.

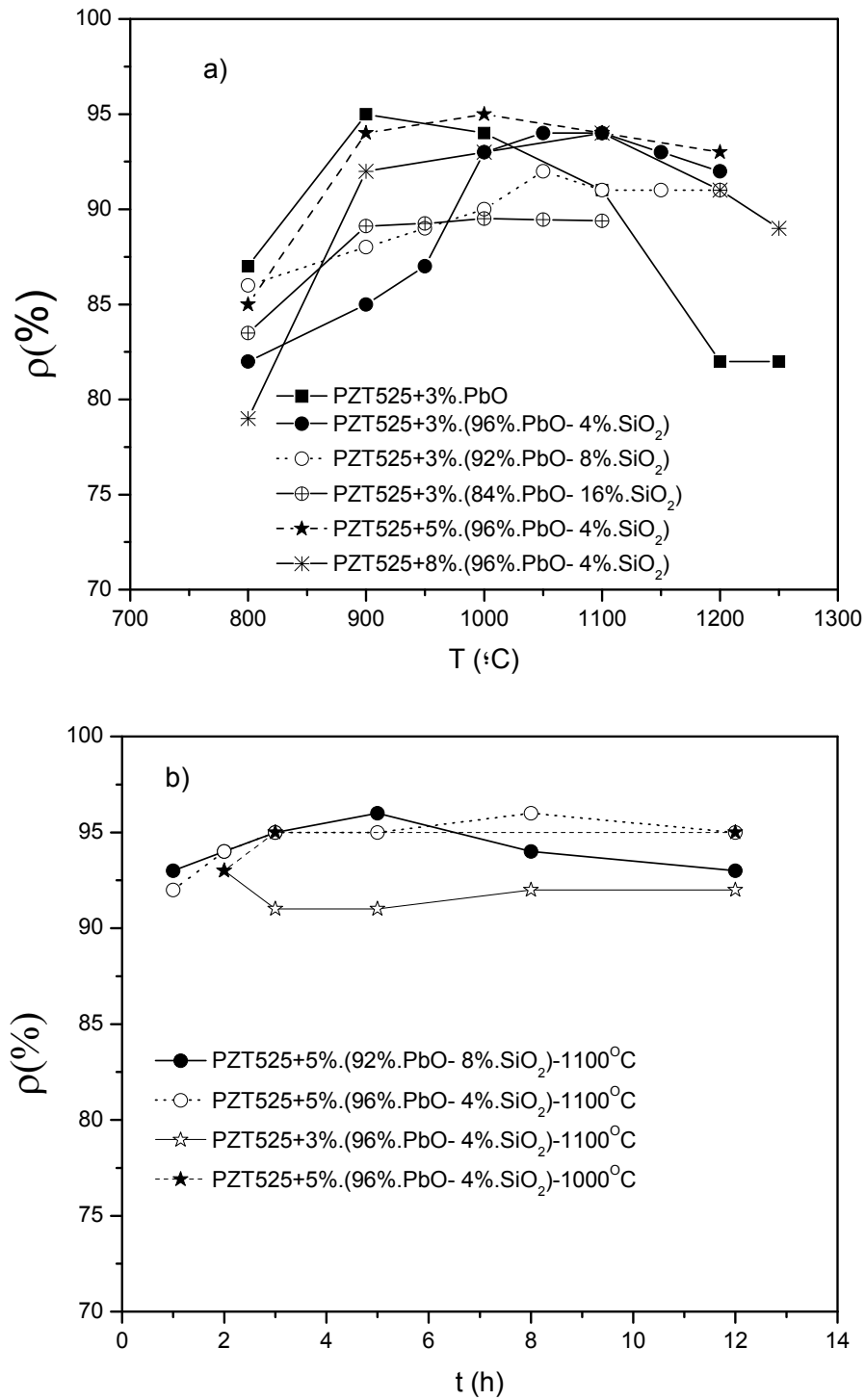


Figure 5.13 - Variation of the relative density of the sintered samples as a function of: a) the sintering temperature for 2h of holding time b) holding time at constant temperature of 1000 $^{\circ}\text{C}$ and 1100 $^{\circ}\text{C}$, using the Archimedes' method.

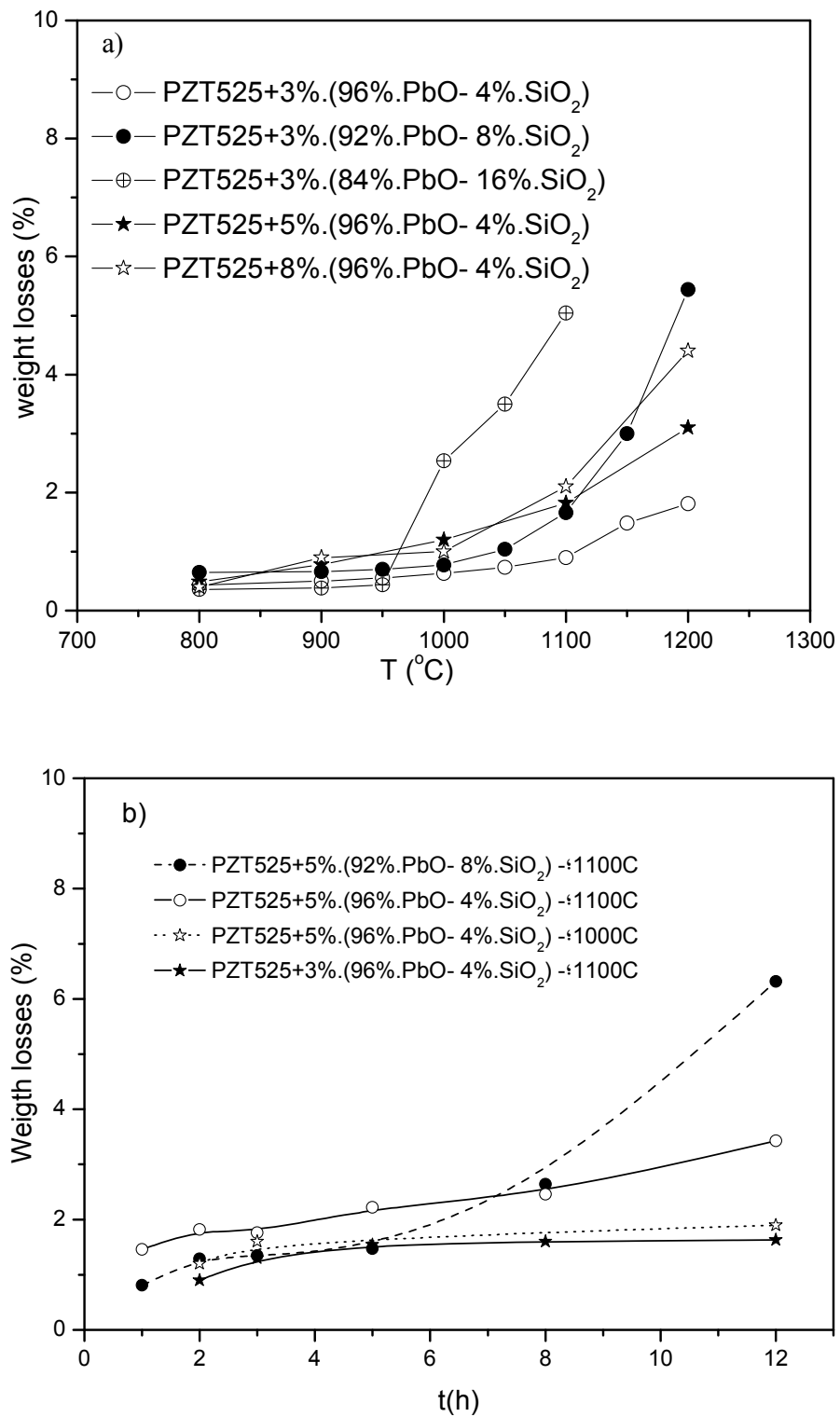


Figure 5.14 - Variation of the weight losses as a function of: a) the sintering temperature for 2 hour of holding time and b) the holding time at constant temperature of 1000°C and 1100°C.

The losses are also increased by the holding time at sintering temperature. These losses are more pronounced with the increase of the frit content in the ceramic and the increase of SiO_2 in the liquid phase. The weight losses using these liquid phases are larger than in ceramics without flux at a sintering temperature of $1250^\circ C$ and holding time of 16 hours, which normally is below 3wt% [112, 353].

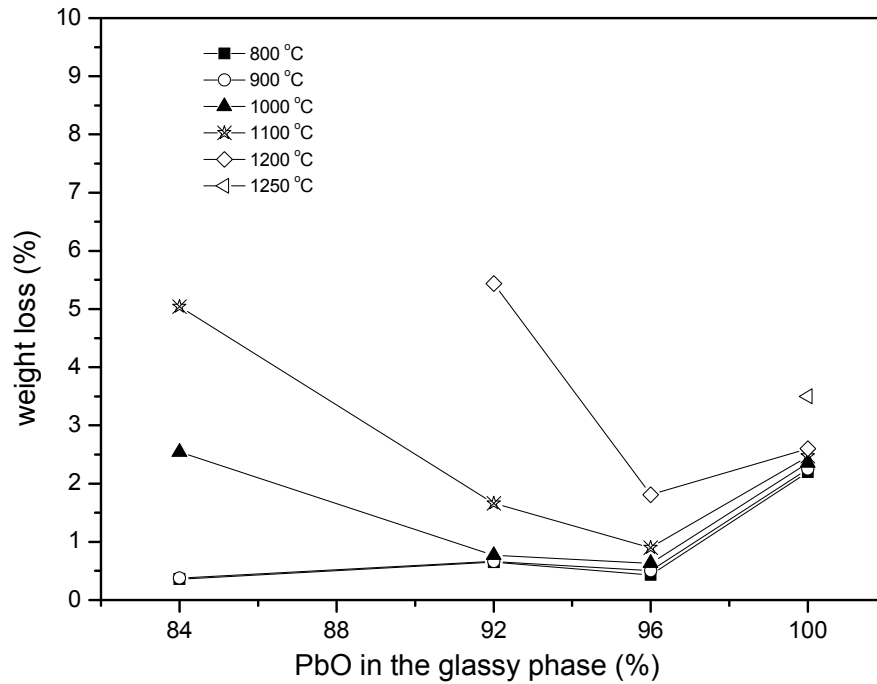


Figure 5.15 - Variation of the weight losses as a function of the PbO content in the glassy phase.

5.2.2. X-ray diffraction analyses

The crystalline phases present in PZT ceramics using different sintering temperatures, holding times and glass contents were analyzed using the powder XRD method. For sintering temperatures above $1150^\circ C$ a second phase of ZrO_2 was found in almost all the compositions. Figure 5.16 shows the XRD patterns of PZT ceramic with 3wt% of glass (4 % of SiO_2 in the glass composition) for different sintering temperatures and holding times. The second phase appears at $1200^\circ C$ for sintering times higher than 5h and its content increases for larger times.

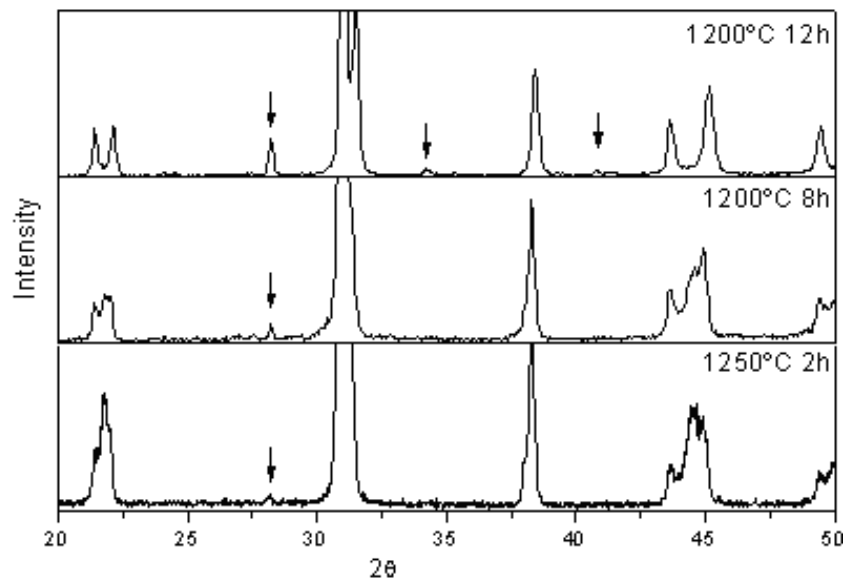


Figure 5.16 - XRD patterns of PZT for 3wt% of glass in ceramic for different sintering temperature and holding times. The arrows in the figure, indicate the peaks corresponding to ZrO_2 the phase.

Figure 5.17 shows the XRD patterns for PZT with 3 wt% of glass in ceramic at different sintering times at 1100°C. It is observed that the ZrO_2 second phase is not present. In general, the ZrO_2 second phase is not present in any of the samples sintered at temperatures below 1100°C and holding time lower than 8 h.

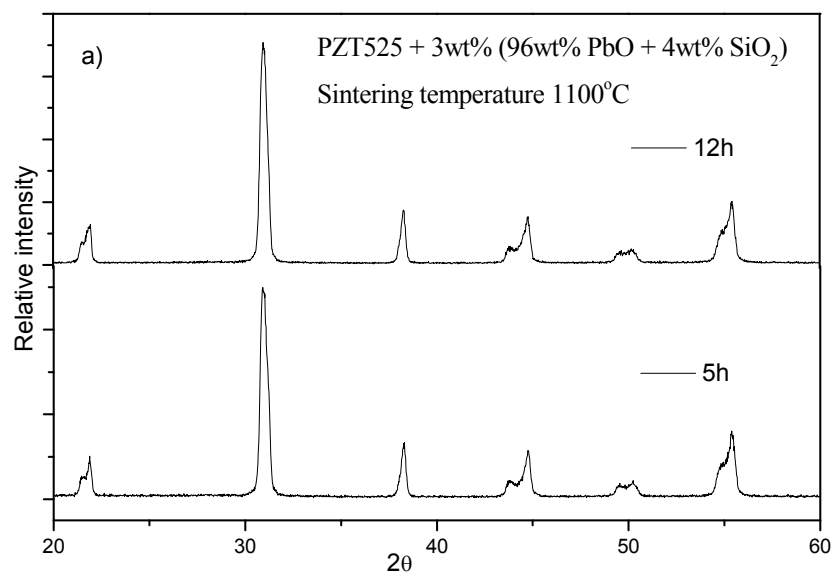


Figure 5.17 - XRD patterns for PZT with 3 wt% of glass in ceramic at different sintering times at 1100°C.

5.2.3. *Microstructure evolution*

The ceramics obtained using different liquid phases at 1100 °C show dense microstructures, as is observed in Figure 5.18. This is in good agreement with the reported densities (Figure 5.13). A well-formed matrix of grains with a maximum diameter size of ~ 12 µm is obtained, as shown in Figure 5.18, for a sample sintered at 1100 °C during 12 hours. The grains have a rounded shape for all the samples sintered at temperature lower than 1150 °C.

In Figure 5.18 both samples show very uniform microstructures with well developed grains. The grain growth occurred without pore separation and residual pores are situated in the junction of three or more grains. Uniform microstructures, like the ones here obtained, with well developed grains and reduced porosity, can also be obtained in pure PZT, but sintered at higher temperatures, for $T \geq 1200^\circ\text{C}$. However, the use of additives, which lowers the sintering temperature, leads either to finer microstructures, as is the case of $PbO-WO_3$ [354], V_2O_5 [355] and CuO [356] additives, or to non-uniform compacts with large residual pores, like in the case of PbO in excess [357, 358]. It can be also observed in Figure 5.18a) that the grains are surrounded by a viscous phase, well infiltrated in the grain junctions and showing a good adaptation to the grain surfaces as expected in face of its good efficiency in the promotion of the densification. In Figure 5.18b), for 12 h, larger grains and a reduction in the amount of the viscous phase are observed in accordance with the determined larger weight losses for longer sintering times (Figure 5.14b)).

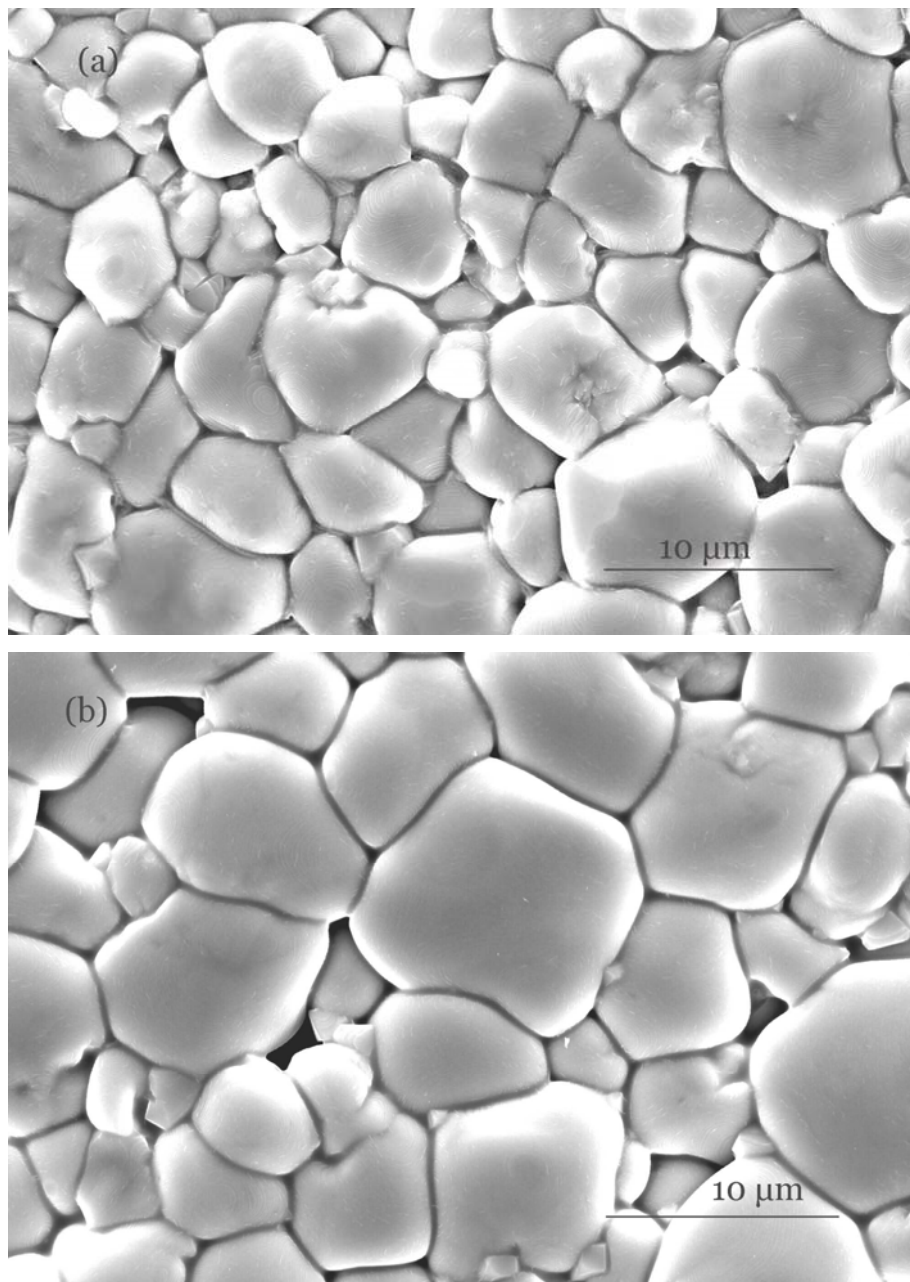


Figure 5.18 - The microstructures of the samples with 5wt% of glassy phase and 4wt% of SiO_2 content in glass for: a) 2 h and b) 12 h at 1100 °C.

It can be seen from Figure 5.19 that the grain size increases with increasing the density. The slower grain growth for low densities is caused by the interconnected pores, which have a strong pinning effect on the grain boundary and restrain the grain boundary movement [353, 359]. Therefore it is necessary to attain high densities to increase the grain size.

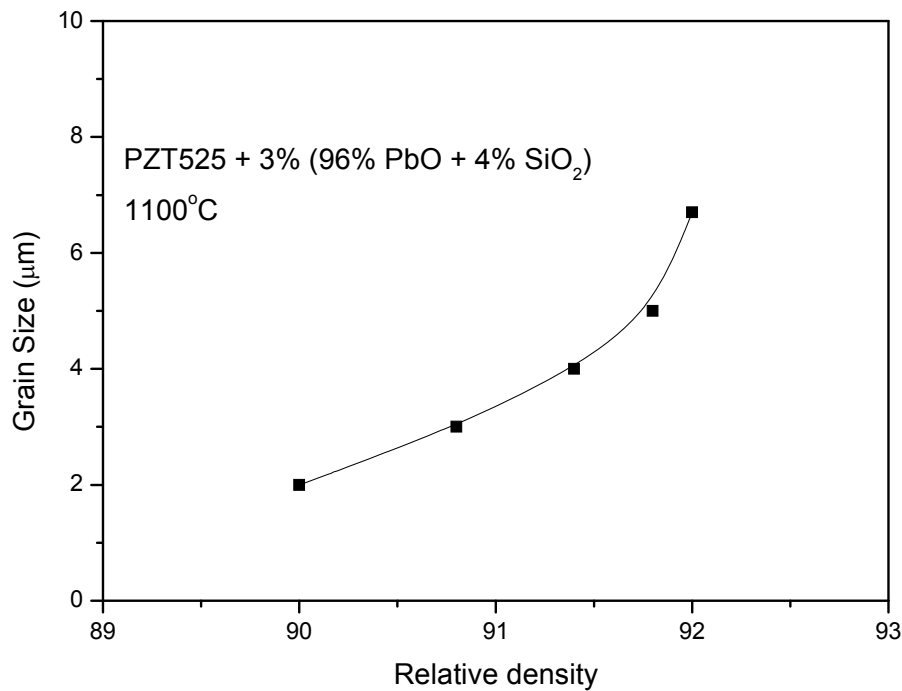


Figure 5.19 - Variation of the grain size with the relative density for 3 wt% of the liquid phase.

The variation of the grain size with the amount of the glass in the ceramics and sintering temperature is shown in Figure 5.20. The grain growth is favoured when the temperature and the glass amount increases. Therefore using a large quantity of frit in ceramics and high temperatures it is expected to obtain large grains. However, at temperatures higher than 1150 °C it appears a second phase, which imposes this limit for the sintering temperature.

The substitution of PbO by SiO₂ in the glass increased the grain growth (Figure 5.21) and the grain size is also increasing when higher temperatures are used. However, the same problem is found, *i.e.*, a ZrO₂ second phase is formed when high temperatures and large quantity of SiO₂ is used.

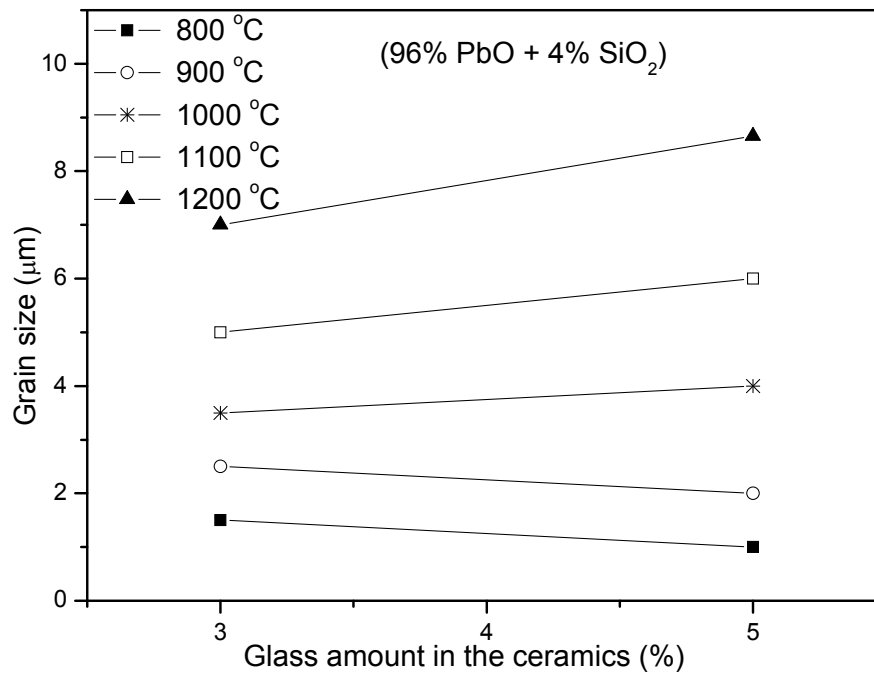


Figure 5.20 - Variation of the grain size with the amount of glass in the ceramics for different sintering temperature and 2 hours of holding time.

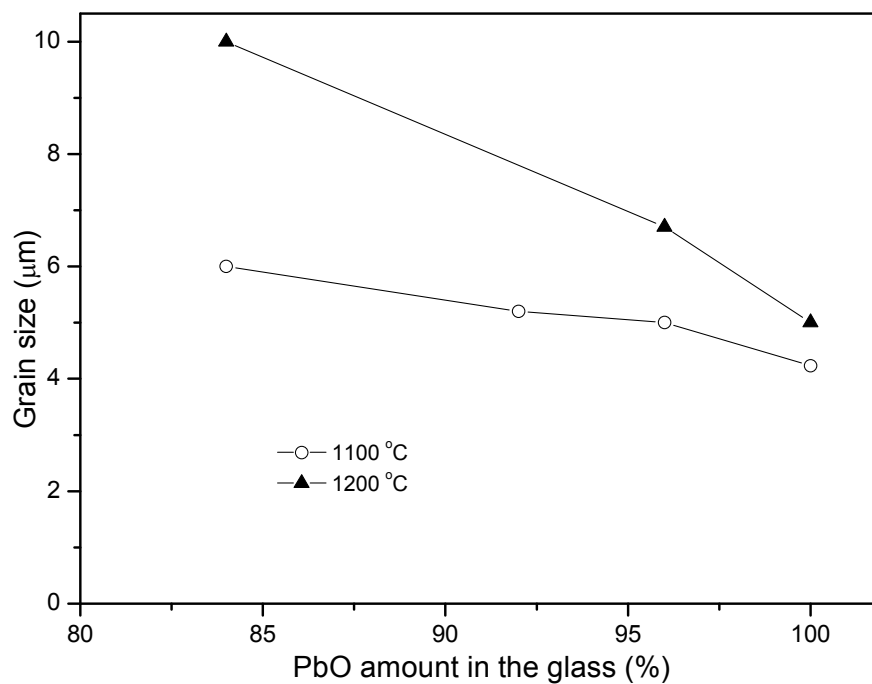


Figure 5.21 - Variation of the grain size with the amount of PbO in the glass for 2 h of holding time and 1100 and 1200 °C of sintering temperature. The amount of the glass in the ceramic is 3 wt%.

The variation of the grain size with the sintering time at 1100 °C is shown in the Figure 5.22a. The grain growth rate slow down with the sintering time and the grain size does not achieve significant values. Figure 5.22b shows the variation of the grain size with the sintering temperature. For temperatures above 950 °C the increasing of the amount of the liquid phase is followed by an increase of the grain growth and the same is observed when the SiO₂ amount in the glass composition is increased. The grain growth is then stimulated by the increase of the sintering temperature, the sintering time, the glass amount in the ceramic and the SiO₂ content of the glass.

The grain growth kinetics is described by the Equation 5.1. This equation has been used to determine the grain growth kinetics parameters of the PZT ceramics.

$$G^n - G_o^n = Kt \exp\left(-\frac{Ea}{RT}\right) \quad (5.1)$$

G is the average grain size at time (t) and at absolute temperature (T), G_o is the initial grain size, n is the kinetic grain growth exponent value, K is a constant, Ea is the activation energy and R is the gas constant (8.314 J/mol K). For G_o << G, Equation 5.1 is simplified to

$$G^n \approx Kt \exp\left(-\frac{Ea}{RT}\right) \quad (5.2)$$

In terms of the grain growth kinetics, the value of the n exponent in Equation (5.2) obtained from the slope of log(G) versus log(t), is approximately 5.6. The activation energy (Ea) for the grain growth was determined from the slopes of the Arrhenius plots of log(G) versus 1/T and it is approximately 214 kJ/mol for the sample with 3wt% (96wt% PbO + 4wt% SiO₂) of glass, Figure 5.23. For the sample with 5wt% (96wt% PbO + 4wt% SiO₂) these values were n = 4.8 and the activation energy 348 kJ/mol. The grain growth is faster in the ceramic with 5% of glass phase (Figure 5.22), although it is required a higher thermal activation energy.

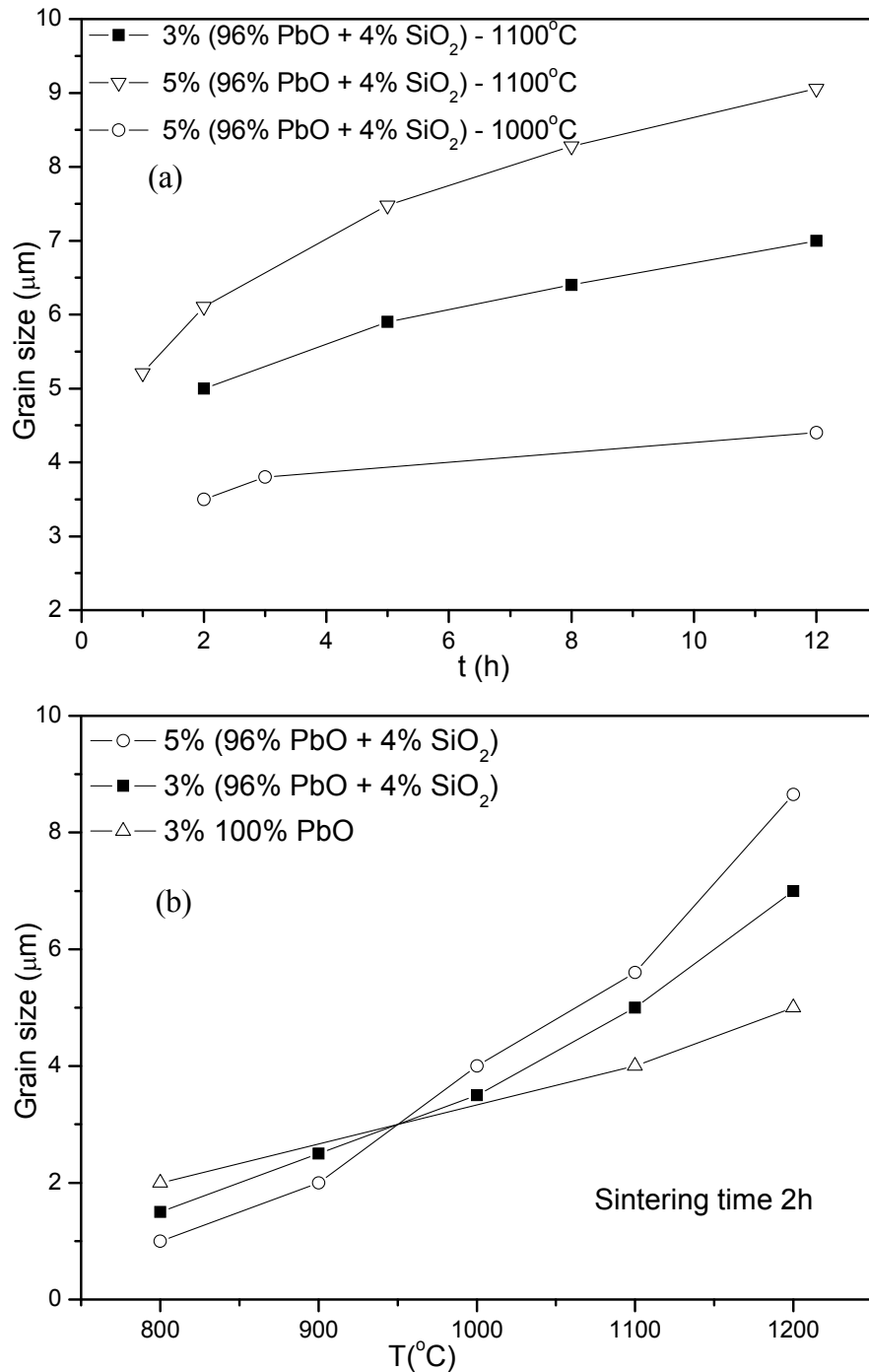


Figure 5.22 - Variation of the grain size a) with time and b) with sintering temperature for several SiO₂ amounts in the glass and amounts of glass added to the ceramic.

Usually, the increase of the quantity of the liquid phase until some limit accelerates the grain growth, being more accentuated for higher temperatures. The value of the n exponent for the grain growth kinetic reported by other authors for PZT ceramics without a liquid phase is 2.3 [279] and 3 [279, 360] for PZT ceramic doped with Nb and Bi and obtained by

hot pressing. These values are attributed to the presence of pores, inclusions and impurities which interrupt the free displacement of the grain boundary [360]. The activation energy in ceramics doped with Nb and Bi was found to be of 366 kJ/mol and 398 kJ/mol, respectively, comparable to those here determined [279].

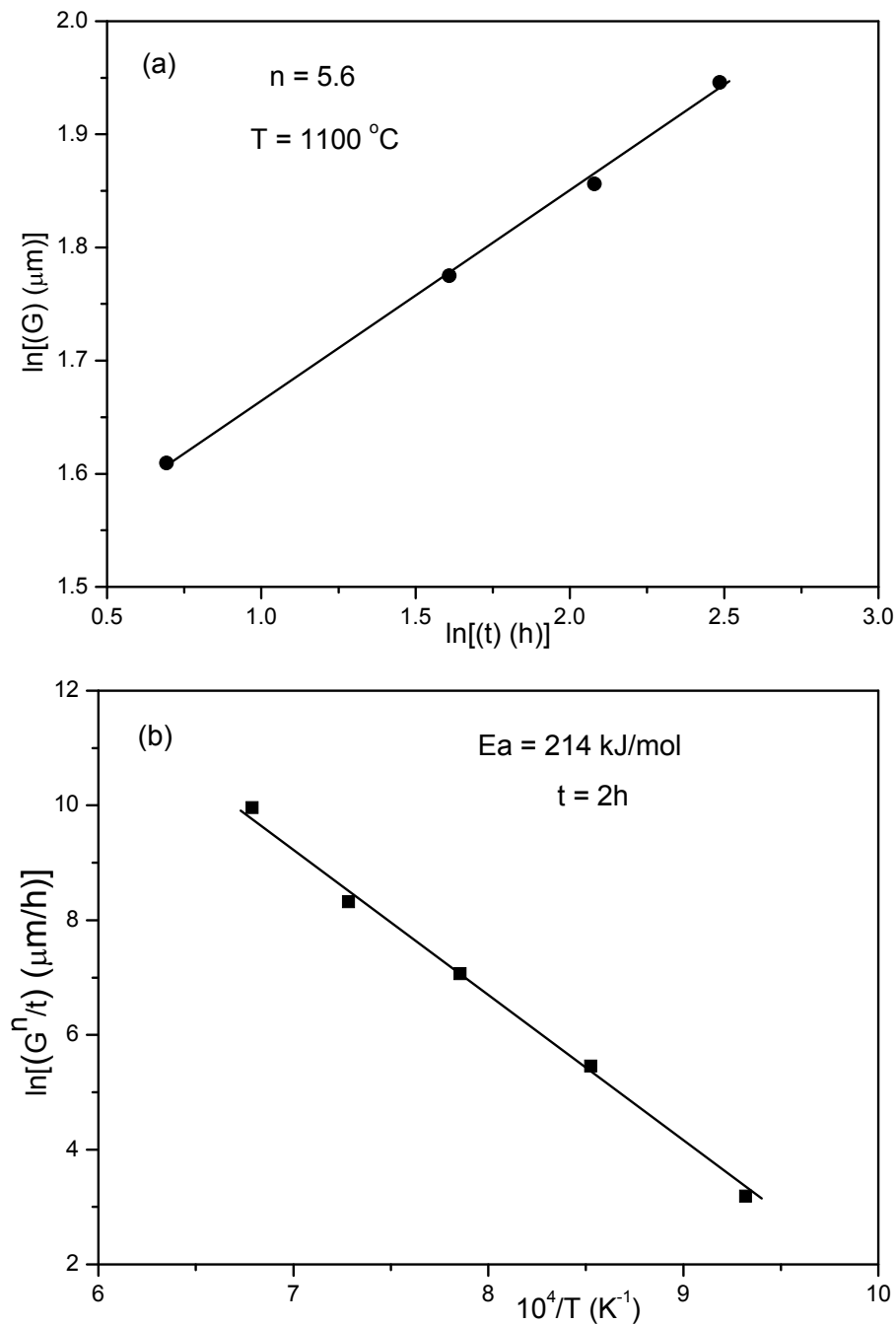


Figure 5.23 - The relation between a) $\log(G)$ vs $\log(t)$ and b) $\ln(G^n/t)$ vs $\ln(1/T)$ for sample PZT525 with 3 wt% of glass of composition 96%PbO + 4% SiO₂.

5.2.4. Dielectric characterisation

It will be investigated how the amount of the liquid phase, the temperature and the sintering time affect the dielectric properties of the ceramics.

In Figure 5.24 it is shown the dielectric permittivity of PZT ceramics with 3wt% of frit, at room temperature, in relation to the amount of PbO in the frit. The dielectric permittivity shows a maximum for a glass composition of 96 wt% PbO. The dielectric permittivity at the Curie temperature decreases with the decrease of the PbO concentration in glass (Figure 5.25). This difference is not large for concentrations of PbO higher than 96 wt%, but it decreases abruptly for lower contents (Figure 5.25).

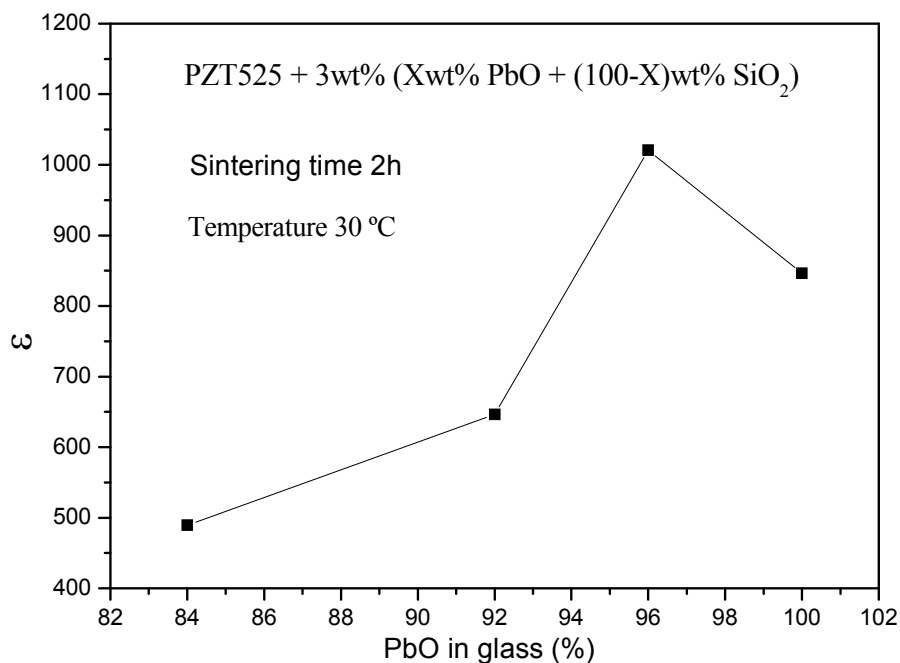


Figure 5.24 - Variation of the dielectric permittivity at room temperature in relation to PbO content in the glass.

The dielectric properties in this material sintered using any of the liquid phases are poorer than in the material without liquid phase (see Figure 5.3a). These can be related with: a) the increasing of the volatilization of the PbO during sintering, when the liquid phase is present; b) the precipitation (solidification) of the liquid phase in the grain boundaries forming a layer with low dielectric properties.

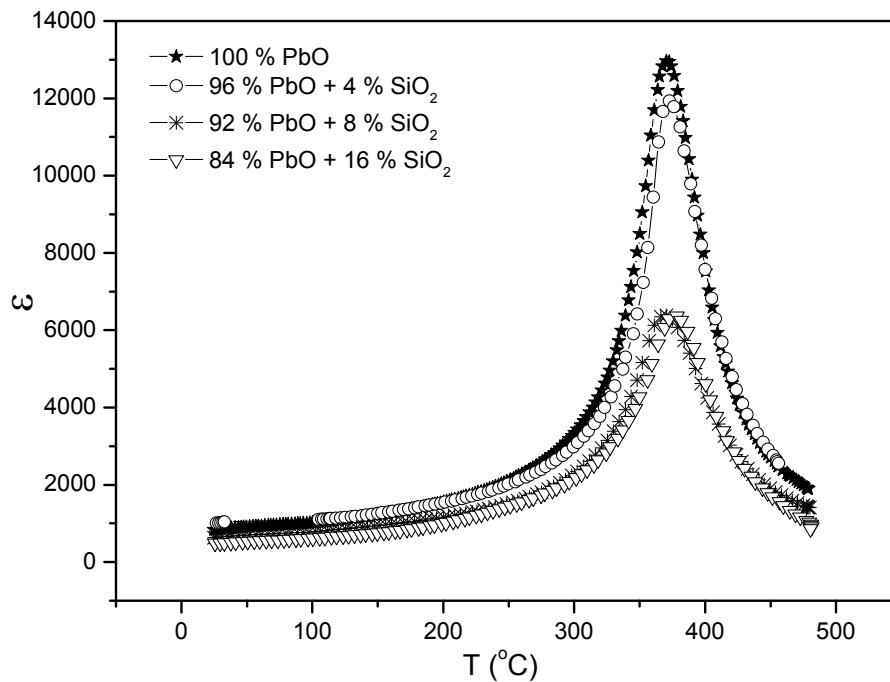


Figure 5.25 - Dielectric permittivity of the PZT525 ceramic, sintered at 1100 °C, measured at 1 M Hz, for different amounts of PbO in 3 wt% of glass.

A strong dependence of the permittivity on the sintering temperature is observed for temperatures lower than 1100°C (Figure 5.26a). This result can not be attributed directly to the density of the samples because in both cases the density is very similar. The increasing of the grain size ($\sim 3,5$ to $6 \mu\text{m}$) and the decreasing of the liquid phase content due to volatilization ($\sim 1,2$ to $1,8$ wt% losses) with the increasing of the temperature can explain this behaviour (Figure 5.27 and Figure 5.18b). Although the densification attained for the ceramics sintered (with 5wt% of glassy phase and 96 wt% of PbO in the glass) at 1000 °C is near 95%, it is necessary to increase the sintering temperature in order to increase the dielectric properties.

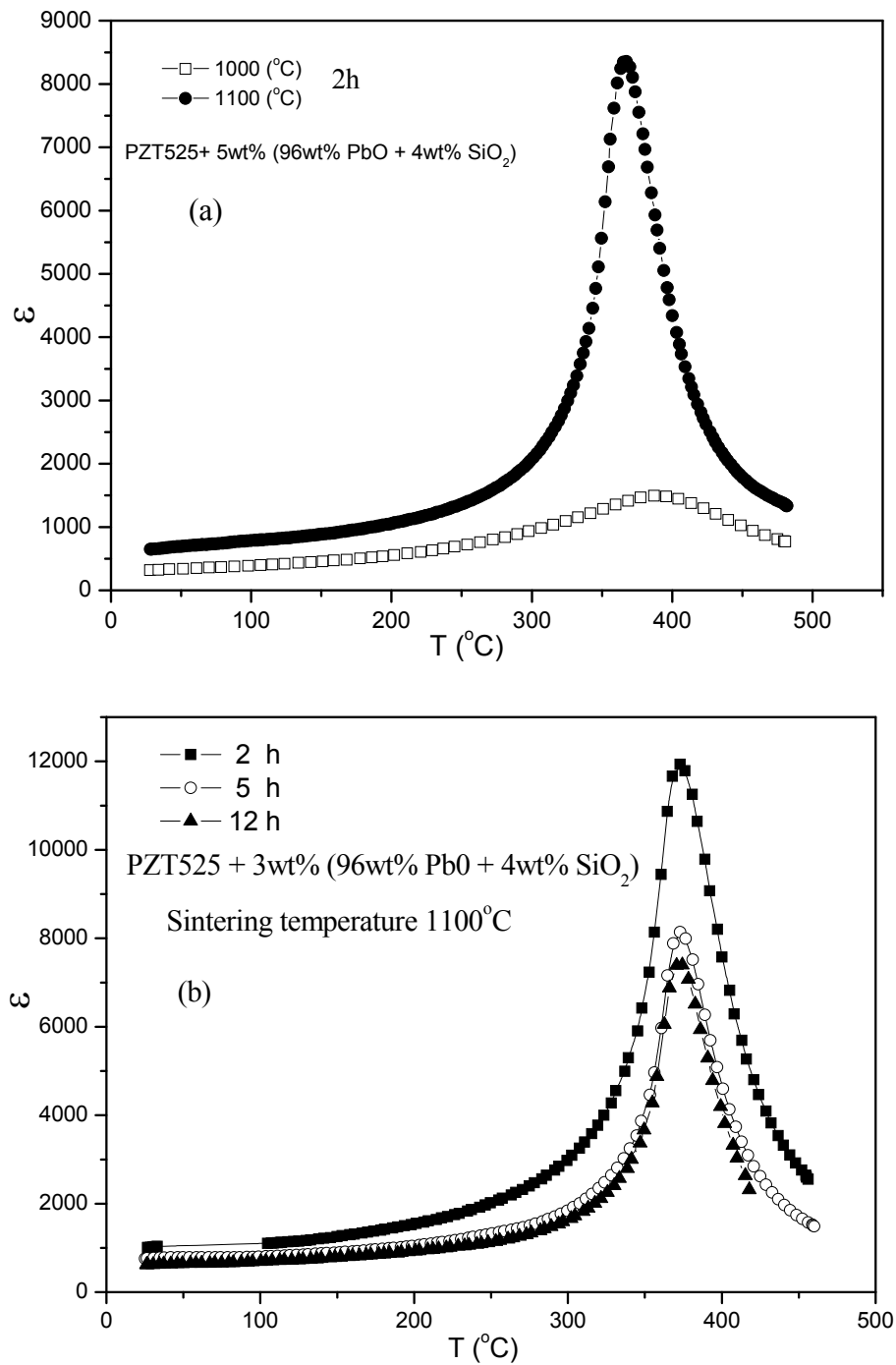


Figure 5.26 - Dielectric permittivity of the PZT525 ceramic as a function of the temperature, at 1 MHz: a) for 5wt% of glass and different sintering temperatures; b) for 3wt% of glass and different sintering times.

It seems reasonable that the presence of liquid phases in the grain boundaries decreases the dielectric properties due to the fact that this phase is not ferroelectric. The dielectric

properties also decrease with the increasing of the sintering time (Figure 5.26b), from 2h to 5h. Concomitantly, it is observed a decrease in the relative density, from 93 to 90, with increasing the sintering time up to 3h. The density and the weight loss have a maximum and a minimum, respectively, for approximately 2 hours of sintering time, in a sample with 3% of glassy phase and 4% of SiO_2 of glass composition, sintered at 1100 °C (Figure 5.13b and Figure 5.14b). The density varied until it gets stable after 5 hours of sintering time. The same behaviour is observed in the dielectric properties of these ceramics (Figure 5.26b).

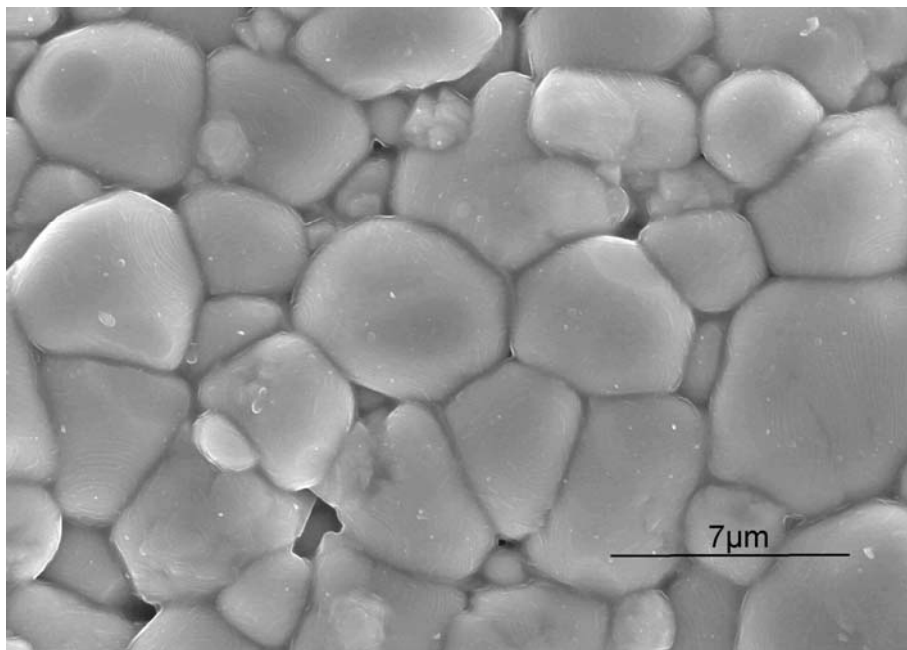


Figure 5.27 - Microstructure of the sample with 5% of glassy phase and 96 wt% of PbO content in the glass for 12 h of holding time and 1000 °C of sintering temperature. Notice the presence of liquid phase in the grain boundary.

It is also important to emphasize the dielectric losses of these materials, which are, in the case of the 3 wt% (96 wt% PbO + 4 wt% SiO_2) frit composition and for temperatures below 300°C, in the range of 0.005 to 0.03 at 1 kHz. These dielectric losses are equivalent or lower than the ones reported PZT ceramics without liquid phases, which have typical dielectric losses of 0.01 to 0.02 [361]. The increasing of the SiO_2 content in the glass increases the dielectric losses, but in all the cases they are smaller than 0.04 for frequencies of 1 kHz and temperatures below 300°C (Figure 5.28). The dielectric losses have a similar behaviour when the glass amount in the ceramics is increased from of 3 to 5wt% for the

composition 96 wt% PbO + 4 wt% SiO₂. The liquid phase formed during sintering can create an amorphous interphase in the grain boundaries (Figure 5.27), which seems to reduce the conductivity and to decrease the dielectric properties of the ceramics.

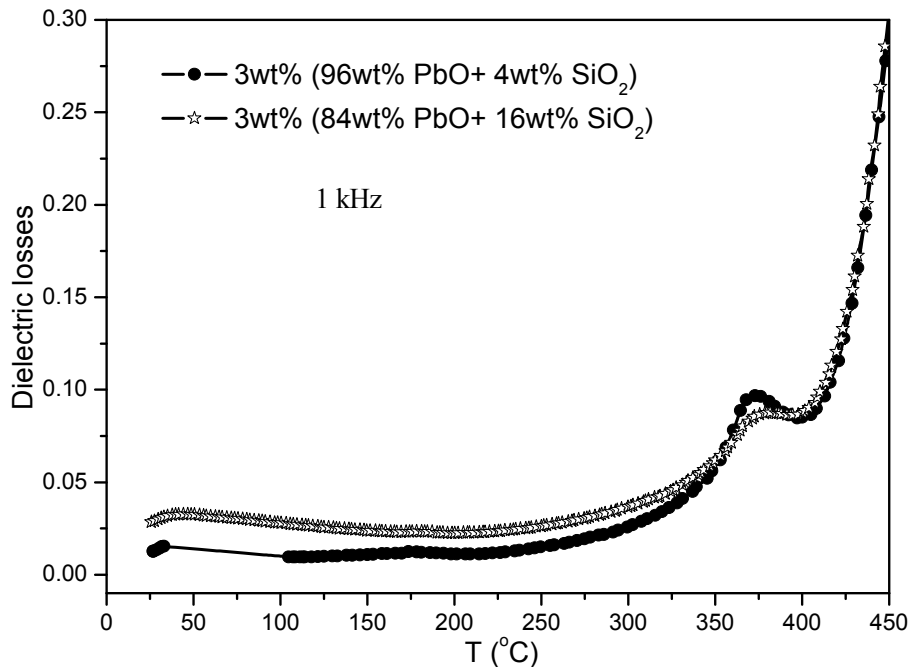


Figure 5.28 - Dielectric losses of PZT525 ceramic as a function of the temperature for different PbO contents in glassy phase for 1100°C of sintering temperature and 2h of holding time.

The different parameters, correspondent to the Curie-Weiss equation are dependent on the sintering temperature, frit composition and concentration. In Figure 5.29 it is plotted the temperature dependence of the inverse of the dielectric permittivity near T_{max} , at 1 MHz, of the PZT ceramic sintered at 1100 °C for 2 hours with 3wt% of glass in ceramic and 92wt% of PbO in the glass. The Curie constant for temperatures lower and higher than T_c are near their ratio predicted by the Curie-Weiss law (Equation 1.7). It is predicted in the DLG theory that the value of the Curie constant at $T < T_c$ is twice that for $T > T_c$. On the other hand, in a second order phase transition, the temperature of the maximum of the permittivity is equal to the Curie-Weiss temperature, but in this case there is a discrepancy ($T_c \neq T_o$) between the maximum of the transition and the values determined for the Curie-Weiss law (Figure 5.29). This is due to an extra contribution to the permittivity due to charge movement in the material.

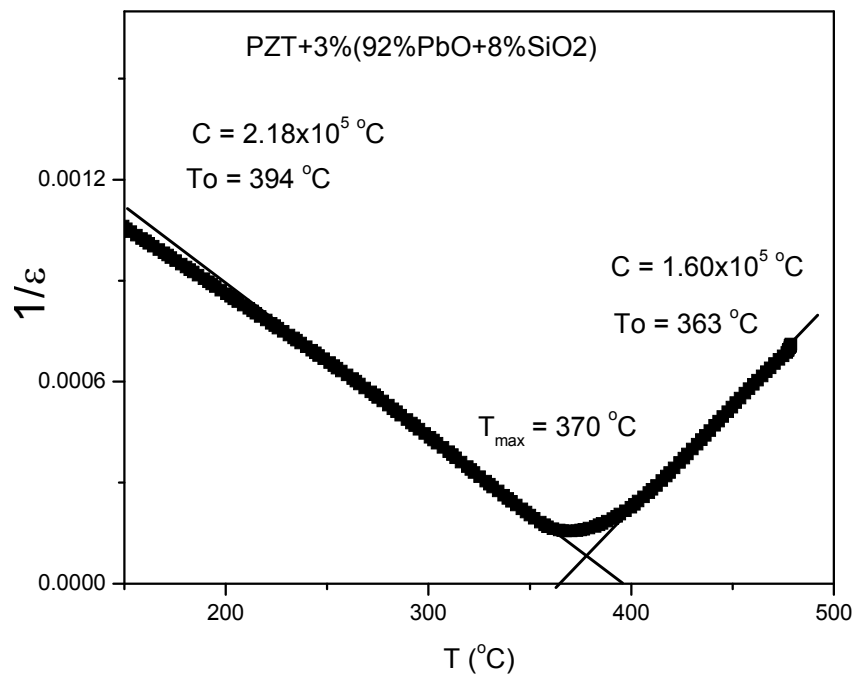


Figure 5.29 - Temperature dependence of the inverse of the dielectric permittivity near T_{max} , at 1 MHz, in the PZT ceramic sintered at 1100 °C for 2 hours. C is the Curie constant, T_{max} is the transition temperature and T_o is the Curie-Weiss temperature.

Table 5.3 - Values of the different parameters of the Curie-Weiss law in ceramics with different glass compositions, amount of frit, sintering temperature and holding time.

General parameters measured at 1MHz			$\epsilon = \frac{C}{T - T_o}$			
			$T < T_c$		$T > T_c$	
PZT + glass % sintering conditions	ϵ_{max}	T_{max} (°C)	$C \times 10^5$ (°C)	T_o (°C)	$C \times 10^5$ (°C)	T_o (°C)
PZT +3%(96%PbO+4%SiO ₂), 2h, 1100°C	11900	372	2.66	388	1.92	382
PZT +3%(96%PbO+4%SiO ₂), 12h, 1100°C	7400	374	1.35	384	1.16	330
PZT+5%(96%PbO+4%SiO ₂), 2h, 1100°C	10500	348	1.97	360	1.55	354
PZT+5%(96%PbO+4%SiO ₂), 12h, 1100°C	1500	388	1.38	441	1.00	350
PZT+3%(92%PbO+8%SiO ₂), 2h, 1100°C	6400	370	2.18	394	1.60	363

In Table 5.3 it is resumed several parameters; the permittivity in the transition temperature (ϵ_{max}), the transition temperature (T_{max}), the Curie constant (C) and the Curie-Weiss temperature (T_o), which help to understand the influence of the sintering

temperature, holding time, frit composition and the amount of glass added to ceramic, on the dielectric properties. The values resumed in Table 5.3 are in agreement with the previous analysis of the dielectric measurements.

5.3. PZT crystal growth using the seeded polycrystalline conversion method

One main objective to introduce the liquid phase in the ceramic is to obtain larger grain size ceramics with high density at low sintering temperature and without a second phase. As said before with the use of 3-5 wt% of PbO-SiO₂ frit in PZT, the sintering temperature was reduced for less than 100 °C and 95% of theoretical density was achieved, but the grain sizes were not different from those obtained without liquid phases. Other methods to increase the grain size are necessary to take into account. Therefore, the final section of this chapter is devoted to describe the preliminary intent to grow PZT crystals in ceramics using the seeded polycrystalline conversion method (SPC). This method has been recently reported to promote also the grain growth in the ceramic matrix by using single crystals inside a powder matrix (chapter 2). The PZT single-crystals were prepared as already discussed (chapter 3) and embedded in the PZT ceramics with a liquid phase to increase the grain boundary mobility.

Many materials show abnormal grain growth when a liquid phase is added [362]. Abnormal grain growth was found in PZT when the liquid phases of 7PbO+0.7MgO+2SiO₂ and 7PbO+0.7MgO were used [363]. In our work, it was found abnormal grain growth when 3wt% of liquid phase of 96%PbO+4%SiO₂ was added to the PZT. In Figure 5.30 it is shown the microstructures of a sample with the last composition. Several grains with sizes much larger than the average grain size are found in the sample, always near a large pore. These large pores would be formed by the coarse of several pores during the grain growth.

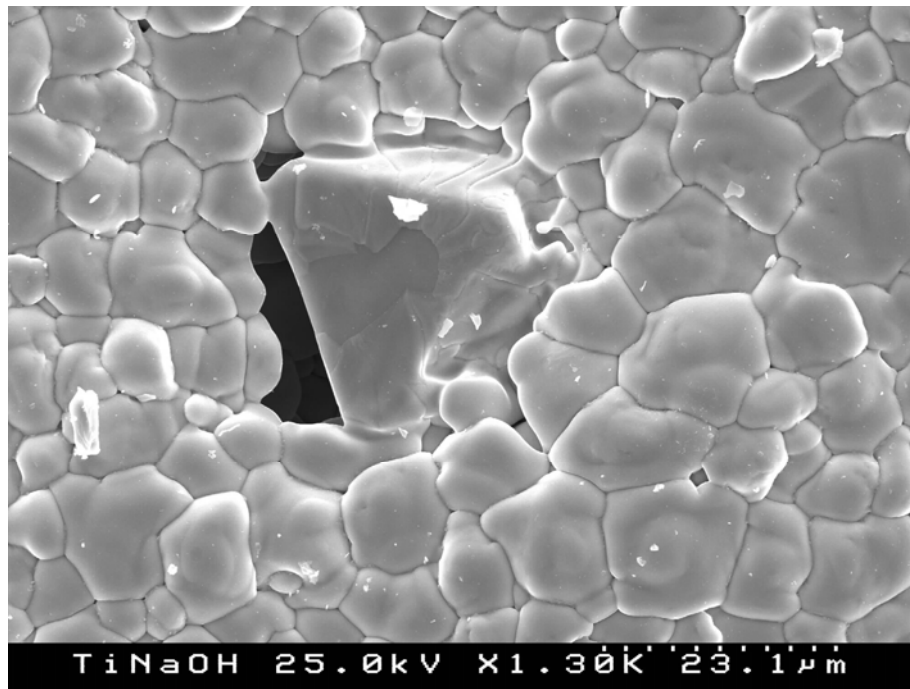


Figure 5.30 - Microstructure of a sample with 3wt% of glassy phase of 96%PbO+4%SiO₂, for 8 h of holding time at 1200 °C, showing an example of a large grain formation.

These liquid phases were selected to promote the crystal growth inside the ceramic. The best results were obtained using 7PbO+0.7MgO+2SiO₂ and 7PbO+0.7MgO as liquid phase. In Table 5.4 it is resumed the principal characteristics of sintering and crystal growth with these liquid phases. In these samples, 5wt% of PZT single crystals were added (with medium size of 20-30 µm) and the initial particle size of the ceramic were lower than 1 µm. Large pores appear near each crystal or abnormal grain growth as a coarsening process of several pores during the grain growth (Figure 5.30) for large holding time. In Figure 5.31 it is shown a PZT ceramic sample with a liquid phase of 7PbO+0.7MgO+2SiO₂, and 5wt% of PZT single crystals added and then sintered at 1200°C, for 2 h. For larger holding times the crystals grow and the pores coarsen. Holding times larger than 6 hours were not used due to the formation of a second phase.

Table 5.4 - Liquid phases used to grow crystals. These samples were sintered at 1200 (°C).

Frit composition (mol)	Frit used weight (%)	Crystal used weight (%)	Initial particle size (µm)	Initial crystal size (µm)	Sinter. time (h)	Final density (%)	Final crystal size (µm)
7PbO+0.7MgO	3	5	1	20 - 30	4	94	45
7PbO+0.7MgO+2SiO ₂	3	5	1	20 - 30	2	94	60

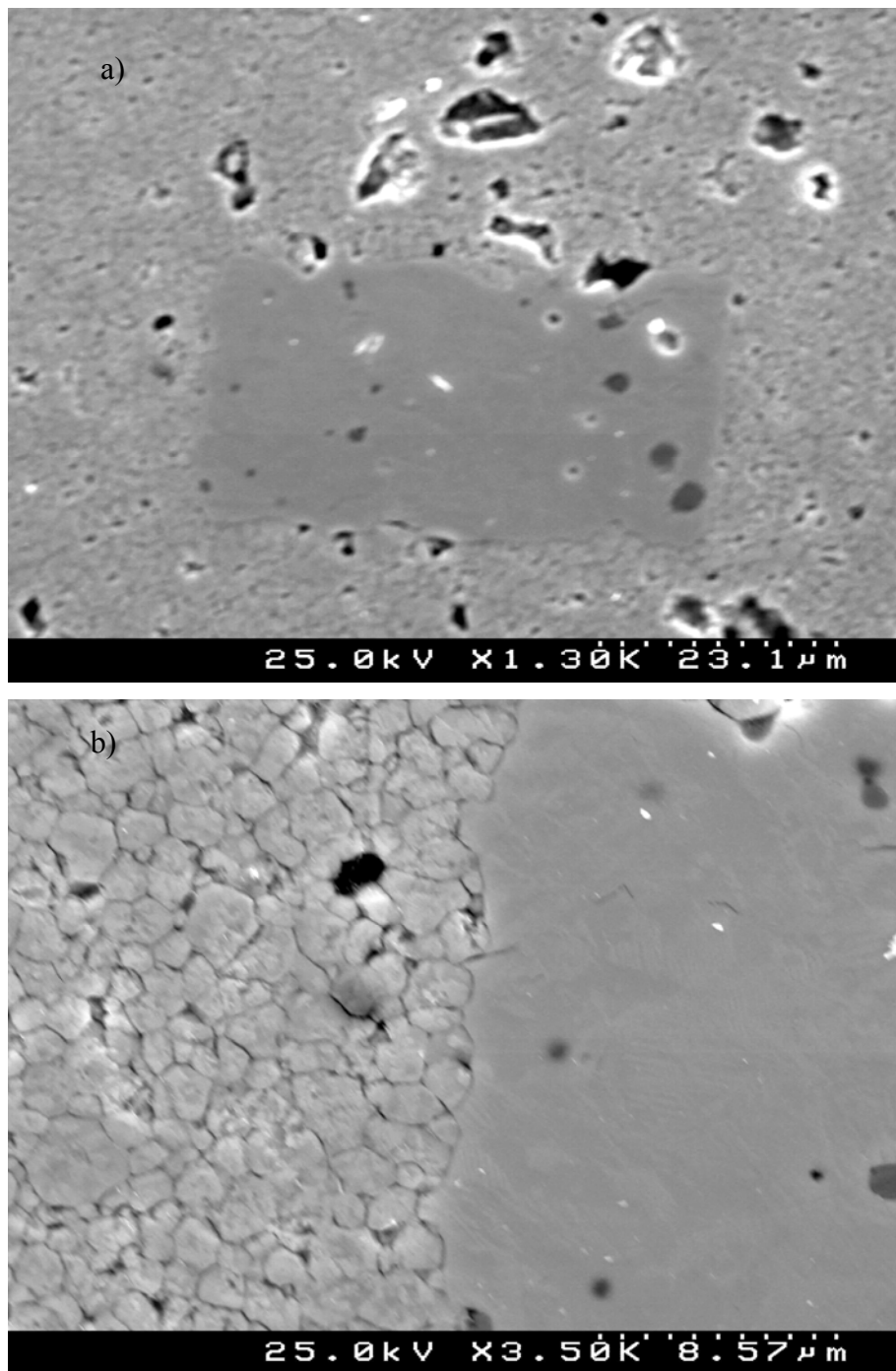


Figure 5.31 - Micrograph of PZT ceramic with liquid phase of $7\text{PbO}+0.7\text{MgO}+2\text{SiO}_2$. To those samples, 5wt% of PZT single crystals were added and then sintered at $1200\text{ }^\circ\text{C}$ for 2 h. The image b) is a zoom of the a) one.

In Figure 5.32 it is shown the micrographs of PZT ceramic with 3wt% of liquid phase ($7\text{PbO}+0.7\text{MgO}$) when 5 wt% of PZT single crystals were added and then sintered at $1200\text{ }^\circ\text{C}$ for 4 hours. Here, the crystal growth is clearly observed, a crystal growing at the

expenses of the small grains of the matrix. In the initial stage of the crystal growth the pores are not coarsened, but with the crystal growing more, the pores coarsen forming a large pore which stops the crystal growth.

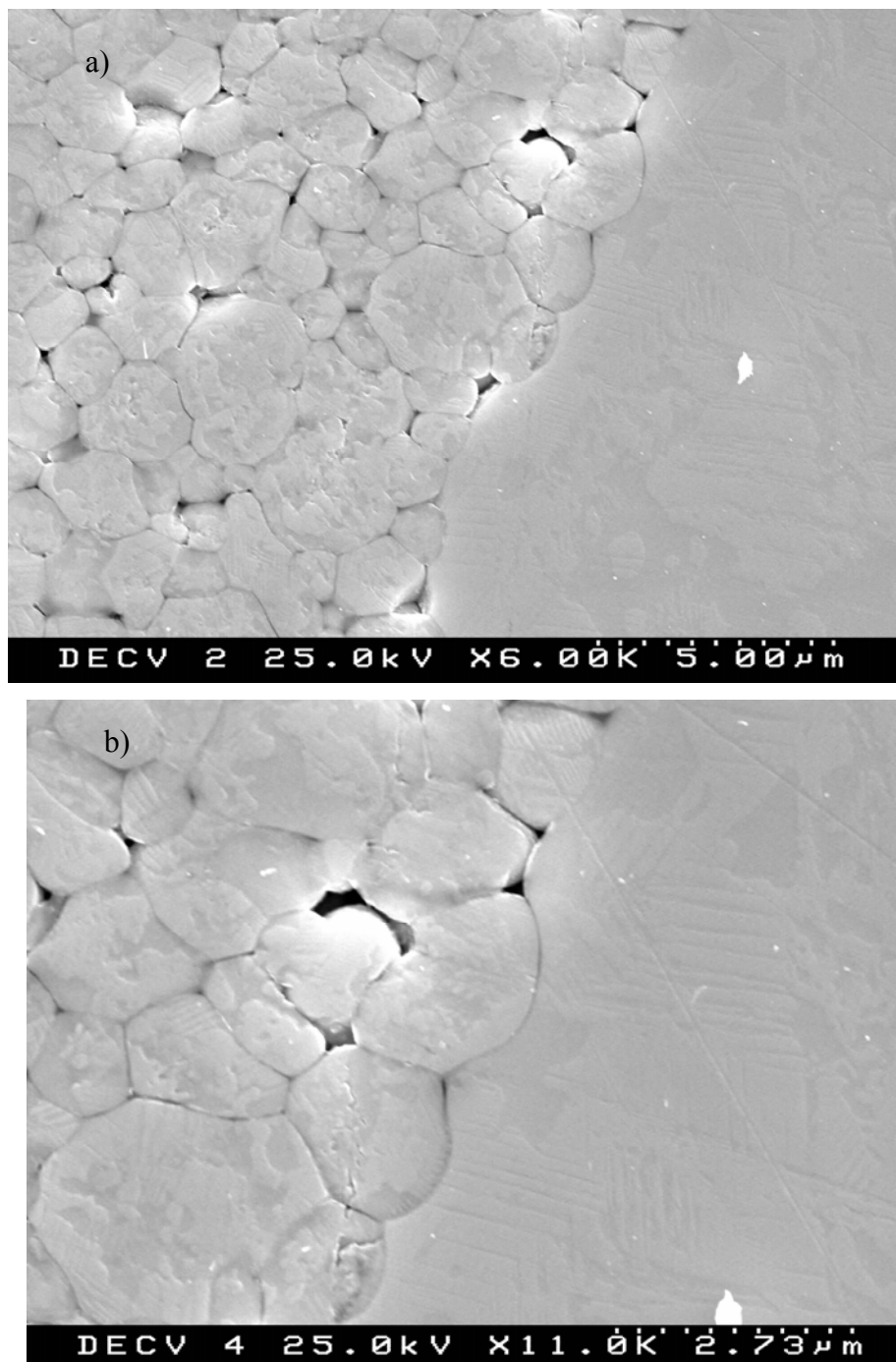


Figure 5.32 - Micrograph of PZT ceramic with liquid phase of 7PbO+0.7MgO. In these samples, 5 wt% of PZT single crystals were added and then sintered at 1200 °C, for 4 hours.

CHAPTER 6

General conclusions

The knowledge of the properties of the PZT system is of great interest both from scientific and technical point of view. The understanding of the causes for which this system may present a high electro-mechanical response, principally in the morphotropic phase boundary (MPB), could help the design of new materials with optimised response. For this propose the dependence of the dielectric properties and the domain structure on the grain size and the composition were the main interest of this work. An important part of this thesis work is devoted to the growth and properties study of PZT single crystals. As a result, the main conclusions may be summarized as follows:

PZT single crystals

- PZT single crystals were successfully grown by a high-temperature solution method using a (PbO-KF-PbCl₂)-B₂O₃ flux. An optimized thermal profile was successful for the growing of large single crystals, with sizes of $\sim 3 \times 3 \times 3 \text{ mm}^3$. These presented cubic shapes and twinned crystals were commonly observed. The obtained crystals may present cracks and other defects but impurities were not detected.
- The low temperature rhombohedral phase with R3c spacial group is not detected for compositions of $x \leq 0.65 \pm 0.03$ at room temperature.
- Single crystals with composition in the morphotropic phase boundary don't show the coexistence of two phases, tetragonal and rhombohedral, as is observed in polycrystalline samples. Instead, a pseudo-cubic phase that is rhombohedral at temperatures lower than $\sim 180\text{K}$ and tetragonal at higher temperatures was found.
- The measurements of the domain structure are reported by using the piezoresponse force microscopy technique. A domain system of coexisting 90° and 180° domains, forming a "herringbone" structure with mostly flat 90° domain walls oriented along the [110] direction, is observed in the tetragonal side of the diagram. The widths of the 90° domains (twins) forming laminar structures are within the range of 0.7 -

1.5 μm , whereas 180° domain walls, oriented parallel to the [100]-direction (polar axis), exhibit a periodicity in the range of 250 to 500 nm.

- Hysteresis loop is obtained along the [001] direction. The values of the spontaneous polarization ($\approx 40 \mu\text{C}/\text{cm}^2$) and the coercive field ($\approx 39 \text{ kV}/\text{cm}$) are estimated from this loop.
- The spontaneous polarization does not show a maximum in the MPB, although a maximum is found in the dielectric measurement.

PZT ceramics

- The dielectric properties increase with the grain size and have a maximum around the MPB, near the composition with 52.5% of Zr content.
- The small bend observed in dielectric permittivity near room temperature is not associated to any structural phase transition. This inflexion has probably related to domains, defects and disorder in the oxygen octahedrons.
- The maximum of the electro-mechanical properties around the MPB is not explainable by a mixture of phases or by a monoclinic phase. It can be due to the decrease of the distortion when the Zr amount is near 52%, probably due to an increase of the domain movement.
- The characteristic feature of the domain configuration in PZT ceramics is a band structure composed of 90° domains (herringbone pattern), where the domains walls are oriented parallel to the {110} planes.
- The use of liquid phases (system PbO-SiO₂) may decrease the sintering temperature of PZT and densified samples are achieved at temperatures 100°C lower than the one needed without liquid phase. Second phases are formed for temperature higher than 1150°C and longer sintering times.
- The liquid phase formed during the sintering can create an amorphous interphase in the grain boundaries, which seems to reduce the dielectric losses and the dielectric permittivity of the ceramics.
- The liquid phases enhance the grain growth, particularly for compositions of 72%PbO:7%MgO:21%SiO₂, 91%PbO:8%MgO and 96%PbO:4%SiO₂ for amounts of liquid phases in the ceramics lower than 5wt%.

- PZT crystals used as seeds inside a polycrystalline PZT matrix showed to have condition to grow out and to promote the grain growth of the matrix too, but the growth was limited by the large pores formed around the crystals. The previous elimination of these pores are, so, essential to promotion an effective grain growth in a subsequent heating stage.
- The experimental conditions for an extensive grain growth in ceramics were not yet achieved, namely in what concerns the seeded polycrystal conversion method. This topic needs to be pursued with the use of a special sintering technique, such as HIP, to eliminate the porosity preliminarily to the grain growth heating treatments and the subsequent study of the thermal cycle conditions.

Future work

The results obtained in this work emerged from the examination of the properties of PZT single crystals and the study of the grain growth in ceramics. However, further studies regarding these two subjects are required to answer some unsolved questions. Accordingly, a future work could be focused in the following issues:

- The growth mechanism of the obtained PZT single-crystals depends on several factors. However, a deeper understanding of the growth mechanism requires a detailed study of the growth conditions, such as flux viscosity, supersaturation or solute diffusion (Such study is expected to increase the knowledge on crystal growth).
- The complex domain pattern in PZT crystals was attributed to the presence of ferroelastic and ferroelectric domains. It is believed that different thermal treatments of the grown crystals may clarify the relation between the observed twinned domain structure and the ferroelastic phase. On the other hand, a better understanding of the domain distribution in the rhombohedral phase is necessary.
- The experimental setup used for piezoelectric characterisation must be improved for allowing measurements in stress-free crystals and for obtaining d_{33} as well as d_{31} and d_{15} piezoelectric coefficients, which are very important for a comprehensive study of the piezoelectric properties.

General conclusions

- The temperature dependence of the spontaneous polarization and the determination of all the parameters of the energy function are also key points for future works.
- The study of the possible changes in symmetry between tetragonal and rhombohedral or monoclinic phases, using XRD technique in the presence of low electric fields for crystals with compositions around the MPB.
- A small bend was observed near room temperature and this bend increased with the increasing of sintering holding time and it is not associated to any structural phase transition. The exact understanding of the origin of this behaviour needs more experimental work.

Appendix I

Phenomenological theory for ferroelectricity

Statistical mechanics provides the link between the microscopic and the macroscopic physical description of the solid state. A general form of the macroscopic description of the solid is an expression for its free energy or other thermodynamic function. Many different types of experimental observations can be reduced to a single phenomenological expression and, to be useful, this should be an explicit expression for an appropriate thermodynamic function.

In this section it is considered only reversible processes, *i.e.*, those depending only on the state or condition of the material described and not on the path taken to reach that particular condition. Reversible processes are described by thermodynamic potentials. A thermodynamic potential is a variable of state associated to a thermodynamic system that has dimensions of energy. The qualification of "potential" is used because, in a certain sense, it describes the amount of potential energy available in the thermodynamic system under certain restrictions (related to the natural variables of the potential). In addition, these potentials help to predict if a thermodynamic change will be spontaneous or will need same energy contribution to proceed.

The internal energy (U) is a thermodynamic potential, which for a ferroelectric material takes the form

$$dU = TdS + Xdx + EdP \quad (\text{I.1})$$

where T , S , X , x , E and P are the absolute temperature, entropy, stress, strain, electric field and polarization, respectively. The term TdS represents the heat flux absorbed or given by the system, Xdx the work made on the system or by the system and EdP is the polarization due to an electric field.

Thermodynamic potentials are expressed in terms of intensive variables T , X , E and extensive ones, S , x , P , but it is sufficient to use only three of them, namely one from each of the conjugated pairs (X, x) , (T, S) , (E, P) . The common thermodynamic energy potentials are shown in Table I.1.

Table I.1 - Common thermodynamic potential energies [22].

Name	Potential	Appropriate variables
Helmholtz function	$A = U - TS$	T, x, P
Gibbs function	$G = U - TS - Xx - E$	T, X, E
Elastic Gibbs function	$G_1 = U - TS - Xx$	T, X, P
Electric Gibbs function	$G_2 = U - TS - EP$	T, x, E
Internal energy	U	S, x, P
Enthalpy	$H = U - Xx - EP$	S, X, E
Elastic enthalpy	$H_1 = U - Xx$	S, X, P
Electric enthalpy	$H_2 = U - EP$	S, x, E

In 1937 Landau developed [364] a general theory for the phase transition between two phases with different symmetries. In this theory, all the symmetry elements of the low-symmetry phase are already present in the high-symmetry phase. The low-symmetry phase is this characterized by a broken symmetry of the high-symmetry phase. This requires an additional thermodynamic variable which specifies the thermodynamic state of the low-symmetry phase. This new variable is called the order parameter (Q). The difference in Gibbs energy between both phases, which stabilizes the low-symmetry phase, depends on the thermodynamic parameters and on the order parameter:

$$G = G(T, P, N, Q...) \tag{I.2}$$

The Gibbs free energy is in an equilibrium state when:

$$\frac{\partial G}{\partial Q} = 0 \tag{I.3}$$

Ginzburg, in 1946 [365], used the second order phase transitions theory developed by Landau to develop the first phenomenological theory for the ferroelectricity developed in the years of the 40's, where the thermodynamic potential is written in the form:

$$\Phi = \left(\Phi_o + \alpha P^2 + \frac{\beta}{2} P^4 \right) - EP \quad (I.4)$$

where E is the electric field strength, P is the polarization, Φ_o is the thermodynamic potential in the equilibrium state and the coefficients α and β depend on the temperature T and on the composition.

Devonshire, in 1949 [154, 366, 367], further developed the thermodynamic theory for the ferroelectricity. Years later, many of the aspects of the phenomenological problem were developed by different authors, among who we emphasize E.M. Lifshitz (1980) [368], V.L. Ginzburg (1987) [369] and A.P. Levanyuk (1998) [370, 371]. Here, we condensate the phenomenological treatment given by those former three authors, known today as the theory of Landau-Ginzburg-Devonshire (LGD) for ferroelectricity.

The differential of the Gibbs' energy for a ferroelectric crystal is:

$$dG = -SdT + Xdx + EdP \quad (I.5)$$

It is found a good agreement with the experimental results if the variation of the polarization with temperature, $P(T)$, is expressed as:

$$P^2(T) = \psi(T)P_o^2 \quad (I.6)$$

where P_o is the polarization at the transition temperature and $\psi(T)$ is a function that depend of the temperature. This allows one to expand G as a power series around a center c , in a general form like

$$\begin{aligned} f(x) &= f(c) + \alpha_1(x-c) + \alpha_2(x-c)^2 + \alpha_3(x-c)^3 + \alpha_4(x-c)^4 + \dots \\ &= f(c) + \sum_{n=1}^{\infty} \alpha_n(x-c)^n \end{aligned} \quad (I.7)$$

The odd terms must not be considered due to the symmetry of the potential in the material without external influence, that is $f(x) = f(-x)$, and the α_n coefficients must be determined. Around the center $c = P_o = 0$, $G(P)$ can be written in the following way [117, 119]:

$$\begin{aligned} \Delta G &\approx \alpha_1^X (P_1^2 + P_2^2 + P_3^2) + \alpha_{11}^X (P_1^4 + P_2^4 + P_3^4) + \alpha_{12}^X (P_1^2 P_2^2 + P_2^2 P_3^2 + P_3^2 P_1^2) + \\ &\alpha_{111}^X (P_1^6 + P_2^6 + P_3^6) + \alpha_{112}^X (P_1^4 (P_2^2 + P_3^2) + P_2^4 (P_1^2 + P_3^2) + P_3^4 (P_1^2 + P_2^2)) + \end{aligned}$$

$$\begin{aligned}
 & \alpha_{123}^X P_1^2 P_2^2 P_3^2 - \frac{1}{2} c_{11}^P (X_1^2 + X_2^2 + X_3^2) - c_{12}^P (X_1 X_2 + X_2 X_3 + X_3 X_1) - \\
 & \frac{1}{2} c_{44}^P (X_4^2 + X_5^2 + X_6^2) - Q_{11} (X_1 P_1^2 + X_2 P_2^2 + X_3 P_3^2) - Q_{12} (X_1 (P_2^2 + P_3^2) + \\
 & X_2 (P_3^2 + P_1^2) + X_3 (P_1^2 + P_2^2)) - Q_{44} (X_4 P_2 P_3 + X_5 P_1 P_3 + X_6 P_1 P_2)
 \end{aligned} \tag{I.8}$$

where α_1 , α_{ij} and α_{ijk} are the dielectric stiffness and the higher order stiffness coefficients at constant stress, the c_{ij} are the elastic compliance coefficients measured at constant polarization and the Q_{ij} are the cubic electrostriction constants written in polarization notation (Equation 1.27). The expression comprehends all sixth power terms in polarization, but contains only fourth order terms in electrostrictive and elastic behaviour. The reduced tensor notation is used to describe the stress tensor (see section 1.1.5).

The first partial derivatives of the energy with respect to components of P , X and T give the conjugate parameters: the electric field E_i , the negative of the strain $-x_{ij}$, and the entropy change $-S$, respectively.

$$\frac{\partial \Delta G}{\partial P_i} = E_i \quad (\text{a}) \quad \frac{\partial \Delta G}{\partial X_{ij}} = -x_{ij} \quad (\text{b}) \quad \frac{\partial \Delta G}{\partial T} = -S \quad (\text{c}) \tag{I.9}$$

Appropriate second partial derivatives give the dielectric stiffnesses ($\alpha_1 = \eta_{ij}$), the reduced elastic compliances tensor c_{ij} and the piezoelectric polarization related coefficients b_{ij} :

$$\frac{\partial^2 \Delta G}{\partial P_i \partial P_j} = \eta_{ij} \quad (\text{a}) \quad \frac{\partial^2 \Delta G}{\partial X_i \partial X_j} = -c_{ij} \quad (\text{b}) \quad \frac{\partial^2 \Delta G}{\partial P_i \partial X_j} = -b_{ij} \quad (\text{c}) \tag{I.10}$$

In this work we will evaluate the PZT phases with chemical compositions not far from the MPB, i.e., the cubic, the tetragonal and the designated high temperature rhombohedral phases. Considering a stress free material, $X_{ij} \equiv 0$, and the restrictive polarization direction for each phase (Table 1.3), we have the following three possible solutions for Equation I.8 [325]:

For the cubic phase

$$\Delta G = 0 \quad (\text{I.11})$$

For the tetragonal one

$$\Delta G = \alpha_1^X P_3^2 + \alpha_{11}^X P_3^4 + \alpha_{111}^X P_3^6 \quad (\text{I.12})$$

And for the rhombohedral

$$\Delta G = 3\alpha_1^X P_3^2 + 3(\alpha_{11}^X + \alpha_{12}^X)P_3^4 + (3\alpha_{111}^X + 6\alpha_{112}^X + \alpha_{123}^X)P_3^6 \quad (\text{I.13})$$

Without applied field, $E_i \equiv 0$, the condition for the appearance of a minimum in the free energy is that Equation (I.10) must have positive values (the necessary conditions for a local minimum of any function $f(x)$ are: $\frac{\partial f(x)}{\partial x} = 0$ and $\frac{\partial^2 f(x)}{\partial x^2} > 0$. These are only necessary conditions, but not sufficient).

Using Equations (I.9), (I.11), (I.12) and (I.13) we have

For the cubic phase

$$P = 0 \quad (\text{I.14})$$

For the tetragonal one

$$\alpha_1^X P_3 + 2\alpha_{11}^X P_3^3 + 3\alpha_{111}^X P_3^5 = 0 \quad (\text{I.15})$$

There are five possible solutions for this polynomial equation, namely:

$P_3 = 0$, which is the trivial solution and corresponds to a non polar material and the others are included in the solution of

$$\alpha_1^X + 2\alpha_{11}^X P_3^2 + 3\alpha_{111}^X P_3^4 = 0 \quad (\text{I.16})$$

Changing the variable to $P_3^2 = t$ one gets

$$\alpha_1^X + 2\alpha_{11}^X t + 3\alpha_{111}^X t^2 = 0 \quad (\text{I.17})$$

which has an easy solution. Returning then to the original variable, one arrives to the next four solutions

$$P_3^2 = \frac{-\alpha_{11}^X \pm \left[(\alpha_{11}^X)^2 - 3\alpha_1^X \alpha_{111}^X \right]^{1/2}}{3\alpha_{111}^X} \quad (\text{I.18})$$

In order to have a real solution, $(\alpha_{11}^X)^2 - 3\alpha_1^X \alpha_{111}^X \geq 0$. Using the same approach, it is conceivable to infer that P_3 has a real solution when it is considered the positive sign in Equation (I.18), *i.e.*,

$$P_3^2 = \frac{-\alpha_{11}^X + \left[(\alpha_{11}^X)^2 - 3\alpha_1^X \alpha_{111}^X \right]^{1/2}}{3\alpha_{111}^X} \quad (\text{I.19})$$

For the rhombohedral case

$$\alpha_1^X P_3 + 2(\alpha_{11}^X + \alpha_{12}^X) P_3^3 + (3\alpha_{111}^X + 6\alpha_{112}^X + \alpha_{123}^X) P_3^5 = 0 \quad (\text{I.20})$$

again with five solutions. Proceeding in the same way as before, excluding the trivial solution $P_3 = 0$, one has

$$\alpha_1^X + 2(\alpha_{11}^X + \alpha_{12}^X) P_3^2 + (3\alpha_{111}^X + 6\alpha_{112}^X + \alpha_{123}^X) P_3^4 = 0 \quad (\text{I.21})$$

with the following solutions

$$P_1^2 = P_2^2 = P_3^2 = \frac{-(\alpha_{11}^X + \alpha_{12}^X) + \left[(\alpha_{11}^X + \alpha_{12}^X)^2 - \alpha_1^X (3\alpha_{111}^X + 6\alpha_{112}^X + \alpha_{123}^X) \right]^{1/2}}{3\alpha_{111}^X + 6\alpha_{112}^X + \alpha_{123}^X} \quad (\text{I.22})$$

In general, the coefficients α depend on the temperature T and on the composition.

Spontaneous elastic strains

In ferroelectric single domain states, the spontaneous elastic strains, under the condition $X_i \equiv 0$ may be deduced from Equation I.9 leading to the following relations:

For the cubic phase

$$x_1 = x_2 = x_3 = x_4 = x_5 = x_6 = 0 \quad (\text{I.23})$$

For the tetragonal one

$$x_3 = Q_{11} P_3^2 \quad x_1 = x_2 = Q_{12} P_3^2 \quad x_4 = x_5 = x_6 = 0 \quad (\text{I.24})$$

And for the rhombohedral case

$$x_1 = x_2 = x_3 = (Q_{11} + 2Q_{12})P_3^2 \quad x_4 = x_5 = x_6 = Q_{44}P_3^2 \quad (\text{I.25})$$

Relative dielectric stiffnesses

The relative dielectric stiffnesses (η_{ij}) were derived from Equation I.10 resulting in:

Cubic phase

$$\eta_{11} = \eta_{22} = \eta_{33} = 2\alpha_1^X \varepsilon_o \quad \eta_{12} = \eta_{23} = \eta_{31} = 0 \quad (\text{I.26})$$

Tetragonal phase

$$\begin{aligned} \eta_{33} &= (2\alpha_1^X + 12\alpha_{11}^X P_3^2 + 30\alpha_{111}^X P_3^4) \varepsilon_o \\ \eta_{11} = \eta_{22} &= (2\alpha_1^X + 2\alpha_{12}^X P_3^2 + 2\alpha_{112}^X P_3^4) \varepsilon_o \\ \eta_{12} = \eta_{23} = \eta_{31} &= 0 \end{aligned} \quad (\text{I.27})$$

Rhombohedral phase

$$\begin{aligned} \eta_{11} = \eta_{22} = \eta_{33} &= (2\alpha_1^X + (12\alpha_{11}^X + 4\alpha_{12}^X)P_3^2 + (30\alpha_{111}^X + 28\alpha_{112}^X + 2\alpha_{123}^X)P_3^4) \varepsilon_o \\ \eta_{12} = \eta_{23} = \eta_{31} &= (4\alpha_{12}^X P_3^2 + (16\alpha_{112}^X + 4\alpha_{123}^X)P_3^4) \varepsilon_o \end{aligned} \quad (\text{I.28})$$

Equations I.26 to I.28 were multiplied by ε_o to give relative dielectric stiffnesses.

Dielectric susceptibility coefficients

In the high temperature region, where the crystal has cubic symmetry, the dielectric constant is independent on the direction and is given by

$$\varepsilon = 1 + \frac{4\pi}{\eta} \quad (\text{I.29})$$

However in the temperature region where the crystal has lower symmetry, the dielectric constant is no longer independent on the direction and has to be described by a tensor. It is, in practice, more convenient to work in terms of the dielectric susceptibility (χ) and its reciprocal (η), the dielectric stiffness. They are connected by Equation 1.6 and the susceptibility for the different phases are given by:

Cubic phase

$$\chi_{ij} = \eta_{ij}^{-1} \quad (\text{I.30})$$

Tetragonal phase

$$\chi_{ij} = \eta_{ij}^{-1} \quad (\text{I.31})$$

Rhombohedral phase

In the rhombohedral state, the polarization can be along the $\langle 111 \rangle$ directions of the original cubic axes. It is, in the practice, more convenient to rotate these axes so that the new a_3 axis is along the previous $[111]$ direction. The susceptibility coefficients defined by Equation I.28 based on the original axes can be determined from the following relation:

$$\begin{aligned} \chi_{11} = \chi_{22} = \chi_{33} &= \frac{\eta_{11}^2 - \eta_{12}^2}{\eta_{11}^3 - 3\eta_{11}\eta_{12}^2 + 2\eta_{12}^3} \\ \chi_{12} = \chi_{23} = \chi_{31} &= \frac{\eta_{12}^2 - \eta_{11}\eta_{12}}{\eta_{11}^3 - 3\eta_{11}\eta_{12}^2 + 2\eta_{12}^3} \end{aligned} \quad (\text{I.32})$$

The piezoelectric polarization related coefficients

The piezoelectric polarization related coefficients b_{ij} can be derived from Equation I.10c as shown below:

Cubic

$$b_{ij} = 0 \quad (\text{I.33})$$

Tetragonal

$$b_{33} = 2Q_{11}P_3 \quad b_{31} = b_{32} = 2Q_{12}P_3 \quad b_{15} = b_{24} = Q_{44}P_3 \quad (\text{I.34})$$

Rhombohedral

$$\begin{aligned} b_{11} = b_{22} = b_{33} &= 2Q_{11}P_3 \\ b_{12} = b_{13} = b_{23} = b_{21} = b_{31} = b_{32} &= 2Q_{12}P_3 \\ b_{15} = b_{16} = b_{26} = b_{24} = b_{35} = b_{34} &= Q_{44}P_3 \end{aligned} \quad (\text{I.35})$$

Piezoelectric strain coefficients

The piezoelectric strain coefficients d_{ij} for the tetragonal or rhombohedral phases can be related to the b_{ij} coefficients by $d_{ij} = \chi_{ij} b_{ij}$. Then:

$$\begin{aligned} d_{33} &= \chi_{33} \varepsilon_o b_{33} = 2\chi_{33} \varepsilon_o Q_{11} P_3 \\ d_{31} &= \chi_{33} \varepsilon_o b_{31} = 2\chi_{33} \varepsilon_o Q_{12} P_3 \\ d_{15} &= \chi_{11} \varepsilon_o b_{15} = \chi_{11} \varepsilon_o Q_{44} P_3 \end{aligned} \quad (I.36)$$

The dielectric susceptibility coefficients in I.36 are based on the original cubic axes.

The piezoelectric voltage coefficients:

The piezoelectric voltage coefficients g_{ij} are related to the b_{ij} coefficients by a factor of $(\varepsilon - 1)/\varepsilon$, where ε is the dielectric constant. PZT compositions have $\varepsilon \gg 1$, thus the g_{ij} coefficients are approximately equal to the b_{ij} coefficients. Hence, for the rhombohedral and tetragonal phases the g_{ij} coefficients are:

$$g_{33} \approx b_{33} = 2Q_{11} P_3 \quad g_{31} \approx b_{31} = 2Q_{12} P_3 \quad g_{15} \approx b_{15} = Q_{44} P_3 \quad (I.37)$$

Using the last equations it is possible to determine the spontaneous polarization and the strain, the dielectric and the piezoelectric properties from the dielectric susceptibility, higher-order stiffness and electrostrictive constants.

The general characterisation of a thermodynamic system is achieved when all the constants or parameters of the Gibbs free energy function are known. The parameters must be obtained from experimental data or using a combination of experimental and theory.

Evaluation of the coefficients of the energy function

The parameters in the free energy function depend on the temperature and on the composition and also on, when considered, the application of an electrical field or a mechanical stress on the material. In order to simplify the equation numbers, in the following it is considered only a phase transition of the first order, or of the first order near to the second one *i.e.*, when the Curie temperature is different of the Curie-Weiss one ($T_c \neq T_0$). This is the case found in our crystals and all the parameters were assumed to be independent on the temperature, except the dielectric stiffness constant α_l which was given linear temperature dependence and a sign that changes from negative to positive at T_0 . α_l is obtained from the experimental data through the Curie-Weiss law [325]:

$$\alpha_1 = \frac{(T - T_0)}{2\varepsilon_0 C} \quad (\text{I.38})$$

where C is the Curie constant, ε_0 is the vacuum permittivity and T_0 is the Curie-Weiss temperature.

Tetragonal

The higher-order dielectric stiffness coefficients α_{11} and α_{111} are determined in the transition temperature (T_c) from paraelectric to ferroelectric where the Gibbs free energy is equal in the cubic and in the tetragonal phases. Hence, from Equations I.11 and I.12

$$\alpha_{1(Tc)}^X P_{3(Tc)}^2 + \alpha_{11(Tc)}^X P_{3(Tc)}^4 + \alpha_{111(Tc)}^X P_{3(Tc)}^6 = 0 \quad (\text{I.39})$$

This has six solutions, two of them being $P_{3(Tc)}^2 = 0$, and the others

$$\alpha_{1(Tc)}^X + \alpha_{11(Tc)}^X P_{3(Tc)}^2 + \alpha_{111(Tc)}^X P_{3(Tc)}^4 = 0 \quad (\text{I.40})$$

On the other hand, at T_c the internal electric fields are zero and hence, from Equation I.9a, we have

$$\alpha_{1(Tc)}^X P_{3(Tc)} + 2\alpha_{11(Tc)}^X P_{3(Tc)}^3 + 3\alpha_{111(Tc)}^X P_{3(Tc)}^5 = 0 \quad (\text{I.41})$$

Here there are five possible solutions. One of them, $P_{3(Tc)} = 0$, is the trivial solution corresponding to a non-polar material. The other solutions are obtained by solving

$$\alpha_{1(Tc)}^X + 2\alpha_{11(Tc)}^X P_{3(Tc)}^2 + 3\alpha_{111(Tc)}^X P_{3(Tc)}^4 = 0 \quad (\text{I.42})$$

At T_c , the internal electric fields and the free energy are both zero and therefore Equations I.40 and I.42 must be equal. Hence, one obtains the following relations for the coefficients:

$$\alpha_{11(Tc)}^X = -\frac{\alpha_{1(Tc)}^X}{P_{3(Tc)}^2} \quad (\text{a}) \quad \alpha_{111(Tc)}^X = \frac{\alpha_{1(Tc)}^X}{P_{3(Tc)}^4} \quad (\text{b}) \quad (\text{I.43})$$

Since α_{11} and α_{111} were considered to be independent on the temperature, it is possible to write Equations I.38 and I.43 without the sub-indices (T_c)

$$\alpha_{11}^X = -\frac{\alpha_{1(Tc)}^X}{P_{3(Tc)}^2} \quad (\text{a}) \quad \alpha_{111}^X = \frac{\alpha_{1(Tc)}^X}{P_{3(Tc)}^4} \quad (\text{b}) \quad \alpha_{1(Tc)}^X = \frac{Tc - T_0}{2\varepsilon_0 C} \quad (\text{c}) \quad (\text{I.44})$$

Then, substituting the Equations I.44 into I.19 we have

$$P_3^2 = \psi P_{3(T_c)}^2 \quad (\text{I.45})$$

where

$$\psi = \frac{2}{3} \left[1 + \left(1 - \frac{3(T - T_0)}{4(T_c - T_0)} \right)^{1/2} \right] \quad (\text{I.46})$$

The coefficients α_{12} and α_{112} are not present in the free energy function for the tetragonal phase (Equation I.12) or in the first order derivative (Equation I.15), but do arise in the second order one (Equations I.27 and 1.6). Using experimental data of the susceptibilities χ_{11} and χ_{33} together with a piezoelectric measurement, it is possible to obtain all the parameters by fitting the experimental data with Equation I.16 [326]. This can be done for each composition. To obtain the coefficients α_{12} and α_{112} with the composition it is necessary to use single crystals in all the region of composition under study. In the literature it is proposed same approximations to obtain the last parameters [117, 321, 322, 325]. The parameters T_c , C , T_0 , $P_{s(T_c)}$ can also be obtained from experimental data.

Rhombohedral

The last Equations I.44, I.45 and I.46, valid for the tetragonal phase, are similar to those obtained for the rhombohedral one. Considering that the free energy in the transition temperature (T_c) is equal both in the cubic and in the rhombohedral phases, from Equation I.11 and I.13 we have

$$3\alpha_1^X + \zeta P_3^2 + \xi P_3^4 = 0 \quad (\text{I.47})$$

$$\text{with } \zeta = 3(\alpha_{11}^X + \alpha_{12}^X) \quad (\text{a}) \quad \text{and} \quad \xi = 3\alpha_{111}^X + 6\alpha_{112}^X + \alpha_{123}^X \quad (\text{b}) \quad (\text{I.48})$$

At T_c , the internal electric fields are zero and from Equation I.21,

$$\alpha_1^X + \frac{2}{3} \zeta P_3^2 + \xi P_3^4 = 0 \quad (\text{I.49})$$

Again, at T_c the internal electric fields and the free energy are zero and therefore Equations I.48 and I.49 must be equal. Then, the coefficients are:

$$\zeta = -\frac{6\alpha_{1(Tc)}^X}{P_{3(Tc)}^2} \quad (a) \qquad \xi = \frac{3\alpha_{1(Tc)}^X}{P_{3(Tc)}^4} \quad (b) \quad (I.50)$$

Then, substituting Equations I.44c and I.50 into I.22 we have

$$P_3^2 = \psi P_{3(Tc)}^2 \quad (I.51)$$

where

$$\psi = \frac{2}{3} \left[1 + \left(1 - \frac{3(T - T_0)}{4(Tc - T_0)} \right)^{1/2} \right] \quad (I.52)$$

Since ζ and ξ are considered independent on the temperature, it is possible to obtain them by fitting the experimental data for different compositions

$$\zeta = -\frac{3(Tc - T_0)}{\varepsilon_o CP_{3(Tc)}^2} \quad (a) \qquad \xi = \frac{3(Tc - T_0)}{2\varepsilon_o CP_{3(Tc)}^2} \quad (b) \quad (I.53)$$

The coefficients α_{11} , α_{12} , α_{111} , α_{112} and α_{123} are determined using the experimental data of χ_{11} and χ_{33} together with two other measurements (piezoelectric, polarization, strain). It is possible to obtain all the parameters by fitting the experimental data. Using the inverse of the permittivity with the temperature (Equation I.28) it is possible to obtain the parameters Tc , C and T_0 [326]. The last procedure can be repeated for each composition.

In the literature there are some approximations to obtain the parameters from these measurements. The coefficients can be obtained by fitting the spontaneous polarization dependence of the dielectric constants. Haun *et al.* and Amin *et al.* [117, 118, 325] reported the parameters Tc , C , T_0 , $P_{s(Tc)}$ as functions of the composition (x), obtained from experimental data. One of the approximations given by Amin *et al.* [325] is:

$$\begin{aligned} Q_{11} &= 6.6 \times 10^{-2} m^4/C^2 \\ Q_{12} &= -3.2 \times 10^{-2} m^4/C^2 \\ Q_{44} &= 1.5 \times 10^{-2} m^4/C^2 \end{aligned} \quad (I.54)$$

$$Tc = (211.8 + 486.0x - 280.0x^2 + 74.42x^3)^\circ C \quad (I.55)$$

$$T_0 = (208.2 + 489.6x - 322.8x^2 + 164.7x^3 - 63.81x^4)^\circ C \quad (I.56)$$

Appendix I

$$P_{s(T_c)} = (0.11914 + 0.20007x + 0.04854x^2 - 0.0002914x^3) C/m^2 \quad (\text{I.57})$$

$$\alpha_1^X = \frac{T - T_0}{2\varepsilon_o C} \quad (\text{and} \quad \alpha_{1(T_c)}^X = \frac{T_c - T_0}{2\varepsilon_o C})$$

$$\alpha_{11}^X = -\frac{\alpha_{1(T_c)}^X}{P_{3(T_c)}^2} \quad (\text{I.58})$$

$$\alpha_{12}^X = \phi \alpha_{1(T_c)}^X \quad (\text{I.59})$$

$$\alpha_{111}^X = \frac{\alpha_{1(T_c)}^X}{P_{3(T_c)}^4} \quad (\text{I.60})$$

$$\alpha_{112}^X = \frac{800}{\varepsilon_o C} \quad (\text{I.61})$$

$$\alpha_{123}^X = \frac{[-45000(1-x) - 20000x]}{\varepsilon_o C} \quad (\text{I.62})$$

Appendix II

Calculus of other thermodynamic coefficients.

In section 4.5 the thermodynamic parameters were determined using the experimental results of the dielectric permittivity and polarization. The thermodynamic coefficients can be determined when the dielectric properties are measured and if it is known one or two of the following coefficients: the piezoelectric strain coefficients (d_{ij}), the piezoelectric voltage coefficients (g_{ij}), the piezoelectric polarization related coefficients (b_{ij}), the electrostriction constants (Q_{ij}) or the spontaneous elastic strain (x_{ij}). In our work these parameters were not measured. The precise measurement of two of these parameters as a function of the temperature, together with the dielectric permittivity, allows calculating the other parameters (using Equations I.24, I.25, I.34 - I.37 of appendix I).

Expressions similar to those obtained for the polarization in Equations I.45 and I.51 for the tetragonal and rhombohedral field can be obtained for the spontaneous elastic strain as follows.

Tetragonal phase

Substituting Equation I.45 and I.46 in Equation I.24 gives

$$x_3 = \psi x_{3(Tc)} \quad (\text{II. 1})$$

where ψ is given by Equation I.46 and $x_{3(Tc)}$ is

$$x_{3(Tc)} = Q_{11} P_{3(Tc)}^2 \quad (\text{II. 2})$$

The spontaneous elastic strain can be determined from the X-ray diffraction, which for the [001] direction is

$$x_3 = \frac{(c_T - a'_C)}{a'_C} \quad (\text{II. 3})$$

where c_T is the cell constant and a'_C is the cell parameter of the cubic structure extrapolated into the tetragonal region, determined by

$$a'_c = (a_T^2 c_T)^{\frac{1}{3}} \quad (\text{II. 4})$$

The spontaneous elastic strain should be determined at several temperatures to obtain better results.

Rhombohedral phase

Substituting Equation I.51 and I.52 in Equation I.25 gives

$$x_3 = \psi \alpha_{3(T_c)} \quad (\text{II. 5})$$

where ψ is given by Equation I.52 and $x_{3(T_c)}$ is

$$x_{3(T_c)} = (Q_{11} + 2Q_{12})P_{3(T_c)}^2 \quad (\text{II. 6})$$

The spontaneous elastic strain can be determined from the X-ray diffraction, which for the [001] direction is

$$x_3 = \frac{(90 - \alpha_R)}{90} \quad (\text{II. 7})$$

where α_R is the rhombohedral angle of the unit cell.

In our study the structure of the crystals were determined by X-ray diffraction at 180 K and the result of the unit cell are resumed in Table 4.6. The spontaneous elastic strains were calculated at 180 K using Equations II.3 and II.7 and then calculated the $x_{3(T_c)}$ at the transition temperature using the Equations II.1 and II.5 and the parameters are reported in Table 4.11. The results of these calculi are summarized in Table II.1, and agree with those reported in the literature [117-119, 321-323]. The values for the crystal PZT52 are not reported because the X-ray diffraction at 180 K reveals a pseudo-cubic structure. The knowledge of $x_{3(T_c)}$ at the transition temperature allows obtaining the temperature dependence of the spontaneous elastic strain and this is plotted in Figure 4.56.

Table II.1 - Spontaneous elastic strain calculated at 180 K and at T_c.

crystal	$x_{3(180K)}$	$x_{3(T_c)}$
PZT65	9.22×10^{-4}	1.34×10^{-4}
PZT60	1.72×10^{-3}	1.82×10^{-4}
PZT46	2.64×10^{-2}	2.69×10^{-3}
PZT42	2.50×10^{-2}	3.02×10^{-3}

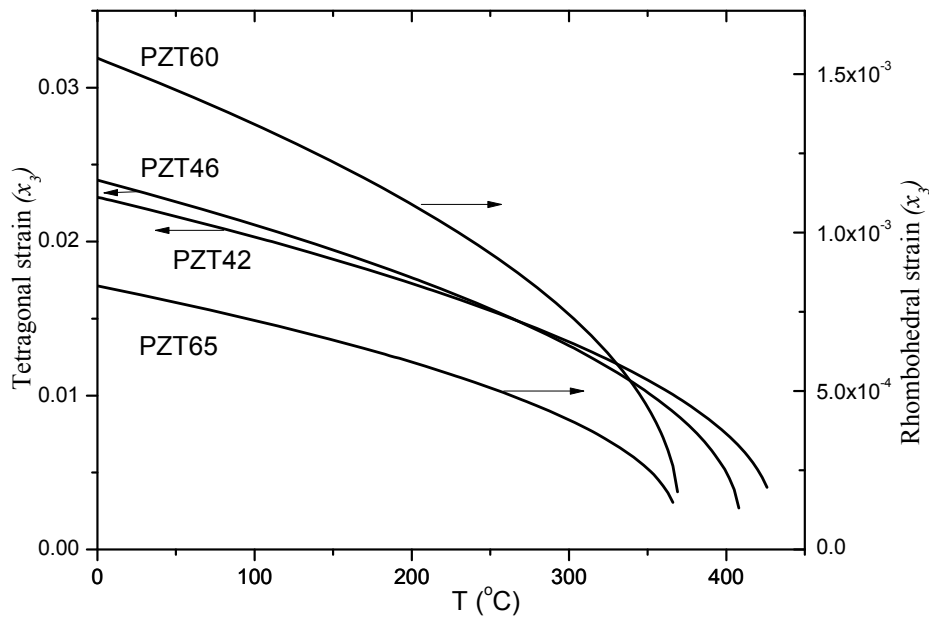


Figure 4.56 - Temperature dependence of the calculated spontaneous elastic strain.

The electrostriction constants (Q_{ij}) and the spontaneous polarization at T_c are not reported in Table II.1 because they were not separated from $x_{3(T_c)}$. These parameters can only be separated by measuring directly one of them or indirectly using the hysteresis loop or the piezoelectric coefficients. For example, the values of $Q_{11} = 6 \times 10^{-3} \text{ (m}^4/\text{C}^2\text{)}$, $x_3 = 9.6 \times 10^{-4}$, $b_{33} = 4.8 \times 10^{-3} \text{ (Vm/N)}$ and $g_{33} = 4.8 \times 10^{-3} \text{ (Vm/N)}$, were calculated for a crystal with $x=0.5$ using Equations I.24, I.36 and I.37. The values of $P_3(30^\circ\text{C}) = 0.40 \text{ (C/m}^2\text{)}$ and $d_{33}(30^\circ\text{C}) = 20 \text{ (pm/V)}$ are presented in sections 4.4.2 and 4.4.3 respectively. The values obtained for these parameters are an order of magnitude lower than the reported in literature [117, 118, 321, 322, 325, 326]. A possible explanation for this is the clamping of the crystal by the araldite polymer, as previously discussed.

The values of the different parameters summarized in this chapter correspond to PZT single crystals and they were obtained by fitting the experimental data of the dielectric permittivity, not directly. The measurement of the polarization using another method is necessary to confirm these results.

References

1. Wang, Z. L. and Kang, Z. C., *Functional and smart materials structural evolution and structure analysis*. 1998, New York: Plenum Press. XXIII, 514.
2. Vilarinho, P. M., *Functional materials: Properties, processing and applications*, in *Scanning Probe Microscopy: Characterization, Nanofabrication and Device Application of Functional Materials*, Vilarinho, Rosenwaks and Kingon, Editors. 2005. p. 3-33.
3. Amorín, G. H., *Preparação e propriedades de cristais e de cerâmicos e perovskites ferroelétricas com camadas de bismuto Texto policopiado Preparation and properties of ferroelectric single crystals and ceramics of bismuth layered perovskites sob orientação de Maria Elisabete J. V. Costa e de Andrei L. Kholkin*, in *Departamento de Engenharia Cerâmica e do Vidro*. 2005, Universidade de Aveiro.: Aveiro, Portugal. p. [8], XXIV, 219.
4. Shuvalov, L. A. *Symmetry aspects of Ferroelectricity*. in *Proceeding of the Second International Meeting on Ferroelectricity, Kyoto, 1969*. 1970: Journal of the Physical Society of Japan.
5. Isupov, V. A., *Properties of $Pb(Ti,Zr)O_3$ piezoelectric ceramics and nature of their orientational dielectric polarization*. Soviet Physics Solid State, USSR, 1968. **10**(4): p. 989.
6. Noheda, B., *et al.*, *Stability of the monoclinic phase in the ferroelectric perovskite $PbZr_{1-x}Ti_xO_3$* . Physical Review B, 2000. **63**(1): p. 014103.
7. Damjanovic, D. *Secrets of PZT*. in *plenary lectures in 17th international symposium on the applications of ferroelectrics and meeting of the electronics division of the American ceramic society*. 2008. Santa Fe, New Mexico, February 24 - 27, 2008.
8. Carl, K. and Hardtl, K. H., *Origin of maximum in electromechanical activity in $Pb(Zr_xTi_{1-x})O_3$ ceramics near morphotropic phase boundary*. Physica Status Solidi A-Applied Research, 1971. **8**(1): p. 87.
9. Soares, M. R., Senos, A. M. R. and Mantas, P. Q., *Phase coexistence region and dielectric properties of PZT ceramics*. Journal of the European Ceramic Society, 2000. **20**(3): p. 321-334.
10. Soares, M. R. T., Senos, A. M. O. R. and Mantas, P., *A transição morfotrópica dos cerâmicos PZT*, in *Departamento de Engenharia Cerâmica e do Vidro*. 2001, Universidade de Aveiro: Aveiro, Portugal. p. XVII, 186.11.
11. Haertling, G. H., *Ferroelectric ceramics: history and technology*. Journal American ceramic society, 1999. **82** (4): p. 21.

12. Waser, R., *Modeling of electroceramics - Applications and prospects*. Journal of the European Ceramic Society, 1999. **19**(6-7): p. 655-664.
13. Haertling, G. H., *Electrooptic ceramics and devices” in Electronic ceramics: properties, devices and applications*, ed. Levinson. 1988, New York: Dekker.
14. Vest, R. W., *Metallo-organic decomposition (MOD) processing of ferroelectric and electro-optic films: A review*. Ferroelectrics, 1990. **102**(1): p. 53 - 68.
15. Sheppard, L. M., *Advances in processing of ferroelectric thin-films*. American Ceramic Society Bulletin, 1992. **71**(1): p. 85-95.
16. Schwartz, R. W., *et al.*, *Sol-gel processing of PZT thin Films: A review of the state-of-the-art and process optimization strategies*. Integrated Ferroelectrics, 1995. **7**(1-4): p. 259-277.
17. Auciello, O. and Ramesh, R., *Electroceramic thin films. Part1. Processing*. Mrs Bulletin, 1996. **21**(6): p. 21-21.
18. Dong, S. X., *et al.*, *Near-ideal magnetoelectricity in high-permeability magnetostrictive/piezofiber laminates with a (2-1) connectivity*. Applied Physics Letters, 2006. **89**(25).
19. Valasek, J., *Piezo-electric and allied phenomena in Rochelle salt*. Physical Review, 1921. **17**(4): p. 475-481.
20. Shirane, G. and Jona, F., *Ferroelectric Crystals*. 1962, Oxford: Pergamon Press.
21. Fatuzzo, E. and Merz, W. J., *Ferroelectricity*. Series of monographs on selected topics in solid state physics 7. 1967, Amsterdam: North-Holland. X, 289.
22. Lines, M. E. and Glass, A. M., *Principles and applications of ferroelectrics and related materials*. The international series of monographs on physics. 1977, Oxford: Clarendon Press. XIII, 680.
23. Xu, Y., *Ferroelectric Materials and their Applications*, ed. Publ. 1991, North-Holland, Amsterdam: Elsevier Sci.
24. Uchino, K., *Ferroelectric devices*. Materials engineering. 2000, New York: Marcel Dekker. X, 308.
25. Setter, N., *ABC of Piezoelectricity and Piezoelectric Materials*, in *Piezoelectric Materials in Devices*, Setter, Editor. 2002, Ceramics Laboratory, EPFL: Lausanne, Switzerland. p. 1-27.
26. Fasquelle, D. and Carru, J. C., *Electrical characterizations of PZT ceramics in large frequency and temperature ranges*. Journal of the European Ceramic Society, 2008. **28**(10): p. 2071-2074.
27. Moulson, A. J. and Herbert, J. M., *Electroceramics, Materials, Properties and Applications* 1990, London: Chapman and Hall.
28. Sawyer, C. B. and Tower, C. H., *Rochelle salt as a dielectric*. Physical Review, 1930. **35**(3): p. 0269-0273.
29. Camlibel, I., *Spontaneous polarization measurements in several ferroelectric oxides using a pulsed-field method*. Journal of Applied Physics, 1969. **40**(4): p. 1690.

References

30. Jaffe, B., Cook Jr, W. R. and Jaffe, H., *Piezoelectric ceramics*. Non-metallic solids 3. 1971, London: Academic Press. IX, 317.
31. Ikeda, T., *Fundamentals of piezoelectricity*. 1990, New York Oxford University Press.
32. Waanders, J. W., *Piezoelectric Ceramics: Properties and Applications*. 1991, Eindhoven-The Netherlands: Philips Components.
33. Nye, J. F., *Physical Properties of Crystals*. 1985, New York: Oxford University Press
34. Cross, L. E., *Ferroelectric Ceramics-Tutorial Reviews, Theory, Processing and Applications*, ed. Setterand Colla. 1993, Basel: Birkhauser Verlag.
35. Newnham, R. E., *Proc. Chemistry of Electronic Ceramic Materials*. 1990: (National Institute of Standards and Technology, Jackson, WY) Special Publication 804.
36. Damjanovic, D., *Ferroelectric, dielectric and piezoelectric properties of ferroelectric thin films and ceramics*. Reports on Progress in Physics, 1998. **61**(9): p. 1267-1324.
37. Nye, J. F., *Physical Properties of Crystals* 1990, Oxford: Clarendon Press.
38. Matthias, B. and Vonhippel, A., *Domain structure and dielectric response of barium titanate single crystals*. Physical Review, 1948. **73**(11): p. 1378-1384.
39. Arlt, G., *Twinning in ferroelectric and ferroelastic ceramics - stress relief*. Journal of Materials Science, 1990. **25**(6): p. 2655-2666.
40. Cao, W., *Phenomenological theories of ferroelectric phase transitions*. British Ceramic Transactions, 2004. **103**(2): p. 71-75.
41. Cohen, R. E., *Origin of Ferroelectricity in Perovskite Oxides*. Nature, 1992. **358**(6382): p. 136-138.
42. Newnham, R. E., *Structure - Property Relations* 1975, New York: Springer Verlag.
43. Lang, S. B., *Sourcebook of pyroelectricity*. Ferroelectrics and related phenomena 2. 1974, London: Gordon and Breach Science. XV, 562 p.
44. Zhang, P. L., *et al.*, *An unusual pyroelectric response*. Solid State Communications, 1988. **67**(12): p. 1215-1217.
45. Morozov, M., *Softening and hardening transitions in ferroelectric Pb(Zr,Ti)O₃ ceramics*. 2005, Electrotechnique d'Etat de St. Pétersbourg, Russie: St. Pétersbourg.
46. Berlincourt, D., *et al.*, *Transducer properties of lead titanate zirconate ceramics*. Proceedings of the Institute of Radio Engineers, 1959. **47**(3): p. 482-482.
47. Berlincourt, D. and Krueger, H. H. A., *Domain processes in lead titanate zirconate and barium titanate ceramics*. Journal of Applied Physics, 1959. **30**(11): p. 1804-1810.
48. Damjanovic, D., *et al.*, *Properties and applications of modified lead titanate ceramics*. Proceedings of the 1998 Ieee International Frequency Control Symposium, 1998: p. 770-778.

49. Hatanaka, T. and Hasegawa, H., *Dielectric Properties of Pb(Zr_xTi_{1-x})O₃ Single Crystals Including Monoclinic Zirconia*. Japanese Journal of Applied Physics Part 1-Regular Papers Short Notes & Review Papers, 1995. **34**(9B): p. 5446-5448.
50. Merz, W. J., *Switching Time in Ferroelectric BaTiO₃ and its Dependence on Crystal Thickness*. Journal of Applied Physics, 1956. **27**(8): p. 938-943.
51. Lynch, C. S., *The effect of uniaxial stress on the electro-mechanical response of 8/65/35 PLZT*. Acta Materialia, 1996. **44**(10): p. 4137-4148.
52. Lynch, C. S. and Evans, A. G., *Effects of off-axis loading on the tensile behavior of a ceramic-matrix composite*. Journal of the American Ceramic Society, 1996. **79**(12): p. 3113-3123.
53. Jackson, W. and Reddish, W., *High permittivity crystalline aggregates*. Nature, 1945. **156**(3972): p. 717-717.
54. Rushman, D. F. and Strivens, M. A., *The permittivity of polycrystals of the perovskite type*. Trans. Faraday Soc., 1946. **42**: p. A231-238.
55. Westphal, W. B. and Matsui, T., *Dielectric and X-Ray Studies of Ca_xBa_{1-x}TiO₃ and Ca_xSr_{1-x}TiO₃*. Phys. Rev, 1961. **124**: p. 1354.
56. Mitchell, R. H., *Perovskites modern and ancient 2002*, Ontario: Almaz Press.
57. Cady, W. G., *Piezoelectricity*. 1962, New York: Dover Publications.
58. Hoshino, S., Okaya, Y. and Pepinsky, R., *Crystal structure of the ferroelectric phase of (GLYCINE)₃ H₂SO₄*. Physical Review, 1959. **115**(2): p. 323-330.
59. Kay, M. I. and Kleinber. R., *Crystal-structure of triglycine sulfate*. Ferroelectrics, 1973. **5**(1-2): p. 45-52.
60. Broadhurst, M. G., *et al.*, *Piezoelectricity and pyroelectricity in polyvinylidene fluoride - model*. Journal of Applied Physics, 1978. **49**(10): p. 4992-4997.
61. Takahashi, N. and Odajima, A., *Ferroelectric reorientation of crystallites in polyvinylidene fluoride*. Ferroelectrics, 1981. **32**(1-4): p. 49-59.
62. Safari, A., *Development of piezoelectric composites for transducers*. Journal De Physique Iii, 1994. **4**(7): p. 1129-1149.
63. Janas, V. F., *et al.*, *Processing of 1-3 piezoelectric ceramic/polymer composites*. Journal of the American Ceramic Society, 1995. **78**(9): p. 2425-2430.
64. Goodman, G., *Ferroelectric properties of lead metaniobate*. Journal of the American Ceramic Society, 1953. **36**(11): p. 368-372.
65. Francombe, M. H. and Lewis, B., *Structural and electrical properties of silver niobate and silver tantalate*. Acta Crystallographica, 1958. **11**(3): p. 175-178.
66. Subbarao, E. C., *Crystal chemistry of mixed bismuth oxides with layer-type structure*. Journal of the American Ceramic Society, 1962. **45**(4): p. 166-169.
67. Swartz, S., Schulze, W. A. and Biggers, J. V., *Fabrication and electrical properties of grain oriented Bi₄Ti₃O₁₂ ceramics*. Ferroelectrics, 1981. **38**(1): p. 765 - 768.
68. Takenaka, T. and Sakata, K., *Grain-orientation and electrical-properties of hot-forged Bi₄Ti₃O₁₂ ceramics*. Japanese Journal of Applied Physics, 1980. **19**(1): p. 31-39.

69. Nassau, K., Levinste. H. J. and Loiacono, G. M., *Ferroelectric lithium niobate .1. growth domain structure dislocations and etching*. Journal of Physics and Chemistry of Solids, 1966. **27**(6-7): p. 983-988.
70. Nassau, K., Levinste. H. J. and Loiacono, G. M., *Ferroelectric lithium niobate .2. preparation of single domain crystals*. Journal of Physics and Chemistry of Solids, 1966. **27**(6-7): p. 989-996.
71. Abrahams, S. C., Hamilton, W. C. and Reddy, J. M., *Ferroelectric lithium niobate .4. single crystal neutron diffraction study at 24 degrees c*. Journal of Physics and Chemistry of Solids, 1966. **27**(6-7): p. 1013.
72. Abrahams, S. C., Levinste. H. J. and Reddy, J. M., *Ferroelectric lithium niobate .5. polycrystal X-ray diffraction study between 24 degrees and 1200 degrees c*. Journal of Physics and Chemistry of Solids, 1966. **27**(6-7): p. 1019.
73. Abrahams, S. C., Reddy, J. M. and Bernstei. J. L., *Ferroelectric lithium niobate. Part.3. Single crystal X-ray diffraction study at 24 degrees c*. Journal of Physics and Chemistry of Solids, 1966. **27**(6-7): p. 997.
74. Amorin, G. H., *et al.*, *Ferroelectric and dielectric anisotropy in high-quality SrBi₂Ta₂O₉ single crystals*. Applied Physics Letters, 2004. **85**(23): p. 5667-5669.
75. Goldman, I. M. and Wul, B., *ibid.*, 1946. **51**: p. 21.
76. Matthias, B. T., *New ferroelectric crystals*. Physical Review, 1949. **75**(11): p. 1771-1771.
77. Shirane, G., *Phase Transitions in Solid Solutions Containing PbZrO₃*. Physical Review, 1951. **84**(4): p. 854-855.
78. Ricote, J., *et al.*, *A TEM and neutron diffraction study of the local structure in the rhombohedral phase of lead zirconate titanate*. Journal of Physics-Condensed Matter, 1998. **10**(8): p. 1767-1786.
79. Clarke, R. and Whatmore, R. W., *Growth and Characterization of PbZr_xTi_{1-x}O₃ Single Crystals*. Journal of Crystal Growth, 1976. **33**(1): p. 29-38.
80. Yamashita, Y., *et al.*, *Effects of B-site ions on the electromechanical coupling factors of Pb(B'B'')O₃-PbTiO₃ piezoelectric materials*. Japanese Journal of Applied Physics Part 1-Regular Papers Short Notes & Review Papers, 1998. **37**(9B): p. 5288-5291.
81. Yamashita, Y., *et al.*, *Effect of molecular mass of B-site ions on electromechanical coupling factors of lead-based perovskite piezoelectric materials*. Japanese Journal of Applied Physics Part 1-Regular Papers Short Notes & Review Papers, 2000. **39**(9B): p. 5593-5596.
82. Yamamoto, T., *et al.*, *Electrical-properties and microstructure of Ca modified PbTiO₃ ceramics*. Japanese Journal of Applied Physics Part 1-Regular Papers Short Notes & Review Papers, 1987. **26**: p. 57-60.
83. Rittenmyer, K. M. and Ting, R. Y., *Piezoelectric and dielectric-properties of calcium and samarium modified lead titanate ceramics for hydroacoustic applications*. Ferroelectrics, 1990. **110**: p. 171-182.

84. Takeuchi, K., *et al.*, *Electromechanical coupling properties of calcium doped lead titanate ceramics*. IEEE Transactions on Ultrasonics Ferroelectrics and Frequency Control, 1986. **33**(6): p. 808-808.
85. Yamashita, Y., *et al.*, *(Pb,Ca)[(Co_{1/2}W_{1/2}),Ti]O₃ piezoelectric ceramics and their applications*. Japanese Journal of Applied Physics, 1981. **20-4**,: p. 183.
86. Frantti, J., *Notes of the recent structural studies on lead zirconate titanate*. Journal of Physical Chemistry B, 2008. **112**(21): p. 6521-6535.
87. Corker, D. L., *et al.*, *A neutron diffraction investigation into the rhombohedral phases of the perovskite series PbZr_{1-x}Ti_xO₃*. Journal of Physics-Condensed Matter, 1998. **10**(28): p. 6251-6269.
88. Glazer, A. M., Roleder, K. and Dec, J., *Structure and disorder in single-crystal lead zirconate, PbZrO₃*. Acta Crystallographica Section B-Structural Science, 1993. **49**: p. 846-852.
89. Sawaguchi, E., Maniwa, H. and Hoshino, S., *Antiferroelectric structure of lead zirconate*. Physical Review, 1951. **83**(5): p. 1078-1078.
90. Eremkin, V. V., Smotrakov, V. G. and Fesenko, E. G., *Structural phase-transitions in PbZr_{1-x}Ti_xO₃ crystals*. Ferroelectrics, 1990. **110**: p. 137-144.
91. Fesenko, E. G., Eremkin, V. V. and Smotrakov, V. G., *Phase-X, T-diagram of PbZr_{1-x}Ti_xO₃ crystals*. Fizika Tverdogo Tela, 1986. **28**(1): p. 324-326.
92. Ujma, Z. and Handerek, J., *Phase-transitions and spontaneous polarization in PbZrO₃*. Physica Status Solidi a-Applied Research, 1975. **28**(2): p. 489-496.
93. Scott, B. A. and Burns, G., *Crystal-growth and observation of ferroelectric phase of PbZrO₃*. Journal of the American Ceramic Society, 1972. **55**(7): p. 331.
94. Sawaguchi, E., *Ferroelectricity versus antiferroelectricity in the solid solutions of PbZrO₃ and PbTiO₃*. Journal of the Physical Society of Japan, 1953. **8**(5): p. 615-629.
95. Weston, T. B., Webster, A. H. and McNamara, V. M., *Lead zirconate-lead titanate piezoelectric ceramics with iron oxide additions*. Journal of the American Ceramic Society, 1969. **52**(5): p. 253.
96. Uchida, N. and Ikeda, T., *Studies on Pb(Zr-Ti)O₃ ceramics with addition of Cr₂O₃*. Japanese Journal of Applied Physics, 1967. **6**(11): p. 1292.
97. Kulcsar, F., *Electromechanical properties of lead titanate zirconate ceramics modified with certain 3-valant or 5-valent additions*. Journal of the American Ceramic Society, 1959. **42**(7): p. 343-349.
98. Kulcsar, F., *Electromechanical properties of lead titanate zirconate ceramics modified with tungsten and thorium*. Journal of the American Ceramic Society, 1965. **48**(1): p. 54.
99. Atkin, R. B., Holman, R. L. and Fulrath, R. M., *Substitution of Bi and Nb ions in lead zirconate-titanate*. Journal of the American Ceramic Society, 1971. **54**(2): p. 113.

100. Banno, H. and Tsunooka, T., *Piezoelectric properties and temperature dependences of resonant frequency of WO₃-MnO₂-modified ceramics of Pb(Zr-Ti)O₃*. Japanese Journal of Applied Physics, 1967. **6**(8): p. 954.
101. Härdtl, K. H., *Electrical and mechanical losses in ferroelectric ceramics*. Ceramics International, 1982. **8**(4): p. 121-127.
102. Gerson, R., *Variation in ferroelectric characteristics of lead zirconate titanate ceramics due to minor chemical modifications*. Journal of Applied Physics, 1960. **31**(1): p. 188-194.
103. Park, J. H., *et al.*, *Piezoelectric properties of Nb₂O₅ doped and MnO₂-Nb₂O₅ Co-doped Pb(Zr_{0.53}Ti_{0.47})O₃ ceramics*. Journal of Materials Science-Materials in Electronics, 1995. **6**(2): p. 97-101.
104. Okazaki, K. and Nagata, K., *Effects of density and grain-size on electrical properties of piezoelectric ceramics*. Electronics & Communications in Japan, 1970. **53**(11): p. 147.
105. Demartin, M., *et al.*, *The Influence of Processing and Microstructure on the Piezoelectric and Mechanical Properties of Fine Grained PZT Ceramics*, in *Electroceramics IV*. 1994. p. 393-396
106. Ichinose, N. and Kimura, M., *Preparation and properties of lead zirconate-titanate piezoelectric ceramics using ultrafine particles*. Japanese Journal of Applied Physics Part 1-Regular Papers Short Notes & Review Papers, 1991. **30**(9B): p. 2220-2223.
107. Martiren, H. T. and Burfoot, J. C., *Grain-size effects on properties of some ferroelectric ceramics*. Journal of Physics C-Solid State Physics, 1974. **7**(17): p. 3182-3192.
108. Mishra, S. K. and Pandey, D., *Effect of particle-size on the ferroelectric behavior of tetragonal and rhombohedral Pb(Zr_xTi_{1-x})O₃ ceramics and powders*. Journal of Physics-Condensed Matter, 1995. **7**(48): p. 9287-9303.
109. Okazaki, K. and Nagata, K., *Effects of grain-size and porosity on electrical and optical properties of PLZT ceramics*. Journal of the American Ceramic Society, 1973. **56**(2): p. 82-86.
110. Ogawa, T., *Highly functional and high-performance piezoelectric ceramics*. American Ceramic Society Bulletin, 1991. **70**(6): p. 1042-1049.
111. Kudo, S., Tashiro, S. and Igarashi, H., *Oxygen-atmosphere firing of piezoelectric lead-zirconate-titanate ceramics substituted with lead antimonate niobate having submicron particle sizes*. Japanese Journal of Applied Physics Part 1-Regular Papers Short Notes & Review Papers, 1995. **34**(9B): p. 5303-5305.
112. Kim, S., *et al.*, *Fabrication of fine-grain piezoelectric ceramics using reactive calcination*. Journal of Materials Science, 1991. **26**(16): p. 4411-4415.
113. Randall, C. A., *et al.*, *Intrinsic and extrinsic size effects in fine-grained morphotropic-phase-boundary lead zirconate titanate ceramics*. Journal of the American Ceramic Society, 1998. **81**(3): p. 677-688.

114. Kim, S. B., *et al.*, *Effect of grain-size and poling on the fracture mode of lead zirconate titanate ceramics*. Journal of the American Ceramic Society, 1990. **73**(1): p. 161-163.
115. Buesssem, W. R., Cross, L. E. and Goswami, A. K., *Phenomenological theory of high permittivity in fine-grained barium titanate*. Journal of the American Ceramic Society, 1966. **49**(1): p. 33.
116. Kamel, T. A. and de With, G., *Grain size effect on the poling of soft Pb(Zr,Ti)O₃ ferroelectric ceramics*. Journal of the European Ceramic Society, 2008. **28**(4): p. 851-861.
117. Haun, M. J., *et al.*, *Thermodynamic theory of the lead zirconate-titanate solid-solution system, Part. 5, theoretical calculations*. Ferroelectrics, 1989. **99**: p. 63-86.
118. Haun, M. J., *et al.*, *Thermodynamic theory of the lead zirconate-titanate solid-solution system, Part. 4, tilting of the oxygen octahedra*. Ferroelectrics, 1989. **99**: p. 55-62.
119. Haun, M. J., *et al.*, *Thermodynamic theory of the lead zirconate-titanate solid-solution system, Part. 1, phenomenology*. Ferroelectrics, 1989. **99**: p. 13-25.
120. Foster, C. M., *et al.*, *Single-crystal Pb(Zr_xTi_{1-x})O₃ thin films prepared by metal-organic chemical vapor deposition: Systematic compositional variation of electronic and optical properties*. Journal of Applied Physics, 1997. **81**(5): p. 2349-2357.
121. Chen, H. D., *et al.*, *Electrical-properties maxima in thin-films of the lead zirconate lead titanate solid-solution system*. Applied Physics Letters, 1995. **67**(23): p. 3411-3413.
122. Mishra, S. K., Pandey, D. and Singh, A. P., *Effect of phase coexistence at morphotropic phase boundary on the properties of Pb(Zr_xTi_{1-x})O₃ ceramics*. Applied Physics Letters, 1996. **69**(12): p. 1707-1709.
123. Zhang, D. M., *et al.*, *A study of the dielectric properties of PZT and PT ceramics depending on the lattice distortion*. Canadian Journal of Physics, 2005. **83**(5): p. 527-540.
124. Noheda, B., *et al.*, *A monoclinic ferroelectric phase in the Pb(Zr_{1-x}Ti_x)O₃ solid solution*. Applied Physics Letters, 1999. **74**(14): p. 2059-2061.
125. Frantti, J., *et al.*, *Phase transitions of Pb(Zr_xTi_{1-x})O₃ ceramics*. Physical Review B, 2002. **66**(6): p. 064108.
126. Ranjan, R., *et al.*, *Comparison of the Cc and R3c space groups for the superlattice phase of Pb(Zr_{0.52}Ti_{0.48})O₃*. Physical Review B, 2005. **71**: p. 092101.
127. Amin, A., *et al.*, *Phenomenological and structural study of a low-temperature phase-transition in the PbZrO₃-PbTiO₃ system*. Journal of Solid State Chemistry, 1981. **37**(2): p. 248-255.
128. Arigur, P. and Benguigu, L., *X-ray study of PZT solid-solutions near morphotropic phase-transition*. Solid State Communications, 1974. **15**(6): p. 1077-1079.

129. Arigur, P. and Benguigui, L., *Direct determination of coexistence region in solid-solutions $Pb(Zr_xTi_{1-x})O_3$* . Journal of Physics D-Applied Physics, 1975. **8**(15): p. 1856-1862.
130. Benguigui, L., *Thermodynamic theory of morphotropic phase-transition tetragonal-rhombohedral in perovskite ferroelectrics*. Solid State Communications, 1972. **11**(6): p. 825.
131. Barbulescu, A., Barbulescu, E. and Barb, D., *Phase-transitions in PZT solid-solutions*. Ferroelectrics, 1983. **47**(3-4): p. 221-230.
132. Hanh, L., Uchino, K. and Nomura, S., *Phenomenon of morphotropic tetragonal-rhombohedral phase boundary in ferroelectric ceramics*. Japanese Journal of Applied Physics, 1978. **17**(4): p. 637-641.
133. Isupov, V. A., *Characteristics of coexistence of tetragonal and rhombohedral phases in piezoelectric ceramics based on $PbTiO_3$ and $PbZrO_3$* . Soviet Physics Solid State, USSR, 1976. **18**(4): p. 529-532.
134. Benguigui, L., *Properties of PZT solid-solutions - reply*. Solid State Communications, 1976. **19**(10): p. 979-981.
135. Isupov, V. A., *Thermodynamic analysis of phase transitions in perovskite ferroelectrics*. Soviet Physics Solid State, USSR, 1977. **19**(5): p. 4.
136. Isupov, V. A., *X-ray study of PZT solid-solutions near morphotropic phase-transition - comment*. Solid State Communications, 1975. **17**(11): p. 1331-1333.
137. Isupov, V. A., *Tetragonal-rhombohedral phase boundaries in a piezoceramic of ZTL type*. Soviet Physics Solid State, USSR, 1975. **16**(7): p. 2.
138. Wersing, W., *et al.*, *The morphotropic phase boundary in PZT ceramics prepared by spray drying of salt solutions and by the mixed oxide method*. Silic. Ind., 1985. **3-4**: p. 6.
139. Kala, T., *Contribution to the study of tetragonal and rhombohedral phase coexistence in the $PbZrO_3$ - $PbTiO_3$ system*. Physica Status Solidi A - Applied Research, 1983. **78**(1): p. 277-282.
140. Kakegawa, K., *et al.*, *Compositional fluctuation and properties of $Pb(Zr,Ti)O_3$* . Solid State Communications, 1977. **24**(11): p. 769-772.
141. Cao, W. W. and Cross, L. E., *Distribution-functions of coexisting phases in a complete solid-solution system*. Journal of Applied Physics, 1993. **73**(7): p. 3250-3255.
142. Cao, W. W. and Cross, L. E., *Theoretical-model for the morphotropic phase-boundary in lead zirconate lead titanate solid-solution*. Physical Review B, 1993. **47**(9): p. 4825-4830.
143. Cao, W. W. and Cross, L. E., *The ratio of rhombohedral and tetragonal phases on the morphotropic phase-boundary in lead zirconate titanate*. Japanese Journal of Applied Physics Part 1-Regular Papers Short Notes & Review Papers, 1992. **31**(5A): p. 1399-1402.
144. Soares, M. R., Senos, A. M. R. and Mantas, P. Q., *Phase coexistence in PZT ceramics*. Journal of the European Ceramic Society, 1999. **19**(10): p. 1865-1871.

145. Nettleton, R. E., *Ferroelectric phase transitions: A review of theory and experiment, Part. 1, Introduction and Magnetic Resonance*. Ferroelectrics, 1970. **1**(1): p. 3 - 10.
146. Nettleton, R. E., *Ferroelectric phase transitions: A review of theory and experiment, Part. 2, thermal conductivity*. Ferroelectrics, 1970. **1**(1): p. 87 - 91.
147. Nettleton, R. E., *Ferroelectric phase transitions: A review of theory and experiment, Part. 3, neutron scattering*. Ferroelectrics, 1970. **1**(1): p. 93 - 101.
148. Nettleton, R. E., *Ferroelectric phase transitions: A review of theory and experiment*. Ferroelectrics, 1970. **1**(1): p. 221 - 226.
149. Cochran, W., *Crystal stability and the theory of ferroelectricity*. Physical Review Letters, 1959. **3**(9): p. 412-414.
150. Cochran, W., *Crystal stability and the theory of ferroelectricity*. Advances in Physics, 1960. **9**(36): p. 387-423.
151. Cochran, W., *Crystal stability and the theory of ferroelectricity .2. Piezoelectric crystals*. Advances in Physics, 1961. **10**(40): p. 401-420.
152. Blinc, R. and Zeks, B., *Soft modes in ferroelectrics and antiferroelectrics*. Series of monographs on selected topics in solid state physics 13. 1974, Amsterdam: North-Holland. XII, 317.
153. Shirane, G., Hoshino, S. and Suzuki, K., *X-ray study of the phase transition in lead titanate*. Physical Review, 1950. **80**(6): p. 1105-1106.
154. Devonshire, A. F., *Theory of barium titanate. Part 2*. Philosophical Magazine, 1951. **42**(333): p. 1065-1079.
155. Cross, L. E. and Newnham, R. E., *History of Ferroelectrics*. Reprinted from the Ceramics and Civilization. Huh-Technology Ceramics-Past, Present and Future, Copyright by The American Ceramic Society. Inc, 1987. **111**: p. 289-305.
156. Smolensky, G. A. *Physical phenomena in ferroelectrics with diffused phase transition*. in *Proceeding of the Second International Meeting on Ferroelectricity*. 1970. Kyoto: Journal of the Physical Society of Japan Supplement.
157. Kirillov, V. V. and Isupov, V. A., *Relaxation polarization of $PbMg_{1/3}Nb_{2/3}O_3$ (PMN) - ferroelectric with a diffused phase-transition*. Ferroelectrics, 1973. **5**(1-2): p. 3-9.
158. Moreira, R. L. and Lobo, R., *Phenomenological study of diffuse phase-transitions*. Journal of the Physical Society of Japan, 1992. **61**(6): p. 1992-1995.
159. Megaw, H. D., *Ferroelectricity in Crystals* 1957, London: Methuen.
160. Tomashpo, Y. Y., *et al.*, *Ferroelectric vacuum deposits of complex oxide type structure*. Ferroelectrics, 1974. **7**(1-4): p. 257-258.
161. Lebedev, N. I. and Sigov, A. S., *Surface inhomogeneities and coercive field of thin ferroelectric films*. Integrated Ferroelectrics, 1994. **4**(1): p. 21 - 24.
162. Maugin, G. A., *et al.*, *Nonlinear Electromechanical Couplings*. 1992, Wiley: Chichester.

163. Zhang, H. X., Leppavuori, S. and Karjalainen, P., *Raman-spectra in laser-ablated lead-zirconate-titanate thin-films near the morphotropic phase-boundary*. Journal of Applied Physics, 1995. **77**(6): p. 2691-2696.
164. Souza, A. G., *et al.*, *Monoclinic phase of $PbZr_{0.52}Ti_{0.48}O_3$ ceramics: Raman and phenomenological thermodynamic studies*. Physical Review B, 2000. **61**(21): p. 14283-14286.
165. Lima, K. C. V., *et al.*, *Raman study of morphotropic phase boundary in $PbZr_{1-x}Ti_xO_3$ at low temperatures*. Physical Review B, 2001. **63**(18).
166. Frantti, J., *et al.*, *Low-temperature Raman studies of $Pb(Zr_xTi_{1-x})O_3$ and $Pb_{1-3y/2}Nd_yTiO_3$ ceramics*. Japanese Journal of Applied Physics Part 1-Regular Papers Short Notes & Review Papers, 1999. **38**(9B): p. 5679-5682.
167. Frantti, J., *et al.*, *Neutron diffraction studies of $Pb(Zr_xTi_{1-x})O_3$ ceramics*. Japanese Journal of Applied Physics Part 1-Regular Papers Short Notes & Review Papers, 2000. **39**(9B): p. 5697-5703.
168. Burns, G. and Scott, B. A., *Raman studies of underdamped soft modes in $PbTiO_3$* . Physical Review Letters, 1970. **25**(3): p. 167.
169. Foster, C. M., *et al.*, *Anharmonicity of the lowest-frequency $A_1(TO)$ phonon in $PbTiO_3$* . Physical Review B, 1993. **48**(14): p. 10160-10167.
170. Burns, G. and Scott, B. A., *Lattice modes in ferroelectric perovskites - $PbTiO_3$* . Physical Review B, 1973. **7**(7): p. 3088-3101.
171. Burns, G. and Scott, B. A., *Raman spectra of polycrystalline solids - application to $Pb(Zr_{1-x}Ti_x)O_3$ system*. Physical Review Letters, 1970. **25**(17): p. 1191.
172. Koochpayeh, S. M., *Crystals growth of functional oxides using an image furnace*. 2007, University of Birmingham.
173. Scheel, H. J. and Fukuda, T., *Crystal Growth Technology*. 2003, John Wiley & Sons: Ltd. Chichester, England.
174. Thomas, E. L., *Crystal growth and the search for highly correlated ternary intermetallic antimonides and stannides*, in *Department of Chemistry*. 2006, Louisiana State University: Louisiana.
175. Elwell, D. and Scheel, H. J., *Crystal Growth from High Temperature Solution*. 1975, London: Academic Press.
176. Tolksdorf, N., *Crystal Growth and Materials*, ed. Kalidias and Scheel. 1977, Amsterdam: North-Holland.
177. Wood, J. D. C. and White, E. A. D., *Growth stoichiometric magnesium aluminate spinel crystals by flux evaporation*. Journal of Crystal Growth, 1968. **3-4**: p. 480-484.
178. Jona, F., Shirane, G. and Pepinsky, R., *Optical study of $PbZrO_3$ and $NaNbO_3$ single crystals*. Physical Review, 1955. **97**(6): p. 1584-1590.
179. Coe, I. M., Brice, J. C. and Tansley, T. L., *Statistical barrier model of crystal-growth*. Journal of Crystal Growth, 1975. **30**(3): p. 367-370.
180. Roy, B. N., *Crystal Growth from Melts*. 1992, England: John Wiley & Sons.

References

181. Hurle, D. T., *Handbook of Crystal Growth, Part. 2: Basic Techniques*. 1994, North Holland: Elsevier Science.
182. Tolksdorf, W., *Flux Growth*, in *Handbook of Crystal Growth 2: Basic Techniques.*, Hurle, Editor. 1994, Elsevier Science: North Holland.
183. Wanklyn, B. M. and Watts, B. E., *Nucleation sites on platinum surfaces in flux growth*. *Materials Research Bulletin*, 1984. **19**(6): p. 711-716.
184. Bennett, G. A., *Seeded growth of garnet from molten salts*. *Journal of Crystal Growth*, 1968. **3-4**: p. 458-462.
185. Tolksdorf, W., *et al.*, *Growth of yttrium-iron-garnet multilayers by liquid-phase epitaxy for single-mode magneto-optic wave-guides*. *Journal of Crystal Growth*, 1987. **83**(1): p. 15-22.
186. Holman, R. L. and Fulrath, R. M., *Intrinsic nonstoichiometry in lead zirconate lead titanate system determined by Knudsen effusion*. *Journal of Applied Physics*, 1973. **44**(12): p. 5227-5236.
187. Fushimi, S. and Ikeda, T., *Phase equilibrium in system PbO-TiO₂-ZrO₂*. *Journal of the American Ceramic Society*, 1967. **50**(3): p. 129.
188. Ikeda, T. and Fushimi, S., *Preliminary study on growth of lead zirconate-titanate crystals*. *Journal of the Physical Society of Japan*, 1962. **17**(7): p. 1202.
189. Webster, A. H., *et al.*, *The system PbO-ZrO₂-TiO₂ at 1100°C*. *Journal of the Canadian Ceramic Society*, 1965. **34**: p. 97-102.
190. Kutty, T. R. N. and Balachandran, R., *Direct precipitation of lead zirconate titanate by the hydrothermal method*. *Materials Research Bulletin*, 1984. **19**(11): p. 1479-1488.
191. Liu, X. Y., *Single-crystal-like materials by the self-assembly of cube-shaped lead zirconate titanate (PZT) microcrystals*. *Langmuir*, 2005. **21**(8): p. 3207-3212.
192. Cheng, H. M., *et al.*, *Reaction-mechanisms in the formation of lead zirconate-titanate solid-solutions under hydrothermal conditions*. *Journal of the American Ceramic Society*, 1993. **76**(3): p. 625-629.
193. You, D. J., *et al.*, *Domain structure in a micron-sized PbZr_{1-x}Ti_xO₃ single crystal on a Ti substrate fabricated by hydrothermal synthesis*. *Applied Physics Letters*, 2004. **84**(17): p. 3346-3348.
194. Kanda, T., *et al.*, *Performance of hydrothermal PZT film on high intensity operation*. *Sensors and Actuators a-Physical*, 2001. **89**(1-2): p. 16-21.
195. Yanagisawa, K. and Kanai, H., *Crystal growth of lead zirconate titanate with additives under hydrothermal conditions*. *Japanese Journal of Applied Physics Part 1-Regular Papers Short Notes & Review Papers*, 1997. **36**(9B): p. 6031-6034.
196. Yanagisawa, K., *et al.*, *Stability and single crystal growth of dielectric materials containing lead under hydrothermal conditions*. *Journal of the European Ceramic Society*, 1999. **19**(6-7): p. 1033-1036.
197. Cho, S. B., *Hydrothermal synthesis of acicular lead zirconate titanate (PZT)*. *Journal of Crystal Growth*, 2001. **226**(2-3): p. 313-326.

198. Tsaur, J., *et al.*, *Preparation and application of lead zirconate titanate (PZT) films deposited by hybrid process: Sol-gel method and laser ablation*. Japanese Journal of Applied Physics Part 1-Regular Papers Short Notes & Review Papers, 2002. **41**(11B): p. 6664-6668.
199. Shimizu, M., *et al.*, *Growth of ferroelectric $PbZr_xTi_{1-x}O_3$ thin films by metalorganic chemical vapor deposition (MOCVD)*. Journal of Crystal Growth, 2002. **237**: p. 448-454.
200. Maiwa, H., *Measurement of electric-field-induced displacements in (Pb, La)TiO₃ thin films using scanning probe microscopy*. Japanese Journal of Applied Physics. Part. 1 - Regular Papers Short Notes & Review Papers, 2000. **39**(9B): p. 5403-5407.
201. Zhang, W. X., Sasaki, K. and Hata, T., *Analysis of sputter process on a new ZrTi+PbO target system and its application to low-temperature deposition of ferroelectric $Pb(Zr,Ti)O_3$ films*. Japanese Journal of Applied Physics Part 1-Regular Papers Short Notes & Review Papers, 1996. **35**(3): p. 1868-1872.
202. Wakabayashi, S., *et al.*, *Static characteristics of piezoelectric thin film buckling actuator*. Japanese Journal of Applied Physics Part 1-Regular Papers Short Notes & Review Papers, 1996. **35**(9B): p. 5012-5014.
203. Tsuchiya, K., Kitagawa, T. and Nakamachi, E., *Development of RF magnetron sputtering method to fabricate PZT thin film actuator*. Precision Engineering-Journal of the International Societies for Precision Engineering and Nanotechnology, 2003. **27**(3): p. 258-264.
204. Fujii, S., *Growth of PZT crystal by using $PbO-KF-PbCl_2$ flux*. Nippon Seramikkusu Kyokai Gakujutsu Ronbunshi-Journal of the Ceramic Society of Japan, 1991. **99**(6): p. 520-522.
205. Hatanaka, T. and Hasegawa, H., *Observation of domain-structures in tetragonal $Pb(Zr_xTi_{1-x})O_3$ single-crystals by chemical etching method*. Japanese Journal of Applied Physics Part 1-Regular Papers Short Notes & Review Papers, 1992. **31**(9B): p. 3245-3248.
206. Kobayashi, J., *Growing of ferroelectric $PbTiO_3$ crystals*. Journal of Applied Physics, 1958. **29**(5): p. 866-867.
207. Sholokhovitch, M. L., *The single crystals of the solid solution containing less than 12 percent of PbO and B_2O_3* . Izvestiya Akademii Nauk SSSR Fizika, 1960. **24**: p. 1242.
208. Ikeda, T. and Fushimi, S., *Single Crystals of Lead Zirconate-Titanate Solid Solutions*. Japanese Journal of Applied Physics, 1964. **3**: p. 171-172.
209. Fushimi, S. and Ikeda, T., *Optical study of lead zirconate-titanate*. Journal of the Physical Society of Japan, 1965. **20**(11): p. 2007.
210. Tsuzuki, K., *et al.*, *Growth of $Pb(Zr-Ti)O_3$ single crystal by flux method*. Japanese Journal of Applied Physics, 1968. **7**(8): p. 953.
211. Tsuzuki, K., Sakata, K. And wada M., *Growing and some properties of $Pb(Zr-Ti)O_3$ single crystal*. Japanese Journal of Applied Physics, 1969. **8**(6): p. 816-817.

212. Tsuzuki, K., *et al.*, *Growth of ferroelectric Pb(Zr_xTi_{1-x})O₃ single-crystals*. Japanese Journal of Applied Physics, 1973. **12**(10): p. 1500-1503.
213. Clarke, R. and Glazer, A. M., *Observation of critical behavior in thermal-expansion of PbZr_{0.9}Ti_{0.1}O₃*. Journal of Physics C-Solid State Physics, 1974. **7**(12): p. 2147.
214. Clarke, R. and Glazer, A. M., *Critical phenomena in ferroelectric crystals of lead zirconate titanate*. Ferroelectrics, 1976. **14**(1): p. 695 - 697.
215. Clarke, R., Whatmore, R. W. and Glazer, A. M., *Growth and characterization of PbZr_xTi_{1-x}O₃ single crystals*. Ferroelectrics, 1976. **13**(1): p. 497 - 500.
216. Clarke, R. and Glazer, A. M., *Critical phenomena in ferroelectric-crystals of lead zirconate-titanate*. Acta Crystallographica Section A, 1975. **31**: p. S194-S194.
217. Roleder, K., *The complex phase-composition of solid PbZr_xTi_{1-x}O₃ solutions for x greater-than 0.95*. Acta Physica Polonica A, 1980. **58**(5): p. 623-629.
218. Roleder, K., *Additional critical-point in PbZr_xTi_{1-x}O₃ at 0.97-less-than-x-less-than-0.98*. Ferroelectrics, 1988. **79**: p. 499-502.
219. Roleder, K. and Dec, J., *The defect-induced ferroelectric phase in thin PbZrO₃ single-crystals*. Journal of Physics-Condensed Matter, 1989. **1**(8): p. 1503-1510.
220. Roleder, K., *et al.*, *Raman-scattering in PbZr_{1-x}Ti_xO₃ single-crystals with low Ti content and a study of the Ti influence*. Journal of Physics-Condensed Matter, 1989. **1**(12): p. 2257-2268.
221. Roleder, K., Kugel, G. E. and Fontana, M. D., *Glass-like behavior in PbZr_{1-x}Ti_xO₃ with small Ti content*. Ferroelectrics, 1990. **112**: p. 225-235.
222. Roleder, K. and Kugel, G. E., *Dielectric behavior of PbZr_{0.99}Ti_{0.01}O₃ single-crystals in the paraelectric and intermediate phases*. Ferroelectrics, 1990. **106**: p. 287-292.
223. Roleder, K., Grzywacz, D. and Wolak, J., *Time-dependent properties of PbZr_xTi_{1-x}O₃ crystals*. Ferroelectrics, 1991. **124**(1-4): p. 219-224.
224. Roleder, K., *et al.*, *Behaviour of a polar relaxation mode around the phase transition point in the antiferroelectric PbZrO₃ single crystal*. Journal of Physics-Condensed Matter, 1996. **8**(49): p. 10669-10678.
225. Ujma, Z. and Handerek, J., *The pyroelectric effect in single-crystal and ceramic PbZrO₃*. Ferroelectrics, 1981. **33**(1-4): p. 37-42.
226. Handerek, J., Pisarski, M. and Ujma, Z., *The influence of an electric-field and hydrostatic-pressure on dielectric-properties and phase-transitions in PbZrO₃*. Journal of Physics C-Solid State Physics, 1981. **14**(14): p. 2007-2016.
227. Handerek, J. and Roleder, K., *The influence of space-charge polarization on phase-transition diffusion in PbZrO₃ crystals*. Ferroelectrics, 1987. **76**(1-2): p. 159-166.
228. Dec, J., *S-domain walls in NaNbO₃ and PbZrO₃ crystals*. Ferroelectrics, 1988. **81**: p. 1087-1090.
229. Dec, J., *Jerky phase-front motion in PbTiO₃ crystals*. Journal of Physics C-Solid State Physics, 1988. **21**(7): p. 1257-1263.
230. Dec, J., *Monodomain state formation in antiferroelectric NaNbO₃ and PbZrO₃ crystals*. Ferroelectrics, 1989. **97**: p. 197-200.

231. Kugel, G., *et al.*, *Raman-scattering study of the phase-transitions in pure and Ti or Ba doped PbZrO₃ single-crystal*. *Ferroelectrics*, 1990. **107**: p. 103-108.
232. Eknadosiants, E. I., *et al.*, *Domain-structure of rhombohedral PbZr_xTi_{1-x}O₃ crystals*. *Ferroelectrics*, 1990. **111**: p. 283-289.
233. Turik, A. V., *et al.*, *Nature of dielectric permittivity of PbTiO₃ single-crystals*. *Physica Status Solidi B-Basic Research*, 1979. **94**(2): p. 525-528.
234. Leontyev, N. G., *et al.*, *The inhomogeneity in PbZr_{1-x}Ti_xO₃ crystals grown from a solution in melt*. *Kristallografiya*, 1981. **26**(6): p. 1318-1319.
235. Leontev, N. G., Fesenko, O. E. and Smotrakov, V. G., *Accurate defined phase T, x-diagram of PbZr_{1-x}Ti_xO₃ crystals*. *Fizika Tverdogo Tela*, 1983. **25**(7): p. 1958-1963.
236. Fesenko, O. E., Smotrakov, V. G. and Leontiev, N. G., *Phase-T-x-E diagram of PbZr_{1-x}Ti_xO₃ crystals*. *Ferroelectrics Letters Section*, 1984. **2**(1): p. 33-36.
237. Fesenko, O. E., Smotrakov, V. G. and Leontiev, N. G., *A study of phase T-x-E diagram of PbZr_{1-x}Ti_xO₃ crystals*. *Ferroelectrics*, 1985. **63**(1-4): p. 189-196.
238. Perez, J. A., *et al.*, *Growth of lead zirconate titanate single crystals by the high temperature solution method*. *Advanced Materials Forum Iii, Pts 1 and 2*, 2006. **514-516**: p. 184-187.
239. Kinase, W., Kobayashi, J. and Yamada, N., *Optical anisotropy of tetragonal barium titanate*. *Physical Review*, 1959. **116**(2): p. 348-350.
240. Bauerle, D., Clarke, R. and Martin, T. P., *Ferroelectric-paraelectric phase-transition in PbTi_{0.1}Zr_{0.9}O₃*. *Physica Status Solidi B-Basic Research*, 1975. **71**(2): p. K173-K176.
241. Whatmore, R. W. and Glazer, A. M., *Structural phase-transitions in lead zirconate*. *Journal of Physics C-Solid State Physics*, 1979. **12**(8): p. 1505-1519.
242. Roleder, K., *et al.*, *Problem of the transient phase between the para-electric and the antiferroelectric phase in PbZrO₃*. *Ferroelectrics*, 1986. **70**(3-4): p. 181-190.
243. Fesenko, E. G., *et al.*, *Domain-structure peculiarities of lead-titanate crystals*. *Ferroelectrics*, 1973. **6**(1-2): p. 61-65.
244. Fesenko, E. G., *et al.*, *Some peculiarities of domain-structures of lead titanate crystals*. *Kristallografiya*, 1973. **18**(5): p. 1014-1017.
245. Gavriilya, V. G., *et al.*, *Spontaneous polarization and coercive field of lead titanate*. *Soviet Physics Solid State, USSR*, 1970. **12**(5): p. 1203.
246. Gavriilya, V. G. and Fesenko, E. G., *Piezoelectric effect in lead titanate single crystals*. *Soviet Physics Crystallography, USSR*, 1971. **16**(3): p. 549.
247. Whatmore, R. W., Clarke, R. and Glazer, A. M., *Tricritical behavior in PbZr_{1-x}Ti_xO₃ solid-solutions*. *Journal of Physics C-Solid State Physics*, 1978. **11**(14): p. 3089-3102.
248. Leontiev, N. G., Smotrakov, V. G. and Fesenko, E. G., *Phase-diagram of PbZr_{1-x}Ti_xO₃ with x-less-than-0.1*. *Inorganic Materials*, 1982. **18**(3): p. 374-378.
249. Jankowskasumara, I., *et al.*, *Ti-induced and modified dielectric relaxations in PbZr_{1-x}Ti_xO₃ single-crystals (x-less-than-or-equal-to-0.03) in the frequency-range 10Hz-10MHz*. *Journal of Physics-Condensed Matter*, 1995. **7**(30): p. 6137-6149.

250. Leyderman, A. V., Leont'ev, I. N. and Fesenko, O. E., *Dipole order and stability of the ferroelectric and antiferroelectric states in lead zirconate*. Physics of the Solid State, 1998. **40**(7): p. 1204-1207.
251. Menguy, N., *et al.*, *Transmission electron microscopy studies of $Pb(Zr_{0.99}Ti_{0.01})O_3$ single crystals*. Journal of Physics and Chemistry of Solids, 1999. **60**(5): p. 625-629.
252. Tsuzuki, K., Sakata, K. and Wada, M., *Dielectric properties of single-crystals of $PbZr_xTi_{1-x}O_3$ solid-solutions (x is-similar-to 0.5)*. Ferroelectrics, 1974. **8**(1-2): p. 501-503.
253. Buhlmann, S., Muralt, P. and Von Allmen, S., *Lithography-modulated self-assembly of small ferroelectric $Pb(Zr,Ti)O_3$ single crystals*. Applied Physics Letters, 2004. **84**(14): p. 2614-2616.
254. Sawaguchi, E., Shirane, G. and Takagi, Y., *Phase transition in lead zirconate*. Journal of the Physical Society of Japan, 1951. **6**(5): p. 333-339.
255. Jona, F., *et al.*, *X-ray and neutron diffraction study of antiferroelectric lead zirconate, $PbZrO_3$* . Physical Review, 1957. **105**(3): p. 849-856.
256. Fesenko, E. G., *et al.*, *Crystal-growth and study of phase x,T -diagram of $PbZr_{1-x}Ti_xO_3$* . Kristallografiya, 1987. **32**(4): p. 1049-1052.
257. Kugimiya, K., *et al.*, *Process for Producing Single-Crystal Ceramics*. 1990: USA.
258. Harmer, M. P., *et al.*, *Method for Growing Single Crystals from Polycrystalline Precursors*. 2000: USA.
259. Messing, G. L. and Suvaci, E., *Manufacture of highly textured alumina involves using mixture of aluminum metal powder, alumina powder, tabular alumina grains and liquid former and compacting the mixture*. 2001, Penn State Res Found.
260. Messing, G. L., *et al.*, *Templated grain growth of textured piezoelectric ceramics*. Critical Reviews in Solid State and Materials Sciences, 2004. **29**(2): p. 45-96.
261. Kitayama, M., *et al.*, *Modeling and simulation of grain growth in Si_3N_4 - I. Anisotropic Ostwald ripening*. Acta Materialia, 1998. **46**(18): p. 6541-6550.
262. Kitayama, M., *et al.*, *Modeling and simulation of grain growth in Si_3N_4 - II. The alpha-beta transformation*. Acta Materialia, 1998. **46**(18): p. 6551-6557.
263. Takayama, R. and Tomita, Y., *Preparation of epitaxial $Pb(Zr_xTi_{1-x})O_3$ thin-films and their crystallographic, pyroelectric and ferroelectric properties*. Journal of Applied Physics, 1989. **65**(4): p. 1666-1670.
264. Sakashita, Y., *et al.*, *Preparation and electrical-properties of MOCVD-deposited PZT thin-films*. Journal of Applied Physics, 1991. **69**(12): p. 8352-8357.
265. Braun, W., *et al.*, *Epitaxial lead-zirconate-titanate thin-films on sapphire*. Applied Physics Letters, 1993. **63**(4): p. 467-469.
266. Seabaugh, M. M., Kerscht, I. H. and Messing, G. L., *Texture development by templated grain growth in liquid-phase-sintered alpha-alumina*. Journal of the American Ceramic Society, 1997. **80**(5): p. 1181-1188.
267. Hong, S. H. and Messing, G. L., *Development of textured mullite by templated grain growth*. Journal of the American Ceramic Society, 1999. **82**(4): p. 867-872.

268. Suvaci, E., Seabaugh, M. M. and Messing, G. L., *Reaction-based processing of textured alumina by templated grain growth*. Journal of the European Ceramic Society, 1999. **19**(13-14): p. 2465-2474.
269. Suvaci, E. and Messing, G. L., *Critical factors in the templated grain growth of textured reaction-bonded alumina*. Journal of the American Ceramic Society, 2000. **83**(8): p. 2041-2048.
270. Suvaci, E., Oh, K. S. and Messing, G. L., *Kinetics of template growth in alumina during the process of templated grain growth (TGG)*. Acta Materialia, 2001. **49**(11): p. 2075-2081.
271. Hong, S. H. and Messing, G. L., *Anisotropic grain growth in diphasic-gel-derived titania-doped mullite*. Journal of the American Ceramic Society, 1998. **81**(5): p. 1269-1277.
272. Watanabe, H., Kimura, T. and Yamaguchi, T., *Sintering of platelike bismuth titanate powder compacts with preferred orientation*. Journal of the American Ceramic Society, 1991. **74**(1): p. 139-147.
273. Sekiya, T., *et al.*, *High orientation of PZT single crystal grains and piezoelectric properties in 1-3 type composite sheet*. Integrated Ferroelectrics, 2004. **63**: p. 639-642.
274. Muramatsu, H. and Kimura, T., *Preparation of bulk Pb(Zr,Ti)O₃ with crystallographic texture by templated grain growth method*. Journal of Electroceramics, 2004. **13**(1-3): p. 531-535.
275. Muramatsu, H. and Kimura, T., *Effect of PbZr_xTi_{1-x}O₃ composition on crystallographic texture in PZT composites*. Journal of the European Ceramic Society, 2005. **25**(12): p. 2231-2234.
276. Keijsers, M., *et al.*, *Structural and electrical characterization of heteroepitaxial lead zirconate titanate thin films*. Journal of Applied Physics, 1996. **79**(1): p. 393-402.
277. Nagarajan, V., *et al.*, *Dynamics of ferroelastic domains in ferroelectric thin films*. Nature Materials, 2003. **2**(1): p. 43-47.
278. Abothu, I. R., *et al.*, *Sol-gel processing of piezoelectric thin films*. Ferroelectrics, 1999. **232**(1-4): p. 1071-1075.
279. Soares, M. R. T., *A transição morfológica dos cerâmicos PZT*, in *Departamento de Engenharia Cerâmica e do Vidro*. 2001, Universidade de Aveiro: Aveiro, Portugal. p. XVII, 186, [6].
280. Sih, B., *et al.*, *Ferroelectric SrBi₂Ta₂O₉ single-crystal growth and characterization*. Journal of Materials Research, 2001. **16**(6): p. 1726-1733.
281. Kottke, T. and Stalke, D., *Crystal handling at low-temperatures*. Journal of Applied Crystallography, 1993. **26**: p. 615-619.
282. Hooft, R., *COLLECT. Nonius BV, Delft*. 1998: The Netherlands.
283. Otwinowski, Z. and Minor, W., *Methods in Enzymology*. C. W. Carter Jr, R. M. Sweet ed. Vol. 276. 1997, New York: Academic Press. p.307.
284. Blessing, R. H., *An empirical correction for absorption anisotropy*. Acta Crystallographica Section A, 1995. **51**: p. 33-38.

285. Blessing, R. H., *Outlier treatment in data merging*. Journal of Applied Crystallography, 1997. **30**: p. 421-426.
286. Sheldrick, G. M., *SHELXS-97, Program for Crystal Structure Solution*. 1997, University of Göttingen.
287. Sheldrick, G. M., *SHELXL-97, Program for Crystal Structure Refinement*. 1997, University of Göttingen.
288. Kholkin, A. L., *et al.*, *Interferometric measurements of electric field-induced displacements in piezoelectric thin films*. Review of Scientific Instruments, 1996. **67**(5): p. 1935-1941.
289. Alexe, M. and Gruverman, A., *Nanoscale Characterization of Ferroelectric Materials*. 2004, New York Springer-Verlag.
290. Gruverman, A., Auciello, O. and Tokumoto, H., *Imaging and control of domain structures in ferroelectric thin films via scanning force microscopy*. Annual Review of Materials Science, 1998. **28**: p. 101-123.
291. Franke, K., Huelz, H. and Weihnacht, M., *How to extract spontaneous polarization information from experimental data in electric force microscopy*. Surface Science, 1998. **415**(1-2): p. 178-182.
292. Frantti, J., *et al.*, *Neutron diffraction studies of $PbZr_xTi_{1-x}O_3$ ceramics*. Ferroelectrics, 2001. **261**(1): p. 193 - 198.
293. Cox, D. E., Noheda, B. and Shirane, G., *Low-temperature phases in $PbZr_{0.52}Ti_{0.48}O_3$: A neutron powder diffraction study*. Physical Review B, 2005. **71**.
294. Ranjan, R., *et al.*, *Antiferrodistortive phase transition in $Pb(Ti_{0.48}Zr_{0.52})O_3$: A powder neutron diffraction study*. Physical Review B, 2002. **65**(6).
295. Joseph, J., *et al.*, *Structural investigations on $PbZr_xTi_{1-x}O_3$ solid solutions using the X-ray Rietveld method* Journal of Materials Science, 2000. **35**(5): p. 1571.
296. Kanno, I., *et al.*, *Intrinsic crystalline structure of epitaxial $Pb(Zr,Ti)O_3$ thin films*. Journal of Applied Physics, 2005. **97**(7): p. 74101-74101.
297. Idemoto, Y., *et al.*, *Relation between the crystal structure, physical properties and ferroelectric properties of $PbZr_xTi_{1-x}O_3$ ($x=0.40, 0.45, 0.53$) ferroelectric material by heat treatment*. Journal of the Ceramic Society of Japan, 2004. **112**(1): p. 40-45.
298. Liu, H. and Toraya, H., *Ab initio structural study on Nb-doped $Pb(Zr_{0.97}Ti_{0.03})O_3$ ceramic material by synchrotron X-ray diffraction*. Japanese Journal of Applied Physics. Part 1 - Regular Papers Short Notes & Review Papers, 1999. **38**: p. 104-107.
299. Jirak, Z. and Kala, T., *Crystal-structures of ferroelectric phases FR(LT)/FR(HT) in $PbZr_{0.75}Ti_{0.25}O_3$ solid-solutions and their dependence on temperature*. Ferroelectrics, 1988. **82**: p. 79-84.
300. Ito, H., Shiozaki, Y. and Sawaguchi, E., *Crystal-structure of ferroelectric $PbZr_{0.9}Ti_{0.1}O_3$ studied by X-ray and neutron-diffraction profile analysis method*. Journal of the Physical Society of Japan, 1983. **52**(3): p. 913-919.

301. Glazer, A. M., Mabud, S. A. and Clarke, R., *Powder profile refinement of lead zirconate titanate at several temperatures, Part. 1, PbZr_{0.9}Ti_{0.1}O₃*. Acta Crystallographica Section B-Structural Science, 1978. **34**(APR): p. 1060-1065.
302. Martin, C. R. and Aksay, I. A., *Topographical evolution of lead zirconate titanate (PZT) thin films patterned by micromolding in capillaries*. Journal of Physical Chemistry B, 2003. **107**(18): p. 4261-4268.
303. Michel, C., *et al.*, *Atomic structures of 2 rhombohedral ferroelectric phases in Pb(Zr,Ti)O₃ solid solution series*. Solid State Communications, 1969. **7**(12): p. 865.
304. Woodward, D. I., Knudsen, J. and Reaney, I. M., *Review of crystal and domain structures in the PbZr_xTi_{1-x}O₃ solid solution - art. no. 104110*. Physical Review B, 2005. **72**10(10): p. 4110-4110.
305. Kornev, I. A., *et al.*, *Phase diagram of Pb(Zr,Ti)O₃ solid solutions from first principles*. Physical Review Letters, 2006. **97**(15).
306. Eitel, R. and Randall, C. A., *Octahedral tilt-suppression of ferroelectric domain wall dynamics and the associated piezoelectric activity in Pb(Zr,Ti)O₃*. Physical Review B, 2007. **75**(9): p. 4106-4106.
307. Pérez, J. A., *et al.*, *Structural, Electrical and Chemical Characterization of Rhombohedral Lead Zirconate Titanate Single Crystals*. Send to Journal of Physics Condensed Matter, 2008.
308. Souza Filho, A. G., *et al.*, *Raman scattering study of the PbZr_{1-x}Ti_xO₃ system: Rhombohedral-monoclinic-tetragonal phase transitions*. Physical Review B, 2002. **66**(13).
309. Meng, J. F., *et al.*, *Raman phonon modes and ferroelectric phase transitions in nanocrystalline lead zirconate titanate*. Physica Status Solidi a-Applied Research, 1997. **164**(2): p. 851-862.
310. Yi, H. J., *et al.*, *Polarized Raman scattering of highly [111]-oriented Pb(Zr,Ti)O₃ thin films in the rhombohedral-phase field*. Journal of Applied Physics, 2004. **96**(9): p. 5110-5116.
311. Eremkin, V. V., Smotrakov, V. G. and Fesenko, E. G., *Phase-transitions in lead zirconate titanate solid-solutions*. Fizika Tverdogo Tela, 1989. **31**(6): p. 156-161.
312. *IGOR Pro 6*. 1989. p. Technical graphing and data analysis software for scientists and engineers.
313. Dai, X. H., Li, J. F. and Viehland, D., *Weak ferroelectricity in antiferroelectric lead zirconate*. Physical Review B, 1995. **51**(5): p. 2651-2655.
314. Gans, P., *Vibrating molecules an introduction to the interpretation of infrared and raman spectra*. Science paperbacks. Vol. 109. 1971, London: Chapman and Hall.
315. Amin, A., Cross, L. E. and Newnham, R. E., *Calorimetric and phenomenological studies of the PbZrO₃:PbTiO₃ system*. Ferroelectrics, 1981. **37**(1): p. 647 - 650.
316. Zhang, Q. M., Jang, S. J. and Cross, L. E., *High-frequency strain response in ferroelectrics and its measurement using a modified mach-zehnder interferometer*. Journal of Applied Physics, 1989. **65**(7): p. 2807-2813.

317. Lefki, K. and Dormans, G. J. M., *Measurement of piezoelectric coefficients of ferroelectric thin-films*. Journal of Applied Physics, 1994. **76**(3): p. 1764-1767.
318. Damjanovic, D., *et al.*, *Properties of piezoelectric PZT thin films for microactuator applications*. Materials for Smart Systems, 1995. **360**: p. 429-434.
319. Li, J. F., *et al.*, *Piezoelectric properties of sol-gel-derived ferroelectric and antiferroelectric thin-layers*. Journal of Applied Physics, 1994. **75**(1): p. 442-448.
320. Kholkin, A. L., *et al.*, *Seeding effect on micro- and domain structure of sol-gel-derived PZT thin films*. Materials Letters, 2001. **50**(4): p. 219-224.
321. Haun, M. J., *et al.*, *Thermodynamic theory of the lead zirconate-titanate solid-solution system, Part. 2, tricritical behavior*. Ferroelectrics, 1989. **99**: p. 27-44.
322. Haun, M. J., *et al.*, *Thermodynamic theory of the lead zirconate-titanate solid-solution system, Part. 3, Curie constant and 6th-order polarization interaction dielectric stiffness coefficients*. Ferroelectrics, 1989. **99**: p. 45-54.
323. Haun, M. J., *et al.*, *Modeling of the electrostrictive, dielectric and piezoelectric properties of ceramic PbTiO₃*. IEEE Transactions on Ultrasonics Ferroelectrics and Frequency Control, 1989. **36**(4): p. 393-401.
324. Samara, G. A., *Relationship between ionic displacement and Curie temperature and spontaneous polarization in displacive ferroelectrics*. Ferroelectrics, 1971. **2**(4): p. 271.
325. Amin, A., *et al.*, *A phenomenological Gibbs function for the single cell region of the PbZrO₃:PbTiO₃ solid solution system*. Ferroelectrics, 1985. **65**(1): p. 107 - 130.
326. Haun, M. J., *et al.*, *Thermodynamic theory of PbTiO₃*. Journal of Applied Physics, 1987. **62**(8): p. 3331-3338.
327. Amorin, H., Costa, M. E. V. and Kholkin, A. L., *Microstructure and electrical properties of SrBi₂Ta₂O₉ ceramics processed by templated grain growth*. Advanced Materials Forum II, 2004. **455-456**: p. 35-39.
328. Khan, A., *et al.*, *Growth of Pb(Mg_{1/3}Nb_{2/3})O₃-35 mol% PbTiO₃ single crystals from (111) substrates by seeded polycrystal conversion*. Journal of the American Ceramic Society, 1999. **82**(11): p. 2958-2962.
329. Herbiet, R., *et al.*, *Domain wall and volume contributions to material properties of PZT ceramics*. Ferroelectrics, 1989. **98**(1): p. 107 - 121.
330. Zhang, Q. M., *et al.*, *Direct evaluation of domain-wall and intrinsic contributions to the dielectric and piezoelectric response and their temperature-dependence on lead-zirconate-titanate ceramics*. Journal of Applied Physics, 1994. **75**(1): p. 454-459.
331. Dai, X. H., Xu, Z. K. and Viehland, D., *Effect of oxygen octahedron rotations on the phase-stability, transformational characteristics and polarization behavior in the lead-zirconate-titanate crystalline solution series*. Journal of the American Ceramic Society, 1995. **78**(10): p. 2815-2827.
332. Mishra, R. S. K., *et al.*, *Evidence for another low-temperature phase transition in tetragonal PbZr_xTi_{1-x}O₃ (x=0.515,0.520)*. Physical Review B, 2001. **6405**(5): p. 4101.

333. Noheda, B., *et al.*, *The monoclinic phase in PZT: New light on morphotropic phase boundaries*. *Fundamental Physics of Ferroelectrics 2000*, 2000. **535**: p. 304-313.
334. Wada, S., *et al.*, *Enhanced piezoelectric properties of barium titanate single crystals with different engineered-domain sizes*. *Journal of Applied Physics*, 2005. **98**(1).
335. Liu, S. F., *et al.*, *E-field dependence of piezoelectric properties of rhombohedral PZN-PT single crystal*. *Ferroelectrics*, 1999. **221**(1-4): p. 169-174.
336. Chung, H. T. and Kim, H. G., *Characteristics of domain in tetragonal phase PZT ceramics*. *Ferroelectrics*, 1987. **76**(3-4): p. 327-333.
337. Xu, F., *et al.*, *Domain wall motion and its contribution to the dielectric and piezoelectric properties of lead zirconate titanate films*. *Journal of Applied Physics*, 2001. **89**(2): p. 1336-1348.
338. MacLaren, I., *et al.*, *Experimental measurement of stress at a four-domain junction in lead zirconate titanate*. *Journal of Applied Physics*, 2005. **97**(9).
339. Saurenbach, F. and Terris, B. D., *Imaging of ferroelectric domain-walls by force microscopy*. *Applied Physics Letters*, 1990. **56**(17): p. 1703-1705.
340. Hooton, J. A. and Merz, W. J., *Etch patterns and ferroelectric domains in BbTiO₃ single crystals*. *Physical Review*, 1955. **98**(2): p. 409-413.
341. Vries, R. C. and Burke, J. E., *Microstructure of barium titanate ceramics* *J. Am. Ceram. Soc.*, 1957. **40**: p. 200.
342. Arlt, G. and Sasko, P., *Domain configuration and equilibrium size of domains in BaTiO₃ ceramics*. *Journal of Applied Physics*, 1980. **51**(9): p. 4956-4960.
343. Hu, Y. H., *et al.*, *Scanning electron-microscopy and transmission electron-microscopy study of ferroelectric domains in doped BbTiO₃*. *Journal of the American Ceramic Society*, 1986. **69**(8): p. 594-602.
344. Tsurekawa, S., *et al.*, *The continuity of ferroelectric domains at grain boundaries in lead zirconate titanate*. *Scripta Materialia*, 2007. **56**(7): p. 577-580.
345. Munoz-Saldana, J., Hoffmann, M. J. and Schneider, G. A., *Ferroelectric domains in coarse-grained lead zirconate titanate ceramics characterized by scanning force microscopy*. *Journal of Materials Research*, 2003. **18**(8): p. 1777-1786.
346. Wang, Z. Y., *et al.*, *Atomic force microscope observations of domains in fine-grained bulk lead zirconate titanate ceramics*. *Smart Materials & Structures*, 2003. **12**(2): p. 217-222.
347. Warren, W. L., *et al.*, *Electronic domain pinning in Pb(Zr,Ti)O₃ thin-films and its role in fatigue*. *Applied Physics Letters*, 1994. **65**(8): p. 1018-1020.
348. Mitsui, T. and Furuichi, J., *Domain structure of rochelle salt and KH₂PO₄*. *Physical Review*, 1953. **90**(2): p. 193-202.
349. Salje, E. K. H., *Phase Transitions in Ferroelectric and Co-elastic Crystals*. 1990, Cambridge: Cambridge University Press.
350. Kittel, C., *Theory of the structure of ferromagnetic domains in films and small particles*. *Physical Review*, 1946. **70**(11-1): p. 965-971.

References

351. Cao, W. W. and Randall, C. A., *Grain size and domain size relations in bulk ceramic ferroelectric materials*. Journal of Physics and Chemistry of Solids, 1996. **57**(10): p. 1499-1505.
352. Levine, E. M., Robbins, C. R. and McMurdie, H. F., *Phase diagrams for Ceramists*, ed. M. K. Reser. American Ceramic Society, Columbus, OH, 1964, pp.116.
353. He, Z. M. and Ma, J., *Constitutive modeling of the densification of PZT ceramics*. Journal of Physics and Chemistry of Solids, 2003. **64**(2): p. 177-183.
354. Nielsen, E. R., Ringgaard, E. and Kosec, M., *Liquid-phase sintering of Pb(Zr,Ti)O₃ using PbO-WO₃ additive*. Journal of the European Ceramic Society, 2002. **22**(11): p. 1847-1855.
355. Wittmer, D. E. and Buchanan, R. C., *Low-temperature densification of lead zirconate-titanate with vanadium pentoxide additive*. Journal of the American Ceramic Society, 1981. **64**(8): p. 485-490.
356. Corker, D. L., *et al.*, *Liquid-phase sintering of PZT ceramics*. Journal of the European Ceramic Society, 2000. **20**(12): p. 2039-2045.
357. Kingon, A. I. and Clark, J. B., *Sintering of PZT ceramics: Part. 1, Atmosphere control*. Journal of the American Ceramic Society, 1983. **66**(4): p. 253-256.
358. Kingon, A. I. and Clark, J. B., *Sintering of PZT ceramics: Part. 2, Effect of PbO content on densification kinetics*. Journal of the American Ceramic Society, 1983. **66**(4): p. 256-260.
359. He, Z. and Ma, J., *Densification and grain growth during interface reaction controlled sintering of alumina ceramics*. Ceramics International, 2001. **27**(3): p. 261-264.
360. Patel, N. D. and Nicholson, P. S., *Comparison of piezoelectric properties of hot-pressed and sintered PZT*. American Ceramic Society Bulletin, 1986. **65**(5): p. 783-787.
361. Robels, U., Herbiet, R. and Arlt, G., *Coupled losses in PZT near the morphotropic phase boundary*. Ferroelectrics, 1989. **93**(1): p. 95 - 103.
362. Rios, P. R. and Glicksman, M. E., *Topological theory of abnormal grain growth*. Acta Materialia, 2006. **54**(19): p. 5313-5321.
363. Kim, K. W., *et al.*, *Abnormal grain growth of lead zirconium titanate (PZT) ceramics induced by the penetration twin*. Journal of the American Ceramic Society, 2006. **89**(5): p. 1530-1533.
364. Landau, L. D., Zhurnal Eksperimentalnoi i Teoreticheskoi Fiziki, Pisma (Zh. Eksp. Teor. Fiz.), 1937. **7** p. 627.
365. Ginzburg, V. L., *O rasseyanii sveta v zhidkostyakh*. Izvestiya Akademii Nauk Sssr Seriya Fizicheskaya, 1945. **9**(3): p. 174-183 [Journal of Physic USSR. 10, 107 (1946)].
366. Devonshire, A. F., *Theory of barium titanate .Part. 1*. Philosophical Magazine, 1949. **40**(309): p. 1040-1063.

References

367. Devonshire, A. F., *Theory of ferroelectrics*. Advances in Physics, 1954. **3**(10): p. 85-130.
368. Lifshitz, E. M. and Pitaevskii, L. P., *Statistical Physics, Part 2*. Vol. 9. 1980: Pergamon Press.
369. Ginzburg, V. L., *Some remarks on ferroelectricity, soft modes and related problems, Part. 6*. Ferroelectrics, 1987. **76**(1-2): p. 3-22.
370. Levanyuk, A. P., *et al.*, *Improper incommensurate phases - nonanalytic landau free-energy*. Ferroelectrics, 1989. **95**: p. 79-85.
371. Strukov, B. A. and Levanyuk, A. P., *Ferroelectric phenomena in crystals physical foundations*. 1998, Berlin: Springer. X, 308.